The electrocatalytic response of metallophthalocyanines when clicked to electrodes and to nanomaterials

A thesis submitted in fulfilment of the requirement for the degree

Of

DOCTOR OF PHILOSOPHY

Of

Rhodes University

By

Lekhetho Simon Mpeta

September 2020

DEDICATION

To my late mother

('Me' Ithabeleng Berlina Mariti)

Acknowledgements

I would like to pass my grate gratitude to my supervisor **Distinguished Professor Tebello Nyokong** her guidance, insightful comments, support and supervision that made this programme a success, thank you!

I give warm thanks to Ms Gail Cobus organising my first stay at Grahamstown and arranging finances for me.

I also appreciate the National Research Foundation (NRF) research chair for funding this programme.

My final appreciation goes to the S22 lab mates at Rhodes University for making the laboratory a hospitable place for research. I am thankful to their invaluable constructive criticism on my research.

Abstract

Conjugates of nanomaterials and metallophthalocyanines (MPcs) have been prepared and their electrocatalytic activity studied. The prepared nanomaterials are zinc oxide and silver nanoparticles, reduced graphene oxide nanosheets and semiconductor quantum dots. The MPcs used in this work are cobalt (II) (**1a**), manganese(III) (**1b**) and iron (II) (**1c**) 2,9(10),16(17),23(24)- tetrakis 4-((4-ethynylbenzyl) oxy) phthalocyaninato, 2,9(10),16(17),23(24)- tetrakis(5-pentyn-oxy) cobalt (II) phthalocyaninato (**2**), 9(10),16(17),23(24)- tris-[4-tert-butylphenoxy)-2-(4-ethylbezyl-oxy) cobalt (II) phthalocyaninato (**3**), 9(10),16(17),23(24)- tris-[4-tert-butylphenoxy)-2-(pent-4yn-yloxy)] cobalt (II) phthalocyaninato (**4**), cobalt (II) (**5a**) and manganese (III) (**5b**) 2,9(10),16(17),23(24)- tetrakis [4-(4-(5-chloro-1H-benzo [d]imidazol-2-yl)phenoxy] phthalocyaninato and 9(10),16(17),23(24)- tris tert butyl phenoxy- 2- [4-(4-(5-chloro-1H-benzo[d]imidazole-2-yl)phenoxy] cobalt (II) phthalocyaninato (**6**). Some of these MPcs (**1a**, **3** and **4**) were directly clicked on azide grafted electrode, while some (**1b**, **1c**, **2**, **5a** and **5b**) were clicked to azide functionalised nanomaterials and then drop-dried on the electrodes. One phthalocyanine (**5b**) was drop-dried on the electrode then silver nanoparticles were electrodeposited on it taking advantage of metal-N bond. Scanning electrochemical microscopy, voltammetry, chronoamperometry, electrochemical impedance spectroscopy are among electrochemical methods used to characterise modified electrodes. Transmission electron microscopy, X-ray photoelectron spectroscopy, X-ray diffractometry, Raman spectroscopy and infrared spectroscopy were employed to study surface functionalities, morphology and topography of the nanomaterials and complexes. Electrocatalytic activity of the developed materials were studied

towards oxidation of 2-mercaptoethanol, hydrazine and hydrogen peroxide while the reduction study was based on oxygen and hydrogen peroxide. In general, the conjugates displayed superior catalytic activity when compared to individual materials.

Complex **2** alone and when conjugated to zinc oxide nanoparticles were studied for their nonlinear optical behaviour. And the same materials were explored for their hydrazine detection capability.

The aim of this study was to develop sensitive, selective and affordable sensors for selected organic waste pollutants. Conjugates were found to achieve the aim of the study compared to when individual materials were employed.

Table of Contents

List of Abbreviations

AgNPs = Silver nanoparticles

BE = binding energy

CV = cyclic voltammetry

DBU = 1,8-Diazabicyclo [5.4.0]undec-7-ene

DCC = Dicyclohexylcarbodiimide

DMF = Dimethylformamide

DMSO = dimethylsulphoxide

FTIR = Fourier transform infra-red

GCE = glassy carbon electrodes

GPES = general purpose electrochemical system

HOMO = highest occupied molecular orbital

LSV = linear scan voltammetry

LUMO = lowest unoccupied molecular orbital

MPA = mercapto propanoic acid

MPcs = metallophthalocyanines

NPs = nanoparticles

ORR = oxygen reduction reaction

RDE = rotating disc electrode

rGONS = reduced graphene oxide nanosheets

SEM = scanning electron microscopy

SECM = scanning electrochemical microscopy

 TBAB = Tetrabutyl ammonium bromide

TEM = transmission electron microscopy

UME = ultra-micro electrode

UV/vis = ultraviolet/visible

XPS = X-ray photoelectron spectroscopy

XRD = X-ray diffraction

ZONPs = Zinc oxide nanoparticles

List of Symbols

b = the Tafel slope

v = scan rate

α = transfer coefficient,

$n_α$ = number of electrons involved in the rate determining step

K = constant

R = the universal gas constant

T = temperature (298 K)

E_p = peak potential

σ = standard deviation

ΔE = peak potential separation

F = Faraday's constant

I_{cat} = currents in the presence of analyte

I_{buf} = currents in the absence analyte

I_{pa} experimental = Experimental peak current

I_{max} = maximum current

I_{pa} theoretical = theoretical peak current

k_{cat} = the catalytic rate constant

ß = adsorption equilibrium constant

ΔG = Gibbs free energy change due to adsorption

A = effective electrode area

I_l = limiting current

D = diffusion coefficient

V = the kinematic viscosity

ω = rotational

Γ = surface coverage

CHAPTER ONE: Introduction

1. Introduction

This work reports on symmetrical and asymmetrical metallophthalocyanines (MPcs) as electrocatalysts when alone or in the presence of nanomaterials. The MPcs are linked to nanomaterials by click chemistry or by metal-N bond. The nanomaterials employed are reduced graphene oxide nanosheets (rGONS), quantum dots (QDs), silver nanoparticles (AgNPs) and zinc oxide nanoparticles (ZnONPs), there is also a small section on nonlinear optics (NLO) where one Pc is compared for its effectiveness as NLO material or electrocatalyst.

1.1.   Phthalocyanines
1.1.1.   History and general applications

Phthalocyanines (Pcs) are two-dimensional tetrapyrrolic macrocycles containing 18 delocalised π-electrons which are responsible for their intense absorption in the red/near-infrared region [1]. Pcs were first synthesized in 1907 by Braun and Tcherniac, as by-products of the preparation of o-cyanobenzamide from phthalimide and acetic anhydride at high temperature [2]. Phthalocyanine structure was only elucidated later in the 1930s by Linstead and co-workers [3] who later developed synthetic procedures for several metallated phthalocyanines. MPcs have tunable structure since different substituents [4, 5] and central metals [6, 7] can be employed to modify their properties and hence their applications. Due to their remarkable chemical inertness, thermal stability, photo stability and high electronic conjugation, MPcs have widespread applications in nonlinear optics [8-10], photodynamic therapy [11, 12], solar cells [13, 14], as pigments in paint industry [15] and in electrocatalysis [16, 17].

1.1.2. Synthesis

MPcs are generally synthesized by condensation reaction involving substituted precursors. The method is easier to control and cleaner in terms of extent of substitution when compared to direct substitution onto the ring of a pre-existing phthalocyanine. Commonly used phthalocyanine precursors are phthalic anhydride (**1**), phthalic acids (**2**), diiminoisoindoles (**3**), phthalimides (**4**), phthalonitriles (**5**), and o-cyanobenzamides (**6**), Scheme 1.1. Phthalonitriles are more commonly used in the laboratories [18]. When using phthalonitriles, the usual conditions are heating at reflux temperature in the presence of a metal template (for metallated phthalocyanine) in high boiling solvents, for example quinoline and N,N-dimethylaminoethanol (DMAE) [19, 20]. Phthalic anhydrides are used in industrial processes because of low cost [21]. Phthalocyanines can be symmetrical or unsymmetrical depending on the number of precursors used in the synthesis.

1.1.2.1. Symmetrical Metallophthalocyanines

In this case, synthesis of MPcs is achieved by cyclotetramerisation of a phthalonitrile Scheme 1.1, in the presence of a metal salt, a base such as 1, 8-diazabicycloundec-7-ene (DBU) and a suitable solvent as stated above [22, 23].
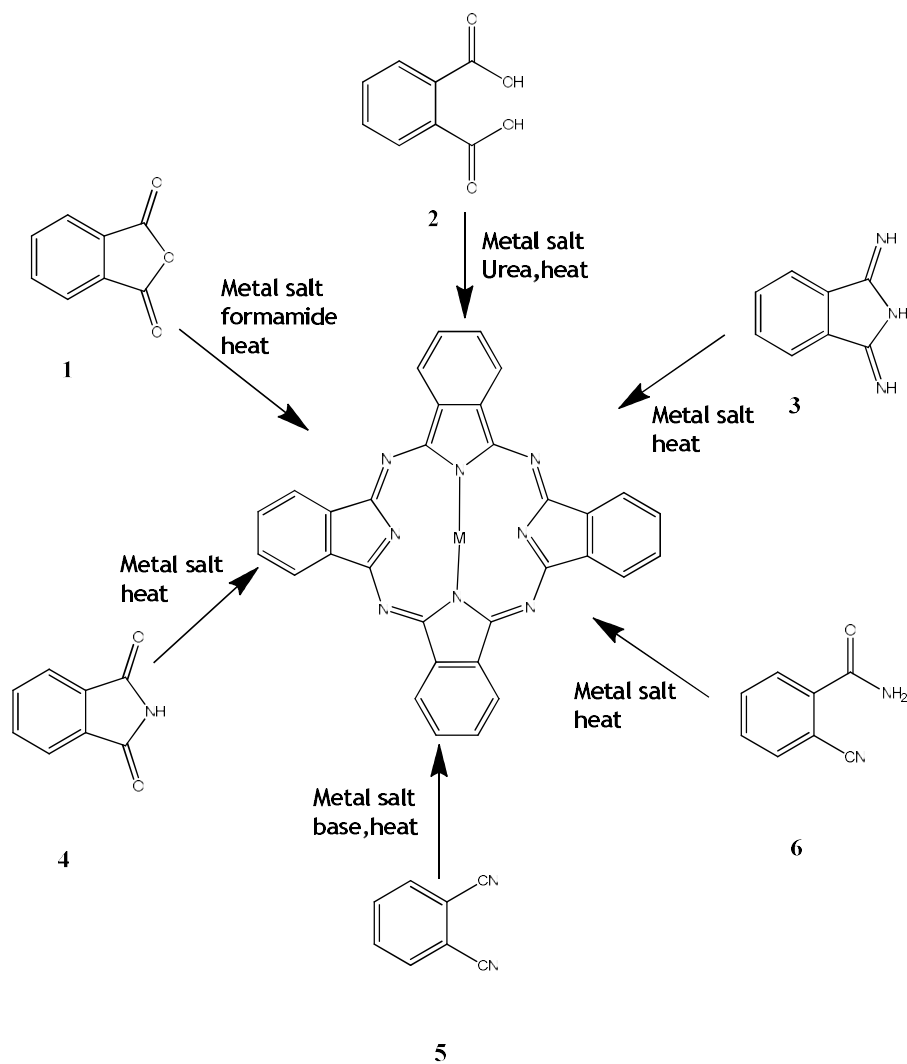
Scheme 1.1: Synthesis routes to metallophthalocyanines via tetramerization of various precursors in presence of a suitable solvent.

In absence of a metal, un-metallated Pc is produced. Un-metallated phthalocyanines (H_2Pc) can also be metallated by heating in the presence of metal or metal salt, using high boiling point solvents.

1.1.2.2. Asymmetrical Metallophthalocyanines

The statistical condensation approach is mainly used for the preparation of the A_3B asymmetric phthalocyanine analogues [24-26]. The method requires two different substituted phthalonitriles (A and B, Scheme 1.2), which upon cyclization reaction give a mixture of six compounds, with the A_3B type Pc being in a good yield, depending on the ratio of the phthalonitriles [27, 28]. Table 1.1 shows the terminal alkynyl MPcs which have been used to modify the electrodes for electrocatalysis [29-35]. As the table shows, there is only one asymmetrical MPc hence this study uses asymmetrical complexes.
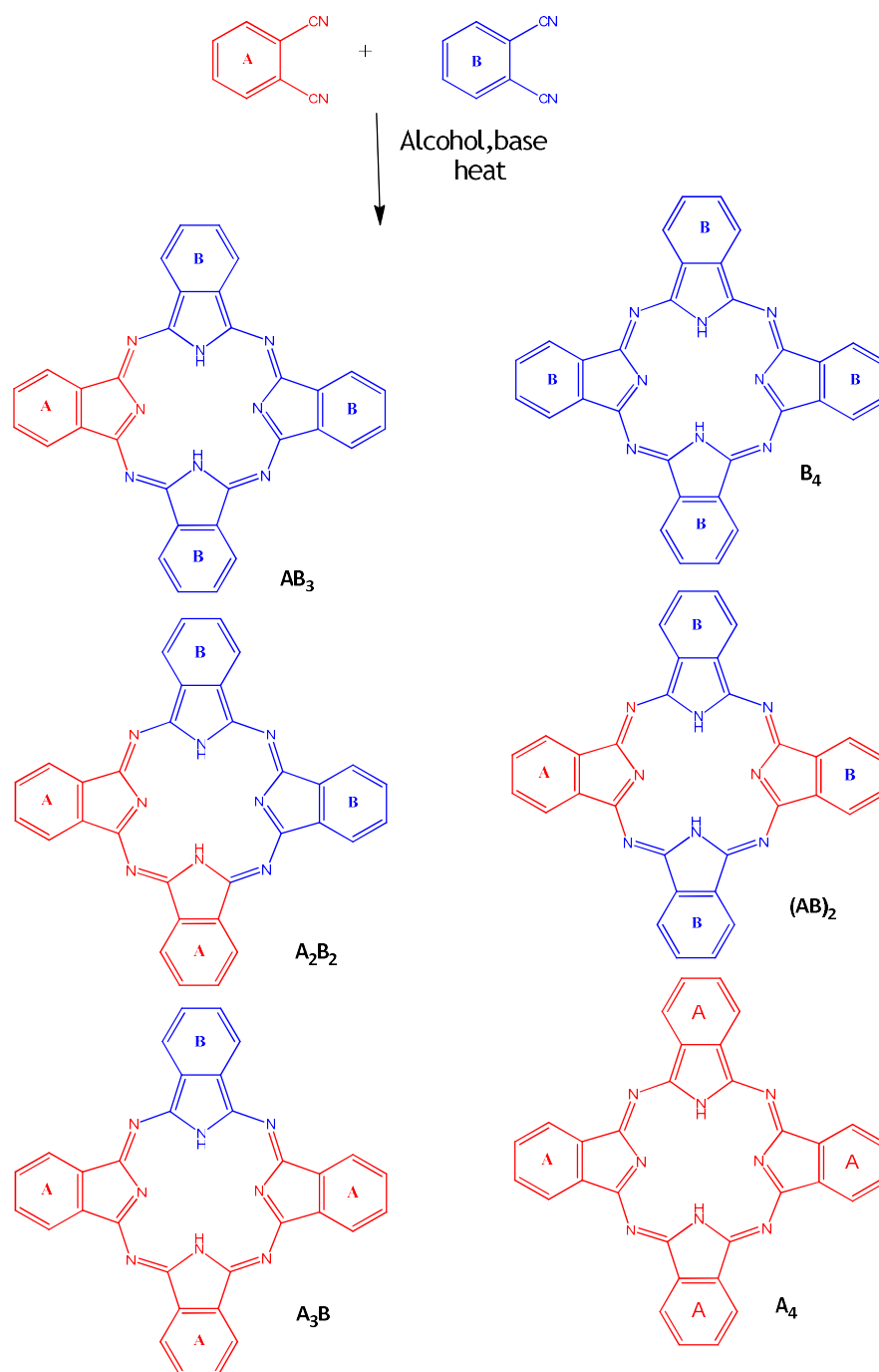
Scheme 1.2: Synthesis of low symmetry phthalocyanines

Table.1.1: Some phthalocyanines molecules bearing alkyn group clicked on to the electrode surface for applications in electrocatalysis.

Structure	Analyte	Electrode	Ref
	Hydrogen evolution reaction (HER)	GCE	[29]
	ORR	GCE	[30]
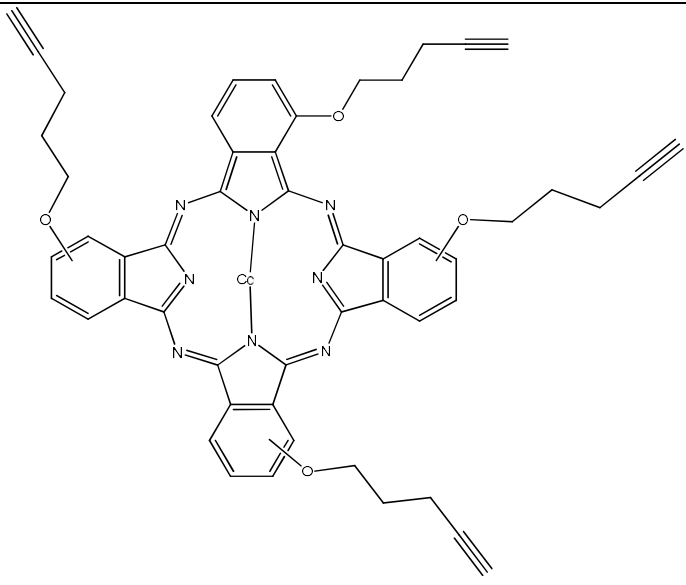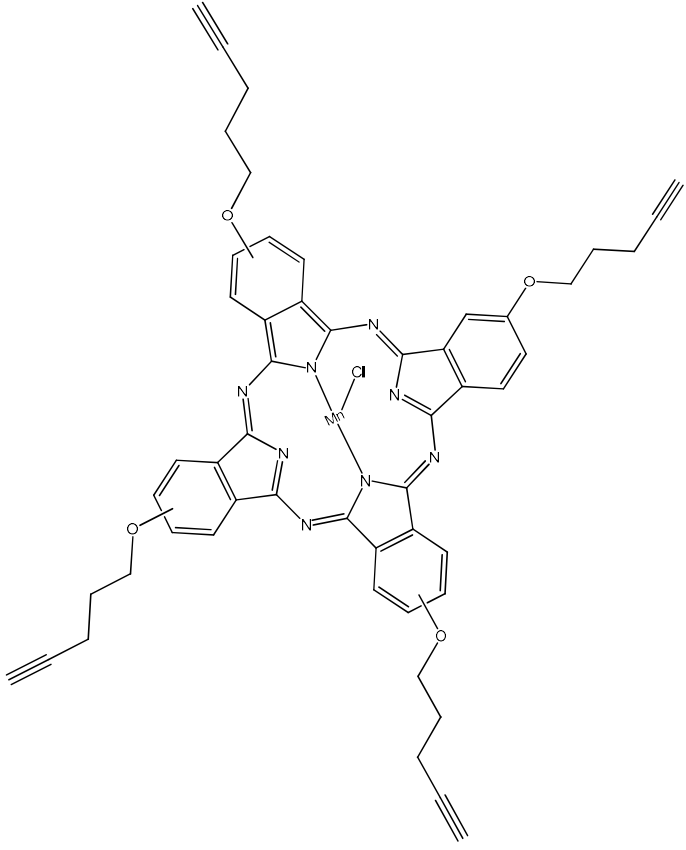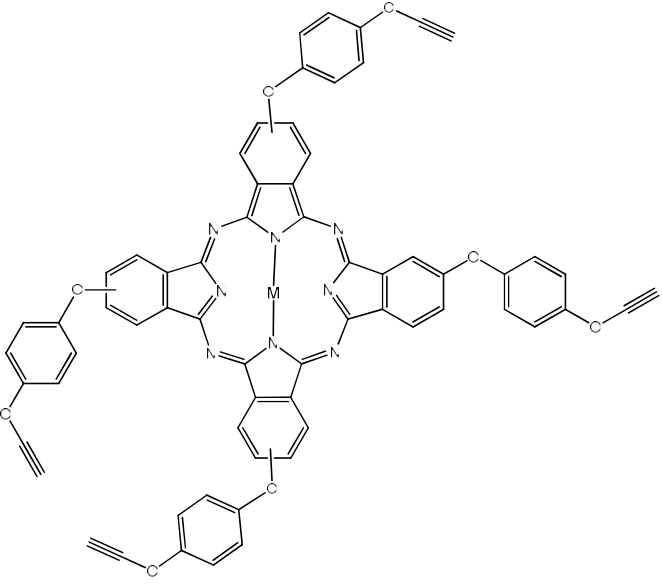
 M= Co or Mn	H₂O₂	Gold electrode	[31]
	Hg(II), Cu(II) Pb(II),Cd(II), As(III)	GCE	[32]
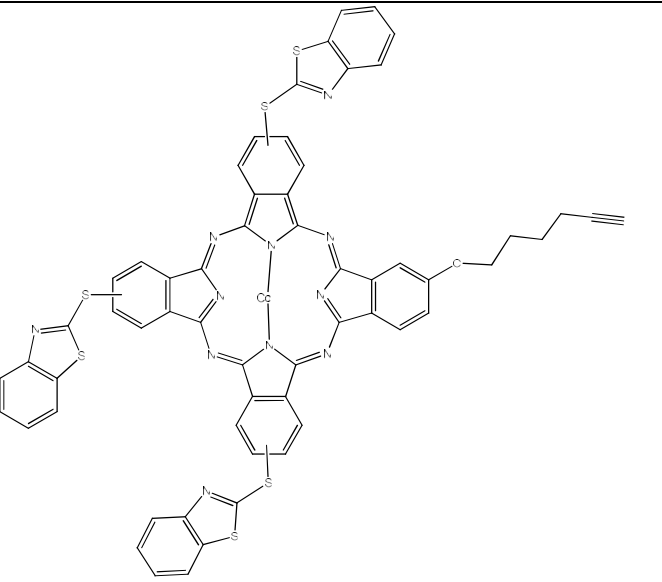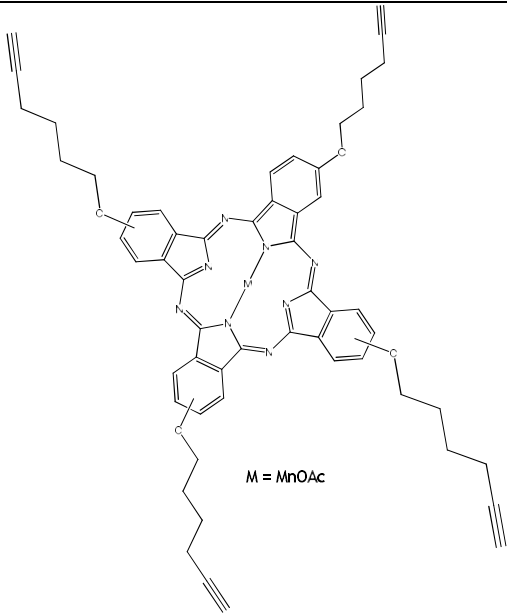
	Hydrazine	GCE	[33]
M = MnOAc			
M = Fe			[34]
M = Co or Ni			[35]

Where GCE= glassy carbon electrode

1.1.3. Metallophthalocyanines employed in this thesis

Table 1.2 shows the MPcs employed in this work, all complexes are new except complex **2.**

Table 1.2: Phthalocyanines used in this work, nanomaterials as well the test analyte

Molecules	Nanomaterials	Analyte	Electrode Modification
  1a = 2,9(10),16(17),23(24)- tetrakis 4-((4-ethynylbenzyl) oxy) cobalt(II) phthalocyaninato **1b =** 2,9(10),16(17),23(24)- tetrakis 4-((4-ethynylbenzyl) oxy) manganese(III) atectate phthalocyaninato **1c =** 2,9(10),16(17),23(24)- tetrakis 4-((4-ethynylbenzyl) oxy) iron(II) phthalocyaninato	QDs azide clicked plus azide rGONS for **1a**	H_2O_2 and O_2	Adsorption of clicked conjugate **1a** also clicked alone
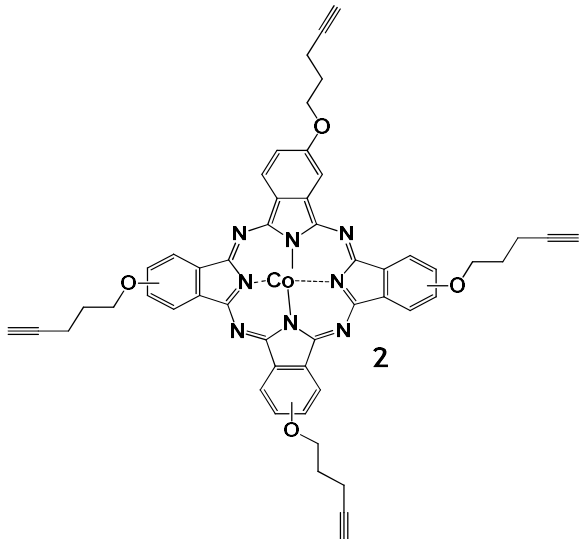
	rGONS azide clicked	2 - ME	Adsorption of clicked conjugate
2 = 2,9(10),16(17),23(24)- tetrakis(5-pentyn-oxy) cobalt (II) phthalocyaninato (Not new) Studied with **1a**			
2	ZnONPs azide clicked	NLO N_2H_4	Adsorption of clicked conjugate

		N₂H₄	Clicked

3 = 9(10),16(17),23(24)- tris-[4-tert-butylphenoxy)-2-(4-ethylbezyl-oxy) cobalt (II) phthalocyaninato
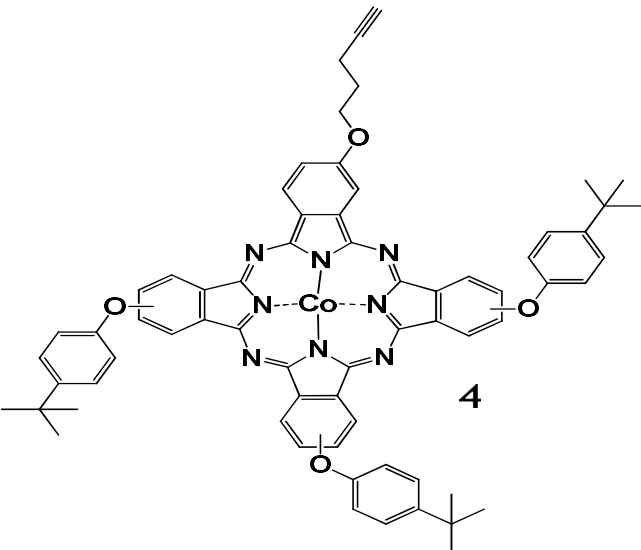
4 = 9(10),16(17),23(24)- tris-[4-tert-butylphenoxy)-2-(pent-4yn-yloxy)] cobalt (II) phthalocyaninato

Studied with **1a**

		N$_2$H$_4$	Electrodeposition **5b**
	AgNPs M-N bond **5b** rGONS (sequential) **5a**		layer sequential (Adsorption) **5a**
5a = 2,9(10),16(17),23(24)- tetrakis [4-(4-(5-chloro-1H-benzo [d]imidazol-2-yl)phenoxy] cobalt(II) phthalocyaninato **5b** = 2,9(10),16(17),23(24)- tetrakis [4-(4-(5-chloro-1H-benzo [d]imidazol-2-yl)phenoxy] manganese(III) chloride phthalocyaninato			
	rGONS	N$_2$H$_4$	sequential (Adsorption)
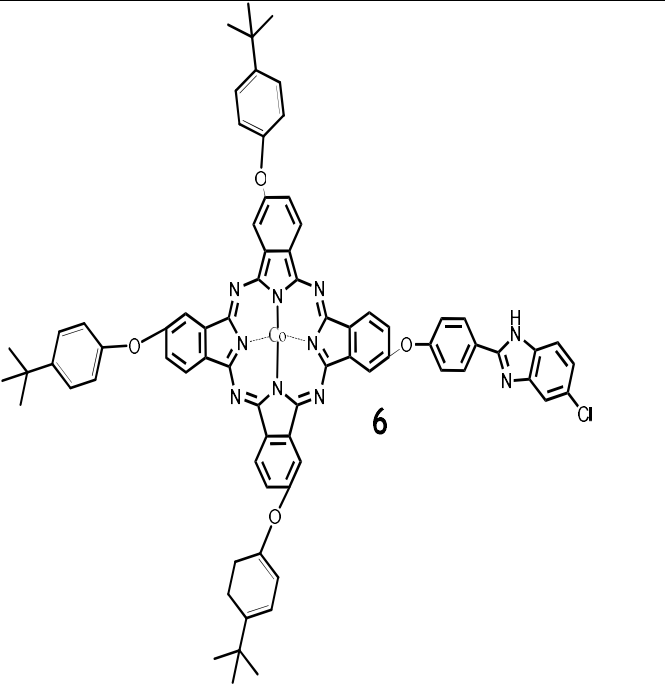
6 = 9(10),16(17),23(24)- tris tert butyl phenoxy-2- [4-(4-(5-chloro-1H-benzo[d]imidazole-2-yl)phenoxy] cobalt (II) phthalocyaninato			

Where QD = semiconductor quantum dots, AgNPs = silver nanoparticles, rGONS = reduced graphene nanosheets and NLO = nonlinear optics, 2-ME = 2-Mercaptoethanol

The complexes in Table 1.2 will be compared as follows.

Group A; Effect of central metal on electrocatalytic behaviour of MPcs

The electrocatalytic property of MPcs are affected by the central metal among other factors. Complex **1** with **Co**, **Mn** and **Fe** as central metals was employed. The other part of this work compares electrocatalytic oxidation of hydrazine using complexes **5a** and **5b** with **Mn** and **Co** as central metals, respectively.

Group B; Effect of nature of substituent

The nature of MPcs substituents also affect the electrocatalytic behaviour of MPcs. Therefore, the effect of substituent was explored by comparing complexes **1a**, **CoPc**, and **2** which consist of substituent having a benzyl ring, without a substituent and aliphatic substituent respectively. These complexes alone and when used with rGONS were compared for electrocatalysis of 2-mecarptoethanol.

Group C; Effect of asymmetry

Whether the MPcs are symmetrical or have low symmetry is reported to have effect on electrocatalytic activity. Some substituents are electron donating due to continuity of the π electron delocalisation and some are electron withdrawing [36, 37]. This thesis compares complexes **1a** with **2** (both are symmetrical), and **3** with **4** (both are asymmetrical) towards electroxidation of hydrazine.

Group D; Effect of different nanomaterial

From the literature, nanomaterials are reported to enhance electrocatalytic activity of MPcs by a synergistic effect [38-40]. MPcs were clicked to rGONS in this thesis to study their catalytic activity. Complex **2** was clicked with ZnONPs and rGONS, and complex **1a** clicked to rGONS and CdTe/ZnS QDs and their electrocatalytic activities in different analytes compared.

Group E; Different applications

The two applications studied in this work are electrocatalysis and nonlinear optics. When MPcs are linked to ZnOPs they are reported to enhance their efficiency for both electrocatalysis [41] and nonlinear optics [42]. Complex **2** when linked to ZnONPs via click chemistry was studied for both electrocatalysis and nonlinear optics applications.

1.2.   Nanomaterials

Nanomaterials are reported to improve electrocatalytic properties of MPcs by synergistic effect, they were therefore conjugated to MPcs in this thesis.

1.2.1. Semiconductor quantum dots

Semiconductor quantum dots (QDs) are colloidal nanocrystalline semiconductors possessing unique properties due to quantum confinement effects. QDs are stable, luminescent and the size can be controlled. The stability of QDs improves their sensitivity and prolong lifetime in their use in sensing. QDs may be functionalized with capping agents which allow for linking to other materials [43, 44]. Due to the availability of precursors and the simplicity of crystallization, Cd-chalcogenide nanocrystals have been the most studies colloidal QDs. Several synthetic methods

have been reported since the first synthesis of the monodispersed CdX (X= S,Se and

Te) nanocrystals [45]. In this thesis, the new MPcs synthesized were conjugated to

QDs via click chemistry for use in electrocatalysis as there is only one reported

example in literature (shown in Table 1.3) [46-49]. Only reference [46] involves

linking via click chemistry. The CdTe core was protected with the shell ZnS to make

CdTe/ZnS (Fig. 1.1) in order to stabilise the quantum dots and ZnS was chosen

specifically to ease coating with a capping agent. QDs were linked to complexes **1**

as examples and used for oxygen and hydrogen peroxide detection.

1.2.2. Graphene oxide nanosheets (GONS)

Graphene is a single-atom-thick sheet of the sp^2-bonded carbon atoms in a hexagonal

two-dimensional lattice, graphene has attracted attention in recent years because

of its unique electrical, catalytic, optical and mechanical properties [50-52]. These

properties make it a good candidate for various applications such as nanoelectronic,

photovoltaic, sensor and catalysis [53-55]. Various methods for preparation of the

high quality GONS have been reported, these include chemical vapour deposition

(CVD) [56], reduction of graphene oxide (GO) [57, 58] and mechanical exfoliation

[59]. Graphene oxide has been used with MPcs for electrocatalysis before [60-71]

because of its good electron transfer properties due to π conjugation however, there

is no reported work (shown in Table 1.3) where MPcs are linked to rGONS via click

chemistry resulting in triazole ring which is known [72] to enhance electron transfer

therefore, this work seeks to close that gap. The representation of rGONS is in Fig

1.1.

1.2.3. Zinc oxides nanoparticles (ZnONPs)

Zinc oxide nanoparticles (ZnONPs) represented in Fig 1.1, are interesting from several points of view. The application of ZnONPs ranges from catalysis to UV-light emitters, transparent high-power electronics, ceramic varistors, surface acoustic wave, and poiezoelectric transducers [73]. There are various reported methods for production of ZnONPs these includes, hydrothermal methods [74], sol-gel methods [75], laser ablation [76], chemical vapour deposition [77], electrochemical deposition [78], thermal deposition [79] and combustion method [80]. The outstanding optical and electrocatalytic of properties of ZnONPs motivated their conjugation to MPc and their subsequent use in non-linear optics and electrocatalysis in this thesis as there is no reported work on ZnONPs clicked to MPcs for sensing and NLO.

1.2.4. Silver nanoparticles (AgNPs)

Sliver nanoparticles (AgNPs) synthesis of much interest to scientific community because of their wide spread applications. They can be synthesized by different methods such as vapour deposition, electrochemical, sol gel, laser pyrolysis and green methods such as by using bacteria, plant extract and fungus [81]. They are used in cancer cell diagnosis and treatment as well as in electrochemical sensing and catalysis [82]. There are reported studies of other metal nanoparticles such as AuNPs and PdNPs being used with MPcs for sensing (Table 1.3) [83-87] but AgNPs have not been reported. The AgNPs were linked to MPc via metal-S bond in this work to study the electrocatalytic effect.

QDs   rGONS

ZnONPs
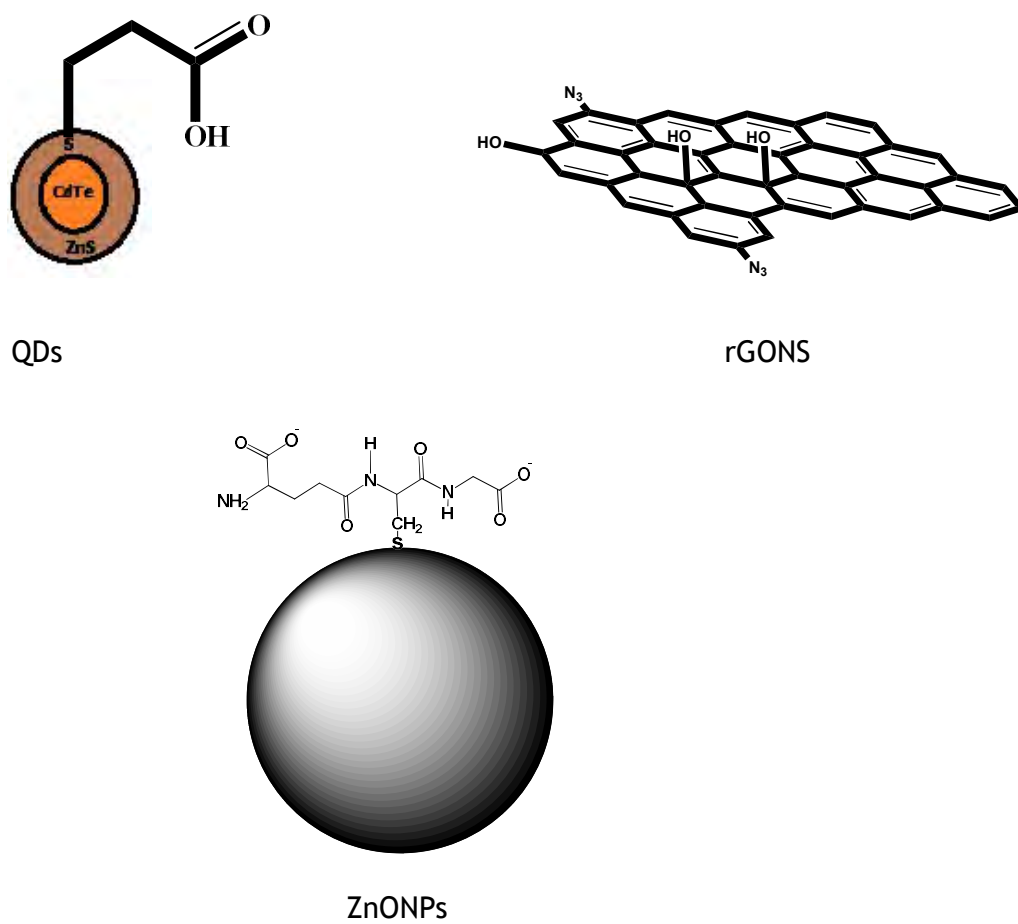
Figure 1.1: Nanomaterials employed in this work

Table.1.3: Examples of carbon nanomaterials, metal nanoparticles linked to MPcs for electrocatalysis.

Conjugate	Applications	Analyte	Ref.
Graphene based nanomaterials			
bi-FePc/rGO	Electrocatalysis	ORR	[60]
CoTCPc/rGO	Electrocatalysis	Hydrogen peroxide	[61]
CoTAPhPcNP-rNDGONS	Electrocatalysis	Hydrogen peroxide	[62]
CoTAPc-rSDGONS	Electrocatalysis	Hydrogen peroxide	[63]
CoTAPc/rGONS,MWCNT			[64]
FePc/GO/CNT	Electrocatalysis	hydrazine	[65]
pCoTAPc/rGO	Electrocatalysis	Cysteine, hydrazine	[66]
ZnPTEPc/rGO	Sensors	Ammonia	[67]
CoTNPc/GO	Electrocatalysis	L-cysteine	[68]
FePc/rGONS	Electrocatalysis	ORR	[69]
CoPc/NDGONS	Electrocatalysis	L-cysteine, reduced L-glutathione, 2-mercaptoethane sulfonic acid	[70]
CoTSPc/GONS	Electrocatalysis	Nitrile	[71]
Metal nanoparticles			
NiTAPc/AuNPs	Electrocatalysis	Hydrazine	[83]
ZnTPPc-AuNPs and InTPPc-AuNPs	NLO		[84]
NiPc/NiNP	Electrocatalysis	Amitrole	[85]
pCoTAPc/PdNPs	Electrocatalysis	Hydrazine	[86]
pNiTSPc/AuNPs	Electrocatalysis	nitrile	[87]
Quantum dots			
NiTAPc/ CdTe-QDs	Electrocatalysis	Chlorophenol	[47]

NiODPc/SWCNT-QDs	Electrocatalysis	pentachlorophenol	[48]
FeTHPc/CdSe /ZnS	Electrocatalysis	Paraquat	[46]
CoTApPc/rGNS/CdSe	Electrocatalysis	ORR	[49]

TAPc= tetra amino Pc, TSPc = tetra sulfo Pc, THPc = tetra hexynyl Pc, TApPc = tetra amino pyrimidin-2-ylthio Pc, ODPc = Octa decyl Pc, TPPc = tetra pentynyl Pc,TAphPcNP= tetra ammino phenoxy nanoparticle, TCPc = tetra carboxy Pc, bi =unsubstituted binuclear Pc, TNPc =tetra nitro Pc, PTEPc = pentinamide tetra ethoxyethoxy, small letter "p" preceding a complexes (CoTAPc and NiTSPc) means they were polymerised. NPs = nanoparticles. rGONS = reduced graphene oxide nanosheets, rNDGONS= reduced nitrogen doped graphene oxide nanosheetS, rSDGONS= reduced sulphur doped graphene oxide nanosheets, NLO = nonlinear optics, ORR= oxygen reduction reaction, CNT = carbon nanotubes

1.3. Electrode modification

MPcs are first immobilised on to the electrode surface, then electrocatalytic study is carried out in a suitable analyte. Therefore, this section deals with methods of electrode modifications.

1.3.1. Drop-dry

Drop-dry involves dispersion of desired electrocatalysts in a solvent such as dimethylformamide, applying to the electrode substrate and allowing to dry. The electrode may be dried in oven if the solvent is not readily volatile. A major advantage of this method is that the electrocatalyst coverage is immediately known from the original solution concentration and droplet volume. Mainly conjugates and sequentially placed materials were used to modify glassy carbon electrodes (GCEs) using this method. For adsorption, the interaction between the macrocycle and support is via $\pi\pi$ interaction.

1.3.2. Electro-grafting (followed by click chemistry)

This method involves reduction of suitable aryl diazonium using electrochemical methods, in this work diazidoaniline was employed. Scheme 1.3 presents the

reaction sequence involved: i) an aryl amine residue is diazotated in presence of NaNO$_2$ and HCl giving an aryl-diazonium, ii) the latter is electro-reduced to an aryl radical. The generated radical attacks the surface (iii) and forms a C-X bond, X being the electrode material [88-90]. In this thesis, the grafted moiety has (R) as an azide functional group which is linked to the MPcs via "Sharpless click" reaction. The Sharpless "click" reaction term was first used in 2001 [91]. A good example of a click chemistry reaction is the Huisgen 1,3-dipolar cycloaddition of azide and alkynes to give triazole linkages [92]. The reaction occurs in the presence of Cu(I) catalyst. This method provides a more stable modification relative to the drop-dry method explained above. Complexes **1a**, **3**, and **4** were clicked to azide grafted GCE using this method. While for complexes **1** and **2** were clicked to nanomaterials before drop-dry method was employed.
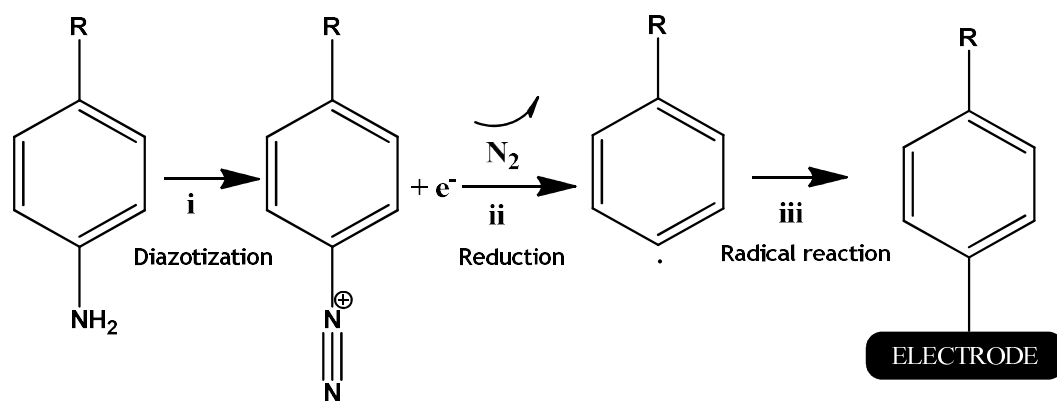
Scheme 1.3: Reaction sequence for the electro-grafting of aryl diazonium modified molecule (R). (The processes i, ii and iii are define under section 1.3.2)

1.3.3. Electrodeposition

Electrodeposition is alternatively called redox deposition. It involves immersion of electrode in an electrolyte solution containing electrode modifier followed by cycling using cyclic voltammetry (CV). This method is used in this work to produce

silver nanoparticles by controlling deposition potential, number of scan rates and electrolyte. Complex **5b** was used with AgNPs to modify GCE using this method.

1.4.   Basics of electrocatalysis

Electrocatalysis is the heterogeneous catalysis of electrochemical reactions, which occur at the electrode-electrolyte interface and where the electrode plays both the role of electron donor/ acceptor and of catalyst. The effect of electrocatalysis is to increase of rate of the electrode reaction, which results in an increase of the Faradaic current [93]. As the current increase can be masked by other non-electrochemical rate-limiting steps, the most straightforward indication for the electrocatalytic effect is the lowering of overpotential at a given current density. Electrocatalysis, as with chemical catalysis, can either be homogenous or heterogeneous in character. In the case of homogenous electrocatalysis, both the catalysts and the substrate are in the same phase in solution. In heterogeneous electrocatalysis, the catalyst is immobilised on the electrode surface. MPcs exhibit catalytic activity for the electrochemical oxidation and reduction of a variety of target analytes in both homogenous and heterogeneous phases [94, 95]. Fig. 1.2 shows the MPc facilitated electron transfer steps during the oxidation of an analyte at the MPc modified electrode surface utilising M^{III}/ M^{II} redox couple. The MPcs act by lowering the overpotential of oxidation or reduction of the target analytes, and are known to mediate the redox process at the central metal and/or ring [96, 97]. The mechanism for the electrocatalytic oxidation process due to the metal centre is given by equations (1.1) and (1.2) [98].

$$M\,(II)Pc(-2) \rightarrow M\,(III)Pc(-2) + e^- \qquad\qquad (1.1)$$

$$M\,(III)Pc(-2) + A \rightarrow M\,(II)Pc(-2) + A_{ox}\ (\text{oxidised species}) \qquad (1.2)$$
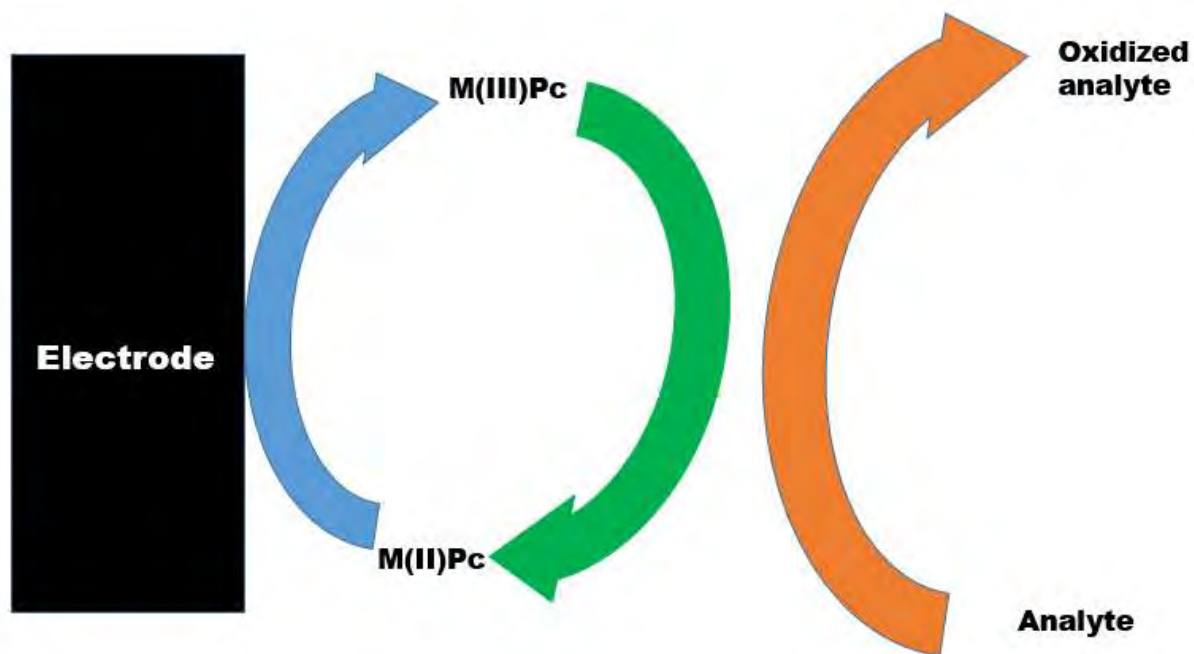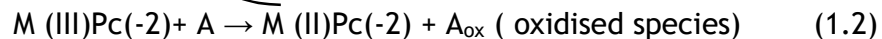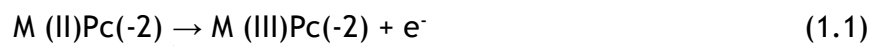
Figure 1.2: Schematic presentation of electroctrocatalytic process promoted by MPc immobilized on the electrode [98].

1.5. Test analytes used in this work

The developed electrocatalysts in this work were tested on analytes such as hydrazine, hydrogen peroxide, oxygen and 2-mercapto ethanol. Analytes different from each other were studied because electrocatalysts are specific to analytes.

1.5.1. Hydrazine

Hydrazine and its simple methyl and dimethyl derivatives have endothermic heats of formation and high heats of combustion. Therefore, these compounds are used as rocket fuels [99]. Hydrazine has been used as a synthetic intermediate to produce several different types of drugs such as carbidopa, dihydralazine, nifuroxazide, isoniad and hydralazine [100]. Having two active nucleophilic nitrogens and four replaceable hydrogens, hydrazine is the starting material for many derivatives such as foaming agents [101] for plastics, antioxidants, polymers, polymer cross-linkers and chain extenders [102], as well as fungicides, herbicides, plant-growth regulators and pharmaceuticals [103]. Hence there is a need to monitor the levels of hydrazine in the environment. As Table 1.1 shows hydrazine has been studied in the presence of MPcs, this time MPcs are incorporated with nanomaterials.

1.5.2. Oxygen reduction

Oxygen is used as a reactant in fuel cells. Fuel cells produce energy in a more efficient and cleaner way than combustion [104]. The oxygen reduction reaction (ORR) has traditionally been carried out with noble metals such as Pt and metal oxides such as RuO_2 and MnO_2 as catalyst. Platinum is very costly and is susceptible to poisoning. Research is now shifted to using non noble metal based metals and non-metal based catalysts. ORR has been studied on alkyl MPcs (Table 1.1), this work combines MPcs with QDs for improved ORR.

1.5.3. Hydrogen peroxide

Hydrogen peroxide is one of the 100 most important chemicals in the world [105]. It is freely miscible with water and reported to be able to cross cell membranes readily, although the pathways it uses to traverse have not been elucidated [106].

The hydrogen peroxide concentrations more than 50 µM are reported to be cytotoxic to a wide range of animals [106], plants and bacterial cells in culture. Hydrogen peroxide is widely used in bleaching agents [107], in wastewater treatment [108], for paper pulp processing and for textile manufacturing [109]. Hydrogen peroxide is produced as an intermediate in fuel cells during oxygen reduction (via 2 electron reaction) at the cathode, it is not a desirable intermediate as it degrades the membranes used in fuel cells, resulting in the decrease of efficiency of the fuel cell. This work reports on the MPcs linked to QDs via click chemistry for detection of hydrogen peroxide. Alkyl MPcs have been used for H_2O_2 but this work is with nanomaterials.

1.5.4. 2-Mercaptoethanol

2-Mercaptoethanol is a liquid at room temperature and possesses a strong unpleasant smell [110]. Is it used in various applications such as brightening agent in copper deposition, ingredient in hair permanent chemicals, corrosion inhibition in steel, a reagent for diagnostic bioassays [111]. MPcs have been used for detection of 2-ME, this thesis is with nanomaterials.

1.6. Nonlinear optics

Nonlinear optics is a study on how light interacts with matter at high intensity. Optical limiting is a specific branch of nonlinear optics, and deals with how certain materials are able to regulate light intensity. This means that certain materials do not transmit light linearly at the high intensities, but, instead, have a fixed intensity transmission. Limiting threshold intensity (I_{lim}) is an important term in the optical liming measurements which may be defined as the input fluence (or energy) at which

the transmittance is 50% of the linear transmittance, Fig. 1.3 [112]. When the I_{lim} value is lower that means the material is a better optical limiter.

Ideally, the output energy of a limiter increases linearly with the input energy until a threshold (I_{lim}) is reached as shown in Fig. 1.4 [112]. After the threshold, the output energy is clamped at a given value, for all input intensity beyond the I_{lim}. This work focuses on the optical limiting that result from nonlinear absorption (NLA). For an optical limiter to be good, it should limit nanosecond or sub-nanosecond light pulses in a wide range of the UV-vis spectrum.
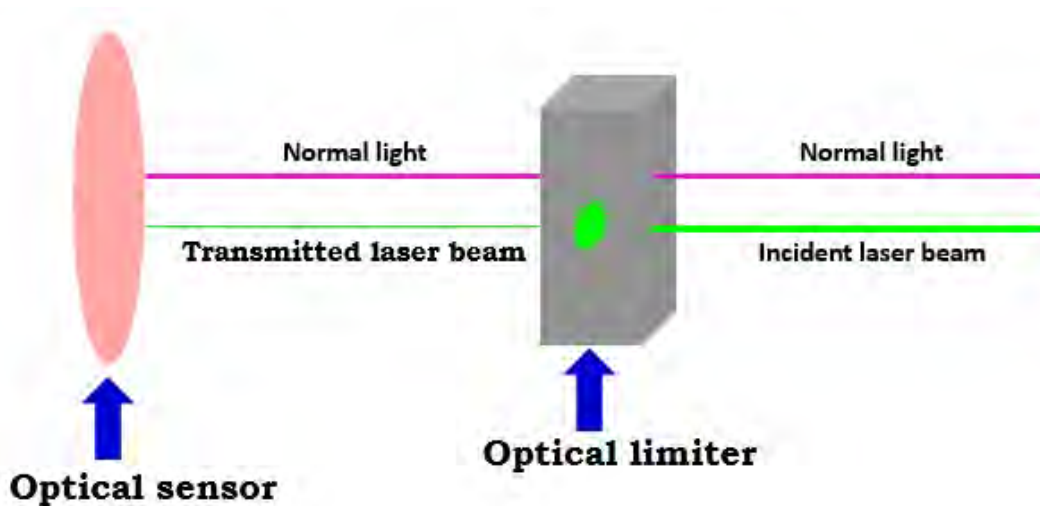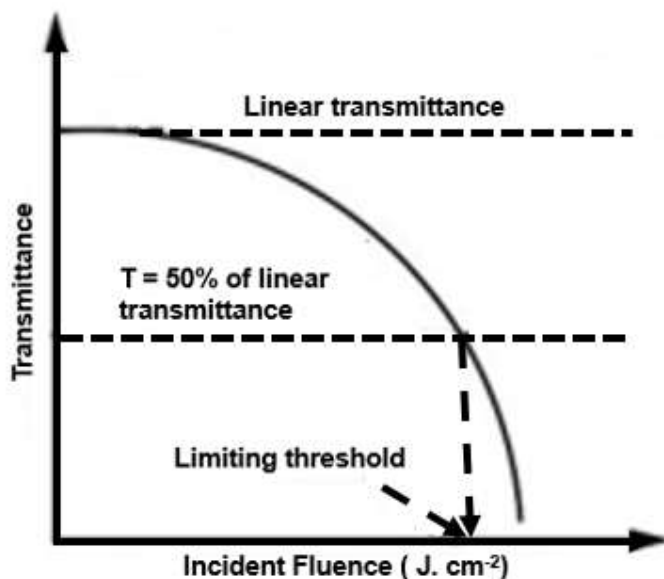
Figure 1.3: The behaviour and an explanation of an optical limiter [112]
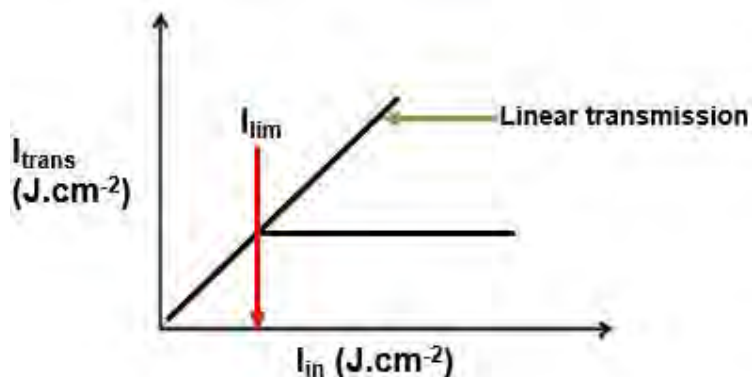
Figure 1.4: The behaviour of an ideal optical limiter, I_{trans} = transmitted fluence, I_{in} = incident fluence.

In this thesis, open aperture Z-scan technique was employed. In Z scan, a sample is allowed to pass through from one point to the other along the path (Z) of a focused Gaussian beam and the transmittance is measured as a function of the sample's position relative to the focus, Fig. 1.5 [113]. There is only one example of alkynyl

Pcs being used in the presence of nanomaterials for NLO [84] hence the interest in this work.
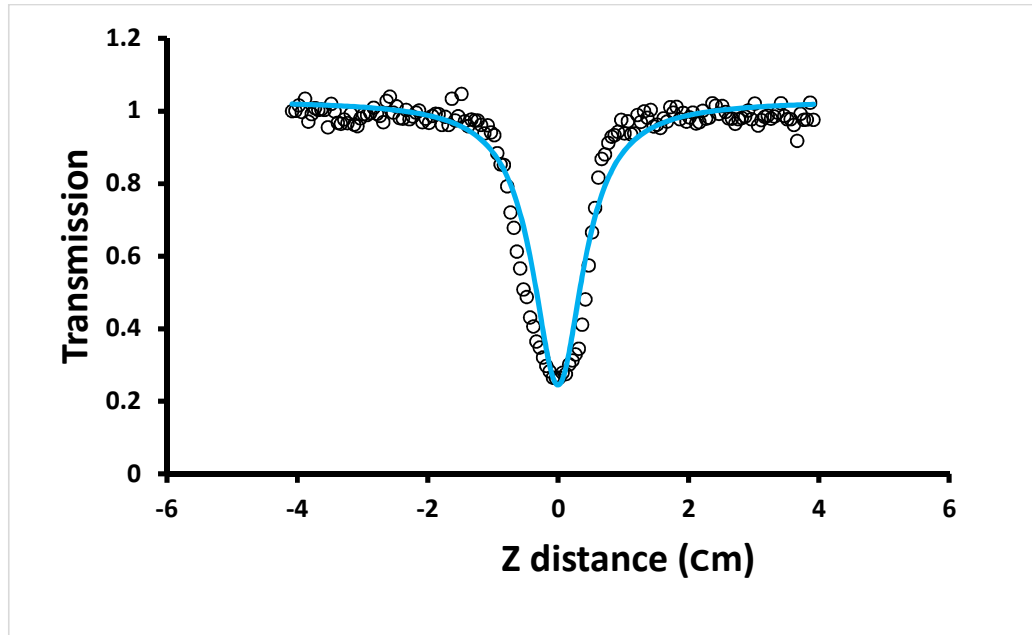
Figure 1.5: Z-scan profiles of InPc in DMF. Open circles represent experimental data while solid line is a theoretical fit [113].

In this work, the signatures from Z scan plots were simulated using Sheik-Bahae treatment for the normalised transmittance ($T_{norm}(z)$) as a function of z-position [114], using Eqn. 1.3.

$$T_{Norm}(z) = \frac{1}{[1+(n-1)\beta_{eff}L_{eff}(\frac{I_0}{1+(\frac{z}{z_0})^2})^{n-1}]^{\frac{1}{n-1}}} \qquad (1.3)$$

where I_0 (maintained at 0.87 GW.cm^{-2} throughout the experiment) represents the intensity of the beam at the focus for two photons absorption (n = 2). z and z_0 respectively represent sample position with respect to the input intensity and

Rayleigh length (which is defined by $\dfrac{\pi w_0^2}{\lambda}$; λ = wavelength of the laser beam and w_0

= beam waist ($\sim$ 2.56 x10^{-3} cm) at the focus (z = 0). β_{eff} is the two-photon nonlinear

absorption coefficient.

L_{eff} is the effectiveness of the sample and is given by Eqn. 1.4.

$$L_{eff} = \frac{1 - e^{-\alpha L}}{\alpha}$$ (1.4)

In Eqn. 1.4, α and L respectively represent the linear absorption coefficient and the

thickness of the sample. After obtaining the β_{eff} values from the linear regression

technique, the third order optical susceptibility ($Im[\chi^{(3)}]$ in esu) which is an

imaginary component was calculated using Eqn. 1.5 [7].

$$Im[\chi^{(3)}] = \frac{(n_0^2 \varepsilon_0 c \lambda \beta_{eff})}{(2\pi)}$$ (1.5)

In Eqn. 1.5, c and n_0 represent the speed of light in vacuum and the linear refractive

index respectively. ε_0 is the permittivity of free space and λ is the wavelength of the

laser light.

There is a direct correlation at a molecular level of $Im[\chi^{(3)}]$ in esu with the

hyperpolarization which gives the nonlinear absorption per mole of the sample

through the relationship shown in Eqn. 1.6 [7]:

$$\gamma = \frac{Im[\chi^{(3)}]}{N^* f^4}$$ (1.6)

where $N^* = C_{mol} N_A$ (C_{mol} represents the concentration of active species in the

excited state in mol), N_A is the Avogadro constant, while f represents Lorenz local

field and is given by Eqn. 1.7:

$$f = \frac{n^2 + 2}{3} \qquad\qquad\qquad (1.7)$$

1.7.   Summary of aims of thesis

The aims of this work are stated below

(a) Synthesis of new MPc complexes with alkynyl terminated substituent in order to enable them to be clicked either directly to the electrode or to the nanomaterials.

(b) Fabrication of rGONS, ZnONPs and CdTe/ZnS QDs nanocomposites with MPcs via click chemistry while AgNPs-MPc was via metal-N bonds.

(c) Investigation of the surface properties of the modified electrodes utilising both electrochemical and non-electrochemical methods.

(d) Application of modified electrodes towards electrocatalysis of hydrazine, hydrogen peroxide, ORR, and 2-mercaptoethanol and to a lesser extend the composites were used for nonlinear optics application.

(e) Investigation of the electrode kinetics associated with the electrocatalysis of the analytes.

(f) Investigation of the kinetics occurring at nanocomposite catalyst/ electrolyte interface.

(g) Investigation of the effect of the nanoparticles on the nonlinear optical properties of MPc.

CHAPTER TWO: Experimental

2. Experimental

2.1. Materials

2.1.1. General reagents

Tetrabutylammonium tetrafluoroborate (TBABF$_4$), 4-azidoaniline hydrochloride, bromo tris (triphenylphosphine) copper (I) (Cu (PPh$_3$)$_3$Br), 1,8–diazobicyclo [5.4.0] undec-7-ene (DBU), hydrazine, trimethylamine and cobalt chloride, hydrogen peroxide, 2-mercaptoethanol, sodium azide, potassium cyanide, silver nitrate, manganese chloride, dimethylethylamine (DMEA), trimethylamine (TEA), manganese (III) acetate (Mn(Ac)), iron (II) chloride, 1-ethyl-3-(3-imethylaminopropyl)-carbodiimde (EDC), iron ferricyanide, iron ferrocyanide, lithium chloride, and N-hydroxyl succinimide (NHS) were obtained from Sigma-Aldrich. Alumina (~0.05, 0.3, 1, 10 µm) was obtained from Unilab. 4-Azidobenzenediazonium tetrafluoroborate salt was synthesized from 4-azidoaniline hydrochloride *in situ* as reported in literature [115].

2.1.2. Solvents

Tetrahydofuran (THF), chloroform, dimethylformamide (DMF), acetonitrile (ACN) and acetone were purchased from Merck. Millipore water was obtained from Milli-Q Water Systems (Millipore Corp. Bedford, MA, USA).

2.1.3. Phthalonitrile synthesis

Syntheses of 4-ethynylbenzyl phthalonitrile (**i**) [116], 4-*tert*-butylphenoxy phthalonitrile (**ii**) [117], 4(pent-4-yn-1-yloxy) phthalonitrile (**iii**) [118] and 4-(4-(5-chloro-1H-benzo[d]imidazol-2-yl)phenoxy) phthalonitrile (**iv**) [119] have been reported in literature.

2.1.4. Phthalocyanines and nanoparticles

Cobalt phthalocyanine (CoPc) was obtained from Sigma-Aldrich. The syntheses of 2,9(10),16(17),23(24)-tetrakis(pent-4-ynoxy) phthalocyaninato cobalt(II) (**2**) [120], rGONS [121] have been reported. Glutathione (GSH) capped ZnO nanoparticles [122] and CdTe/ZnS quantum dots capped with 3-mercaptopropionic acid (MPA) [123] were synthesized as reported in the literature.

2.2. Equipment

- Ultra violet-visible (UV-Vis) absorption spectra were recorded using Shimadzu UV-2250 spectrophotometer.

- Scanning electron microscopy (SEM) images of modified glassy carbon plates (Goodfellow, UK, 1 × 1 cm and 2 mm thick) were obtained using a TESCAN Vega TS 5136 LM electron microscope.

- Infrared (IR) spectra were recorded on a Bruker Alpha IR (100 FT-IR) spectrophotometer.

- Elemental analysis was done using a Vario–Elementar Microcubes ELIII

- Mass spectra data were collected on a Bruker AutoFLEX III Smart-beam TOF/TOF mass spectrophotometer using α-cyano-4-hydrocinnamic acid as the matrix in the positive ion mode.

- Dynamic light scattering (DLS) measurements were performed using a Malvern Zetasizer Nanoseries, Nano-ZS90

- Transmission Electron Microscopy (TEM) images were obtained from a Zeiss Libra TEM 120 model operated at 90 Kv

- Energy dispersive X-ray (EDX) spectrometer (INCA PENTA FET coupled with VAGA TESCAM operated at 20 kV)

- Magnetic circular dichroism (MCD) spectra were measured with a Chirascan plus spectrodichrometer equipped with a 1 T (tesla) permanent magnet by using both the parallel and antiparallel fields.

- Cyclic voltammetry (CV), chronoamperometry (CA) and chronocoulometry (CC) were performed using Autolab potentiostat PGSTAT 302 electrochemical work station (driven by GPES software version 4.9).

- Electrochemical impedance spectroscopy (EIS) studies were performed using an Autolab Potentiostat PGSTAT30 equipped with GPES software version 4.9. The studies were performed between 1.0 Hz and 10 kHz, using a 5 mV rms sinusoidal modulation. A non-linear least squares (NLLS) method based on the EQUIVCRT programme was used for automatic fitting of the obtained EIS data.

- BAS 100B electrochemical analyser was used for the rotating disk electrode (RDE) studies.

- Scanning electrochemical microscopy (SECM) experiments were carried out using Uniscan Model 370 equipment and a 25 μm Pt microelectrode (Uniscan) as the tip. SECM approach curves were done using the Pt microelectrode with a Pt counter electrode and Ag|AgCl wire as the pseudo-reference electrode in $K_3[Fe(CN)_6]/K_4[Fe(CN)_6]$ solution following oxidation at 0.1 V vs. Ag|AgCl.

- X-ray photoelectron spectroscopy (XPS) analysis was done using an AXIS Ultra DLD, with Al (monochromatic) anode equipped with a charge neutraliser, supplied by Kratos. Curve fitting was performed using a Gaussian-Lorentzian peak shape after performing a linear background correction. Glassy carbon plates (Goodfellow, UK) of 1×1 cm and 2 mm thick were used as substrates for SECM and XPS.

- X-ray diffraction (XRD) patterns were performed on a Bruker D8 Discover diffractometer, equipped with a LynxEye detector, under Cu-Kα radiation (λ= 1.5405 Å). Data were collected in the range from 2θ = 10° to 100 °, scanning at 0.010° min^{-1} and 192 s per step.

- All Z-scan experiments described in this study were performed using a frequency-doubled Nd:YAG laser (Quanta-Ray, 1.5 J/10 ns fwhm (full width at half maximum) pulse duration) as the excitation source. The laser was operated in a near Gaussian transverse mode at 532 nm (second harmonic), details have been provided before [124]. The Z-scan experiments were done in THF at room temperature. Complex **2** and its conjugate were dissolved in DMF and solutions of UV-Vis absorbance of 1, 1.5, 2, 2.5 and 3 made. The Z-scans were then recorded for solutions.

2.3. Synthesis of MPcs

2.3.1. Complexes 1a, 1b and 1c, Scheme 3.1

Mixtures of 4-ethynylbenzyl phthalonitrile (**i**) (0.20 g, 0.77 mmol), (0.3 mL) DBU in 1-pentanol (5 mL) and manganese(III) acetate (0.28 g, 0.77 mmol) for **1c** or iron (II) chloride (0.10 g , 0.77 mmol) for **1b**, cobalt (II) chloride (0.23 g, 1.80 mmol) for **1a** were heated at reflux temperature under argon for 15 h. The mixtures were then allowed to cool and methanol was added to precipitate the product, which was further collected by centrifugation. The complexes were purified by column chromatography over silica gel using chloroform as eluent. Chloroform was removed with rotary evaporator under reduced pressure at 85 °C.

1c: Yield: 0.24 g (22%). IR (cm^{-1}): 3553 (C≡C), 1622 (C=C), 3090 (C-H), 3090 (C-H). UV/Vis (DMF), λmax nm (log ε): 668 (3.95), 604 (3.29), 340 (3.49). Anal. Calculated

($C_{70}H_{43}N_8O_6Mn$): C 73.29%, H 3.78%, N 9.77%. Found: C 73.41%, H 3.68%, N 9.76%.

MALDI-TOF-MS (m/z): found = 1146.17; cald = 1146.27 [M] $^+$.

1b: Yield: 0.33 g (35%). IR (cm^{-1}): 3553 (C≡C), 1622 (C=C), 3090 (C-H), 3090 (C-H).

UV/Vis (DMF), λmax nm (log ε): 720 (4.82), 648 (4.12), 340 (4.39). Anal. Calculated:

$C_{68}H_{40}N_8O_4Fe$): C 75.07%, H 3.93%, N 10.15%. Found: C 75.01%, H 3.90%, N 10.20%.

MALDI-TOF-MS (m/z): found = 1088.12; cald = 1088.25 [M] $^+$.

1a: Yield: 0.2421 g (22%). IR (cm^{-1}): 3553 (C≡C), 1622 (C=C), 3090 (C-H), 3090 (C-H).

UV/Vis (DMF), λmax nm (log ε): 668 (4.92), 604 (4.19), 340 (4.44). Anal. Calculated:

C 74.79%, H 3.69%, N 10.26%. Found: C 74.60%, H 3.53%, N 10.22%. MALDI-TOF-MS

(m/z): found = 1091.11; cald = 1091.23 [M] $^+$.

2.3.2. Complex 3, Scheme 3.2

4-*Tert*-butylphenoxy phthalonitrile (**ii**) (0.45 g, 4.42 mmol) and 4-ethybylbenzyl

phthalonitrile (**i**) (0.142 g, 1.12 mmol) were were dissolved in 1-pentanol (3 mL).

Anhydrous cobalt chloride (0.124 g, 2.11 mmol) was added to the mixture in the

presence of catalytic amounts of DBU. The temperature of the reaction mixture was

adjusted to 140 ^{o}C and stirred for 18 h under a nitrogen atmosphere. After cooling

to room temperature, the dark blue mixture was diluted with methanol and the

formed precipitate was collected by centrifugation. The resultant product was

purified by column chromatography over silica gel eluting with CHCl$_3$ and a gradient

of CHCl$_3$–methanol up to 5% methanol to give pure complex (**3**).

Yield: 0.142 g (25%). FT-IR (UATR-TWO^{TM}) ν max/cm^{-1}: 3203 (H-C≡C2918-2850

(Aliph,-C-H), 1599(Ar -C=C-), 1467, 1357 (C-C), 1231 (Ar-O), 1091 (Ar-O-), 741.

UV/Vis (CHCl$_3$): λmax nm (log ε) 668 (4.92), 610 (4.22), 326 (4.34). Anal. Calc. for

$C_{71}H_{58}CoN_8O_4$ (%): C, 74.40; H, 5.10; N, 9.78; Found (%): C, 74.21; H, 5.06; N, 9.64.

MS (MALDI-TOF): (m/z) cald = 1145.16, found = 1145.39 [M] $^+$

2.3.3. Complex 4, Scheme 3.2

Complex **4** was synthesized and purified as for complex **3** except 4-*tert*-butylphenoxy phthalonitrile (**ii**) (0.53 g, 4.42 mmol), 4-(pent-4-yn-1-yloxy) phthalonitrile (**iii**) (0.12 g, 1.03 mmol), anhydrous cobalt chloride (0.14 g, 2.10 mmol) were used.

Yield: 0.131 g (21%). FT-IR (UATR-TWO^{TM}) ν max/cm^{-1}: 3214 (H-C≡C), 2916-2846 (Aliph,-C-H), 1602(Ar -C=C-), 1469,1360 (C-C), 1230 (Ar-O), 1092 (Ar-O-), 719. UV/Vis (CHCl$_3$): λmax nm (log ε) 668 (4.94), 603 (4.28), 329 (4.46). Anal. Calc. for $C_{67}H_{58}CoN_8O_4$ (%): C, 73.28; H, 5.32; N, 10.20; Found (%): C, 73.12; H, 5.03; N, 10.08. MS (MALDI-TOF): m/z cald = 1097.39, found = 1098.61, [M+H] $^+$.

2.3.4. Complex 5a, Scheme 3.3

The 4-(4-(5-chloro-1H-benzo[d]imidazol-2-yl)phenoxy)phthalonitrile (**iv**) (100 mg, 0.27 mmol) were mixed with CoCl$_2$ (9 mg, 0.067 mmoL) and catalytic amount of DBU in DMAE (3 mL). The mixture was degassed by nitrogen and stirred at 140 ºC for 18 h. After cooling to the room temperature, the reaction mixture was precipitated by adding water-methanol (1:1). The precipitate was collected by centrifugation, washed several times with ethanol. The purification of the crude product was performed by column chromatography on silica gel (eluent: CHCl$_3$/THF-100/10).

Yield: 51% (0.042 g). FT-IR (UATR-TWO^{TM}) ν max/cm^{-1}: 3480 (NH), 3113-2847 (C-H (Ar) and intermolecular H bonding), 1594, 1460-1332, 1228, 1114, 835. Anal. Calc. for $C_{84}H_{44}Cl_5CoN_{16}O_4$ (%): C, 64.12; H, 2.82; N, 14.24; Found (%): C, 63.65; H, 2.79;

N, 14.36 MALDI-TOF-MS (m/z): cald = 1542.10 [M] $^+$; found = 1542.70 [M]$^+$. UV–Vis (DMF): λmax (nm) (log ε) 315 (4.99), 601 (4.42), 663 (5.04).

2.3.5. Complex 5b, Scheme 3.3

4-(4-(5-Chloro-1H-benzo[d]imidazol-2-yl)phenoxy) phthalonitrile (**iv**) (0.1 g, 0.27 mmol), anhydrous MnCl$_2$ (0.017 g, 0.14 mmol) and catalytic amount of DBU were dissolved in n-hexanol (2.5 ml). The reaction mixture was purged with argon at room temperature and heated up to 150 °C for 18 h. Then, the reaction mixture was cooled down to room temperature, the product was precipitated by adding methanol/LiCl (0.003g) mixture. The precipitate was collected by centrifugation, washed several times with ethanol, acetone and water remove the soluble by-products and any un-reacted metal salt. The desired pure product was collected by dissolving in DMF and re-precipitating with methanol. Complex **5b** was also synthesized without the addition of LiCl and purified as indicated above and used only for UV-Vis spectral studies to show aggregation without LiCl.

Yield: 0.060 g (56%). FT-IR (UATR-TWO^{TM}) ν max/cm^{-1}: 3480 (NH), 3113-2847 (C-H (Ar) and intermolecular H bonding), 1594, 1460-1332, 1228, 1114, 835. Anal. Calc. for C$_{84}$H$_{44}$Cl$_5$MnN$_{16}$O$_4$ (%): C, 64.12; H, 2.82; N, 14.24; Found (%): C, 63.98; H, 2.80; N, 14.19. MALDI-TOF-MS (m/z): cald = 1573.56 [M] $^+$; found = 1539.18 [M-Cl]$^+$. UV–Vis (DMSO): λmax (nm) (log ε) 372(4.01), 650 (4.82), 715 (4.38).

2.3.6. Complex 6, Scheme 3.4

4-(4-(5-Chloro-1H-benzo[d]imidazol-2-yl)phenoxy)phthalonitrile (**iv**) (100 mg, 0.27 mmol) and 4-*tert*-butylphenoxy phthalonitrile (**ii**) (224 mg, 0.81 mmol) were dissolved in 1-pentanol (4 mL) in presence of anhydrous cobalt chloride (70 mg, 0.54 mmol) and DBU. The temperature of the reaction mixture was heated up to 140 °C

and stirred for 18 h under a nitrogen atmosphere. After cooling to the room temperature, the reaction mixture was precipitated by adding water-methanol (1:1). The formed precipitate was collected by centrifugation. The crude product was purified by column chromatography eluting with $CHCl_3$ and a gradient of $CHCl_3$–THF up to 10% THF to give pure complex **6**.

Yield: 11% (0.030 g). FT-IR (UATR-TWO^{TM}) ν max/cm^{-1}: 3480 (NH), 2916-2846 (Aliph,-C-H), 3113-2847 (C-H (Ar) and intermolecular H bonding), 1594, 1460-1332, 1228, 1114, 835. Anal. Calc. for $C_{75}H_{59}ClCoN_{10}O_4$ (%): C, 71.69; H, 5.48; N, 10.72; Found (%): C, 70.84; H, 5.11; N, 10.28. MALDI-TOF-MS (m/z): cald = 1558.72 [M]$^+$; found = 1558.79 [M]$^+$, UV–Vis (DMF): λmax (nm) (log ε) 328 (4.82), 698 (4.31), 662 (4.93).

2.4. Preparation of nanomaterials

2.4.1. Functionalization of the CdTe/ZnS QDs with azide, Scheme 3.5

The conjugation of CdTe/ZnS QDs with the azide was carried out using a method reported in the literature [46] as follows: MPA capped CdTe/ZnS QDs (50 mg) were dissolved in 2 mL of water. Thereafter EDC (20 mg, 0.104 mmol) and NHS (15 mg, 0.217 mmol) were added to the solution in order to activate the carboxyl functional moiety of the MPA capping the CdTe/ZnS QDs. The mixture was left stirring at room temperature for 2 h after which 20 mg (0.117 mmol) of 4-azidoaniline hydrochloride were added. The solution was left stirring for 24 h leading to the formation of the carbomide linkage between the MPA capped CdTe/ZnS QDs and the 4-azidoaniline hydrochloride. The QDs were precipitated using methanol and purified. The QDs were represented as azide CdTe/ZnS QDs.

2.4.2. Functionalization of the reduced graphene oxide with azide, Scheme 3.7

The GONS purchased from Sigma-Aldrich were produced using Hummer's method [125]. It has recently been shown that rGONS synthesized by Hummer's method contain organosulfate groups on the basal plane as part of its chemical structure, in addition to epoxy and hydroxyl groups [126]. Substitution of organosulfate and a small number of oxides by azide groups has been reported [127]. Briefly, the substitution was as follows: rGONS (10 mg) and sodium azide (5 mg, 0.077 mmol) were dispersed in 25 mL of Millipore water and freeze-dried. The product was obtained via filtration and washed with copious amounts of water and dried at 70 ^{0}C. The resulting rGONS are represented as azide-rGONS.

2.4.3. Functionalization of the ZnONPs with azide, Scheme 3.9

The GSH capped ZnONPs (50 mg) were dissolved in 2 mL of water. Thereafter EDC (20 mg, 0.10 mmol) and NHS (15 mg, 0.12 mmol) were added to the solution in order to activate the carboxyl functional moiety of the GSH capped ZnONPs. The reaction was left stirring at room temperature for 2 h after which 4-azidoaniline hydrochloride (20 mg, 0.12 mmol) was added. The solution was left stirring for 24 h leading to the formation of the carbomide linkage between the GSH capped ZnONPs and the 4-azidoaniline hydrochloride. The ZnONPs were precipitated using methanol. The ZnONPs are represented as azide ZnONPs.

2.5. Conjugation of MPcs to nanomaterials

2.5.1. Conjugation of the azide functionalized CdTe/ZnS QDs to 1a, 1b, and 1c by click chemistry, Scheme 3.6

Complexes **1a** (10.92 mg, 1.00 mmol), **1b** (11.02 mg, 1 mmol), and **1c** (10.88 mg, 1 mmol) were each mixed with azide CdTe/ZnS QDs (22 mg), Cu(PPh$_3$)$_3$Br (15 mg, 2 mmol), and trimethylamine (2 mL) and dissolved in 5 mL DMF. The mixtures were stirred at room temperature for 72 h. The resulting precipitates were washed with water and dried at room temperature to get the desired products represented as clicked **1c**-QDs, **1b**-QDs and **1c**-QDs.

2.5.2. Conjugation of azide-rGONS to complexes 1a and 2 via click chemistry, Scheme 3.8

Complexes **1a** (12.72 mg, 1.23 mmol) or **2** (10.55 mg 1.02 mmol), azide-GONS (30.45 mg), and Cu (PPh$_3$)$_3$Br (15.56 mg, 2.11 mmol) were added to a solvent mixture of 8 mL dimethylformamide (DMF) and 2 mL trimethylamine. The mixture was stirred at room temperature for 48 h under Ar. The reaction was then poured into 100 mL of cold water. The precipitate was filtered off and washed with Millipore water. The conjugates are represented as **1a**-rGONS(linked) and **2**-rGONS(linked). Linked indicated as opposed to rGONS sequentially(seq) added.

2.5.3. The clicking of azide-functionalized ZnONPs to complex 2, Scheme 3.10

Complex **2** (10.92 mg, 1.00 mmol) was mixed with azide ZnONPs (22.23 mg), Cu(PPh$_3$)$_3$Br (12.34 mg, 2,05 mmol), and trimethylamine (TEA, 2.04 mL) in 5.06 mL DMF. The mixture was stirred at room temperature for 72 h. The resulting precipitate was washed with water and dried at room temperature to get desired products represented as **2**-ZnONPs.

2.6. Electrode modification

The glassy carbon electrode (GCE) was employed as the working electrode, while silver|silver chloride (with saturated potassium chloride), and platinum wire were used as reference and counter electrodes respectively. Prior to modification, the GCE was polished on a Buehler-felt pad using alumina(< 10 µm). Between each polish step, Millipore water was used to remove any impurities by sonicating for 15 min. The electrode was then rinsed with millipore water and dried before use. The GCE was modified using three methods namely; 1) drop dry method, 2) electrodeposition method and 2) electrografting and subsequently click chemistry. All the solutions were purged with argon gas for 20 min to remove any dissloved oxygen (except for ORR experiment) before analysis. The argon atmosphere was maintaned above the solution through out the experiments.

2.6.1. Click chemistry of Pc (1a, 3 or 4) onto GCE, Scheme 4.1

The bare GCE surface was first grafted by the electrodeposition and scanning from +0.2 V to -0.1 V for three cycles in a solution of 0.1 mM 4-azidobenzenediazonium tetrafluoroborate salt (containing 0.01 M TBABF$_4$ in 96:4 ACN: HCl (1M)). The electrode was rinsed with DMF then acetone and Millipore water. Following grafting, the click reaction was performed by immersing the grafted-GCE into a solution containing 1 µM of Pc in 1 mL DMF containing 2 mM Cu(PPh$_3$)$_3$Br and 0.5 mL trimethylamine. The electrode was left to click for 18 h. The glassy carbon plates (GCP) surfaces were used for SEM, XPS, SCEM and they were modified by grafting followed by clicking via the same process as applied to the GCE. Complex **1a** was also adsorbed onto electrode without click, represented as **1a**-adsorbed.

2.6.2. Electrodeposition onto GCE

Complex **5b** was dispersed in DMF (1 mg /mL) and sonicated for 1 h, then 1 μL of complex **5b** was dropped on GCE and dried in an oven for 15 min at 60 $^\circ$C, resulting in **5b**. After drying, **5b**-AgNPs was prepared by cyclic voltammetry scanning of **5b** in an aqueous solution (saturated by argon) containing KCN (0.325 g, 4.99 mmol), NaNO$_3$ (0.425 g, 5.00 mmol) and AgNO$_3$ (0.085 g, 0.50 mmol), Scheme 4.2. The potential was scanned (20 scans) from -0.7 V to -1.55 V at 100 mVs^{-1}. The cyanide from KCN solution complexes metallic impurities that maybe be present in the solution, resulting in lowering of onset potentials of silver deposition. The NaNO$_3$ was used as an electrolyte. For comparison purpose, GCE was modified with AgNPs alone was prepared using the above electrodeposition procedure for **5b-**AgNPs**.** In both cases, the modified GCEs were dried in an oven for 15 min at 60 $^\circ$C. The modification of GCP for SECM, SEM and EDX was carried out as outlined above for the GCE.

2.6.3. Adsorption onto GCE

Most complexes or conjugates were adsorbed onto the electrode complete list in Table 4.1. Complex **1a** is indicated as "adsorbed" since it is also clicked in order to differentiate. Modifiers were also applied sequential to the electrodes. For electrode modification via adsorption, MPcs alone or conjugated to QDs (1 mg) or conjugated to rGONS (1 mg) were dissolved in 1 mL DMF. Then, 5 μL of the solution was placed on the GCE, followed by drying in an oven at 60 $^\circ$C overnight. In the case of sequential modification, 1 mg of each material (rGONS, **1a**, **2**, **5a**, or **6**) was dissolved in 1000 μL of DMF and sonicated. Each of the dispersed material (0.5 μL) was dropped on the glassy carbon electrode separately (rGONS, **1a**, **2**, **5a**, **6**) and

sequentially (**1a**-rGONS, **2**-rGONS, **5a-**rGONS or **6-**rGONS) and dried in an oven. The

MPcs were placed on top of nanomaterials.

CHAPTER THREE: Characterization

Publications

This work comprises of published material in the following peer reviewed journals.

1. **Lekhetho S. Mpeta**, Gertrude Fomo, Tebello Nyokong, click chemistry electrode modification using an 4-ethynylbenzyl substituted cobalt phthalocyanine for applications in electrocatalysis. **Journal of Coordination Chemistry** 71 (2018) 1623-1638

2. **Lekhetho S. Mpeta** and Tebello Nyokong, Electrocatalytic activity of ethynylbenzyl phthalocyanines when linked to quantum dots via click chemistry: towards efficient oxygen reduction reaction and H_2O_2 oxidation. **Journal of Electroanalytical Chemistry.** 840 (2019) 218-229

3. **Lekhetho S. Mpeta** and Tebello Nyokong, Enhanced electrocatalytic activity of cobalt phthalocyanines when clicked to graphene oxide nanosheets. **Journal of Porphyrins phthalocyanines** 23 (2019) 821-827

4. **Lekhetho S. Mpeta**, Pinar Sen and Tebello Nyokong, Investigation of electrocatalytic behaviour of low symmetry cobalt phthalocyanines when clicked to azide grafted carbon electrode. **Journal of Electroanalytical Chemistry** 860 (2020) 113896 (1-10)

5. **Lekhetho S. Mpeta**, Kutloano E. Sekhosana and Tebello Nyokong, Nonlinear optical response and electrocatalytic activity of Cobalt phthalocyanines clicked Zinc Oxide nanoparticles, **Journal of Inorganic Acta** 509 (2020) 119661 (1-9)**.**

6. **Lekhetho S. Mpeta**, Pinar Sen and Tebello Nyokong, Development of manganese phthalocyanines decorated silver nanoparticles nanocomposite

for improved electrocatalytic activity.   **Journal of Electroanalytical Chemistry** 866 (2020) 114173 (1-9).

7. **Lekhetho S. Mpeta**, Pinar Sen and Tebello Nyokong. The effects of asymmetry in combination with reduced graphene oxide nanosheets on hydrazine electrocatalytic detection on cobalt phthalocyanines. **Electroanalysis 32 (2020)** 2723-2732.

Other paper published but not related or discussed in this thesis

1. Pinar Sen, **Lekhetho S. Mpeta**, John Mack, Tebello Nyokong. New difluoroboron complexes based on N, O-chelated Schiff base ligands: Synthesis, characterization, DFT calculations, photophysical and electrochemical properties. **Journal of Luminescence** 224 (2020) 117262 (1-10).

3. Synthesis and Characterization

This Chapter deals with characterization of MPcs, nanomaterials and their conjugates.

3.1. MPcs complexes alone, Schemes 3.1 to 3.4

^{1}H NMR spectra for all complexes were not recorded due to the paramagnetic nature of Co, Fe and Mn elements. Mass spectrum confirmed the formation of all complexes since the anticipated molecular ions were obtained. The symmetrical complexes **1a**, **1b**, **1c** (Scheme 3.1), **5a** and **5b** (Scheme 3.3) were synthesized using one phthalonitrile while complexes **3**, **4**, (Scheme 3.2) and **6** (Scheme 3.4) were synthesized using two dissimilar phthalonitriles. Complexes **1a**, **1b** and **1c** (Scheme 3.1) were prepared from the condensation of 4-ethynylbenzyl phthalonitrile (**i**) in the presence of corresponding metal salt in 1-pentanol and using DBU as catalyst. Complexes **5a** and **5b** (Scheme 3.3) were prepared from the cyclotetramerization reaction of 4-(4-(5-chloro-1H-benzo[d]imidazol-2-yl)phenoxy)phthalonitrile (**iv**) in a high boiling solvents (n-hexanol for **5b** and DMAE for **5a**) in the presence of anhydrous salt (MnCl$_2$ for **5b** and CoCl$_2$ for **5a**) and DBU as a strong base. Novel mono alkynyl terminated Co phthalocyanines were synthesized by the statistical condensation reactions of precursor phthalonitriles (Scheme 3.2) with the anhydrous cobalt chloride in 1-pentanol. After work-up, the mixtures were purified by chromatography over silica gel, eluting with CHCl$_3$ and a gradient of CHCl$_3$–methanol up to 5% methanol to give pure CoPcs (**3** and **4**). For synthesis of **6**, 4-(4-(5-chloro-1H-benzo[d]imidazol-2-yl)phenoxy)phthalonitrile (**iv**) and 4-*tert*-butylphenoxy phthalonitrile (**ii**) were dissolved in 1-pentanol in presence of anhydrous cobalt chloride and DBU. The temperature of the reaction mixture was raised to reflux

temperature, followed by stirring for 18 h under a nitrogen atmosphere. After cooling to the room temperature, the reaction mixture was precipitated by adding water-methanol (1:1) mixture. The formed precipitate was collected by centrifugation. The crude product was purified by column chromatography eluting with CHCl$_3$ and a gradient of CHCl$_3$–THF up to 10% THF.
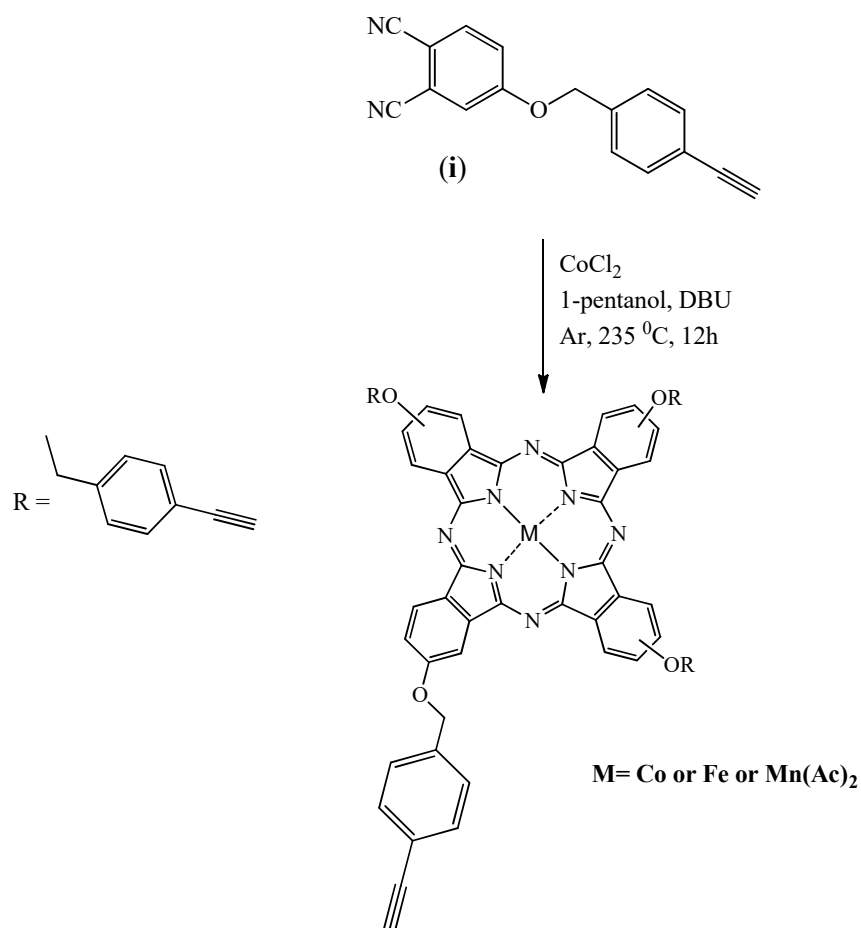
Scheme 3.1: Synthesis scheme for complexes **1a**, **1b** and **1c**
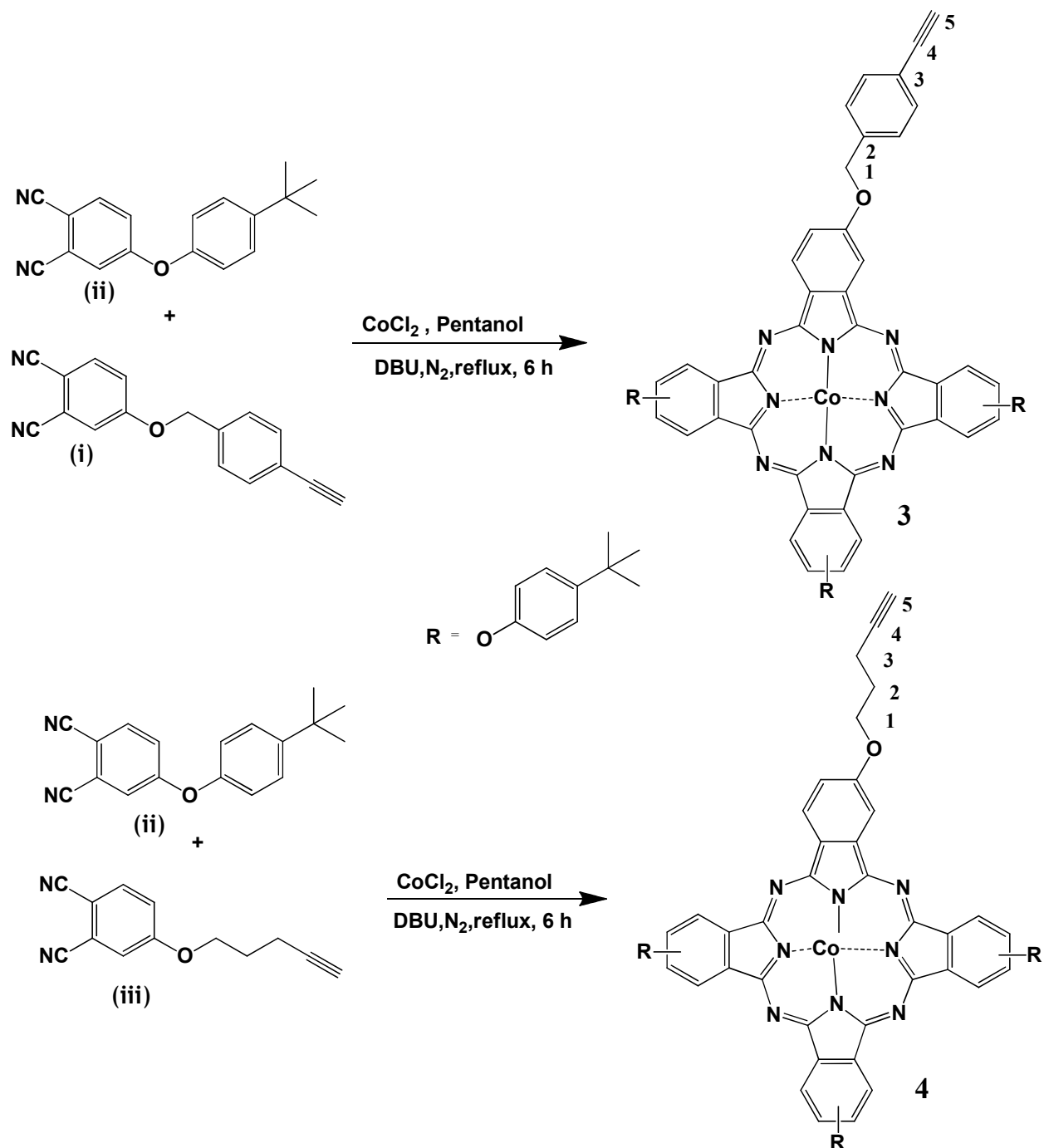
Scheme 3.2: Synthetic route of complexes **3** and **4**.
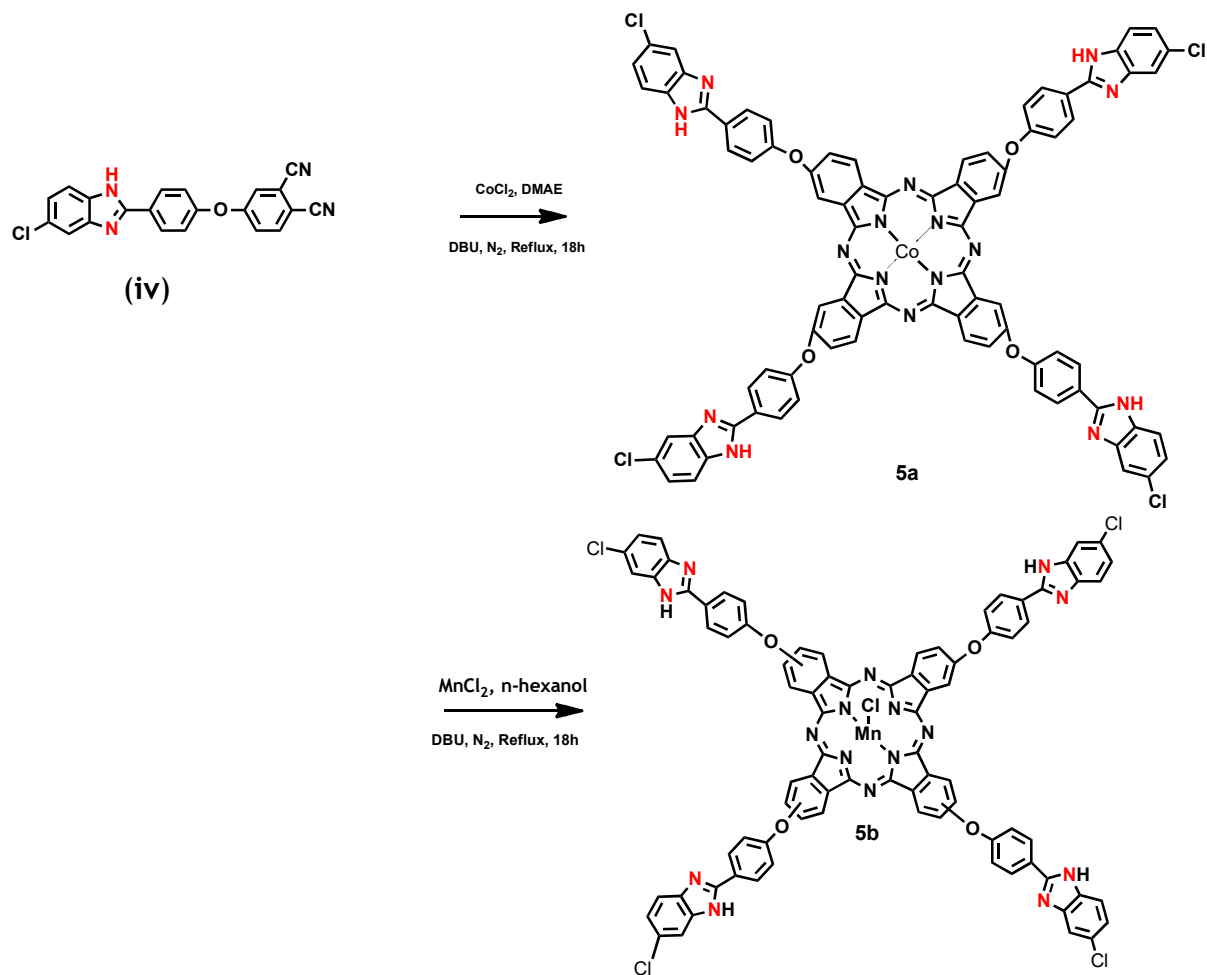
Scheme 3.3: Synthetic route for complexes **5a** and **5b**
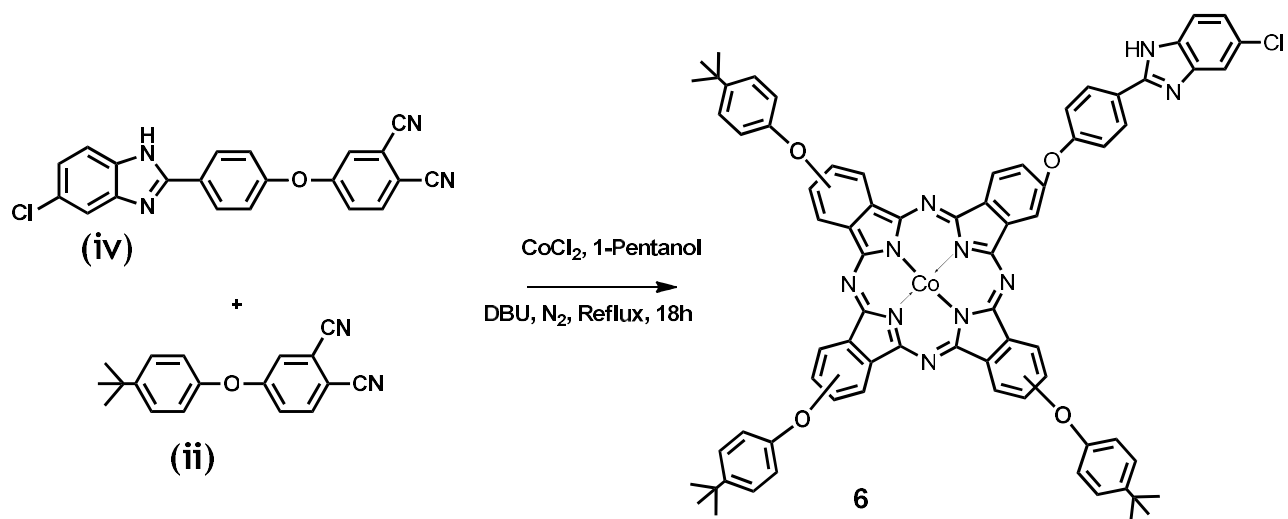
Scheme 3.4: Synthetic route for complex **6**

3.1.1. FTIR spectra

The FT-IR spectra of complexes **1a**, **3** and **4** (as examples) in Fig. 3.1 do not show the nitrile (C≡N) peaks of the phthalonitriles, confirming the cyclotetramerization of precursor phthalonitriles to form corresponding phthalocyanines. The -H-C≡C peaks belonging to the terminal alkynyl groups were observed at 3214 cm^{-1} for complex **3**, 3203 cm^{-1} for complex **4** and 3240 cm^{-1} for **1a**. In addition, the aliphatic –C-H vibrations appeared at between 2916-2846 cm^{-1} and 2918-2850 cm^{-1} resulting from the *tert*-butyl groups and alkynyl group for complexes **3** and **4,** respectively.
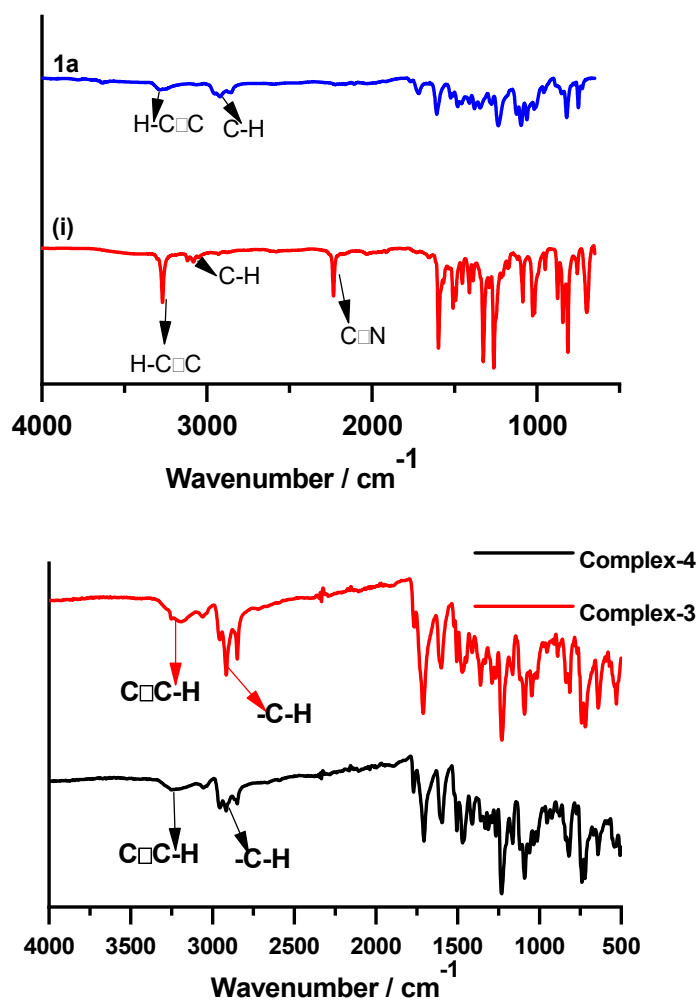
Figure 3.1: FTIR spectra of complex **1a** and precursor (i) and complexes **3** and **4.**

3.1.2. UV-Vis spectra

Metallated phthalocyanines show two characteristic bands in their absorption spectra. The Q band, which is attributed to the π-π* transitions from the highest occupied molecular orbital (HOMO) to the lowest unoccupied molecular orbital (LUMO) of the Pc ring [36]. Fig. 3.2 shows the UV-Vis spectra of complexes **1, 2, 5** and **6** in DMF (as examples), data in Table 3.1. The intense Q band is typical of metallated Pcs. The ethynylbenzyl group (in complex **1a**, 668 nm) results in the blue shift of the Q band compared to the aliphatic alkynyl (in complex **2,** 665 nm) substituted CoPc. It has been reported [36] that when electron-releasing groups are bound to the non-peripheral positions of the Pc ring, the Q bands shift to longer wavelengths, hence Q band of complex **1a** is slightly red-shifted compared to complexes **2** and **CoPc** due to the presence of the electron-rich benzene groups in **1a**. Complexes **1a, 1b** and **1c** are soluble in a wide range of organic solvents including DMF, DMSO, ethanol, toluene, $CHCl_3$. The spectra are typical of cobalt phthalocyanines [128].

Complexes **3** and **4** showed intense single Q-absorption bands at 669 nm in DMF, Table 3.1. The other characteristic absorptions, B bands, are observed between 300-350 nm for **3** and **4** [128].

The UV-Vis spectra of studied cobalt phthalocyanines **6** and **5a** in DMF were shown in Fig. 3.2. The Soret bands were observed at 315 nm and 338 nm for **5a** and **6** respectively. On the other hand, the Q-band were observed at 663 and 661 nm for **5a** and **6** respectively (Table 3.1). Thus, the obtained Q-bands are almost the same and in the range for CoPc [129, 130].

The UV-vis spectra complex **5b** with and without addition of LiCl in DMSO are shown in Fig. 3.3. Without addition of LiCl, the electronic ground state absorption spectra shows broadening due to aggregation due to molecular interactions. However after addition of LiCl, the B-band (372 nm) became more pronounced and the spectrum showed no evidence of aggregation. In addition to the de-aggregation LiCl increased the solubility of the macrocycle [131]. The Q-band was observed at 715 nm typical for manganese (III) phthalocyanines [132], Table 3.1.

The theory of MCD is based on the analyses of the three Faraday terms A_1, B_0 and C_0, which provide information on the state degeneracies and band polarizations that cannot be derived from the UV-vis absorption spectrum alone [130]. The MCD spectrum of complex-**5b** in Fig. 3.3 is similar to what would be expected for a monomeric MnPc as intense A_1 term are observed in the Q and B-band regions with crossover point at 712 nm and 328 nm, respectively, which corresponds to the absorption maxima for MnPc.
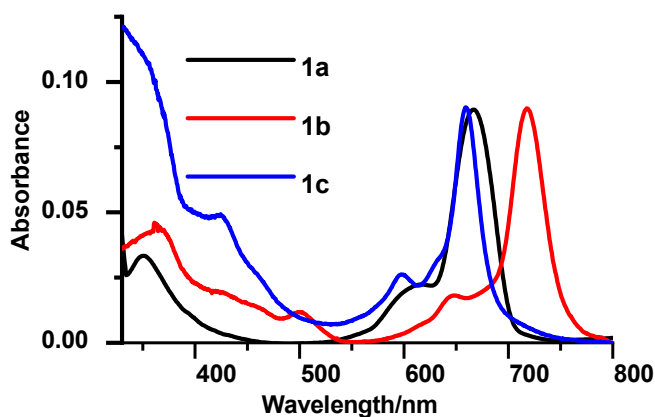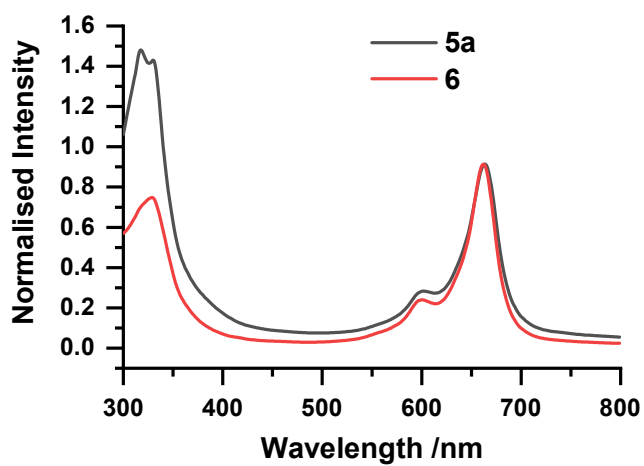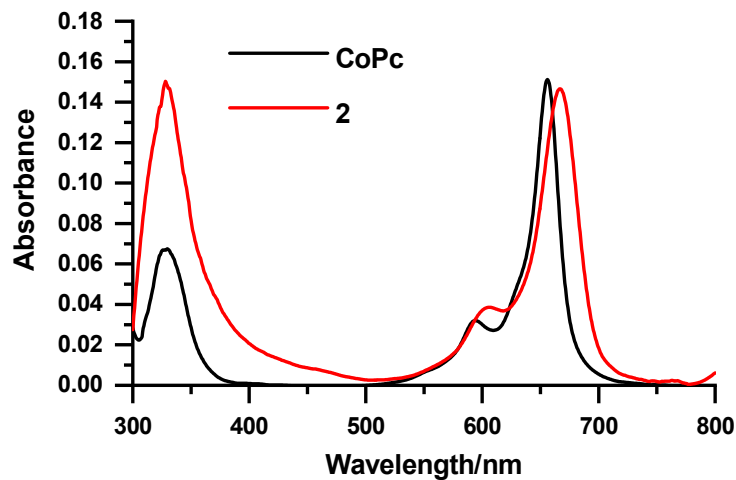
Figure 3.2: UV-Vis spectra of complexes **1a**, **1b**, **1c**, **CoPc**, **2**, **5a** and **6** in DMF (concentration ~ 1×10^{-5} M).
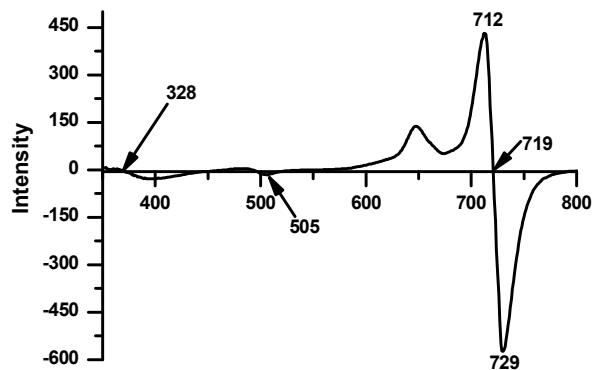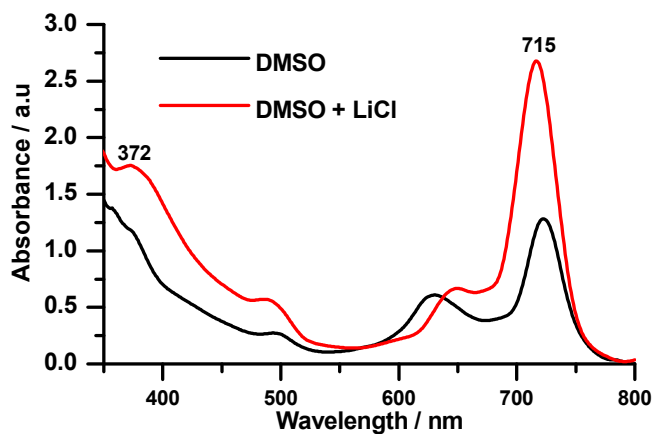
Figure 3.3: MCD and absorption spectra for **5b** in DMSO.

Table 3.1: Spectra in DMF, loading and particle size

complex	Q band/nm	Loading ng/mg	DLS /nm
CoPc	662		
1a-adsorbed	668		
1a-QDs	669	72	35.00
1a-rGONS	667		
1b	718		
1b-QDS	719	60	29.08
1c	661		
1c-QDs	663	70	35.95
2	665		
2-ZONPs	664	83	43.8
2-rGONS	662		
3	669		
4	669		
5a	663		
5b	715		
6	661		

3.1.3. Cyclic Voltammetry (CV) and Differential pulse voltammograms (DPV)

Fig. 3.4 and 3.5 show the cyclic and differential pulse voltammetry of complexes **1a** and **5b** as examples in DMF containing 0.1 M TBABF$_4$. The cyclic voltammogram of complex **1a** (Fig. 3.4 (a)) showed four identifiable redox processes (**I-VI**). From literature [131], peaks (**II**) and (**III**) are attributed to Co (**I**)/Co (**II**) and Co (**III**)/Co (**II**), respectively in DMF. The Co (**III**)/Co (**II**) couple is irreversible, as is often observed for this couple in literature [132]. The rest of the peaks are ring based. Oxidation at the Pc ring occurs by successive loss of one electron from the highest occupied molecular orbital (HOMO) resulting in the formation of $[Pc^{-1}]^{\bullet+}$ and $[Pc^{0}]^{\bullet2+}$ cation radicals. Reduction, on the other hand, occurs by successive gain of electrons by the lowest unoccupied molecular orbital (LUMO) of the phthalocyanine complex resulting in the formation of Pc (−2n) species (where n = number of electrons). Since DPV is more sensitive than CV, it was used to confirm the oxidation and reduction peaks obtained on the cyclic voltammograms for both complexes **1a** and **5b**. The CV of complex-**5b** Fig. 3.5 (a) show quasi-reversible to irreversible which does not change with scan rate. Fig. 3.5 (b) the DPV shows four peaks at $E_{1/2}$ = - 0.72 V (**I**), - 0.13 V (**II**), + 0.42 V (**III**), + 0.95 V (**IV**). The two ill-defined and irreversible peaks located in the positive region (labelled **III** and **IV**) may be related to metal oxidation (Mn(IV)Pc(-2)/Mn(III)Pc(-2) (process **III**) and subsequent ring oxidation (Mn(IV)Pc(-1)/Mn(IV)Pc(-2)) (process **IV**) in comparison with literature [133, 134]. The reversible voltammetric couple located at – 0.13 V can be attributed to Mn(III)Pc(-2)/Mn(II)Pc(-2) redox process and that at -0.72 V to Mn(II)Pc(-2)/Mn(I)Pc(-2) in accordance with the literature [134].
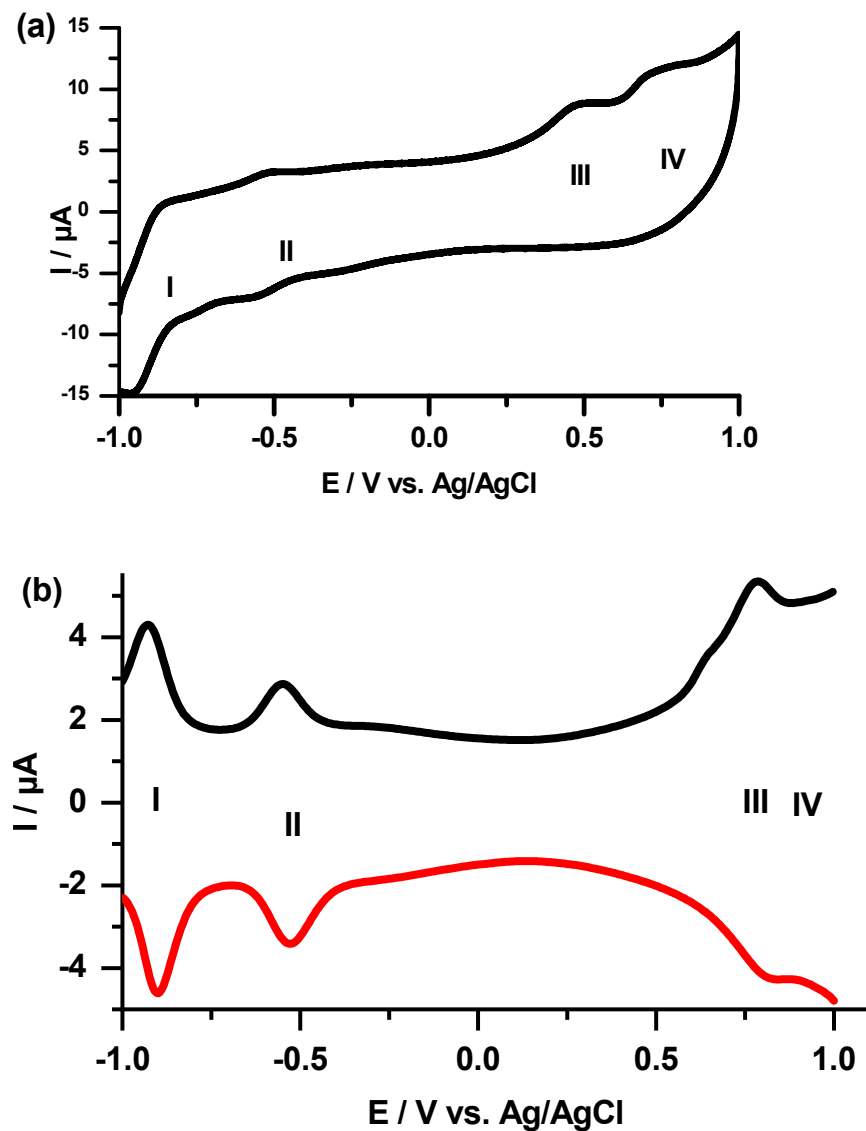
Figure 3.4: (a) Cyclic voltammogram (CV) and (b) differential pulse voltammogram (DPV) profiles of 1×10^{-3} M of complex **1a** in DMF containing 0.1 M TBABF$_4$ supporting electrolyte.
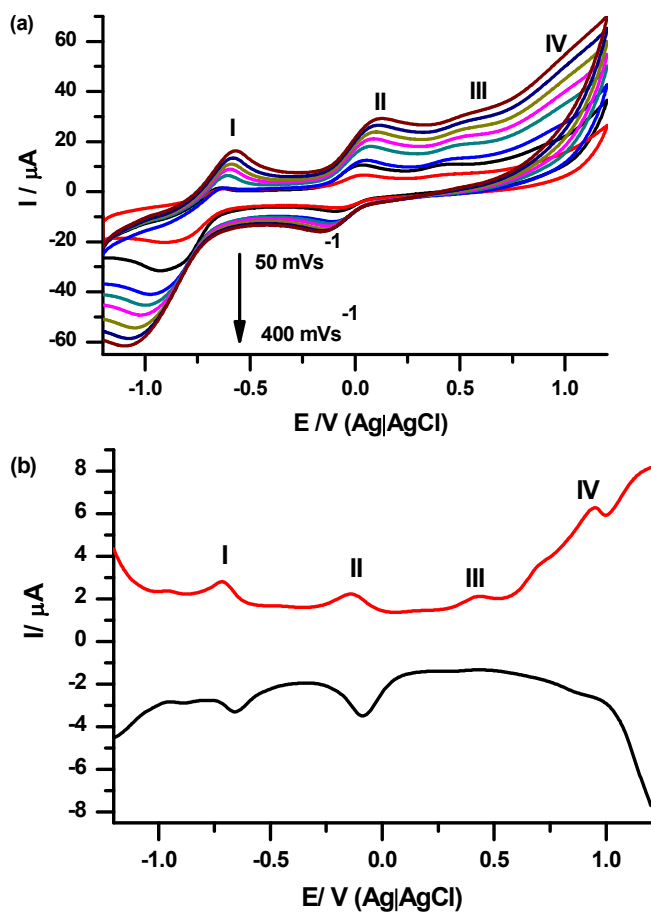
Figure 3.5: (a) Cyclic voltammetry (at different scan rates) and (b) differential pulse voltammetry of **5b** in DMF and 0.1 M TBAF$_4$ supporting electrolyte

3.2. Conjugates of QDs with 1a, 1b and 1c

Complexes **1a**, **1b** and **1c** were linked to semiconductor QDs. Scheme 3.5 shows the formation of the amide bond between mercaptopropionic acid (MPA) capped CdTe/ZnS QDs and 4-azidoaniline hydrochloride using EDC/NHS as coupling agents to form azide CdTe/ZnS. Scheme 3.6 shows the route for the click reaction between alkynyl MPc and azide CdTe/ZnS QDs.
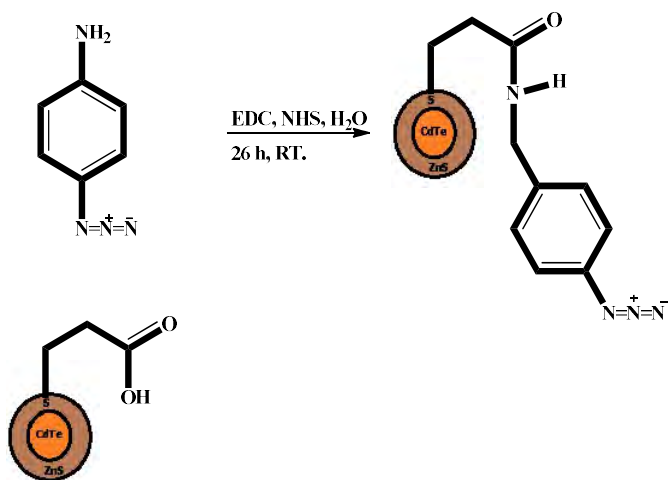
Scheme 3.5: Conjugation of MPA QDs with 4-azidoaniline hydrochloride to form azide QDs
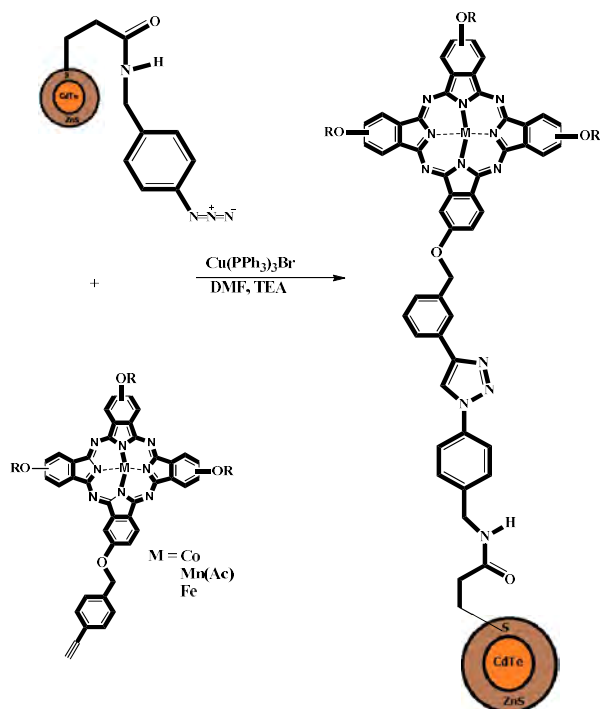
Scheme 3.6: Clicking of alkynyl MPcs with azide QDs

3.2.1. FTIR specra

From Fig. 3.6, the disappearance of the C≡C-H stretch at around 3000 cm^{-1} on the clicked Pcs is an indication that the alkyne terminated Pcs are successfully linked to the quantum dots hence forming triazole ring.
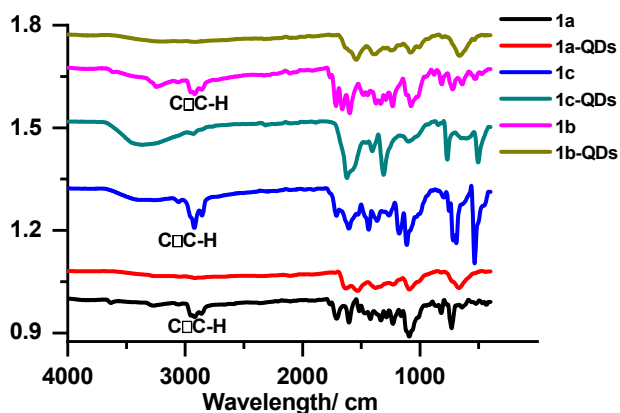
Figure 3.6: FTIR spectra of **1c, 1c**-QDs, **1b, 1b**-QDs, **1c,** and **1c**-QDs.

3.2.2. UV-Vis and Fluorescence spectra

Fig. 3.7 (a) shows Uv-Vis spectra of Pc (**1a**) in the presence of the QDs, the broadening below 600 nm could be due the absorbance of the QDs. QDs have broad absorption and a narrow emission, Fig. 3.7 (b).

The size of the Pcs is approximately of 1 nm while the size of the quantum dots is larger (5.95 nm from DLS, discussed below). Hence, it is likely that more than one Pc can be bonded to the QDs considering the size of Pc relative to QDs. The reverse where more than one QD bind to a Pc is unlikely due to size considerations. The loadings of Pcs onto the QDs (μgPc/mg QDs) were estimated to be 72 μg/mg, 60 μg/mg and 70 μg/mg for **1a**-QDs, **1b**-QDs and **1c**-QDs (Table 3.1), respectively following literature methods, but using absorption instead of fluorescence [135]. The lower loading for **1b** could be a result of the interference caused by the bulky acetate axial ligand, which could have prevented more Pc complexes to be loaded.
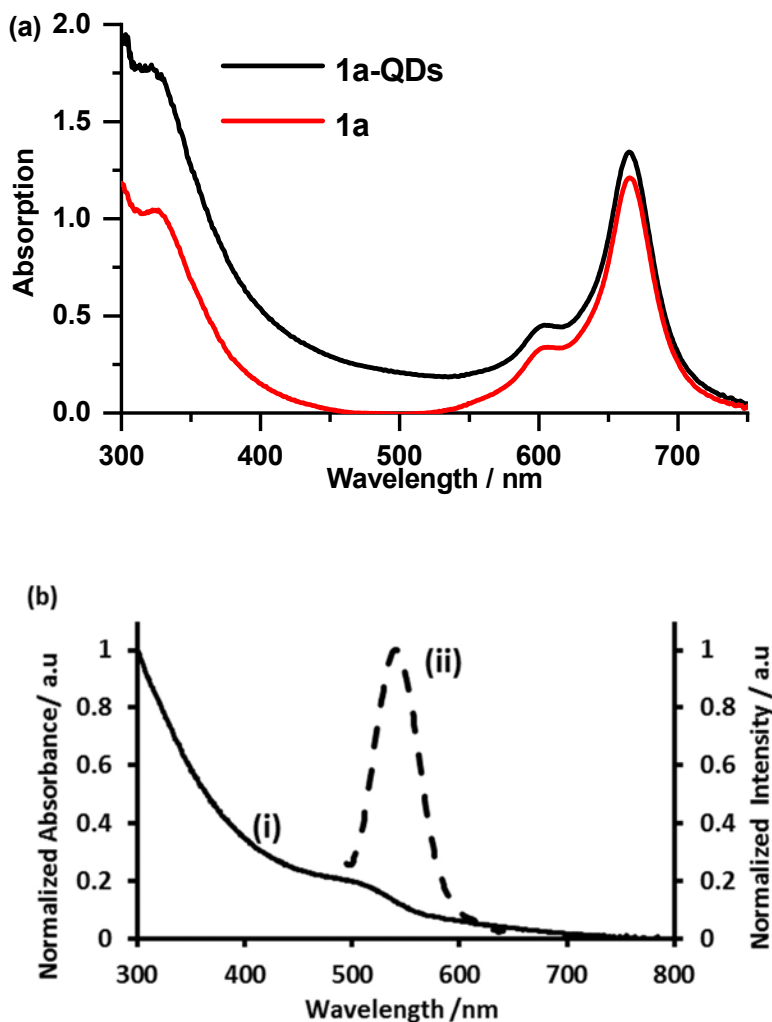
Figure 3.7: UV-Vis spectra of (a) **1c** and **1c**-QDs in DMF. (b) Absorption (i) and emission spectra (ii) of QDs alone in water.

3.2.3. XPS spectra

XPS was used to confirm the click reaction between Pc and QDs. Fig. 3.8 (a) shows a wide scan XPS spectra of QDs, **1a** and **1a**-QDs, showing the expected elements. After clicking, the peaks due to both **1a** and QDs were observed. This could be due to successful linking of QDs to **1a**, however, high resolution N (1s) was carried out for further confirmation.

(a)

(b)
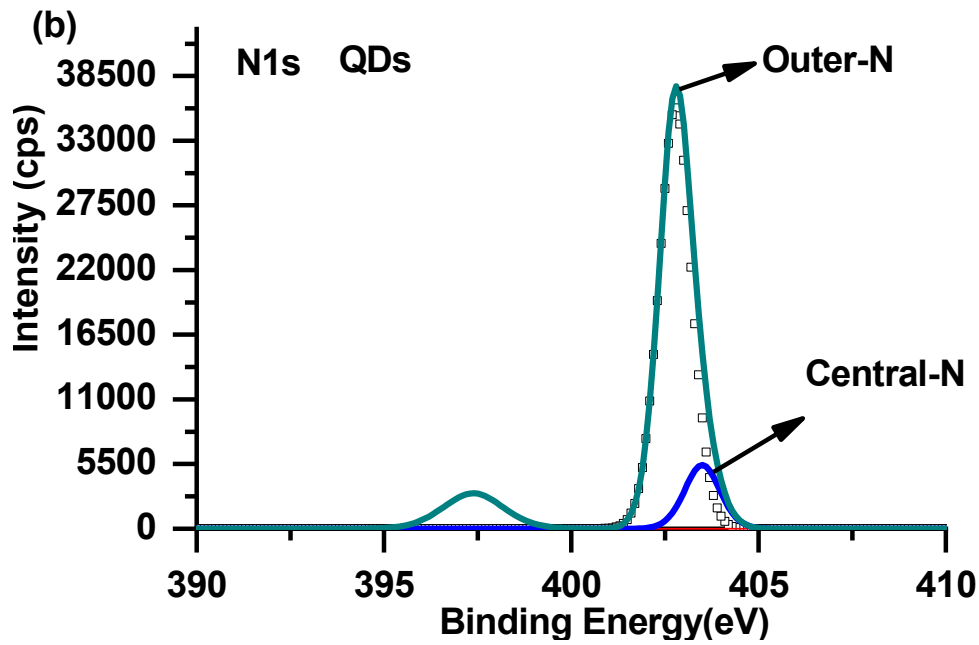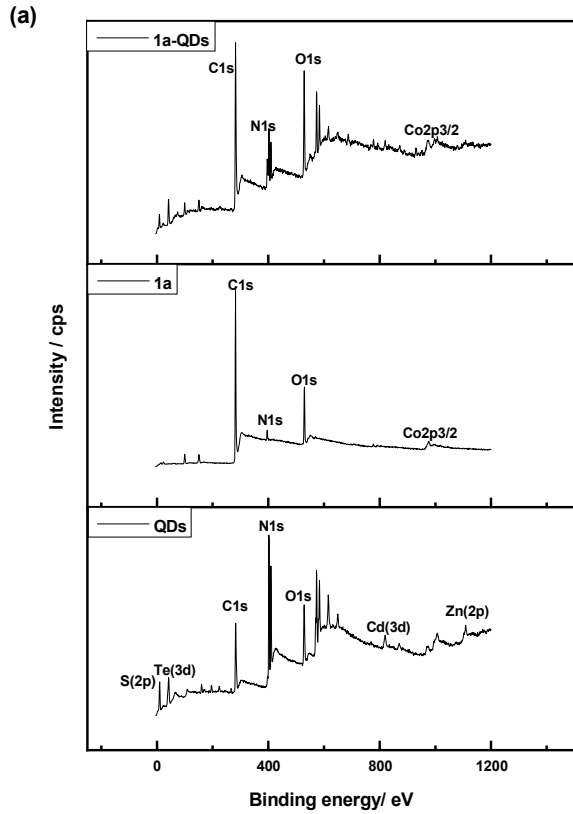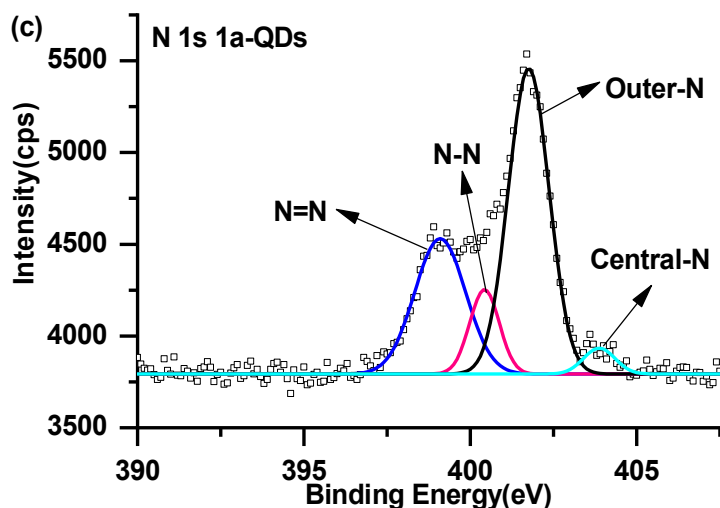
Figure 3.8: (a) Wide scan XPS spectra for azide functionalized QDs, **1a**, and **1a**-QDs. High resolution of deconvoluted N 1s component for (b) azide functionalized QDs and (c) **1a**-QDs.

The linking of azide functionalized QDs to the Pc via click chemistry was confirmed by comparing the N1s spectra. From the N1s spectra of QDs alone, the peak at 403.5 eV is assigned to central, electron deficient N, and the peak at 402.8 eV is assigned to the outer N [136] which confirms presence of azide on QDs. The N1s XPS spectrum of **1a**-QDs show the presence of a peak 403.8 eV which is assigned to the central, electron deficient N of an azide. The observation of this peak could mean that some azide moieties on the QDs were not involved in the click reaction. The central-N peak is highly reduced in intensity in **1a**-QDs (Fig. 3.8 (c)) at 153.09 cps compared to QDs (Fig. 3.8 (b)) alone at 5 396.83 cps, showing that some of the azide are involved in linking.

3.2.4. DLS

To determine the average size of synthesized QDs and their conjugates, a size-distribution analysis was performed using dynamic light scattering (DLS) in aqueous

solution. Fig. 3.9 shows that the average particle size of QDs was 5.95 nm and the sized of conjugates was 35.00 nm, 29.08 nm and 35.95 nm for **1a**-QDs, **1b**-QDs and **1c**-QDs respectively, Table 3.1. The increase in size following conjugation is due to aggregation as a result of π-π stacking between Pcs on adjacent NPs. Pcs are known for their tendency to π-π stack forming H aggregates [137].
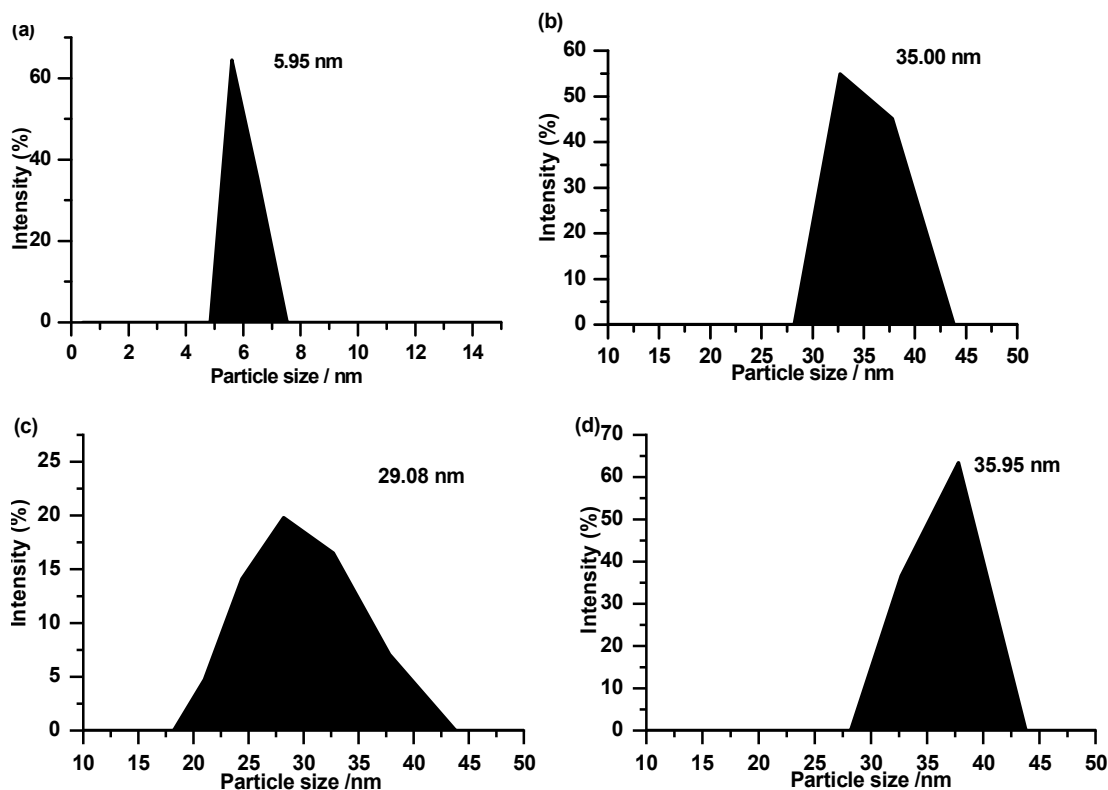
Figure 3.9: Size-distribution analysis by dynamic light scattering of (a) QDs, (b) **1a**-QDs, (c) **1c**-QDs and (d), **1b**-QDs.

3.3. Conjugates of rGONS with CoPc, 1a, 2

Complexes **1a** and **2** were employed for these studies. As stated in the synthesis section, Hummer's method for the synthesis of GONS results in the presence of epoxy, and carbonyl, carboxyl, and hydroxyl groups on the carbon plane and/or edges and defect sites [126]. The organosulfate groups have also been reported to

appear on rGONS when rGONS are prepared using this method [127]. Substitution of organosulfate and a small number of oxides by azide groups has been reported [138] and occurred in this work, Scheme 3.7. Scheme 3.8 shows the route for the click reaction between complex **2** (as an example) and azide-rGONS.
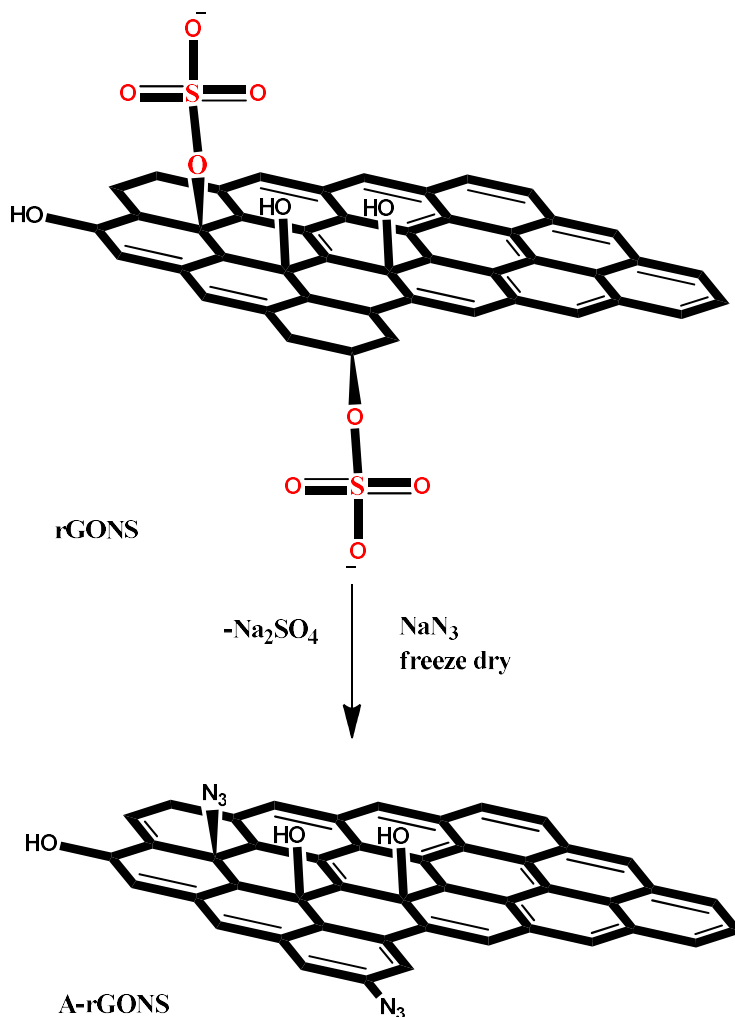
Scheme 3.7: Azide functionalization of rGONS to form azide-rGONS
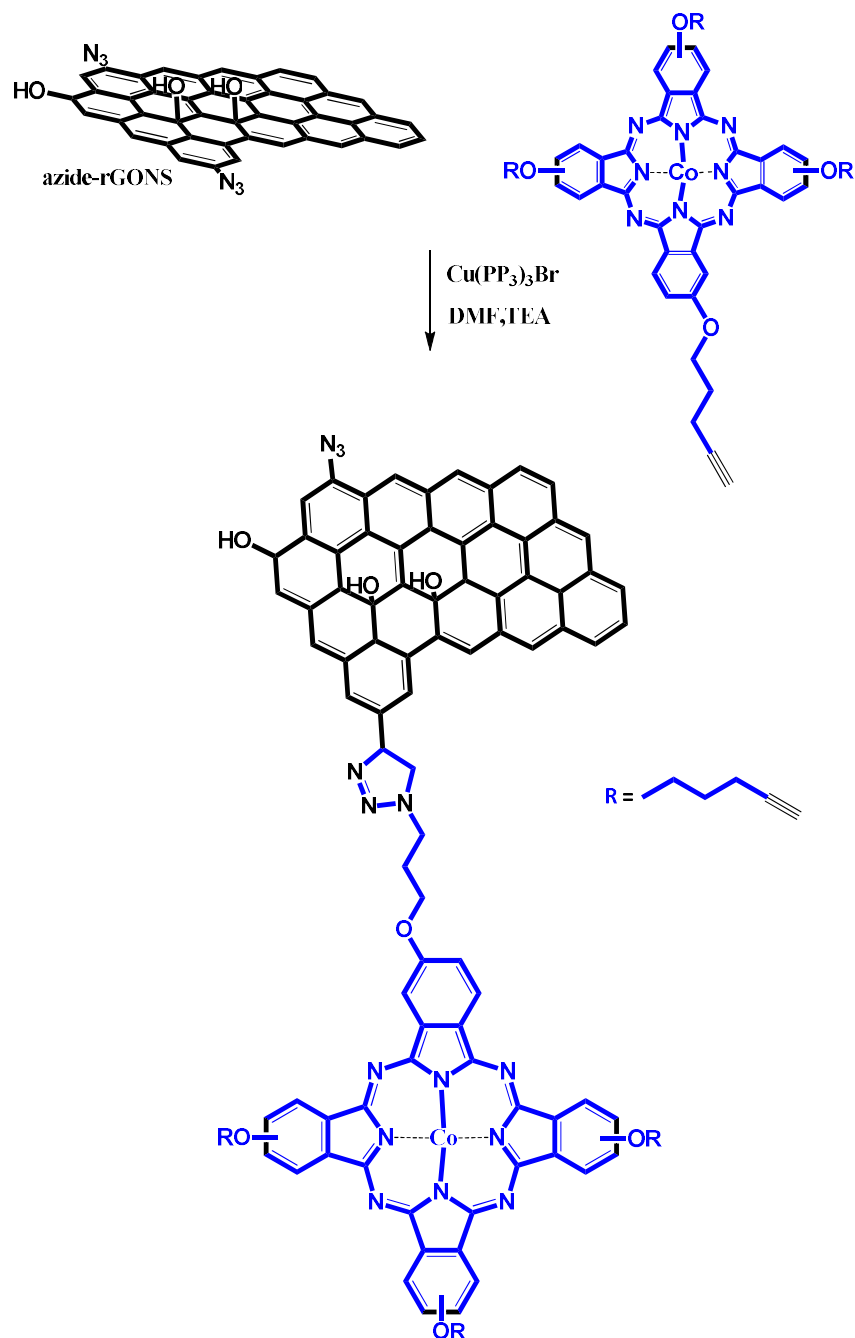
Scheme 3.8. Conjugation of azide-rGONS to **2**-rGONS as an example.

3.3.1. FTIR spectra

Fig. 3.10 shows FTIR spectra of pristine rGONS, azide-rGONS, complex **2,** and **2**-rGONS as examples. The presence of the stretch at 1161 cm^{-1} in rGONS is attributed to the organosulfates and its decrease in intensity after azide functionalization could

be an indication that it has been substituted by the azide. The appearance of peaks at 2103 cm^{-1} after azide functionalization of rGONS which corresponds to N=N=N stretching of an azide could be an indication of successful azide functionalization process. The elemental analysis also showed an increase in nitrogen content after functionalization of azide. rGONS (C: 51.20%, H: 1.87%, N: 1.48%) and azide-rGONS (C: 50.93%, H: 0.24%, N: 1.83%). The disappearance of the alkyne group at 3254 cm^{-1} (from FTIR spectrum of complex **2**) in **2**-rGONS could be a result of the click reaction. Furthermore, there was no copper content form $CuBr(PPh_3)_3$ catalyst used click chemistry.
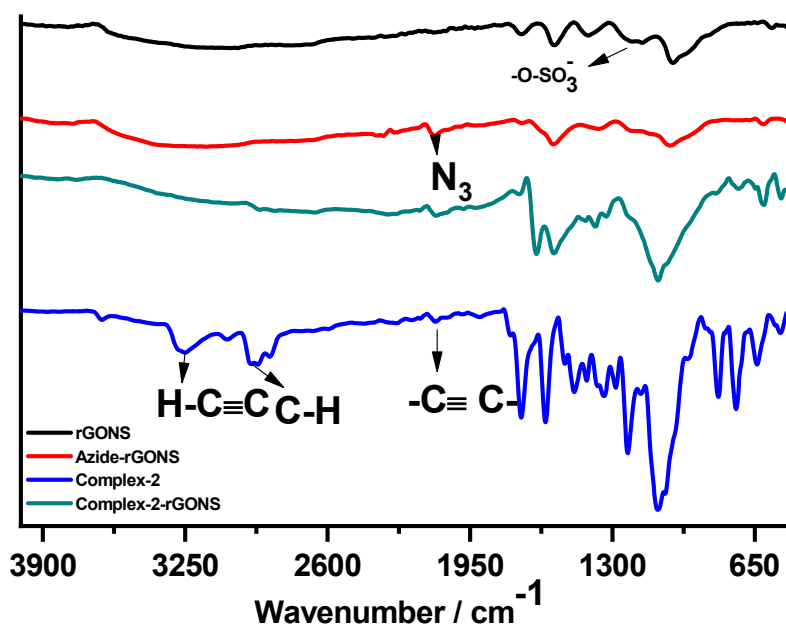
Figure 3.10: FTIR spectra of rGONS, azide-rGONS, complex **2** and **2**-rGONS.

3.3.2. Uv-Vis spectra

The ground state electronic absorption spectra for rGONS, **2** and conjugate are shown in Fig. 3.11. The Q band for **2** is observed at 665 nm and the Soret band at 327 nm, the slight shift of the Q band to 662 nm (Table 3.1) and the disappearance of the Soret band after conjugation with rGONS could be attributed to Pc and rGONS interaction.
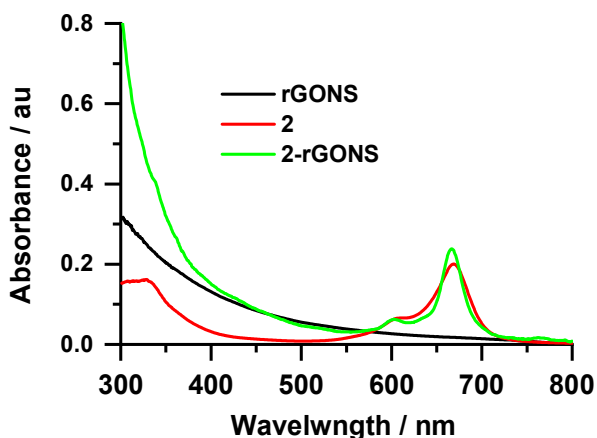
Figure 3.11: Uv-Vis spectra of rGONS, **2** and **2**-rGONS in DMF.

3.3.3. XPS spectra

XPS analysis was employed to confirm the success of the click reaction. Fig. 3.12 (a) shows a wide scan of both rGONS and azide-rGONS. The presence of a peak at 399.15 eV assigned to N1s is an indication that rGONS was successfully functionalized with an azide which compliments IR results. In the high-resolution spectra, the disappearance of central electron deficient (N≡N) peak in Fig. 3.12 (c) which was present at 403.10 eV in Fig. 3.12(b) also further confirms that the azides were involved in the click reaction hence their disappearance after clicking.
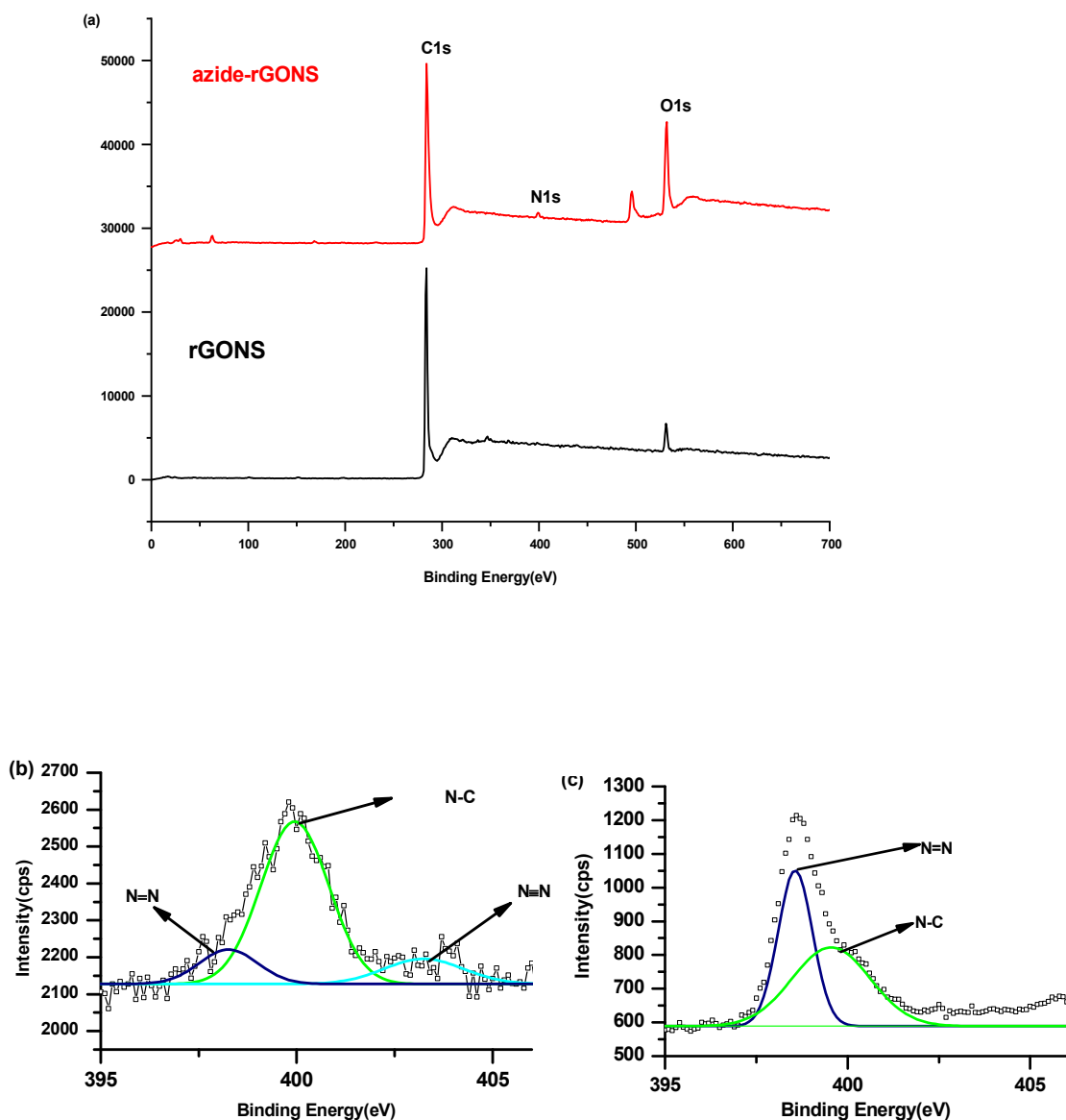
Figure 3.12: (a) wide scan XPS spectra for rGONS and azide-rGONS, N1s high-resolution XPS spectra for (b) azide-rGONS and (c) Complex-**2**-rGONS.

3.3.4. Raman spectra, TEM and XRD

Fig. 3.13(a) shows the Raman spectra for rGONS and azide-rGONS with characteristic D and G peaks where the G band is a result of in-plane vibrations of SP^2 bonded carbon atoms whereas the D band is due to out of plane vibrations attributed to the

presence of structural defects. The rGONS and azide-rGONS have D band at 1291 and 1327 cm^{-1}, respectively while the G band was almost the same and was observed at 1598 cm^{-1}. The I_D/I_G ratios for the rGONS and azide-rGONS were found to be 0.73 and 0.88 respectively. This suggests that azide functionalization could have been successful as there is an increase in disorder after functionalization.

The morphology or rGONS was investigated using TEM Fig. 3.13 (b). The micrograph shows that the nanosheets are randomly compact and disorderly stacked together showing wrinkles typical of graphene materials as reported in the literature [139, 140]. Fig. 3.13(c) shows XRD patterns for rGONS, the characteristic broad peak at 25° which corresponds to (002) plane [141].
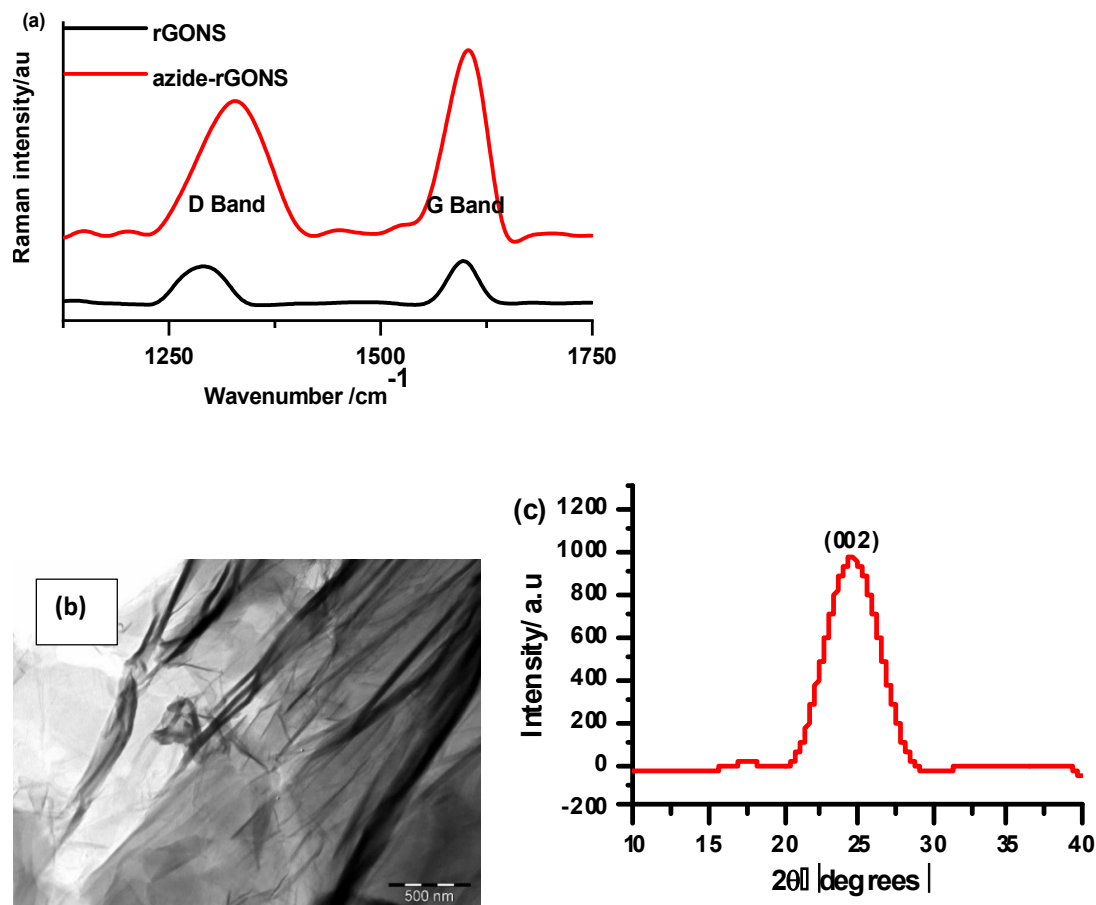
Figure 3.13: Raman spectra (a) TEM micrograph (b), and XRD patterns (c) of rGONS.

3.4. Conjugate of ZnONPs with 2

Scheme 3.9 shows the azide functionalization of ZnONPs using the EDC/NHS coupling agents to form an amide bond, and Scheme 3.10 shows the linking of azide ZnONPs to **2** using click chemistry.
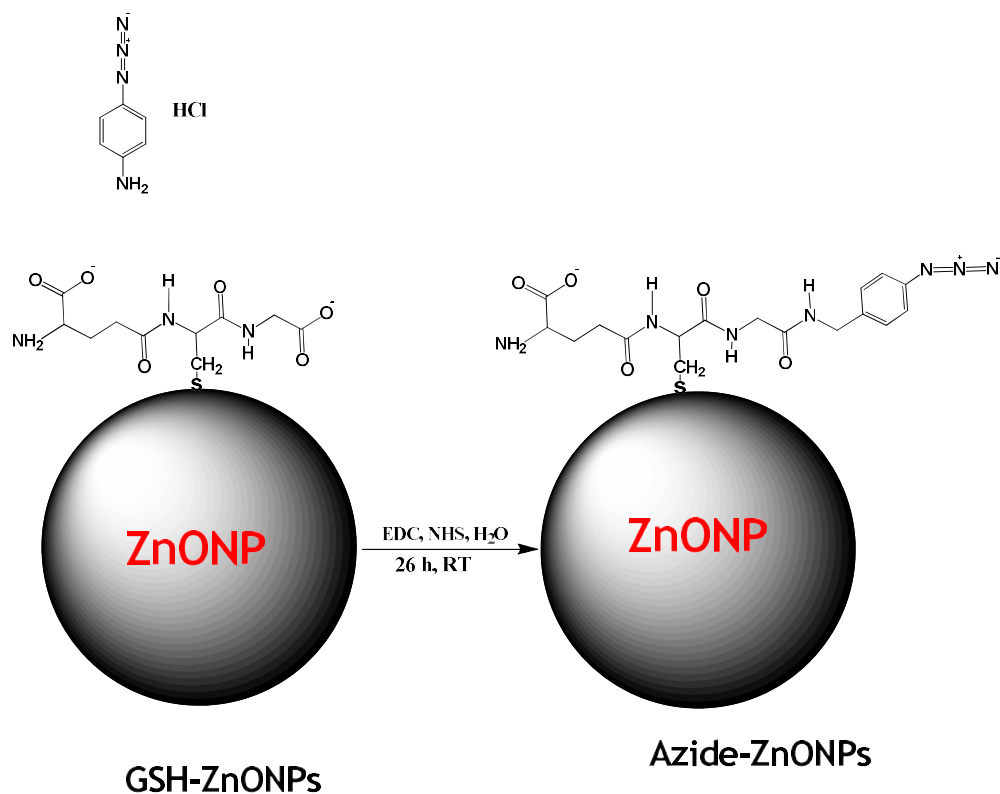
Scheme 3.9: Synthesis of azide-functionalised ZnONPs in aqueous medium using EDC and NHS as cross-linkers at room temperature.
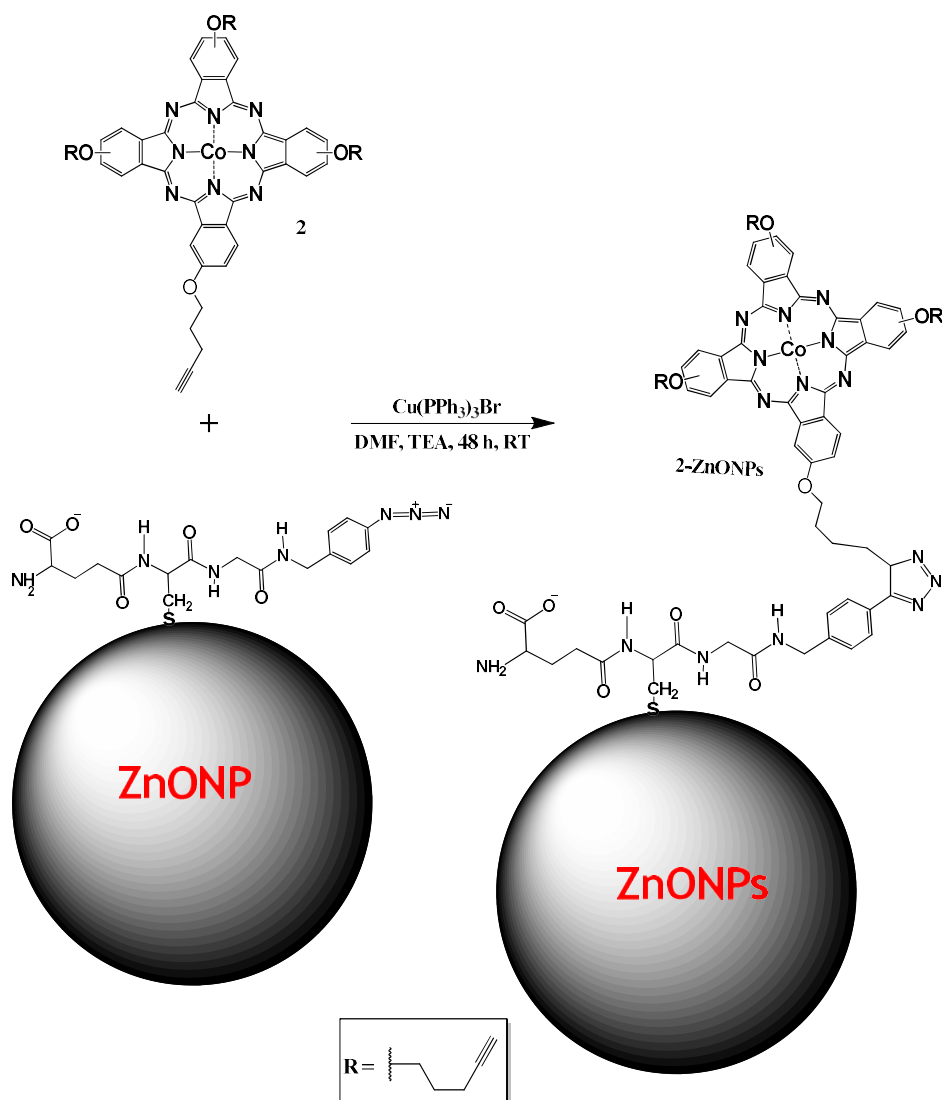
Scheme 3.10: Clicking of azide functionalized ZONPs to complex **2**

3.4.1. FTIR spectra

From Fig. 3.14, the appearance of a peak at 2111 cm^{-1} on azide ZnONPs spectrum which is not present on ZnONPs indicates azide functionalization of ZnONPs was successful. The peaks at 3226, 3287 and 3301 cm^{-1} for GHS-ZnONPs, azide ZnONPs and **2-**ZnONPs respectively are attributed to N-H bond which comes from the GSH capping meaning some GHS remains after azide functionalization. Also, the

disappearances of alkyne H-C stretch (3563 cm^{-1}) of **2** and N$_3$ (2111 cm^{-1}) for azide ZnONPs on the spectrum of **2-Z**nONPs could be attributed to successful click reaction.
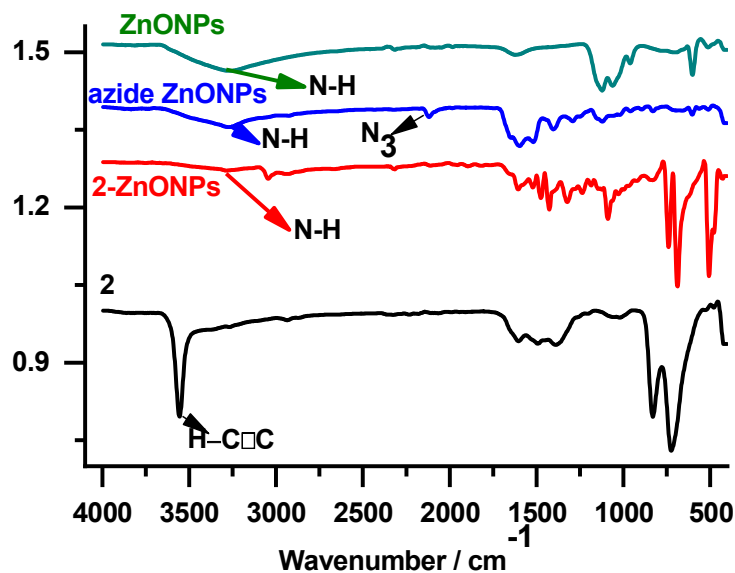
Figure 3.14: FTIR spectra of GSH-ZnONPs, azide ZnONPs, **2**, and **2**-ZnONPs.

3.4.2. UV-Vis and MCD spectra

Fig 3.15 shows the magnetic circular dichroism (MCD) and the UV-Vis absorption spectra of complex **2** in DMF. As stated above a single Q-band at 665 nm (Table 3.1) typical for metallated phthalocyanine was obtained in the absorption spectra [132]. A distinct S-shaped sigmoid curve between 600 and 750 nm was observed in the MCD spectral graph of the **2** with a cross-over point at 667 nm, which corresponds to the same wavelength as that of the absorption maxima. From the MCD spectroscopy, the peaks at 667 and 328 nm bands are assigned as the Q and B bands respectively [142]. There was no change in the Q band maxima of **2** when conjugated to ZnONPs except for the broadening, which is attributed to absorption of ZnONPs (Fig. 3.15).

The loading of Pc onto ZnONPs was determined to be 83 µg/mg using reported literature methods by employing absorption instead of fluorescence [135].
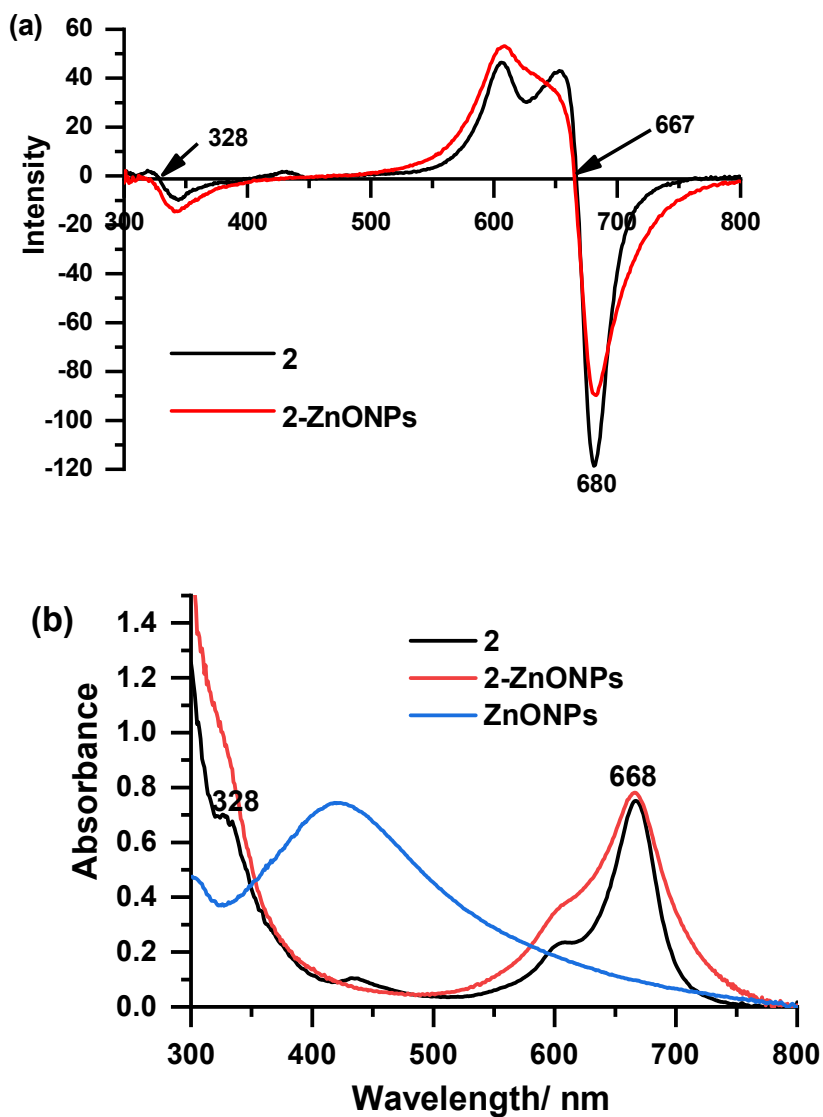
Figure 3.15: (a) MCD spectra (b) electronic absorption and of **2** and **2-ZnONPs** (~×10⁻⁶ M) and azide ZnONPs in DMF.

3.4.3. XPS

The linking of azide functionalized ZnONPs to the **2** via click chemistry was confirmed by comparing the N1s XPS spectra, Fig. 3.16. From the N1s spectra of azide ZnONPs (represented as ZnO-N$_3$ in Fig. 3.16 (a)) alone, the peak at 403.6 eV is assigned to central, electron deficient N, and the peak at 402.7 eV is assigned to the outer N [136] which confirms presence of azide on ZnONPs. The N1s XPS spectrum of **2**-ZnONPs (Fig. 3.16 (b)) show the presence of a peak 403.6 eV which is assigned to the central, electron deficient N of an azide. The observation of this peak could mean that some azide moieties on the ZnONPs were not all involved in the click reaction. The azide peak is highly reduced in intensity in **2**-ZnONPs at 134.3 cps compared to ZnONPs alone at 5420.2 cps, showing that some of the azide are involved in linking.
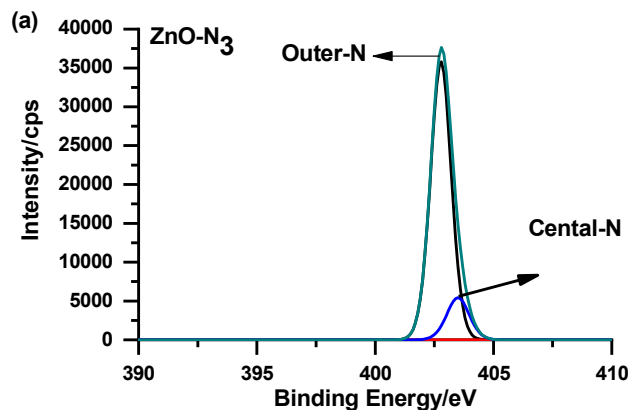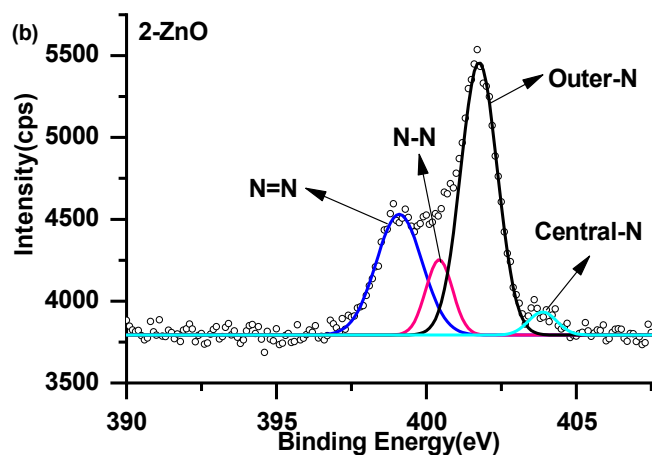
Figure 3.16: High resolution XPS spectra of deconvoluted N 1s component for (a) azide functionalized ZnONPs and (b) **2**-ZnONPs.

3.4.4. DLS

The DLS size of ZnONPs nanoparticles is 6.50 nm and of the Pc conjugate is 43.82 nm (Fig. 3.17), (Table 3.1). There is an increase in size on linking of ZnONPs to **2** due to possible interactions of Pcs on adjacent NPs. Pcs are known for their π-π stacking [142].
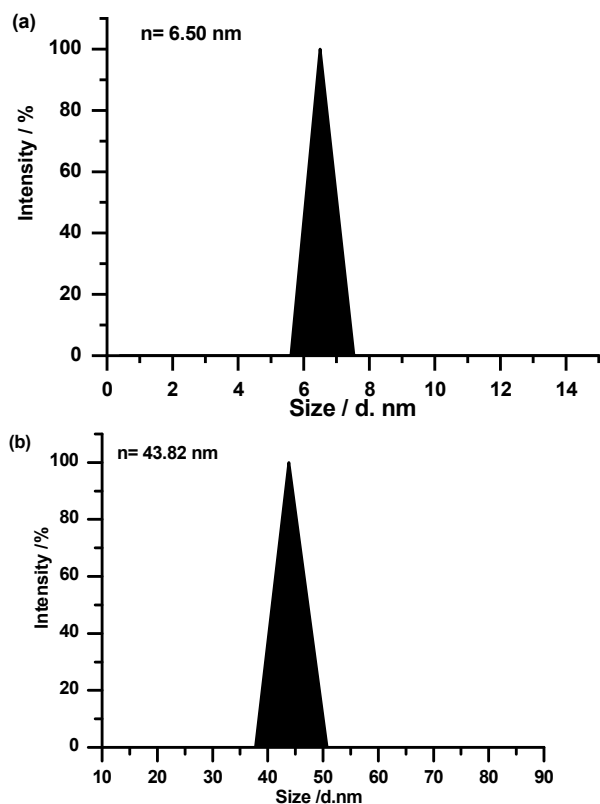
Figure 3.17: DLS graphs showing average particle sizes (a) ZnONPs and (b) **2-ZnONPs.**

3.4.5. XRD, TEM and EDX

Fig. 3.18(a) (right) represents the X-ray diffraction patterns of azide ZnONPs. The diffraction peaks located at 31.69°, 34.42°, 36.14°, 47.49°, 56.70°, 62.88°, 67.90°and 69.06° have been indexed as hexagonal wurtzite phase of ZnONPs [143, 144]. This, further confirms the synthesized nanoparticles were free from impurities as they do not contain any other XRD peaks other than ZnONPs peaks. EDX was used to qualitatively determine the elemental composition of the synthesized azide ZnONPs, Fig. 3.18(a) (left). The presence of Zn and O peaks in Fig. 3.18(a) confirms the successful synthesis of ZnONPs, after conjugation with **2** there was an appearance of Co metal in Fig. 3.18 (b) (left) which comes from the cobalt phthalocyanine used

and this could mean **2** was successfully conjugated to ZnONPs. The appearance of new elements: Cu, P and Br in the EDX spectrum in Fig. 3.18(b) not present in Fig.3.18 (a) could be from the catalyst ($Cu(PPh_3)_3Br$) used in the conjugation reaction. The TEM image of **2**-ZnONPs shows distinct NPs, Fig. 3.18 (b) (right).
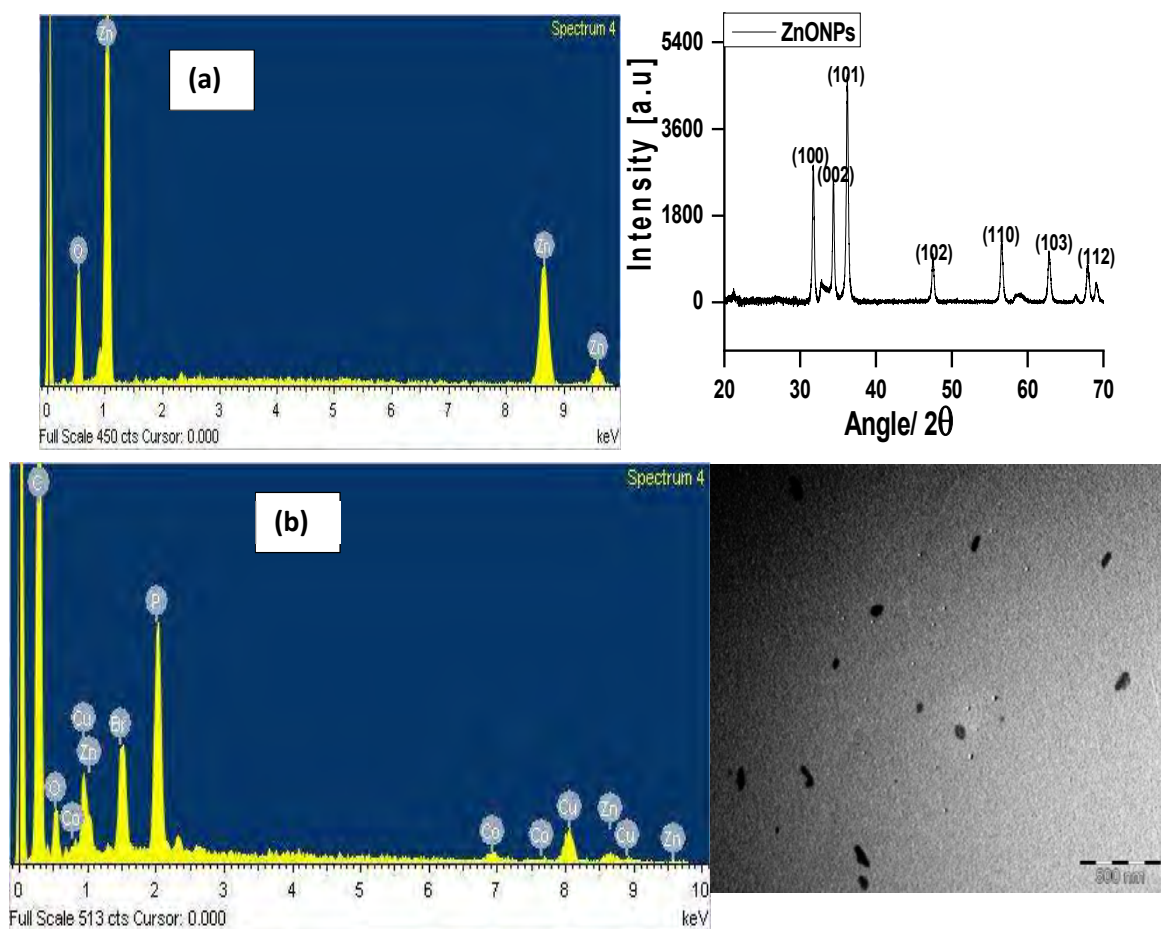
Figure 3.18: (a) EDX (left) and XRD (right) spectra for azide ZnONPs, and **(b)** EDX spectra (left) and TEM image (right) of **2**-ZnONPs.

3.6. Conclusions

XPS results show successful incorporation of azide moiety into rGONS and ZnONPs and confirms their successful conjugation to phthalocyanines via click chemistry. The synthesised nanomaterials were confirmed by TEM, DLS and XRD. The triazole ring was formed after conjugation.

CHAPTER FOUR: Electrode modification and characterization

4. Electrochemical modification and characterization

Various methods were used for modification of glassy carbon electrode in this work namely drop dry method, electrografting and electrodeposition. The electrodes were modified with phthalocyanines alone, or nanomaterials, or conjugates. The conjugates were obtained by using click chemistry and some by using Ag-N bond.

The following techniques were utilised for characterization of modified electrodes scanning electrochemical microscopy (SECM), cyclic voltammetry (CV) electrochemical impedance spectroscopy (EIS), scanning electron microscopy (SEM) and x-ray photoelectron spectroscopy (XPS).

4.1. Grafting and click chemistry of Pc directly onto the electrode, Scheme 4.1

The complexes **1a, 3** and **4** were used to modify the GCE without nanomaterials as shown in the Scheme 4.1. Complex **1a** was both clicked and adsorbed hence indicated in Table 4.1, complexes **3** and **4** were only clicked hence not indicated in Table 4.1

(a)

(b)
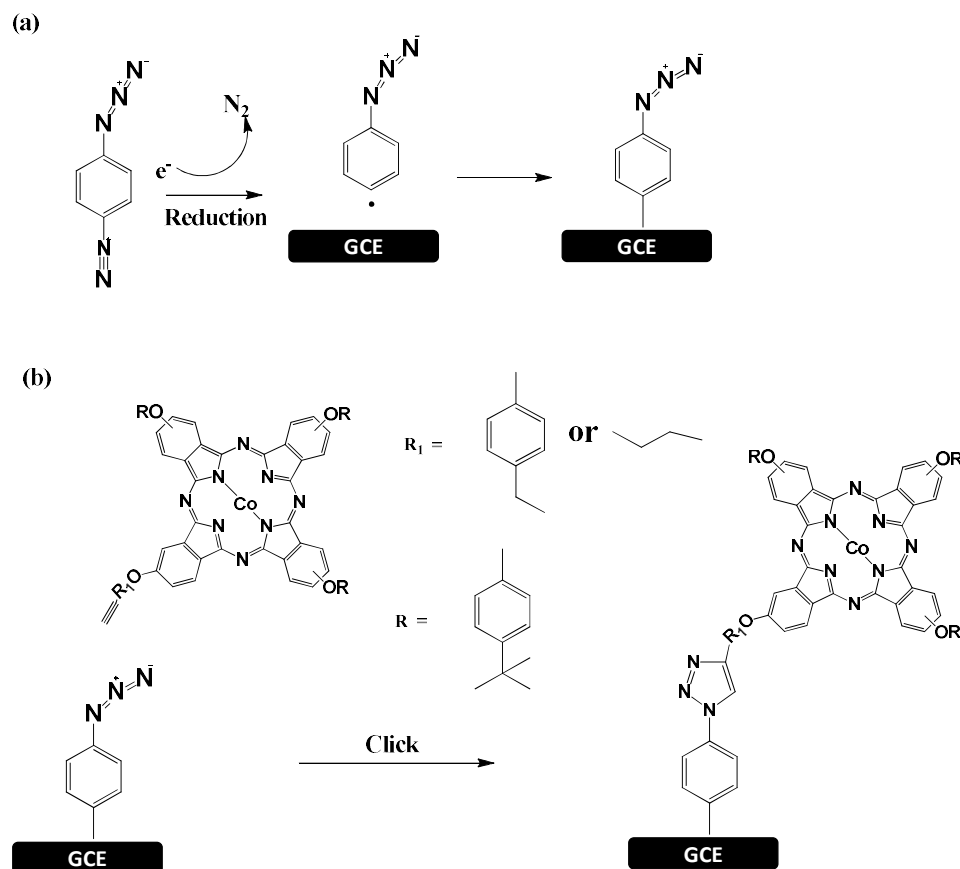
Scheme 4.1: schematic Illustration of grafting of GCE with azide and clicking of complexes **3** and **4** (as examples) on grafted electrode

4.1.1. Cyclic Voltammetry (CV)

From Fig. 4.1 (a), the reduction of 4-azidobenzediazonium to diazonium radicals was confirmed by the appearance of the reduction peak at - 0.5 V on the first cycle and this peak disappeared when the second cycle was recorded, which is an indication that the electrochemical reduction process occurred.

Fig. 4.1 (b) illustrates the response of the bare GCE towards 1 mM ferrocyanide solution and the expected reversible couple is obtained on the bare GCE. The grafting step resulted in the passivation of the GCE. After clicking, the electrode was also tested in the same solution and the passivation continued. This has been

observed before during click reaction [33]. The same behaviour was observed for complexes **3** and **4** in Fig 4.2.
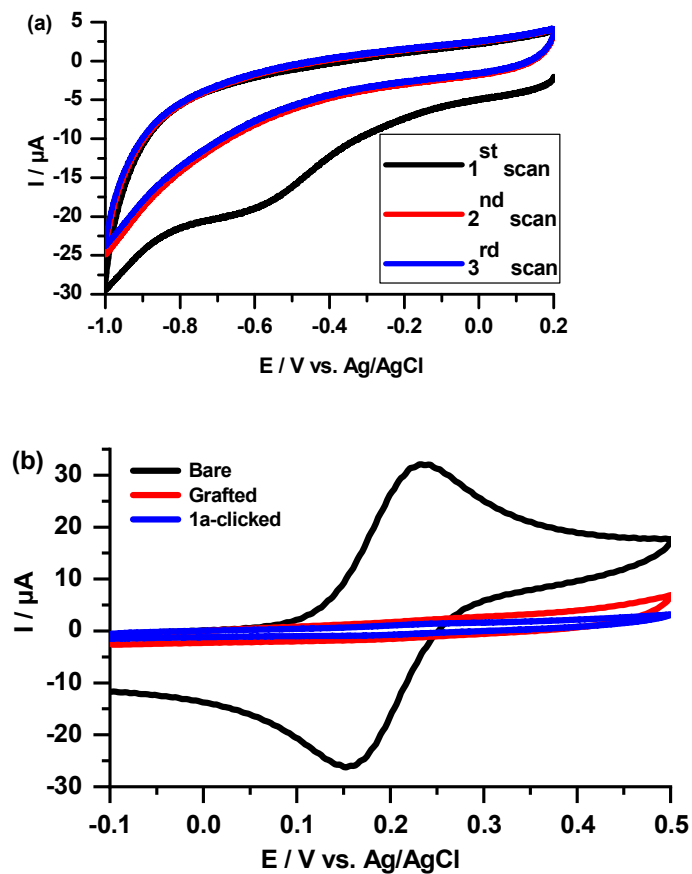
Figure 4.1: Cyclic voltammograms of (a) bare GCE in 0.1 mM 4-nitrobenzenediazonium tetrafluoroborate, in ACN containing 0.1 M TBABF$_4$ and (b) bare GCE, grafted GCE and **1a**-clicked in 1 mM ferrocyanide solution.
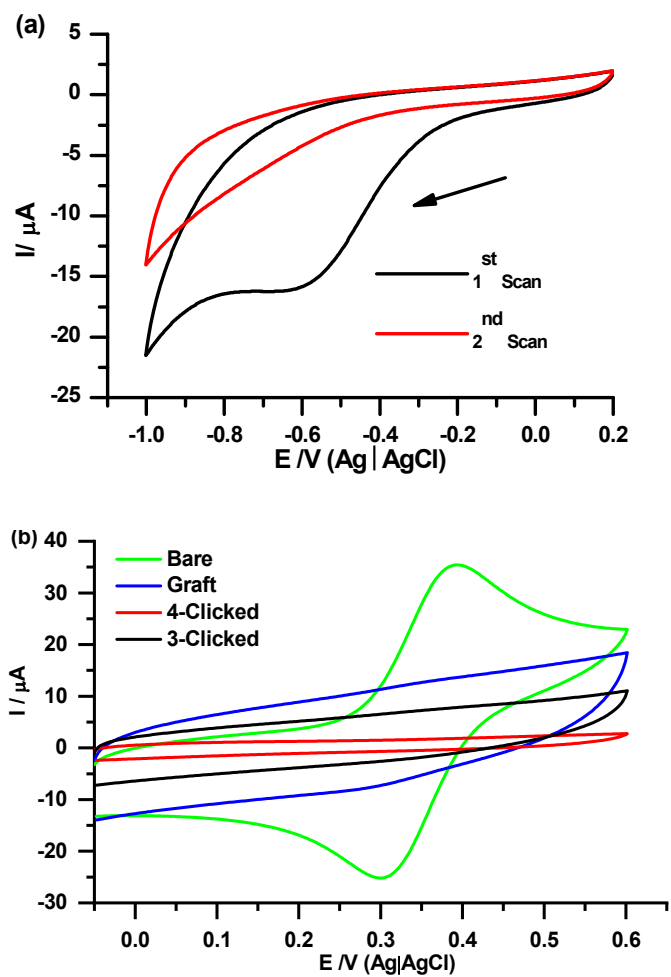
Figure 4.2: Presentation of (a) the grafting of diazonium salt to the GCE and (b) clicking of complexes **3** or **4** to the grafted electrode.

4.1.2. SEM characterization

The SEM images of the electrodes following grafting and clicking are shown in Fig. 4.3 (using **1a** as an example). The bare glassy carbon plate Fig. 4.3 (a) has a homogeneous surface showing that it is unmodified. After grafting, Fig. 4.3 (b) the surface is not homogenous, which is an indication that the surface is modified. In Fig. 4.3 (c) the electrode appears rougher than (b) which is an indication that the clicking of complex **1a** to the grafted glassy carbon plate (b) was successful. Hence, based on the Fig. 4.1 to Fig. 4.3, electrode modification was successful.
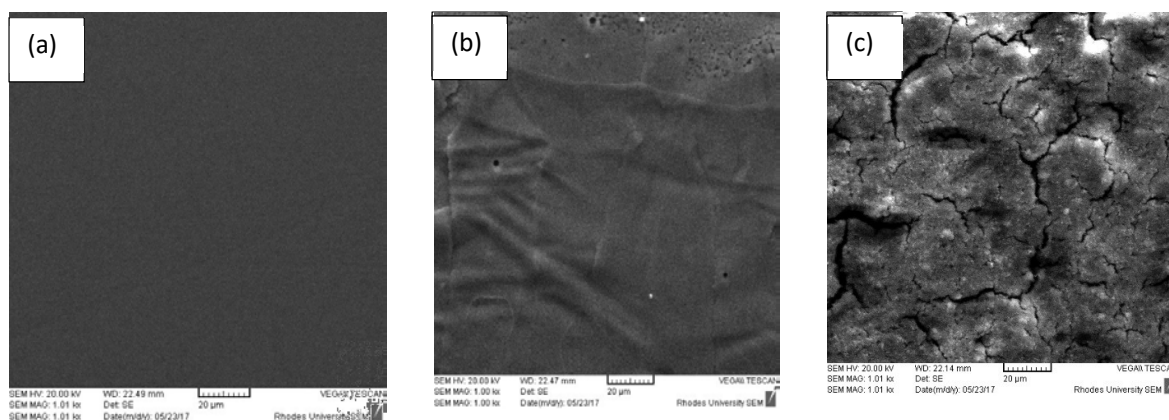
Figure 4.3: SEM images of (a) bare glassy carbon plate, (b) grafted glassy carbon plate and (c) the clicked **1a-**clicked-GCP.

4.1.3. X-ray Photoelectron Spectroscopy (XPS)

The XPS analysis was employed to confirm the successful modification of the electrode surface via click chemistry by analysing elemental composition at the surface. Fig. 4.4 (a) (using **4** as an example) shows wide scan spectra for bare, grafted and clicked electrodes, showing the expected C (1s) peak at 284.9 eV. The O (1s) peak at 529.3 eV may come from air since the modification of the electrode

surface was done in the open environment. The appearance of N (1s) peak at 384.6 eV on grafted and clicked GCE is an indication of a successful grafting. After the grafted GCE was clicked, the Co($2p_{3/2}$) peak is observed at the binding energy of 683.6 eV which is an indication that complex **4** was successfully linked to the grafted surface. From the N1s spectra (Fig. 4.4(b)) of grafted electrode shows a peak at 403.3 eV is assigned to central, electron deficient N, and the peak at 402.8 eV is assigned to the outer N [136] which confirm presence of azide on the grafted electrode. The N1s XPS spectrum of complex (**4**) – GCP clicked show the presence of a peak 403.8 eV which is assigned to the central, electron deficient N of an azide. The observation of this peak could mean that some azide moieties on the grafted electrode were not involved in the click reaction. The azide is reduced in intensity from 60 cps of the grafted electrode to 13 cps for clicked complex-**4** (as an example), showing that some azide are involved in liking. Fig. A1(a) shows the N1s XPS for complex **4** alone with two peaks being observed. Furthermore, an increase in the amounts of C-N for complex-**4** alone (as an example) from 17.38% to 28.42% for clicked complex-**4**-clicked-GCP and C=N from 13.15% to 27.26%, could be due to successful attachment of CoPc on azide functionalized electrodes as CoPc ring has C-N and C=N bonds. The high resolution (C1s) clicked spectra shows a new peak C=N at 285.7 eV in Fig. 4.4(c) which confirms the presence of the Pc on the electrode.

Fig. A1 (b) shows deconvoluted Co 2p XPS spectra of complex-**4** and Fig. A1(c) for clicked complex-**4**. Two distinct peaks are observed at 780.3 eV assigned to Co $2p_{3/2}$ and at 795.3 eV due to Co $2p_{1/2}$ [145]. Both peaks are associated with the Co metal in its +2 oxidation state [145]. Following clicking in Fig. A1(c), both peaks are still present though the Co $2p_{1/2}$ is slightly broadened. The presence of both peaks following clicking shows that the oxidation state of the central metal did not change.
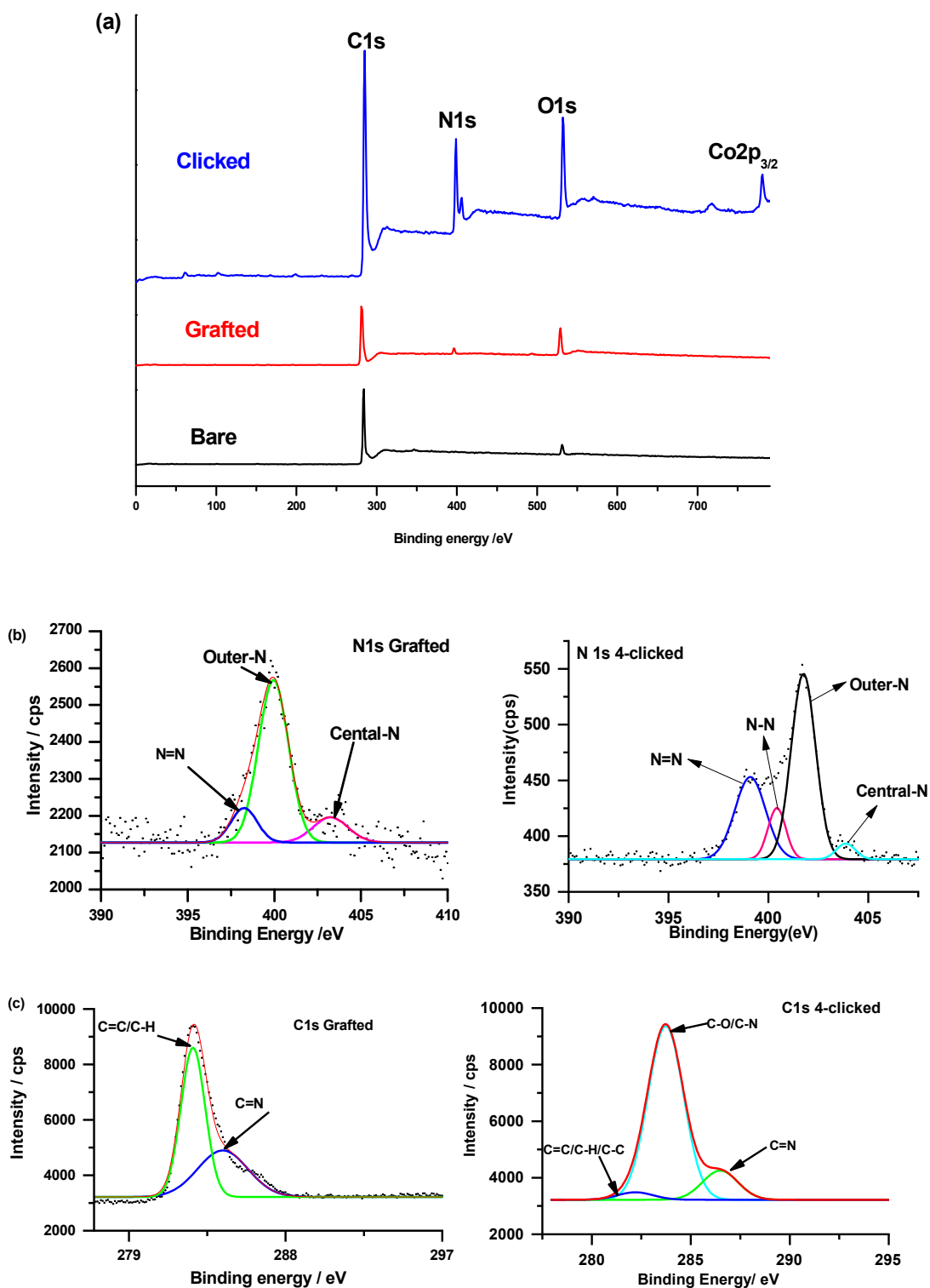
Figure 4.4: (a) Wide scan XPS spectra for bare, grafted and 4-clicked-GCP. High resolution XPS spectrum of (b) N (1s) and (c) C (1s).

4.1.4. Scanning Electrochemical Microscopy (SECM)

Scanning electrochemical microscopy (SECM) was employed to characterize the GCP platforms before and after grafting and clicking. Area scans were done to show the degree of conductivity of the platforms.
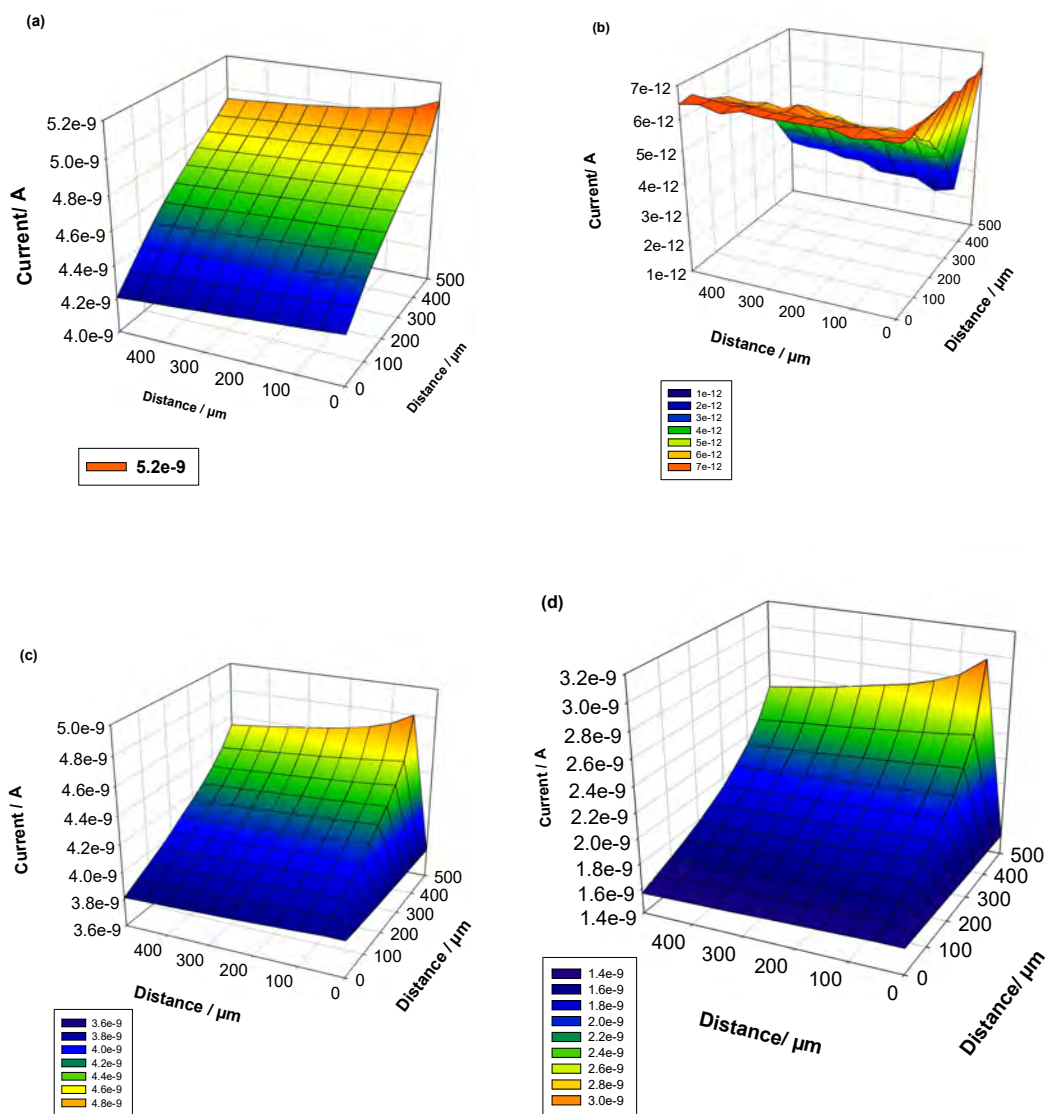
Figure 4.5: SECM area scans for (a) bare GCP, (b) grafted GCP, (c) complex-**3**-clicked-GCP and (d) complex-**4**-clicked-GCP. Carried out in 5 mM $K_3[Fe(CN)_6]/K_4[Fe(CN)_6]$ and 0.1 M KCl using water as a solvent.

The bare surface was scanned for comparison purposes (Fig. 4.5 (a)). The bare GCP

showed that it was smooth and had a maximum current of 5.2 nA. However, after

grafting (Fig. 4.5 (b)) the current dropped to range of 1 to 7 pA which is an indication

that the GCP is passivated by azidoaniline which is insulative in nature. After clicking

the currents ranged from 3.6 to 4.8 nA and 1.4 to 3.0 nA for clicked complexes **3**

and **4** respectively (as examples). Thus, the current ranges were lower than that of

a bare GCP. The SECM results are in agreement with CV results that the largest

currents are observed on the bare electrode and the smallest on the grafted

electrode

Table 4.1: A summary of CV data for the different surfaces in 1 mM $[Fe(CN)6]^{3-/4-}$

Electrode	ΔE_P (mV) 1 mM $Fe(CN)_6{}^{3-/4-}$
Bare GCE	72
QDs	301
1a	
1a-clicked	-
1a-adsorbed	210
1a-QDs	243
1b	294
1b-QDs	186
1c	374
1c-QDs	210
rGONS	90
1a-rGONS(linked)	132
1a-rGONS(seq)	146
2	224
2-rGONS(linked)	140
2-rGONS(seq)	148
ZnONPs	380
2-ZnONPs	120
3-clicked	-
4-cliked	-
5a	250
5a-rGONS(seq)	131
AgNPs	170
5b	360
5b-AgNPs	160
6	183
6-rGONS(seq)	124
CoPc	385

    CoPc-rGONS(seq)   156

[a]seq = sequential.

4.2. Adsorption of clicked conjugates

Clicked QDs conjugates of **1a**, **1b**, **1c** , clicked rGONS conjugate of **1a** and **2** to ZONPs were used to modify electrodes (GCE) by absorption method (**1a** and **2** was also used for sequential modification, labelled Seq) in Table 4.1 and characterized with CV, EIS and SECM in 0.1 M KCl containing $[Fe(CN)_6]^{3-/4-}$ solution. **1a** alone is indicated as **1a**-adsorbed in this section to differentiate from clicked since both methods were used for **1a**. **1b**, **1c** and **2** alone were also adsorbed on the electrodes alone.

4.2.1. Cyclic Voltammetry (CV)

Cyclic voltammetry studies (Fig. 4.6) (using complexes **1** as an example for QDs) were carried out on different electrodes in 1 mM $[Fe(CN)_6]^{3-/4-}$ in 0.1 M KCl. The anodic to cathodic peak potential separation (ΔE_p) are shown in Table 4.1. The lower ΔE_p is related to better charge transfer process.
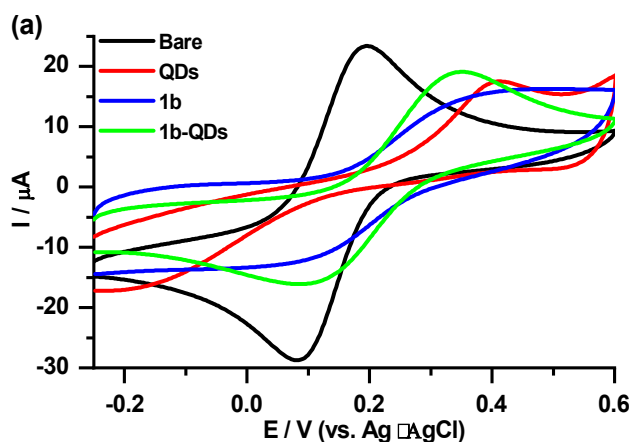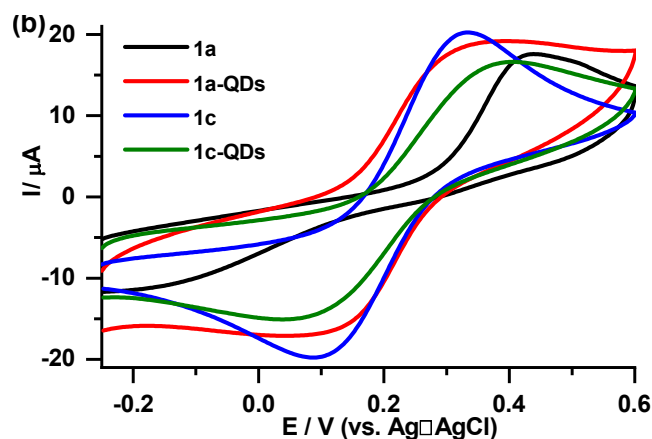
Figure 4.6: Cyclic voltammograms of bare GCE, QDs, **1a**, **1b**, **1c**, **1a**-QDs, **1b**-QDs, and **1c**-QDs In 0.1 M KCl containing 1 mM $[Fe(CN)_6]^{3-/4-}$ solution. Scan rate = 100 mV/s. (Starting potential of scans= -0.25 V).

The ΔE_P of bare GCE (at 72 mV) is closer to the Nernstian value of 58 mV for a one electron process, Table 4.1, this serves an indication of the good charge transfer kinetics for the $[Fe(CN)_6]^{3-/4-}$. The observed changes in ΔE_P values upon modifications confirm alteration on the GCE surface. ΔE_P values of Pcs decreased following conjugation to the QDs, confirming improved charge transfer ability. The following trend can be observed from Table 4.1 for ZnONPs conjugate; **2-**ZnONPs (120 mV) < **2** (224 mV) < azide ZnONPs (380 mV), thus incorporating ZnONPs to **2** results in the decrease of peak separation resulting in be improvement of electron transfer ability of the conjugate. For rGONS conjugates, the ΔE_P values were found to be in the following order: rGONS (90 mV) <**1a**-rGONS(linked) (132 mV) < **2**-rGONS(linked) (140 mV) < **1a**-rGONS(seq) (146 mV) < **2**-rGONS(seq) (148 mV) < **CoPc**-rGONS(seq) (156 mV) < **1a**-adsorbed (210 mV) < **2** (224 mV) < **CoPc** (385 mV). Again, there is generally a decrease in peak separation in the presence of rGONS compared to MPcs alone, this confirms that graphene oxide nanosheets enhance charge transfer, with slightly higher charge transfer ability on rGONS(linked) compared to rGONS(seq). This might

be due to covalent bond easing charge transfer. Also, the substituents on the MPc are found to play a role in the charge transfer as MPc with benzyl substituent (**1a-**adsorbed) is found to result in better charge transfer than when MPc only bears an aliphatic substituent (**2**). The MPc without the substituents (**CoPc**) gave poor results compared to its substituted counterparts.

The Randles-Sevcik Eqn. 4.1 [146] can be applied on $[Fe(CN)_6]^{3-/4}$ redox couple in Fig. 4.6 to determine the effective electrode area.

$$I_p = 2.69 \times 10^5 n^{3/2} A C D^{\frac{1}{2}} v^{1/2}$$ 4.1

where I_p, A, C, D, n, and v are the peak current, the effective surface area, concentration of $[Fe(CN)_6]^{3-/4}$, diffusion coefficient of $[Fe(CN)_6]^{3-/4}$, the number of electrons involved, and scan rate, respectively. The literature value for D = 7.6 × 10^{-6} cm^2s^{-1} [147] for $[Fe(CN)_6]^{3-/4}$ was used. The effective electrode area was determined using Eqn. 4.1 and plotting current at different scan rates. The same scan rate was used for the data from where Q was determined for comparison purposes.

The CoPc derivatives were used as electrode modifiers and cycled in pH 7 buffer, Fig. 4.7. The peaks at around 0.75 V (**III**) are assigned to ring based processes, peaks near -0.5 V (**I**) is assigned to Co^{II}/Co^{I} couple and Co^{III}/Co^{II} processes are near 0 V (**II**) which is a slight shift to the less positive potentials relative to literature [148].The slight difference from Fig. 3.4 could be due to solution versus adsorbed species.

By using the effective area of the modified electrodes determined using Eqn. 4.1 and the total charge determined by integrating the cathodic peak area of Co^{II}/Co^{I} (**I**) Fig. 4.7 and then by employing Eqn. (4.2), surface coverages were calculated.

$$\Gamma = \frac{Q}{nFA} \qquad\qquad (4.2)$$

where Q is the electric charge, n is the number of electrons transferred ($\sim$ 1), F the Faraday constant (96,485 C mol^{-1}) and A is the effective surface area obtained from Eqn. 4.1. The surface coverages reported in this work (ranges from 4.65×10^{-10} mol cm^{-2} to 3.23×10^{-9} mol cm^{-2}) (Table 4.2) and were higher than the reported value for phthalocyanines lying flat on the surface of the electrode (1×10^{-10} mol cm^{-2}) [149] suggesting that the clicking of graphene oxide nanosheets hinder metallophthalocyanines from lying parallel to the electrode surface. In addition to that, the high surface coverage values of Pcs alone could imply a perpendicular orientation on the GCE. The higher surface coverages imply the increase in the electrode surface area which offers more electrocatalytic surface.

Table 4.2: A summary of surface coverages for different electrode^{-}

Electrode	Γ (mol cm^{-2})
1a-adsorbed	1.55×10^{-9}
1a-rGONS(linked)	3.23×10^{-9}
1a-rGONS(seq)	2.84×10^{-9}
2	1.42×10^{-9}
2-rGONS(linked)	2.47×10^{-9}
2-rGONS(seq)	2.52×10^{-9}
CoPc	4.65×10^{-10}
CoPc-rGONS(seq)	2.12×10^{-9}
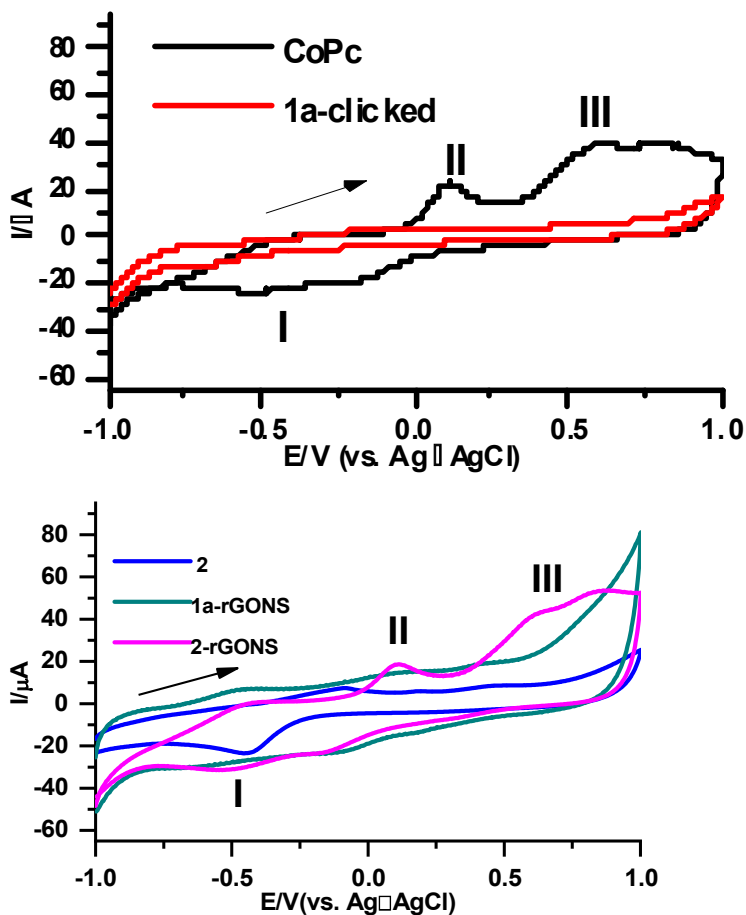
Figure 4.7: Cyclic voltammograms of a selection of modified electrodes containing the CoPc derivatives in 0.5M NaOH solution. Scan rate = 100 mV/s

4.2.2. Electrochemical Impedance Spectroscopy

Electrochemical impedance spectroscopy (EIS) was carried in order to get an insight into charge transfer kinetics occurring at the electrode/electrolyte interface. EIS is an informative and non-destructive technique useful in probing molecules at the surface. There are two plots which are commonly used to show impedance behaviour [150]. These are the Nyquist and Bode plots. The Nyquist plots are shown in Fig. 4.8(a) for **1b** and Fig. A2 (a) for **1c** and conjugates. Fig. 4.8(c) represents the fitting

model used. The Nyquist plot (Fig. 4.8(a), Fig. A2(a), is divided into two frequency regions, the kinetically-controlled (high frequency) region where a semi-circle is observed and the diffusion-controlled (low frequency) region where the Warburg line is observed. On a Nyquist plot the infinite Warburg impedance appears as a diagonal line. Parameters such as the electrolyte resistance (R_s), charge transfer resistance (R_{ct}), capacitance (C_{dl}), and Warburg impedance (W) can be determined from Nyquist plots. A high R_{ct} signifies low conductivity of the electrodes. The obtained charge transfer resistance (as examples) are as follows: bare (11.74 kΩ cm^{-2}), QDs (42.30 kΩ cm^{-2}), **1a**-adsorbed (8.48 kΩ cm^{-2}), **1b** (32.86 kΩ cm^{-2}), **1c** (7.92 kΩ cm^{-2}), **1a**-QDs (4.53 kΩ cm^{-2}), **1b**-QDs (4.10 kΩ cm^{-2}) and **1c**-QDs (2.69 kΩ cm^{-2}), Table 4.3. Generally, QDs increased the conductivity of the electrodes with **1c**-QDs showing least resistance followed by **1b**-QDs. Hence, conjugating QDs to MPc improve electron transfer at the electrode surface. The decrease in R_{ct} values in the presence of QDs is in agreement with the decrease in ΔE values (improve charge transfer ability) discussed above. The Warburg parameter (W), Table 4.3, decreased in the presence of QDs showing slow diffusion. The C also decreased in the presence of QDs, Table 4.3. For probes **1a**, **2**-ZnONPs and **2**-rGONS the EIS studies were not carried out.

(a)
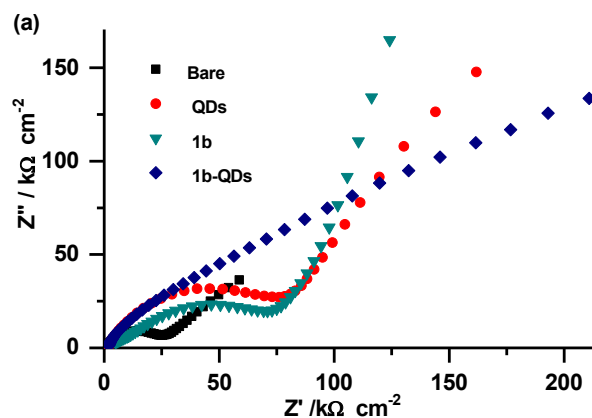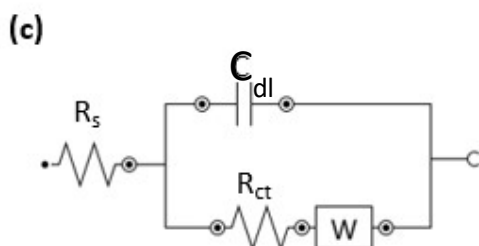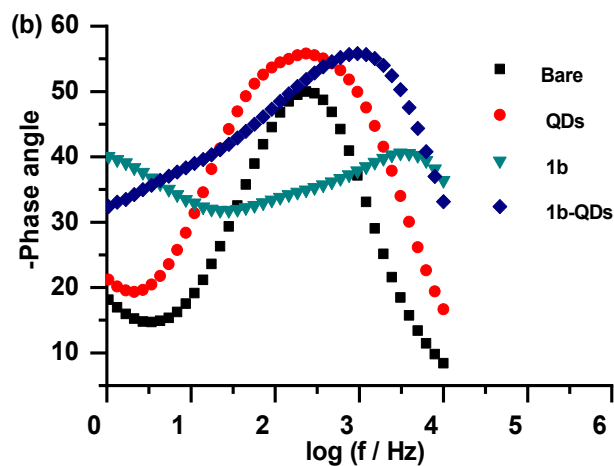
Figure 4.8: (a) Comparative Nyquist plots (b) Bode plot of electrodes and the fitting model used (c), where W is Warburg parameter and C_{dl} is capacitance. In 0.1 M KCl containing 1 mM [K_3[Fe(CN)$_6$]/K_4[Fe(CN)$_6$] solution.

The apparent electron transfer rate constant (k_{app}) was calculated using Eqn. 4.3 [146]:

$$k_{app} = \frac{RT}{n^2\,F^2\,AR_{ct}C} \qquad\qquad 4.3$$

where R_{ct} is charge transfer resistance, C is the concentration of the [Fe(CN)$_6$]$^{3-/4-}$ solution, n is number of electrons transferred, A is the real surface area of the electrode, R is the ideal gas constant, T is the absolute temperature (K), and F is Faraday constant. The real surface area (A) was calculated using Randles Sevcik Eqn. 4.1 above.

The k_{app} values increased for the Pcs in the presence of QDs, showing the importance of linking the two, Table 4.3. It was found out that **1c** and **1c**-QDs had higher k_{app} values than the corresponding of the Pcs and conjugates.

Fig. 4.8(b) (and Fig. A2 (b) for **1c** and its conjugate) shows Bode plots of electrode surfaces. The phase angle values for all the electrodes studied are less than the ideal 90° for a true capacitor leading to the conclusion that these electrodes are of leaky capacitor behavior [151]. On a Bode plot, the Warburg impedance exhibits a phase shift of 45°. Only **1c** electrode could have a Warburg behaviour because the phase angle is 45°. The deviations from 45° for the rest of the electrodes could be related to differences in the roughness of the surfaces.

The slopes of the Bode plots (log Z vs. log f, Fig. A2(c)) are less than ideal – 1.0 for pure capacitor behaviour at the mid frequency region, indicative of pseudo-capacitive behaviour [152]. The data in Table 4.3 gave percentage errors less than 5% making reliable.

Table 4.3. A summary of EIS data on different electrodes in 1 mM $[Fe(CN)_6]^{3-/4-}$ in 0.1 M KCl supporting electrolytes.

Electrode	R_{ct} / kΩ cm^{-2}	W/ kΩ cm^{-2}	C / µF cm^{-2}	k_{app}/10^3 cm s^{-1}	Error (%)
Bare GCE	11.74	7.068	9224	0.31	2.45
QDs	42.30	0.011	3621	1.62	4.89
1a-adsorbed	8.48	0.044	3608	2.79	3.22
1a-QDs	4.53	0.040	1952	7.03	1.98
1b	32.86	0.060	2660	4.43	2.36
1b-QDs	4.10	0.044	1740	7.87	3.47
1c	7.92	0.069	2150	5.22	4.66
1c-QDs	2.69	0.060	778	9.46	3.18
rGONS	8.04	0.082	686	5.74	4.06
5a	38.74	0.075	642	0.62	2.65
5a-rGONS(seq)	18.96	0.053	523	1.97	3.60
6	22.48	0.066	692	1.27	3.61
6a-rGONS(seq)	12.72	0.048	543	2.53	4.01

4.2.3. Scanning electrochemical microscopy (SECM)

SECM approach curves were used to study surface activity of modified surfaces, Fig. 4.9 (using **1b** and **1c** as examples). The bare-GCP produced an increase in current with an increase in proximity to the surface, indicating conductivity. An increase in current was also observed for **1b**, and **1c** (Fig. 4.9(b)). The currents increase further after conjugation with QDs, hence this shows the importance of conjugation. The

trend in activity as revealed by the calculated tip current-limiting current (I/I_{lim}) (at

0 d/a= distance per surface area of the working electrode) is as follows: bare GCP <

1a < **1a**-QDs < **1b** < **1b**-QDs < **1c** < **1c**-QDs. The trend shows **1c**-QDs to produce higher

currents relative to other probes making it suitable for electrocatalysis, the obtained

SECM result is in agreement with EIS data (in terms of R_{CT}, shown in Table 4.3). The

insulating nature of Teflon is judged by the decrease in current as the tip approaches

the surface, Fig. 4.9(a). The area scan technique SECM was used to study the effect

of electrode modification. From Fig. 4.10 it can be seen that unmodified and

modified electrodes give smooth micrographs suggesting that the plates have a

uniform surface and there was uniform immobilization of the probes on the plate.

Also for the modified electrodes in Fig. 4.10 (b-d), the obtained results are similar

to what is reported in the literature [153] in terms of topography and it is an

indication that the electrode modification is complete since a homogenous current

with a regular topography is observed. Electrodes showed varying current of range

0.12 to 0.28 nA (bare GCP) < 3.7 to 4.2 nA (rGONS) < 4.10 to 4.45 nA (GCP-**2**) $\cong$ 4 to

5 nA (GCP-**2**-rGONS(linked)). The bare GCP showed the lowest current, followed by

rGONS. The largest currents were obtained for Pcs and their conjugates. Please note

that the current for bare GCP is different from Fig. 4.5, since a different plate was

employed. Also, different y-axis scan ranges were used for Figs. 4.5 and 4.10.
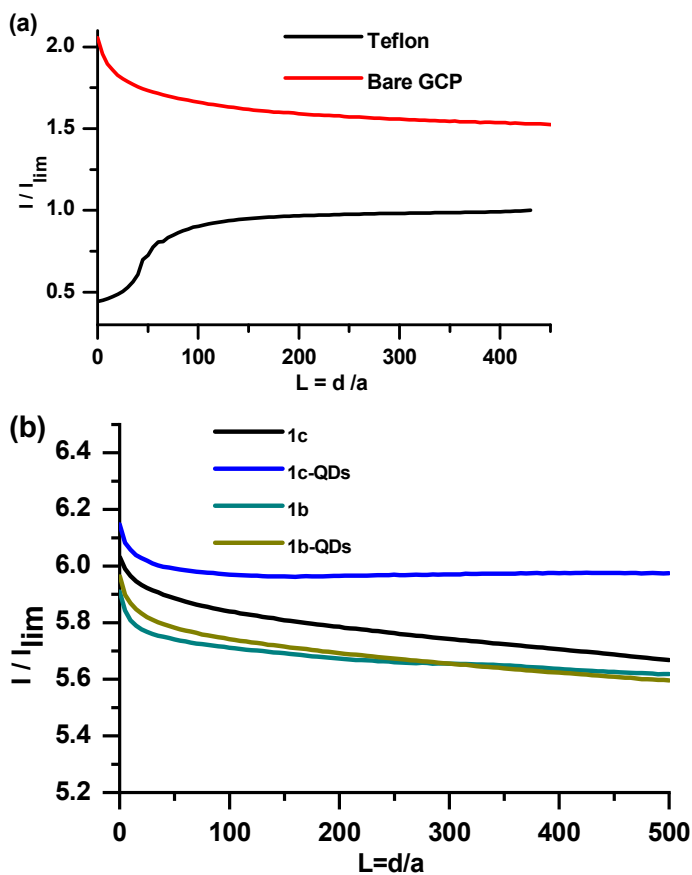
Figure 4.9: SECM approach curve of Teflon, bare GCP, **1b, 1c, 1b**-QDs and **1c**-QDs In 0.1 M KCl containing 5 mM $[Fe(CN)_6]^{3-/4-}$ solution. Scan rate = 100 mV/s.
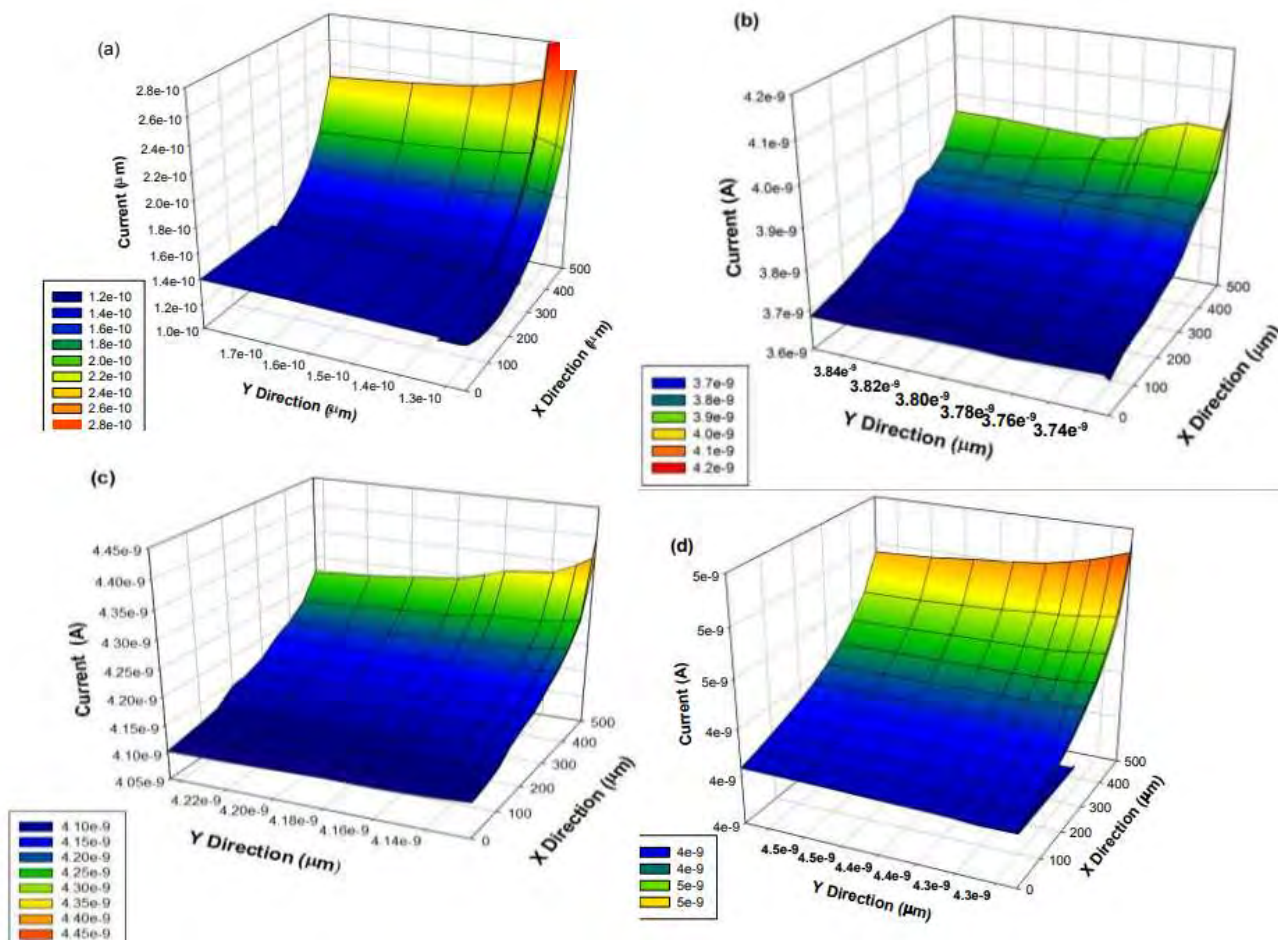
Figure 4.10: SECM Micrograph on (a) bare GCP (b) GCP-rGONS, (c) GCP-**2** and GCP-**2**-rGONS (linked).

4.3. Electrodeposition

Scheme 4.2 shows the electrochemical synthesis of AgNPs on **5b**. For **5b**-AgNPs prior to electrodeposition process, **5b** was first drop dried on the GC plate, followed by the growth of AgNPs. The Ag self-assembles onto the **5b** through the Ag-N bond.
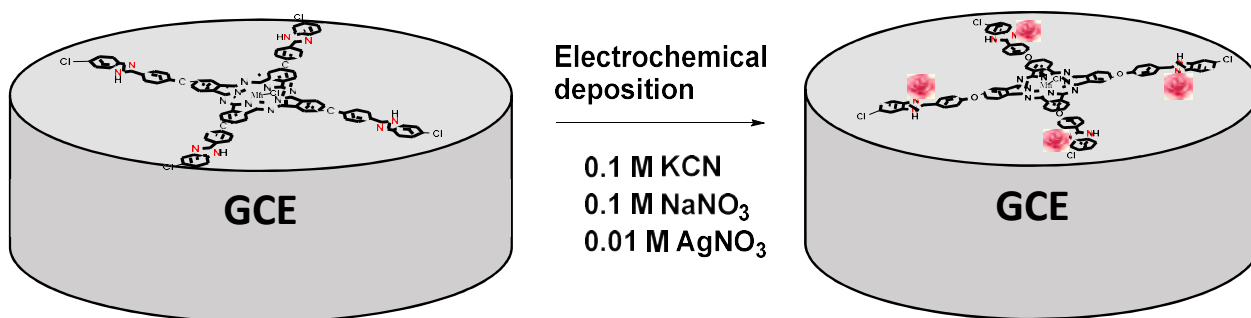
Scheme 4.2. Schematic diagram of **5b**-AgNPs conjugate.

4.3.1. Cyclic Voltammetry

Fig. 4.11 shows cyclic voltammograms for the modified electrodes in 1 mM
$K_3[Fe(CN)_6]/K_4[Fe(CN)_6]$ in 0.1 M KCl solution. The peak potential separation ΔE for
a reversible system such as $K_3[Fe(CN)_6]/K_4[Fe(CN)_6]$ is a good measure of the charge
transfer ability of the electrode with lower values showing a good charge transfer
ability. The decrease in ΔE follows the order: **5b** (ΔE = 360 mV) > AgNPs (ΔE = 170
mV) ≈ **5b**-AgNPs (ΔE = 160 mV), Table 4.1. It can be noted that **5b**-AgNPs showed
lower potential difference than **5b** and this could be the synergistic effect of **5b** and
AgNPs.
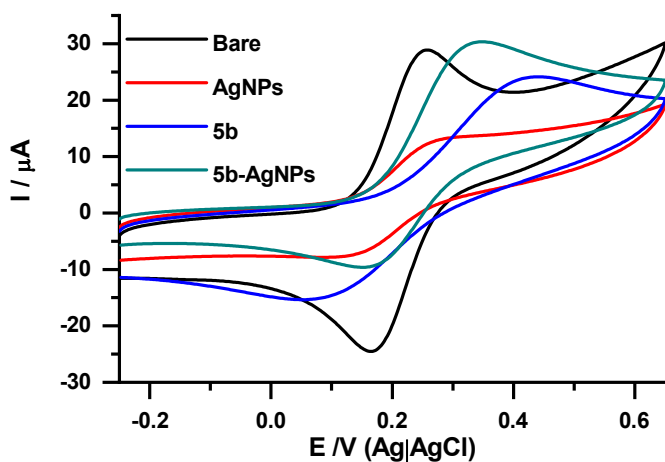
Figure 4.11: Cyclic voltammetry of bare, AgNPs, **5b**, and **5b**-AgNPs in 1 mM
$K_3[Fe(CN)_6]/K_4[Fe(CN)_6]$ solution. Scan rate: 100 mVs^{-1}.

4.3.2. Scanning electron microscopy (SEM) and energy dispersive X-ray analysis (EDX)

SEM images of bare GC plate Fig. A3, **5b** (Fig. A4 (a), AgNPs (Fig. A5 (a) and **5b-AgNPs** (Fig. 4.12a) modified GC plates present different morphologies of the different electrodes. Bare GC plate shows a smooth surface, while the SEM image of adsorbed **5b** shows irregular shapes and a rough surface. The SEM image of the AgNPs show flower-like particles (Fig. A5 (a)) which are also present in **5b**-AgNPs, Fig. 4.12(a).

EDX spectra for **5b**-AgNPs (Fig. 4.12(b)) confirms presence of silver element, the other elements K, Na and O could be from the electrolyte and KCN used in the electrodeposition process. The appearance of extra element (Mn) on the EDX image Fig. 4.12(b) confirm the presence of manganese metal which comes from the phthalocyanine. The Mn is absent in AgNPs alone (Fig. A5 (b)) and present in **5b** alone (Fig. A4 (b)).

SEM HV: 30.00 kV   SEM MAG: 4.57 kx   VEGA\\ TESCAN
WD: 20.17 mm   Det: SE   5 µm
SEM MAG: 4.57 kx   Date(m/d/y): 08/20/19   Rhodes University SEM
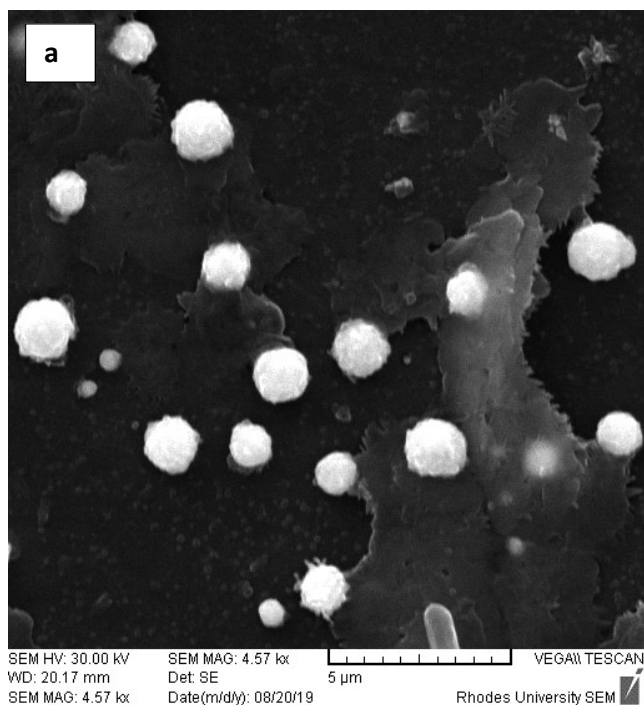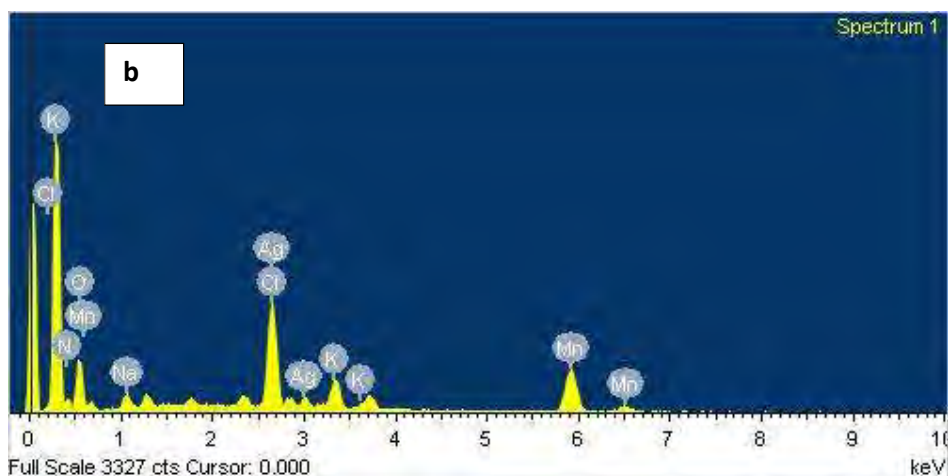
Figure 4.12: (a) SEM image of **5b**-AgNPs and the corresponding (b) EDX spectrum.

4.3.3. Scanning Electrochemical microscopy

The SECM approach curves were used in the study of surface activity of modified surfaces, shown on Fig. 4.13. The bare GCP showed an increase in current with an increase in proximity to the surface indicating conductivity and upon modification with AgNPs, **5b** and **5b**-AgNPs the conductivity increases. The trend in activity as revealed by the calculated tip current-limiting current (I/I_{lim}) (at d/a=0 as mentioned before) is as follows: Bare GCP $<$ **5b** $<$ AgNPs $<$ **5b**-AgNPs. The trend shows **5b**-AgNPs to produce relatively higher currents rendering it suitable for electrocatalysis, the obtained SECM result is in agreement with CV data (in terms of potential difference, discussed below)
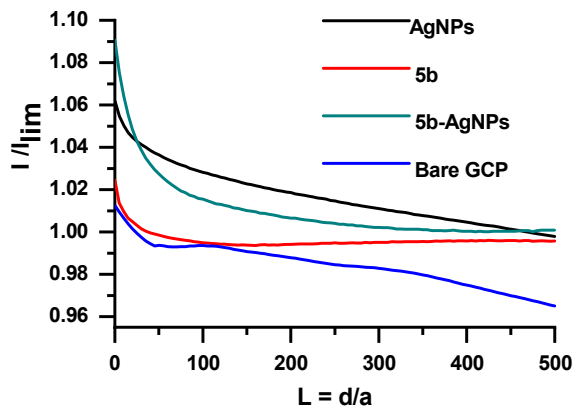
Figure 4.13: SECM approach curve of bare GCP, AgNPs, **5b**, **5b**-AgNPs In 0.1 M KCl containing 5 mM $[Fe(CN)_6]^{3-/4-}$ solution. Scan rate = 100 mV/s.

4.4. Sequential modification only

For electrode modification, 1 mg of each material (rGONS, **5a**, or **6**) was dissolved in 1000 μL of DMF and sonicated. Each of the dispersed material (0.5 μL) was dropped on the glassy carbon electrode separately (rGONS, **5a**, **6**) and sequentially (**5a**-rGONS(seq) or **6**-rGONS(seq)) and dried in an oven. It have been reported that the best catalytic activity is obtained when MPcs are placed on top of nanomaterials [154], hence in this work for the sequentially modified electrodes, rGONS are placed first on the electrode followed by CoPc derivatives.

4.4.1. Cyclic voltammetry

Fig. 4.14(a) shows the CVs of probes in 1 mM $K_3[Fe(CN)_6]/K_4[Fe(CN)_6]$. The obtained anodic to cathodic peak separations (ΔE_p) were 90, 250, 183, 131 and 124 mV for rGONS, **5a**, **6**, **5a**-rGONS(seq) and **6**-rGONS(seq) respectively(as shown in Table 4.1). The lower the (ΔE_p) the better the charge transfer, **6** has lower (ΔE_p) than **5a** this could be attributed to *tert*-butyl phenoxy substituent present in **6** as they are electron donating. Generally, using the combination of cobalt phthalocyanines and

rGONS resulted in the lowering of (ΔE_p) this is due to electron rich π-π system of rGONS. **6**-rGONS(seq) gave better charge transfer than **5a**-rGONS(seq).

Fig. 4.14 (b) shows the cyclic voltammograms of bare, rGONS, **5a, 6, 5a**-rGONS (seq) and **6**-rGONS (seq) in supporting electrolyte (0.20 M NaOH). There are no peaks for bare and rGONS. For CoPc containing electrodes, the peak at around -0.5 V (**I**) is due to $Co^{II}Pc^{-2}/Co^{I}Pc^{-2}$ redox couple and $Co^{III}Pc^{-2}/Co^{II}Pc^{-2}$ processes are near 0 V (**II**) as discussed above. The peak (**III**) at around 0.6 V corresponds to ring based processes as discussed above.
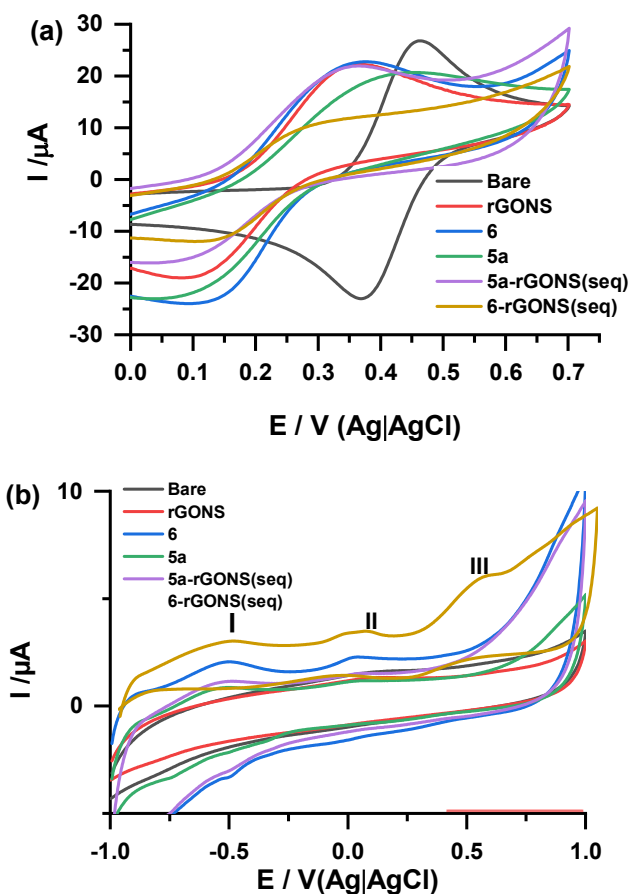
Figure 4.14: Cyclic voltammetry of bare, rGONS, **5a, 6, 5a**-rGONS(seq) and **6**-rGONS(seq) in (a) 1 mM $K_3[Fe(CN)_6]/K_4[Fe(CN)_6]$ solution and (b) 1 mM hydrazine in 0.2 M NaOH. Scan rate: 100 mVs^{-1}.

4.4.2. Electrochemical impedance spectroscopy (EIS)

The insight into the charge transfer process of $K_3[Fe(CN)_6]/K_4[Fe(CN)_6]$ redox couple at the electrodes was obtained from EIS. Fig. 4.15 (a) shows Nyquist plots obtained for bare, rGONS, **5a**, **5a**-rGONS, **6** and **6**-rGONS at frequencies between 10 kHz and 0.1 Hz. The R_{ct} values obtained are provided in Table 4.3, the lower the R_{ct} the better the charge transfer kinetics. **6** gave lower R_{ct} value (22.48 kΩ cm^{-2}) compared **5a** (38.74 kΩ) cm^{-2} due to presence of electron donating substituent in the former. Furthermore, incorporating rGONS to phthalocyanines resulted in the lowering of R_{ct} values which could be attributed to highly conjugated rGONS system.

The apparent charge transfer rate constants (k_{app}), Eqn. 4.3 was largest for **6**-rGONS (k_{app} = 2.53 × 10^3 cms^{-1}) compared to other rGONS based probes however, **1c**-QDs gave the largest k_{app} of all probes, Table 4.3. The results corroborate CV results.
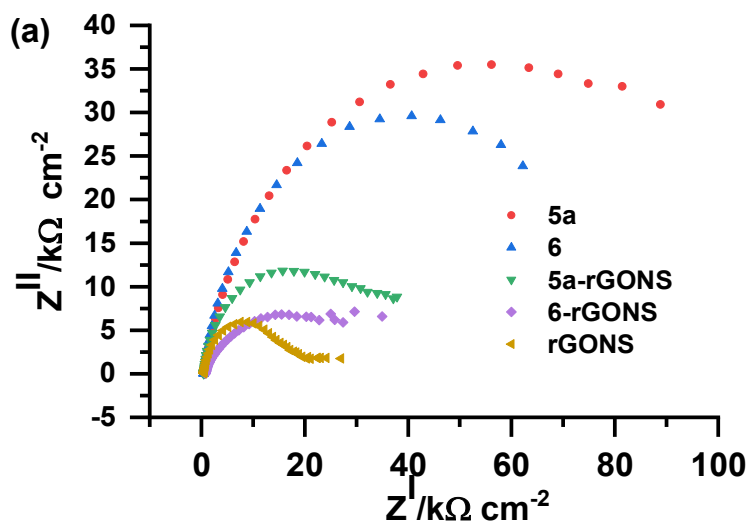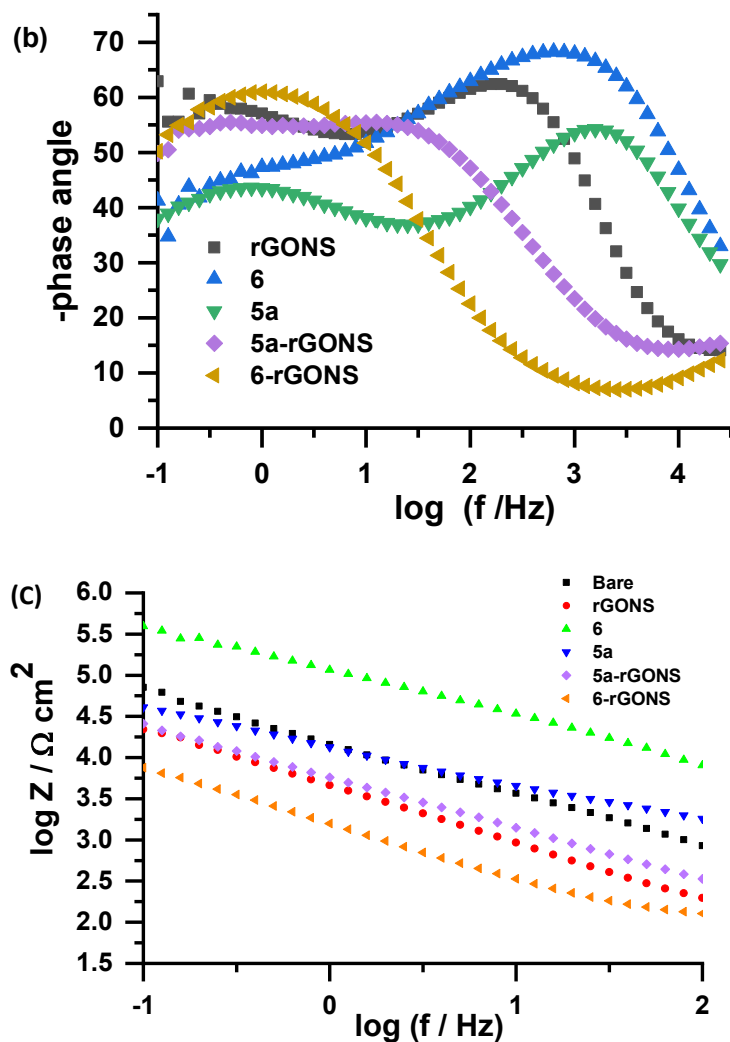
Figure 4.15: Nyquist plots (a), bode plots (b) and (c) plot of log f vs. log Z for rGONS, **5a**, **6**, **5a-**rGONS and **CoPc-**rGONS in 1 mM $K_3[Fe(CN)_6]/K_4[Fe(CN)_6]$ solution.

The Bode plots of phase angle versus log (f/Hz) 1 mM $K_3[Fe(CN)_6]/K_4[Fe(CN)_6]$ solution are shown in Fig. 4.15 (b). The Bode plot for complex **5a** shows a complicated behaviour with two decoupled phenomena having two different relaxation periods suggesting different relaxation behaviour. This behaviour has been observed before and related many factors including film thickness [155], which could result in different diffusion processes within the film. This was also observed for **1b** in Fig. 4.8. All phase angles obtained for probes developed in this study are less than 90° and more than 45° therefore, the results suggest that these electrodes

do not work like an ideal capacitor and permits the diffusion of $[Fe(CN)_6]^{3-/4-}$ redox

probe [151]. The slopes in Fig.4.15 (c) of Bode plots (log Z vs. log f) are all less than

- 1.0 for a pure capacitor behaviour at mid frequency, this suggests that all modified

platforms possess pseudo-capacitive behaviour which is agreement with the results

obtained in Fig. 4.15 (b).

4.8. Conclusions

The modified electrodes were electrochemically analysed and found to have higher

effective electrode area. This implies an increase in the surface area on which the

electrocatalysis reactions are to occur. Generally, the conjugates showed improved

electron transfer abilities than individual materials.

CHAPTER FIVE: Electrocatalysis

5. Electrocatalysis

This focuses on the examination of the different catalytic platforms towards electrocatalysis of hydrazine, 2-mercaptoethanol, hydrogen peroxide and oxygen reduction reaction.

5.1. Hydrazine detection

5.1.1. Clicked Pcs without nanomaterials

Complexes **1a**, **3** and **4** were employed

5.1.1.1. Cyclic voltammetry

Hydrazine was chosen as a test analyte as it has been reported in the literature that CoPc derivatives readily oxidises this analyte [156-158]. Fig. 5.1(a) shows a comparative CVs of the bare GCE, grafted, **1a**-clicked and **1a**-adsorbed in a potential window of 0 to 0.75 V vs Ag/AgCl reference electrode and Fig. 5.1(b) for complexes **3**-clicked and **4**-clicked.
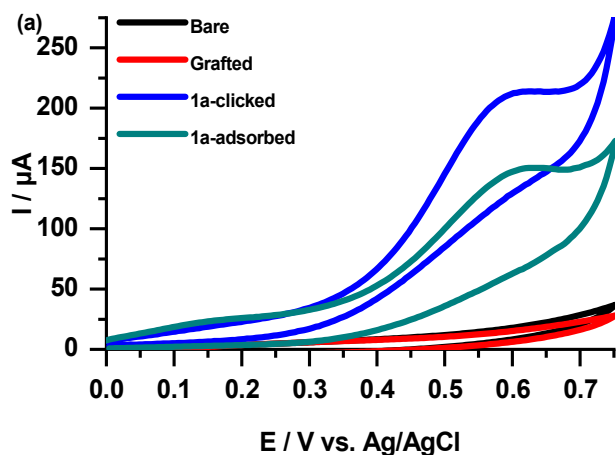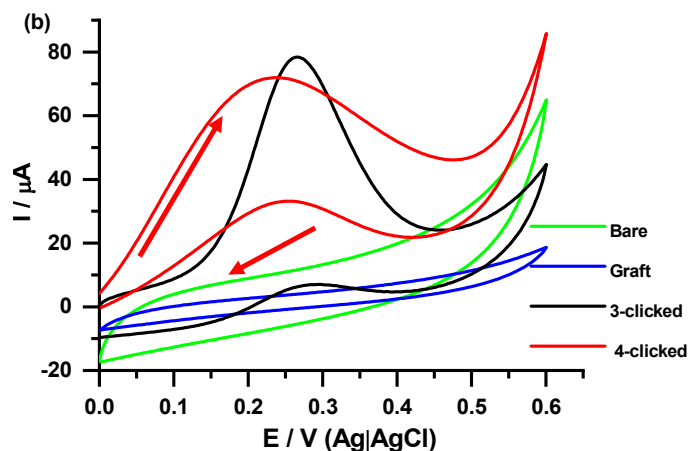
Figure 5.1: Cyclic voltammetry of bare, grafted, **1a**-clicked, **3**-clicked, **4**-clicked and **1a**-adsorbed in 4 mM hydrazine in 0.2 M NaOH. Scan rate 100 mVs^{-1}.

The results showed that the bare and the grafted electrodes were not able to sense hydrazine. In contrast, the **1a**-clicked showed a defined oxidation peak at 0.54 V (Table 5.1), with an onset potential of 0.3 V. On the other hand, **1a**-adsorbed showed slightly higher oxidation potential (0.58 V) and lower peak currents. Higher currents were observed for clicked hence, clicking increases the sensitivity of the electrode. The oxidation potentials obtained are more negative than for the reported for clicked CoPc (hexynyl in Table 5.1) at 0.72 V [35] in which an aliphatic substituent was used for clicking, meaning the aromatic substituent used in this work eased oxidation of hydrazine due to the electron donating nature of the substituent resulting in low oxidation potentials [159]. Complex-**4**-clicked showed a less positive potential (0.21 V) than complex-**3**-clicked (0.26 V), Table 5.1. However, the latter had more defined peak, showing the importance of the presence of the benzene ring before the alkynyl. The oxidation on both the forward and reverse scans in Fig. 5.1 (b) is attributed to regeneration of the active catalyst responsible for the oxidation of hydrazine [160]. The obtained oxidation potentials for **3** and **4** are less positive

than the reported ones in the literature at 0.72 V for symmetrical alkynyl substituted CoPc derivatives [35] Table 5.1.

The proposed mechanism for electroxidation of hydrazine on CoPc as reported in the literature [161, 162] is via Eqns. 5.1 to 5.4.

$$[Co(I)Pc]_{surface}^- \rightleftarrows [Co(II)Pc]_{surface} + e^-$$ 5. 1

$$[Co(II)Pc]_{surface} + N_2H_4 + OH^- \xrightarrow{rds} [Co(I)Pc...N_2H_3]_{surface}^- + H_2O$$ 5. 2

$$[Co(I)Pc...N_2H_3]_{surface}^- \rightarrow [Co(I)Pc]_{surface}^- + *N_2H_3$$ 5. 3

$$*N_2H_3 + 3OH^- \xrightarrow{fast} N_2 + 3e^- + 3H_2O$$ 5. 4
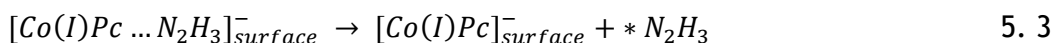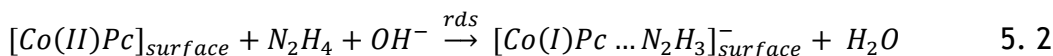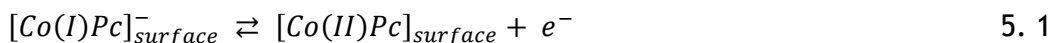
In a reaction involving only one step with one electron (like mechanism shown above), the Tafel slope will be determined by the symmetry, which is usually 0.5 (corresponding to a Tafel slope of 120 mV).

As stated in literature [161,162], for most CoPc complexes, oxidation of hydrazine starts at potential more positive than that of the Co (**II**)/(**I**) redox couple, so the assumption the catalytic species is the Co(**II**)Pc.

The onset potential is a potential at which the sharp increase in reduction current is observed. The onset potential is measured by linearly extrapolating the fast rising current wave (or peak) to the linear extrapolation of the baseline (background) current, and the intercept potential.

Table 5.1: Electrochemical results in hydrazine

Electrode	E/V	Background corrected current / µA	Tafel slope /mVdec^{-1}	k/M^{-1}s^{-1}	LoD/ µM	Reference
1a-clicked	0.54	123	56	8.45×10^3	3.28	This work
1a-adsorbed	0.58	56	73	6.23×10^3	10.2	This work
ZnONPs	0.92	56	54	4.14×10^4	12.84	This work
2	0.86	74	102	5.71×10^4	8.62	This work
2-ZnONPs	0.81	92	94	7.26×10^4	4.35	This work
3	0.26	113	118	5.6×10^6	0.94	This work
4	0.21	183	152	2.1×10^6	1.54	This work
5a	0.62	6.45	95	5.09×10^4	5.04	This work
5a-rGONS(seq)	0.72	12.71	118	1.08×10^6	1.67	This work
AgNPs	0.78	100.21	85	8.15×10^4	4.66	This work
5b	0.83	100.21	76	2.48×10^2	5.68	This work
5b-AgNPs	0.71	118.30	115	1.90×10^5	2.43	This work
6	0.63	22.31	98	8.05×10^4	4.31	This work
6-rGONS(seq)	0.70	101	78	1.37×10^6	0.82	This work
CoPc(hexynyl)	0.72	399	212	7.84×10^2	6.09	[35]
MnPc(hexynyl)	0.34	-	-	4.10×10^3	15.4	[33]
CoPc(phenyl)	0.2	-	-	2.98×10^3	4.3	[156]
FePc(hexynyl)	0.10	-	65.8	8.84×10^2	1.09	[34]

seq = sequential.

5.1.1.2. Stability test

For practical application of any electrochemical sensor, the stability is essential. The stability test for **1a**-clicked and **1a**-adsorbed were done by running 10 consecutive scans in the 0.2 M NaOH supporting electrolyte solution containing 4 mM hydrazine (Fig.5.2).
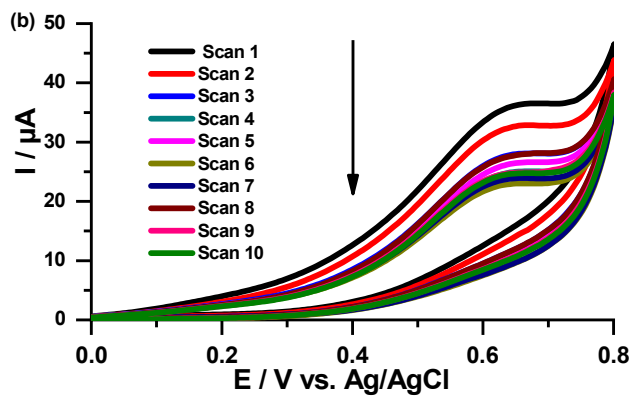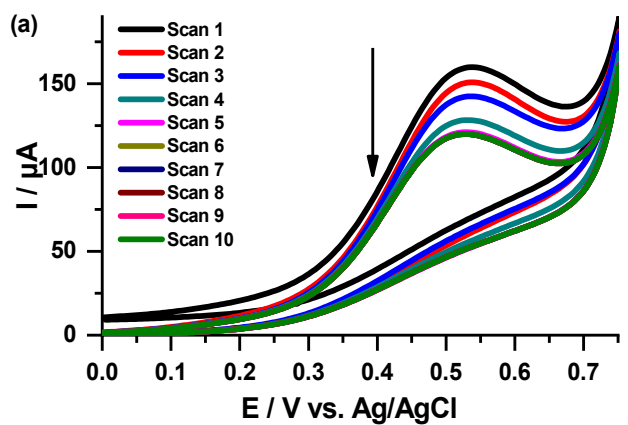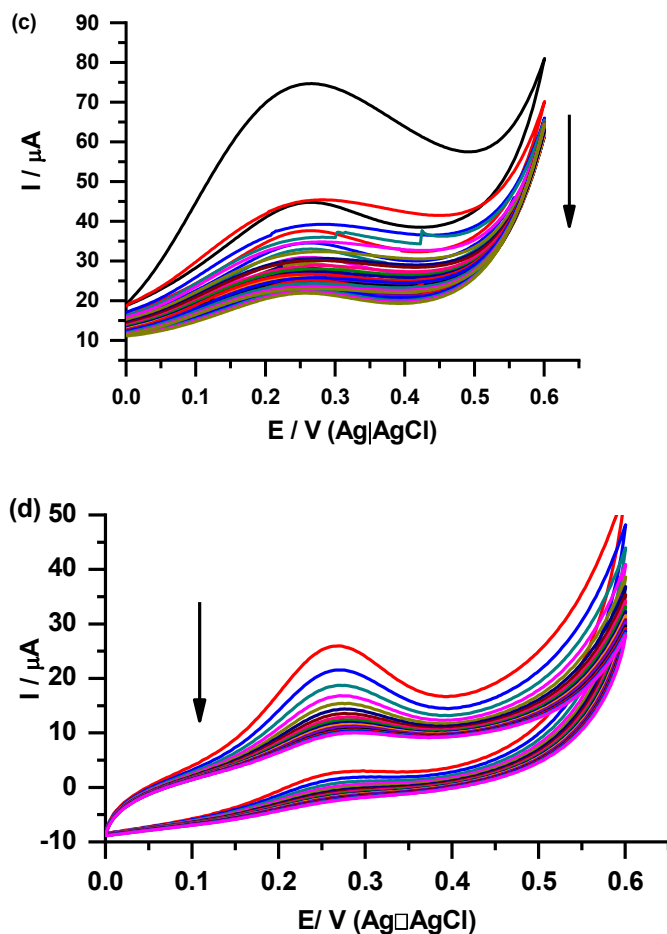
Figure 5.2: Cyclic voltammograms of continuous repetitive scans (10) with (a) **1a**-clicked, (b) **1a**-adsorbed, (c) **3**-clicked and (d) **4-**clicked in 4 mM hydrazine with 0.2 M NaOH.

For **1a**-clicked Fig. 5.2(a) the current decreased for the first four scans and from 5th scan the peak current and potential became stable. On the other hand, the **1a**-adsorbed Fig. 5.2(b) showed a decrease in current without becoming stable for all 10 scans. Therefore, the clicked electrode is more stable than when MPcs are adsorbed, this makes a clicked electrode more appropriate for use in sensing. Complex-**3-**clicked Fig. 5.2(c) and complex-**4-**clicked Fig. 5.2(d) showed similar stability behaviour however, the current decreased faster after the first scan for complex-**3-**clicked, while complex-**4-**clicked showed a steady decrease in current

which stabilized after the 20th scan, hence complex-**4**-clicked is slightly more stable than complex-**3**-clicked.

5.1.1.3. Kinetic studies of hydrazine detection

Fig. 5.3(a) shows the CVs for detection of hydrazine at different scan rates (using complex-**4**-clicked-GCE as an example). The shift in the peak potential with the increase in scan rates is an indication that hydrazine electro-oxidation on the surfaces of the modified electrodes is an irreversible process. The linear increase in the current signal when plotted against the square root of scan rate (Fig. 5.3(c)) is an evidence that the electro-oxidation of hydrazine is diffusion controlled [98].

(b)

$y= 0.076x\ 0.5341$ 4-clicked

$R^2 = 0.99976$

3-clicked

$y= 0.059x\ 0.5262$

$R^2 = 0.99976$

x-axis: $\log (v/\ mVs^{-1})$

y-axis: $E/V(Ag|AgCl)$

(c)

3-clicked

$y= 0.2083x +0.423$

$R^2= 0.9985$

4-clicked

$y = 0.2017x +0.356$

$R^2= 0.99964$

x-axis: $(v /\ mVs^{-1})^{1/2}$

y-axis: $I /\ \mu A$
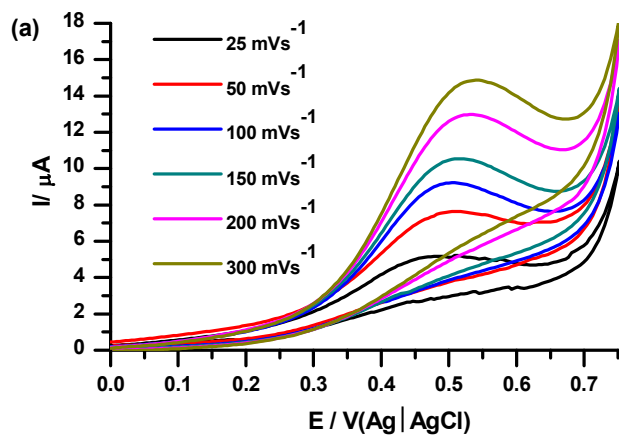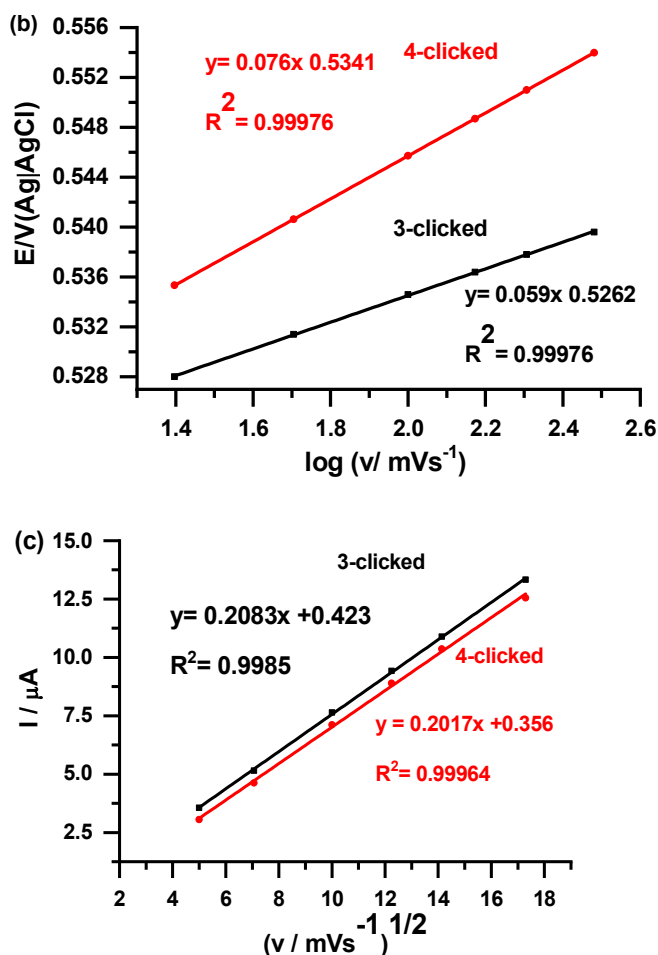
Figure 5.3: Cyclic voltammograms for the detection of hydrazine (in 0.2 M NaOH) at different scan rates (a), plot of oxidation peak potential vs. log v (b) and (c) plot of peak current vs. square root of scan rate. Electrode = complex-**4**-clicked (for example).

For reversible or irreversible systems without kinetic complications, I_p varies linearly with $V^{1/2}$, intercepting the origin. Although the plots of I_p vs. $V^{1/2}$ presented in Fig. 5.3 (c) are linear (R^2 = 0.9985 and 0.99964), they do not cross the origin of the axes. This is a characteristic for the electronic process preceded by electro-chemical reaction and followed by a homogenous chemical reaction.

The relationship between peak potential and scan rate for an irreversible diffusion-controlled process is given by Eqn. 5.5 [163].

$$E_p= \frac{b}{2}\log v + K \qquad\qquad 5.5$$

where E_p is the peak potential, v is the scan rate, K is a constant, and b indicates

the Tafel slope. From Fig. 5.3 (b) plot of E_p versus log v, Tafel slopes of 118 and 152

mV decade^{-1} for complex-**3**-clicked and complex-**4**-clicked respectively were

obtained and for complex-**3**-clicked the value is within the standard range of 60-120

mV decade^{-1}. Tafel slopes outside this range have no kinetic meaning and are usually

indicative of an electrode surface passivation [164]. The Tafel slope for **1a**-clicked

is lower than that of the corresponding **1a**-adsorbed, Table 5.1. A Tafel slope of near

60 mV/decade (as is the case in this work for **1a**-clicked) is obtained when α=1, and

one electron is transferred during the rate-determining step [165].

5.1.1.4. Chronoamperometry studies

After determining the catalytic rate constants, the limit of detections (LoD) were

calculated using chronoamperograms at different hydrazine concentration (linear

plot shown as insert in Fig. 5.4 (a)) at t= 0.246 s.
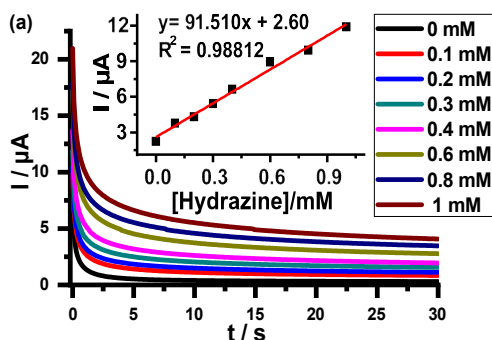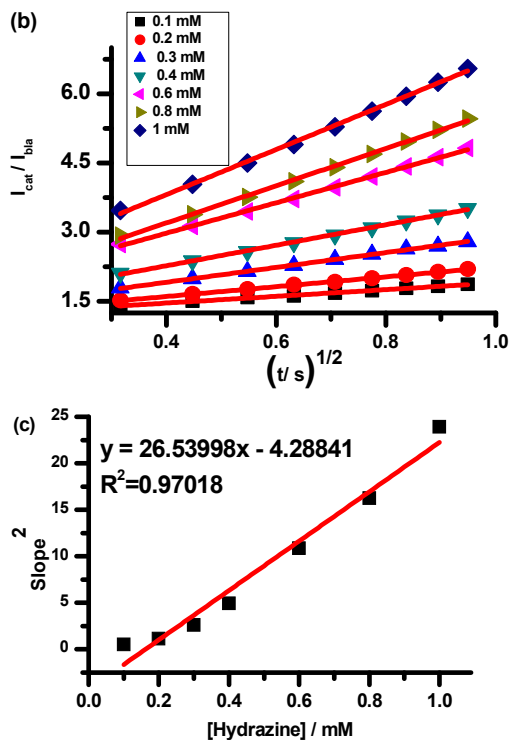
Figure 5.4: (a) Chronoamperograms for different concentration of hydrazine (in 0.2 M NaOH) recorded using **1a**-clicked. Insert: current-concentration plot for hydrazine (at t= 0.246). (b) Plot of (I_{cat} / I_{bla}) versus $t^{1/2}$ and plot (c) the square of the slope-concentration of hydrazine.

The **1a**-clicked was employed for chronoamperometric studies as an example.

The obtained LoDs were 3.28 µM, 0.94 µM and 1.54 µM for **1a**-clicked, **3**-clicked and **4**-clicked respectively, according to the 3δ/slope ratio, where δ is the standard deviation of the blank (electrodes in the supporting electrolyte, 0.2 M NaOH). The obtained LoD were lower than the reported for symmetrical CoPc at 6.09 µM [35] and 4.3 µM [156], Table 5.1. The lower LoD for **3**-clicked compared to **4**-clicked shows the importance of have the benzene ring before the alkynyl group rather than only aliphatic chains.

For **1a**-adsorbed, the LoD is 10.2 µM and sensitivity is 5.45 µA mM^{-1}, hence clicking performs better than adsorption. The higher LoD than the one tabled for FePc containing hexynyl substituent maybe due to the difference in central metal as FePc

are reported to have low LoDs [34]. The catalytic rate constants (k) for the electrocatalysis of hydrazine on were determined according to the method described in the literature [166] and the Eqn. 5.6.

$$\frac{I_{cat}}{I_{bla}} = y^{\frac{1}{2}}\, \Pi^{1/2} = \Pi^{1/2}(kC_0t)^{1/2} \qquad\qquad 5.6$$

where, I_{cat} and I_{bla} are currents in the presence and in the absence of hydrazine, t = elapsed time in seconds (s) and k = catalytic rate constant ($M^{-1}s^{-1}$). Fig. 5.4(b) shows linear plots of $(^{I_{cat}}/_{I_{bla}}$) vs. $t^{1/2}$ for different concentrations of hydrazine obtained from the chronoamperomogram in Fig. 5.4(a). The slopes of these plots were plotted against the concentration of hydrazine to give linear relationship shown in Fig. 5.4(c) and is represented by Eqn. 5.7.

1a-clicked

$$y= 26.5\ [\text{hydrazine}]\ \left(\tfrac{s^{-1}}{mM}\right) - 4.28s^{-1},\ R^2 = 0.9701 \qquad 5.7A$$

3-clicked

$$y= 6547.2\ [\text{hydrazine}]\ \left(\tfrac{s^{-1}}{mM}\right) - 1379.7s^{-1},\ R^2 = 0.9697 \qquad 5.7B$$

4-clicked

$$y= 1759.9\ [\text{hydrazine}]\ \left(\tfrac{s^{-1}}{mM}\right) - 1526.7s^{-1},\ R^2 = 0.9789 \qquad 5.7B$$

The slope of Fig. 5.4(c) is equal to πk, and this gives a k value of $8.45 \times 10^3\ M^{-1}s^{-1}$ for **1a-**clicked and $5.6 \times 10^6\ M^{-1}s^{-1}$, $2.1 \times 10^6\ M^{-1}s^{-1}$ for **3**-clicked and **4**-clicked respectively, Table 5.1. The k value for **1a**-adsorbed of $6.23 \times 10^3\ M^{-1}s^{-1}$ is less than that of the **1a**-clicked electrode showing the importance of clicking. Asymmetric

complex **3**-clicked gave better performance than symmetrical **1a**-clicked.   The values of k are larger (for **3**-clicked and **4**-clicked) than those obtained for hydrazine oxidation on symmetric tetrakis hexynyl CoPc clicked onto a GCE at 7.84×10^2 $M^{-1}s^{-1}$ [35] and tetrakis ethylbenzyl CoPc (**1a**-clicked) at 8.45×10^3 $M^{-1}s^{-1}$, Table 5.1. This indicates a faster rate of oxidation at the surface of modified electrode used in this work, thereby making low symmetry phthalocyanines suitable candidates for the fabrication of a sensor for fast detection of hydrazine. The high catalytic constant and low LoD of the **1a**-clicked-CGE sensor compared to clicked complexes CoPc (hexynyl) [35] is attributed to the aromatic group that is present in the substituent in complex **1a**. Hence the presence of the aromatic ring improves the performance of the sensor

5.1.1.5. Interference studies

Ammine compounds such as aniline and ammonia have a potential to interfere with the signal of hydrazine in real life application. Hence, the selectivity of the electrode towards hydrazine in the presence of amines was studied (Fig. 5.5) using **1a-**clicked as an example. The square wave voltammograms in the presence of interferences are similar (Fig. 5.5 (d), (e), (f)), except for the small shift towards the positive potentials. The peak current of hydrazine in the presence of studied interferences remained high enough to determine selectivity of hydrazine as the interferences produced negligible oxidation currents and no extra peak. The relative standard deviation (RSD) of the peak heights in Fig. 5.5 (c), (d), (e) and (f) was 4.30%, close RSD for hydrazine only at the **1a**-clicked electrode (4.70%). Therefore, the study confirmed that the developed sensor possesses good sensitivity towards hydrazine.
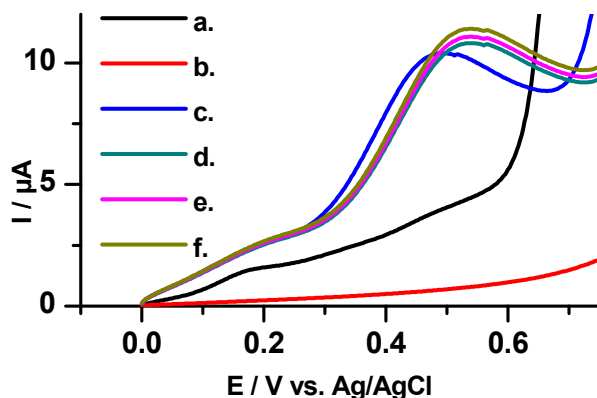
Figure 5.5: Square wave voltammograms of **1a**-clicked in (a) 100 µM ammonia, (b) 100 µM aniline, (c) 25 µM hydrazine, (d) 25 µM hydrazine + 100 µM ammonia, (e) 25 µM hydrazine + 100 µM aniline, (f) 25 µM hydrazine +100 µM aniline + 100 µM ammonia.

5.1.2. Adsorbed conjugates

Complex **2** was used with ZnONPS as an example

5.1.2.1. Cyclic voltammetry

Cyclic voltammetry of the probes in supporting electrolyte only Fig. 5.6(a) do not show defined peaks, but the enhancement in current could be attributed to redox process based on **2**. However, after addition of 1 mM hydrazine Fig. 5.6 (b) azide ZnONPs, **2** and **2**-ZnONPs showed peaks at 0.92 V, 0.86 V and 0.81 V, respectively (Table 5.1). It is noteworthy that the **2**-ZnONPs based electrode shows less positive potential, this could be due to incorporation of ZnONPs which enhances electron transfer properties of **2** due to synergistic behaviour as ZnONPs nanoparticles were also able to detect hydrazine. There was generally small difference in oxidation potentials however, there is lager differences in background corrected oxidation currents (Table 5.1), which were the highest for **2**-ZnONPs suggesting improvement in detection using the conjugates.
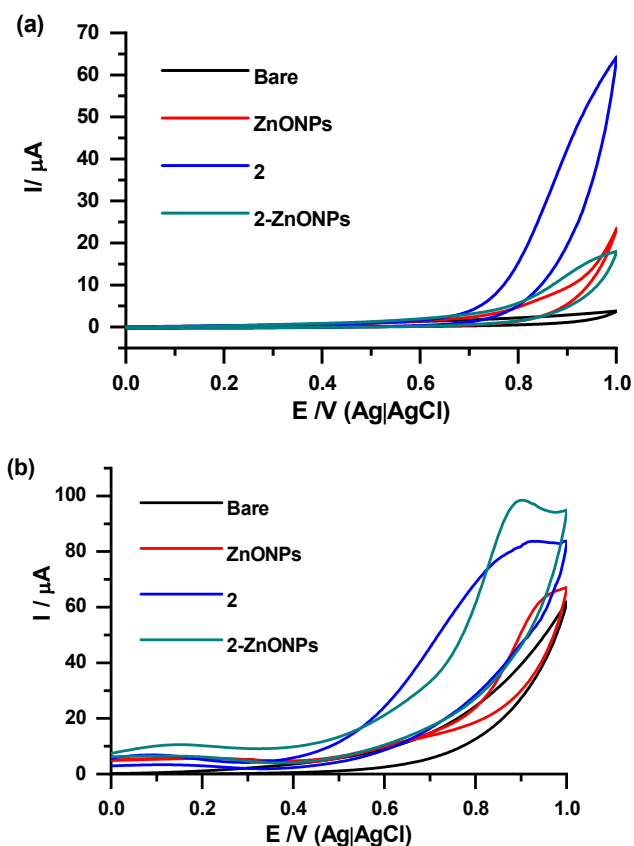
Figure 5.6: Cyclic voltammetry of bare, azide ZnONPs**, 2**, and **2**-ZnONPs in (a) 0.20 M NaOH and (b) 1 mM hydrazine in 0.20 M NaOH. Scan rate 100 mVs^{-1}.

5.1.2.2. Kinetic studies

Cyclic voltammetry experiments were carried out at different scan rates (50-350 mV s^{-1}) and at constant hydrazine concentration (1 mM). Fig. 5.7(b) shows that peak currents were directly proportional to square root of the scan rate ($v^{1/2}$) which is indicative of a diffusion-controlled reaction. For reversible or irreversible systems without kinetic complications, I_p varies linearly with $V^{1/2}$, intercepting the origin. Although the plot of I_p vs. $V^{1/2}$ presented in Fig. 5.3 (b) are linear ($R^2 = 0.99593$), it does not cross the origin of the axes. This is a characteristic for the electronic process preceded by electro-chemical reaction and followed by a homogenous chemical reaction.

The steeper the gradient of the plot the faster the reaction on the modified electrode. The obtained gradients (in $\mu A/ (mV^{-1})^{1/2}$) are in the order ZnONPs (2.497) $<$ **2** (2.632) $<$ **2-ZnONPs** (3.119), thus the reaction is faster on the conjugate. The slope of log I versus log v in Fig. 5.7(c) is 0.48. The slope of such a plot can inform on whether a reaction is diffusion controlled or is dominated by adsorption. For adsorption dominated reactions the slope is 1 and 0.5 for diffusion-controlled reactions [167]. The value of 0.48 is close to 0.5, hence confirming diffusion controlled.

(c)

$y = 0.481x - 5.584$

$R^2 = 0.98565$

(d)

$y = 0.047x + 0.435$

$R^2 = 0.99366$
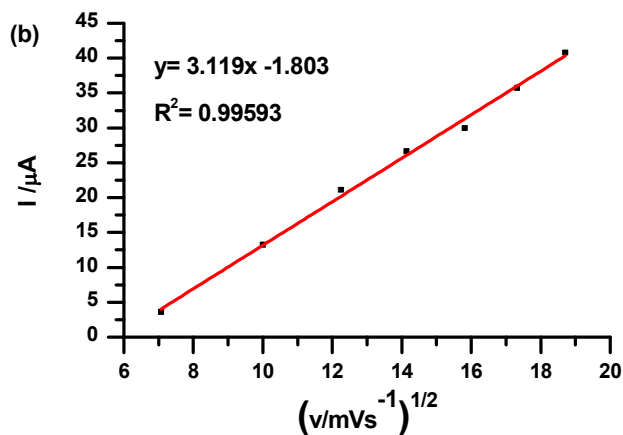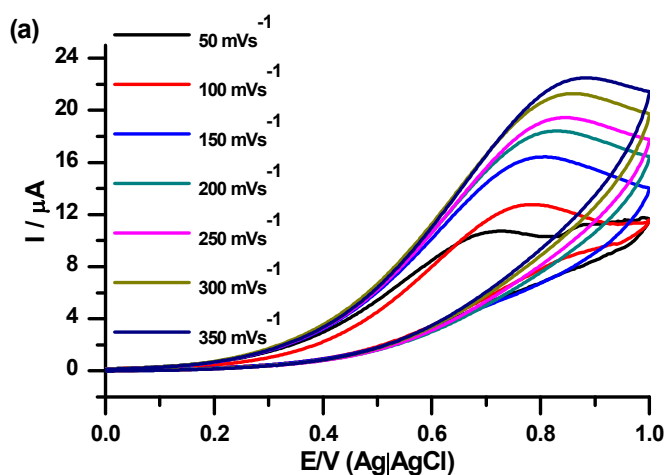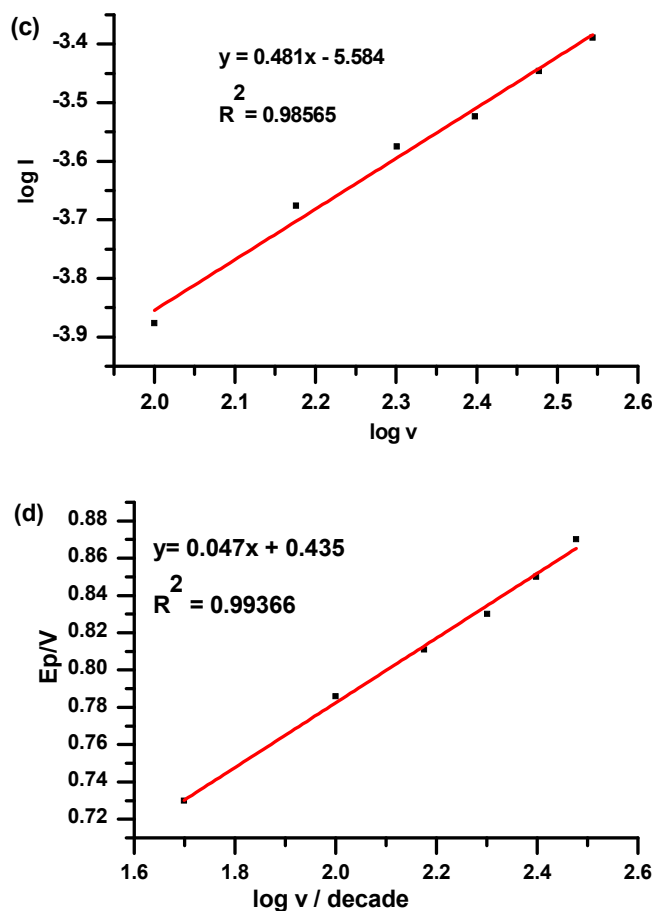
Figure 5.7: Cyclic voltammograms (**2-**ZnONPs) for the detection of 1 mM hydrazine (in 0.20 M NaOH) at different scan rates (a), plot of peak current vs. square root of scan rate (b), plot of log I vs. log v (c) and plot of oxidation peak potential vs. log v (d).

The plot of E_p vs $logv$ (Fig. 5.7 (d)) gave a linear relationship and the Tafel slope was found to be 94 mV dec^{-1} for **2-**ZnONPs. The calculated Tafel slopes for ZnONPs, **2** and **2-**ZnONPs are within the range 60-120 mV decade^{-1}.

5.1.2.3. Chronoamperometry studies

The chronoamperometry data was used to obtain calibration graph from which limits of detection and catalytic rate constants, were determined, Fig. 5.8. The rate constants for the detection of hydrazine using Eqn 5.6 above,

Plots for the I_{cat}/ I_{buf} vs. $t^{1/2}$ for different hydrazine concentrations (figure not shown), were obtained from chronoamperomograms in Fig. 5.8(a) in a same way as in Fig. 5.4(b). The plots of the slopes of these plots vs hydrazine concentrations were linear Fig. 5.8(b) (and represented by Eqns. 5.8)

2-ZnONPs

$$y = 2.2 \times 10^2 \, [Hydrazine] \left(\frac{s^{-1}}{mM} \right) - 0.00401 \, s^{-1}, R^2 = 0.98278 \qquad \text{5.8A}$$

2

$$y = 1.8 \times 10^2 \, [Hydrazine] \left(\frac{s^{-1}}{mM} \right) - 0.02012 \, s^{-1}, R^2 = 0.99321 \qquad \text{5.8B}$$

Azide ZnONPs

$$y = 1.3 \times 10^2 \, [Hydrazine] \left(\frac{s^{-1}}{mM} \right) - 0.02336 \, s^{-1}, R^2 = 0.98278 \qquad \text{5.8C}$$

The k value of 7.26 x10^4 M^{-1}s^{-1} for **2-ZnONPs**, Table 5.1. It is found out that the catalytic rate constant is higher for conjugate than for **2** and ZnONPs (4.14×10^4 M^{-1}s^{-1} and 5.71×10^4 M^{-1}s^{-1} respectively) which could be due to synergistic effect. The obtained value of k is larger than that of the reported value for hydrazine electrocatalysis on tetrakis hexynyl CoPc [35]. This indicates a faster rate of hydrazine electrocatalysis at the modified electrode surfaces developed in this work.
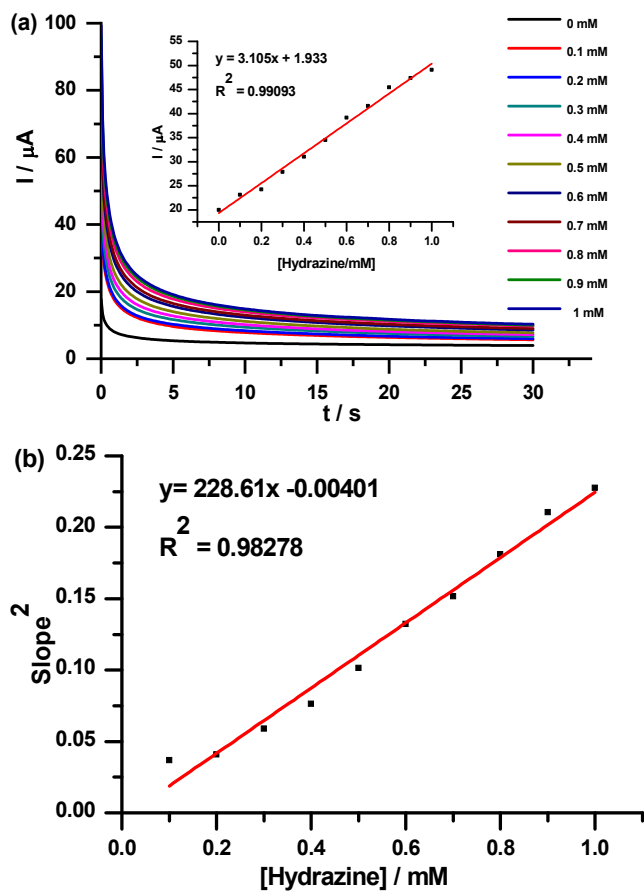
Figure 5.8: (a) Chronoamperograms for **2**-ZnONPs at different concentrations of hydrazine. (Insert) corresponding calibration curves at (t= 0.125s) and (b) plot of hydrazine concentrations versus square of slopes.

The limit of detections (LoDs) were determined as explained above, using Fig. 5.8(a) (insert) and were found to be 12.84 µM for azide ZnONPs, 8.62 µM for **2** and 4.35 µM for **2**-ZnONPs. **2**-ZnONPs shows the better LoD value than those for ZnONPs and **2**. This improvement in the LoD value for **2**-ZnONPs is due to the synergistic effect of ZnONPs as discussed above.

5.1.3. Sequential addition

Complexes **5a** and **6** were used to modify without forming bonds with nanomaterials

5.1.3.1. Cyclic voltammetry

Fig. 5.9 shows CVs of rGONS, **5a**, **6, 5a-**rGONS (seq) and **6-**rGONS (seq) 1 mM hydrazine in 0.2 M NaOH as a supporting electrolyte at a scan rate of 100 mVs^{-1}.
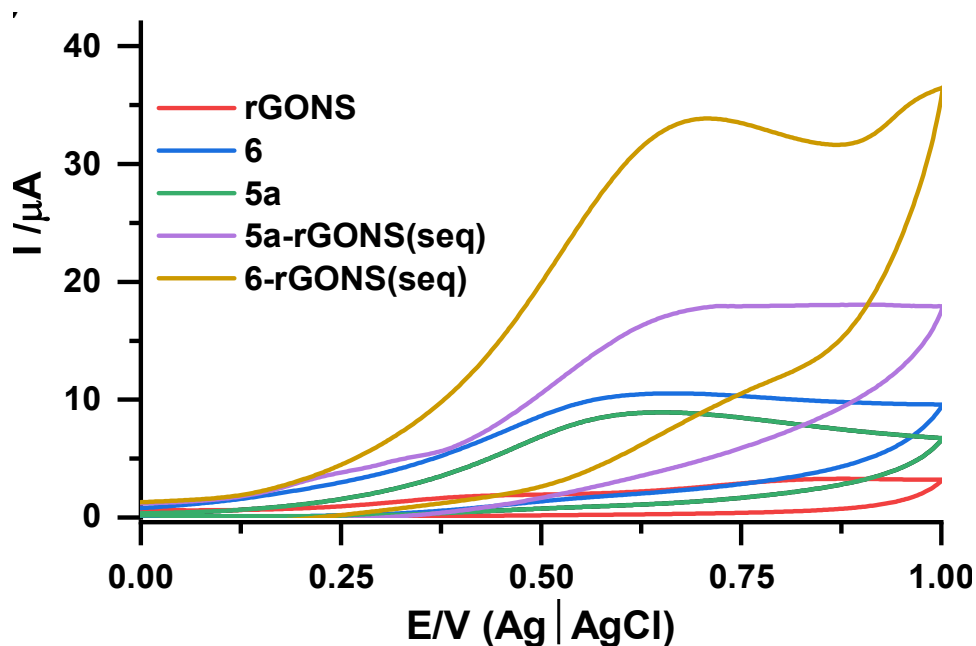
Figure 5.9: Cyclic voltammetry of rGONS, **5a**, **6**, **5a-**rGONS (seq) and **6-**rGONS (seq) in 0.20 M NaOH Scan rate: 100 mVs^{-1}.

rGONS could not detect hydrazine hence no oxidation peaks were observed indicating that there is no direct electron transfer between rGONS and hydrazine as stated above. However, upon modification with **5a, 6, 5a-**rGONS (seq) and **6-**rGONS (seq) the peaks appear, with **6-**rGONS (seq) showing highest corrected background current (101 μA), Table 5.1. However, oxidation potential for **6-**rGONS (seq) was

not low as expected for a good electrocatalyst but the high current is more important

is it responsible for giving better limits of detection (LoD).

5.1.3.2. Kinetic studies of hydrazine detection

Fig. 5.10(a) shows CVs of **5a** in 1 mM hydrazine in 0.20 M NaOH supporting electrolyte

at different scan rates. As scan rate increases, the peak current increases and peak

potential slightly shifted to the more positive potential a characteristic of a diffusion

controlled reaction [98] which resulted in a linear relationship between plot of peak

current vs. square root of scan rate Fig. 5.10(b), indicative of diffusion control.

The plot of E_p vs $\log v$ (Fig. 10 (c)) (Eqn. 5.5) gave a linear relationship and its Tafel

slope was found to be 95 mV dec^{-1} for **5a** which is close to 98 mV dec^{-1} for **6**. All

calculated Tafel slopes are within the range 60-120 mV decade^{-1}.

(b)

y= 0.00316x - 0.00049

R^2 = 0.98405

Y-axis: I / $\perp$A

X-axis: $V^{1/2}$ / (mVs^{-1})$^{1/2}$

(c)

y= 0.0476x+ 0.3888

R^2 = 0.92028

Y-axis: Ep

X-axis: log v
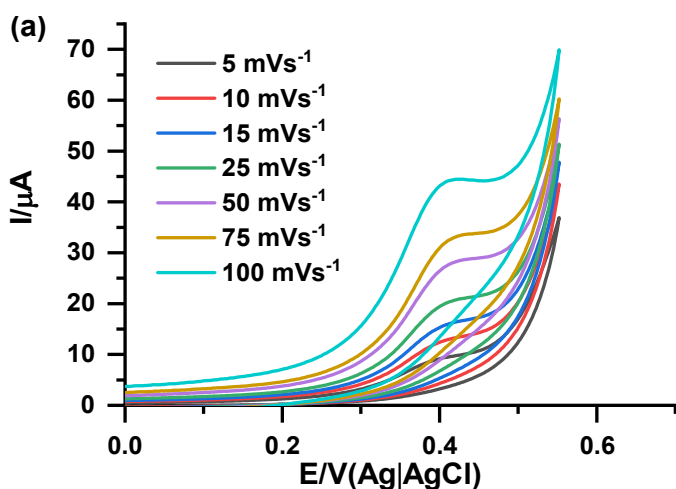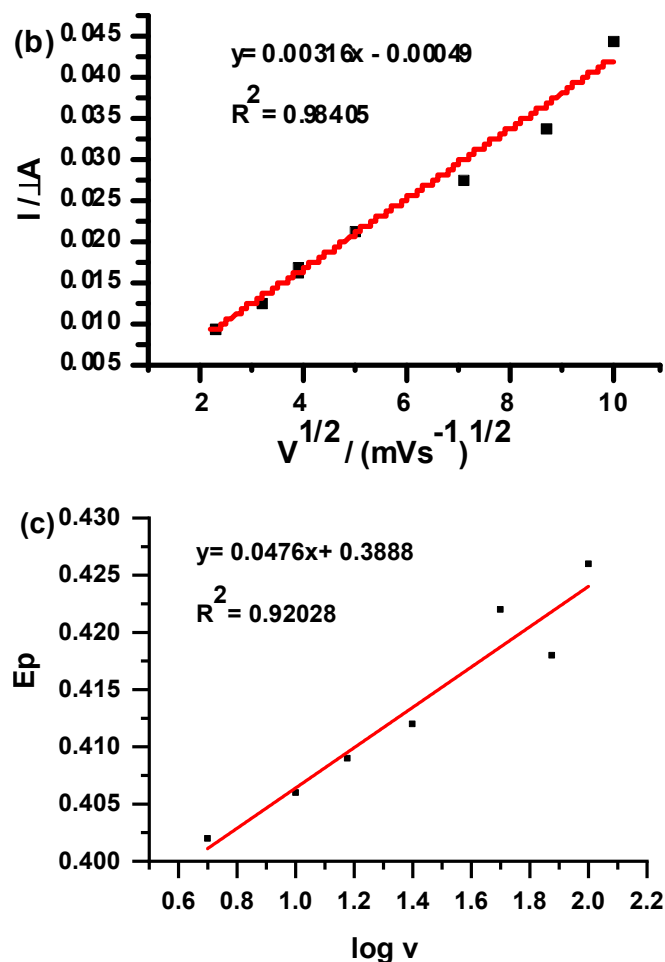
Figure 5.10: Cyclic voltammograms (**5a**) for the detection of 1 mM hydrazine (in 0.20 M NaOH) at different scan rates (a), plot of peak current vs. square root of scan rate (b) and plot of oxidation peak potential vs. log v (c).

5.1.3.3. Chronoamperometry studies

Chronoamperometry was used for the determination of limit of detection (LoD) and catalytic rate constants. Fig. 5.11 (a) shows the chronoamperograms obtained using **6** as an example, in the absence and presence of hydrazine. At low times (t) the catalytic current (I_{cat}) is dominated by the rate of oxidation of hydrazine therefore, t= 0.48 s was used for calculations in this study. Catalytic rate constants were determined as stated above.

Linear plots for the I_{cat}/ I_{buf} vs. $t^{1/2}$ (Fig. 5.11 (b)) for different hydrazine concentration were obtained from chronoamperomograms in Fig. 5.11(a). The slopes of these plots were plotted against the concentration of hydrazine to give another linear relationship shown in Fig. 5.11(c), and given by Eqns. 5.9.

5a

$$y = 1.6 \times 10^2 \, [Hydrazine] \left(\frac{s^{-1}}{mM} \right) + 0.08090 \, s^{-1}, R^2 = 0.99103 \qquad 5.9\text{A}$$

6

$$y = 2.5 \times 10^2 \, [Hydrazine] \left(\frac{s^{-1}}{mM} \right) + 0.33210 \, s^{-1}, R^2 = 0.97167 \qquad 5.9\text{B}$$

5a-rGONS (seq)

$$y = 3.4 \times 10^3 \, [Hydrazine] \left(\frac{s^{-1}}{mM} \right) + 0.29846 \, s^{-1}, R^2 = 0.99897 \qquad 5.9\text{C}$$

6-rGONS (seq)

$$y = 4.3 \times 10^3 \, [Hydrazine] \left(\frac{s^{-1}}{mM} \right) + 0.18986 \, s^{-1}, R^2 = 0.99965 \qquad 5.9\text{D}$$

The catalytic rate constant k was determined from the slope of Fig. 5.11(c). The k for **5a** and **6** were found to be 5.09×10^4 M^{-1}s^{-1} and 8.05×10^4 M^{-1}s^{-1} respectively (shown in Table 5.1), the higher catalytic activity of a low symmetry phthalocyanine **6** could be due to the presence of electron donating group. After combining with phthalocyanines and rGONS, k increased to 1.08×10^6 M^{-1}s^{-1} and 1.37×10^6 M^{-1}s^{-1} for **5a**-rGONS (seq) and **6**-rGONS (seq) respectively, this could be attributed to rGONS which has high π-π-conjugated system. The better catalytic activity of **6**-rGONS (seq) compared to **5a**-rGONS (seq) could be due to presence of electron donating moiety in **6** and low symmetry. The highest catalytic constant reported here is higher

than the values reported in literature $8.84 \times 10^2 \, M^{-1}s^{-1}$ [34], $7.84 \times 10^3 \, M^{-1}s^{-1}$ [35] and

$2.98 \times 10^3 \, M^{-1}s^{-1}$ [156], Table 5.1.

(c)
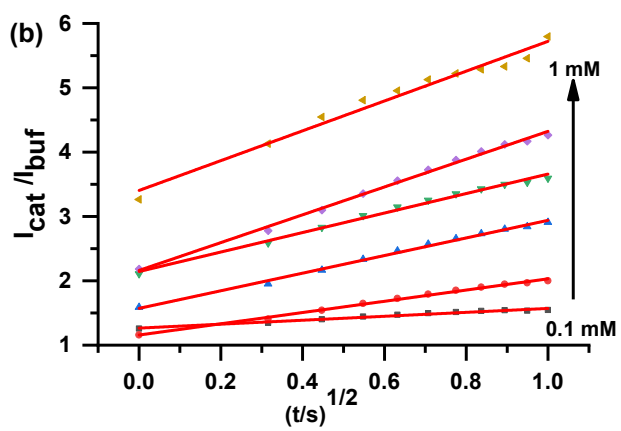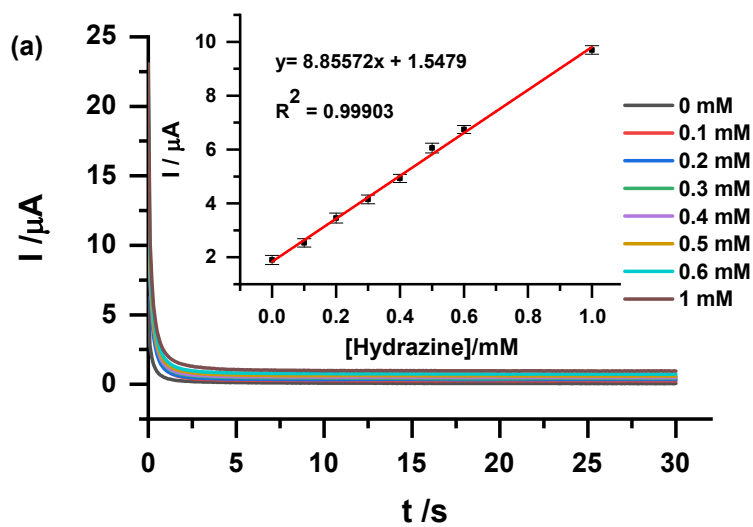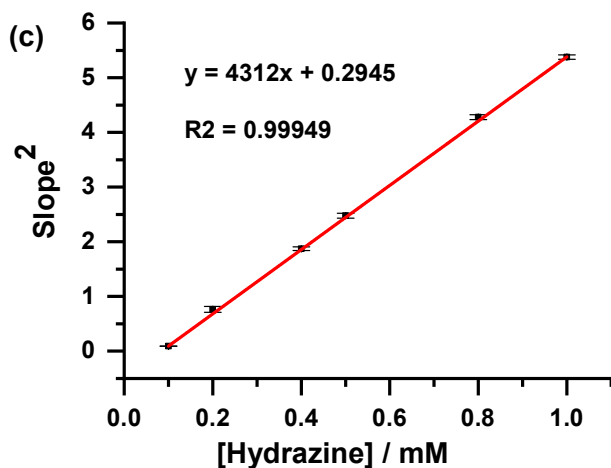
Figure 5.11: (a) Chronoamperogramms for **6** at different concentrations of hydrazine. (Insert) corresponding calibration curves, (b) plots of (I_{cat}/I_{buf}) versus square root of time and (c) plot of hydrazine concentrations versus square of slopes.

The limit of detection (LoD) was calculated using 3σ notation as stated above. The LoDs were found to be 0.82 µM for **6**-rGONS (seq), 1.67 µM for **5a**-rGONS (seq), 4.31 µM for **6** and 5.04 µM for **5a.** Using phthalocyanines together with rGONS resulted in an improvement of LoD which could be due to better electron transfer as rGONS have highly π-π conjugated system. Furthermore, **6** gave better LoD relative to **5a** because of presence of electron donating and withdrawing substituents (push-pull effect). The **6**-rGONS (seq) probe developed in this work produced similar LoD as the probes reported in the literature [156], Table 5.1.

5.1.4. Electrodeposition

Complex **5b** was used as an example

5.1.4.1. Cyclic voltammetry

Fig. 5.12 presents the comparative cyclic voltammograms of the electrodes in 2 mM hydrazine. The obtained hydrazine oxidation potentials are in the order 0.71 V < 0.78 V < 0.83 V for **5b-**AgNPs, AgNPs and **5b** respectively, Table 5.1. It was observed AgNPs, **5b** and **5b-**AgNPs showed electrocatalytic activity since there was no hydrazine oxidation peak on bare GCE. AgNPs on their own show electrocatalytic activity. For **5b**-AgNPs (Fig. 5.12) the catalytic activity was much higher (in terms of background corrected current, Table 5.1) than for **5b** and AgNPs as a result of the synergistic effect. **5b**-AgNPs electrode gave higher peak oxidation current and less positive oxidation potential (Table 5.1) hence displayed better electrocatalytic activity. The peaks near 1.0 V for **5b**-AgNPs **(**more clear) and **5b** (weaker) are due to Pc ring based processes in **5b**, Fig. 5.12, as also observed in Fig. 3.5 (process **IV**).
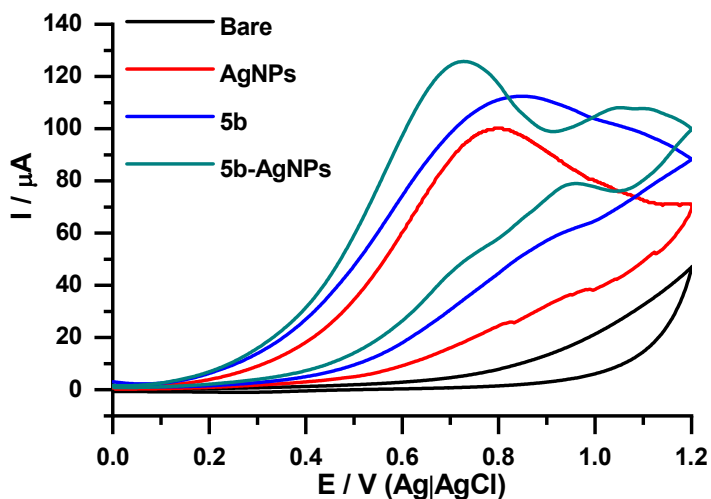
Figure 5.12: Cyclic voltammetry of bare, AgNPs, **5b**, and **5b**-AgNPs in (a) 0.20 M NaOH and (b) 2 mM hydrazine in 0.2 M NaOH. Scan rate: 100 mVs^{-1}.

5.1.4.2. Kinetics

Cyclic voltammetry experiments were carried out to study the influence of different scan rates (50 - 250 mVs^{-1}) at constant hydrazine concentration of 2 mM (Fig. 5.13(a)). The following important information were obtained: first, anodic peak current is directly proportional to square root of the scan rate (Fig. 5.13(b)) indicative of a diffusion-controlled reaction. Second, a plot of Ip/V$^{1/2}$ against V (Fig. 5.13(c)) gave the characteristic shape that is typical for a catalytic process. Lastly, the increase in the scan rate is accompanied by a shift in peak potential (Fig. 5.13(a)), which suggests an irreversible reaction during oxidation of hydrazine on the modified electrode surface.

The plot of E$_p$ vs $\log v$ (Fig. 5.13(d)) (**5b**) gave a linear relationship and its Tafel slope was found to be 76 mV dec^{-1}. And all other probes AgNPs and **5b**-AgNPs gave Tafel slopes in with 60-120 mV dec^{-1} (Table 5.1).

(a)

(b)

$$y = 2.846x - 11.486$$
$$R^2 = 0.98648$$

(c)
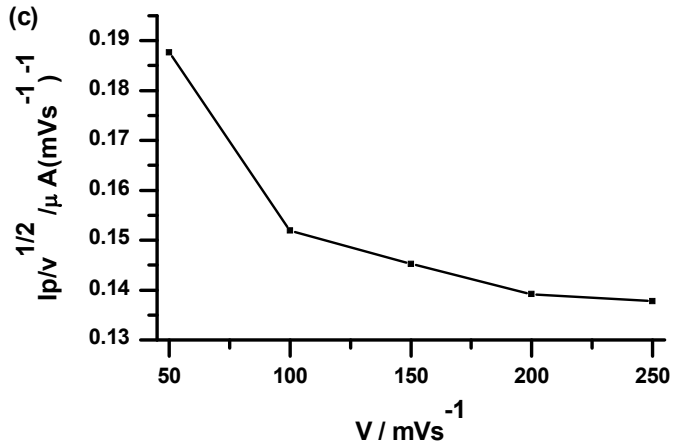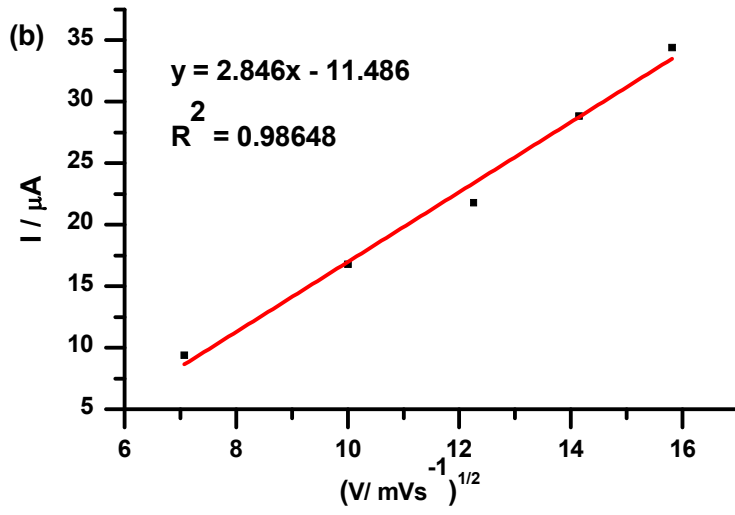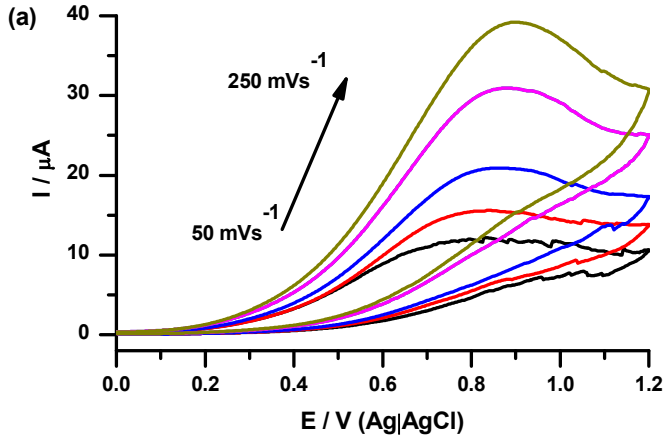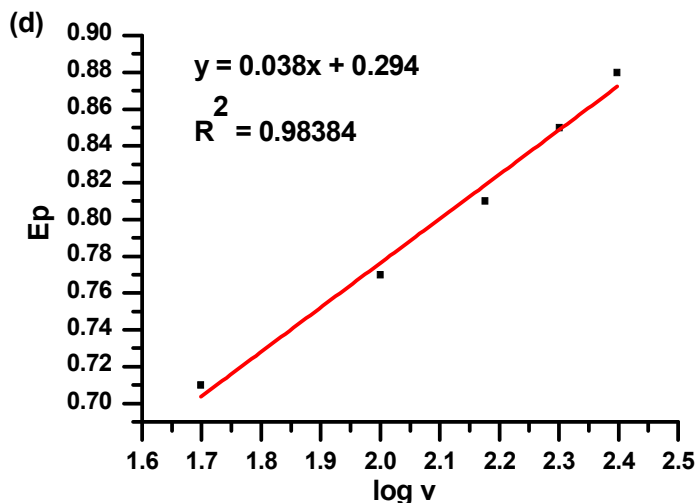
Figure 5.13: Cyclic voltammograms (**5b**) for the detection of 2 mM hydrazine (in 0.20 M NaOH) at different scan rates (a), plot of peak current vs. square root of scan rate (b), Ip/V$^{1/2}$ vs. v (c) and plot of oxidation peak potential vs. log v (d).

5.1.4.3. Chronoamperometry studies

Chronoamperometry was used to determine the rate constants and detection limits of the developed nanocomposite. On average, within 5 s the catalytic current is dominated by electrooxidation of hydrazine in this work (Fig. 5.14(a)). The catalytic constants of the probes were determined using Eqn. 5.6.

Linear plots for the I$_{cat}$/ I$_{buf}$ vs. t$^{1/2}$ (figure not shown, similar to Fig. 5.4(b)) for different hydrazine concentration were obtained from chronoamperograms in Fig. 5.14(a). The slopes of these plots were plotted against the concentration of hydrazine to give another linear relationship shown in Fig. 5.14(b), and given by Eqns. 5.10.

5b

$$y = 1.8 \times 10^2 \, [Hydrazine] \left(\frac{s^{-1}}{mM}\right) + 0.2852 \, s^{-1}, R^2 = 0.97769 \qquad 5.10A$$

AgNPs

$$y = 2.5 \times 10^2 \, [Hydrazine] \left(\frac{s^{-1}}{mM}\right) + 0.0123 \, s^{-1}, R^2 = 0.98456 \qquad 5.10B$$

5b-AgNPs

$$y = 2.8 \times 10^2 \, [Hydrazine] \left(\frac{s^{-1}}{mM}\right) + 0.1986 \, s^{-1}, R^2 = 0.99987 \qquad 5.10C$$

The slope of Fig. 5.14(b) is equal to πk. A k value of 2.48×10^2 $M^{-1}s^{-1}$ was obtained

for **5b** alone (Table 5.1). A higher catalytic rate constant for **5b-**AgNPs (1.90×10^5

$M^{-1}s^{-1}$) than for **5b** (2.48×10^2 $M^{-1}s^{-1}$) and AgNPs (8.15×10^4 $M^{-1}s^{-1}$) which could be due

to synergistic effect. The obtained value of k is larger than that of the reported

value for hydrazine electrocatalysis on Mn tetrakis(5-hexyn-oxy) phthalocyanine

clicked on GCE at 4.1×10^3 $M^{-1}s^{-1}$ [33]. This indicates a faster rate of hydrazine

electrocatalysis at the modified electrode surface in this work. Furthermore, the

obtained sensitivities of the electrodes are 26.34, 45.10 and 61.56 $\mu A \, mM^{-1}$ for AgNPs,

5b and **5b-**AgNPs respectively which confirms that the conjugate gives better

performance.

(b)

y= 178.021x + 0.2852

R^2 = 0.97769

Slope 2
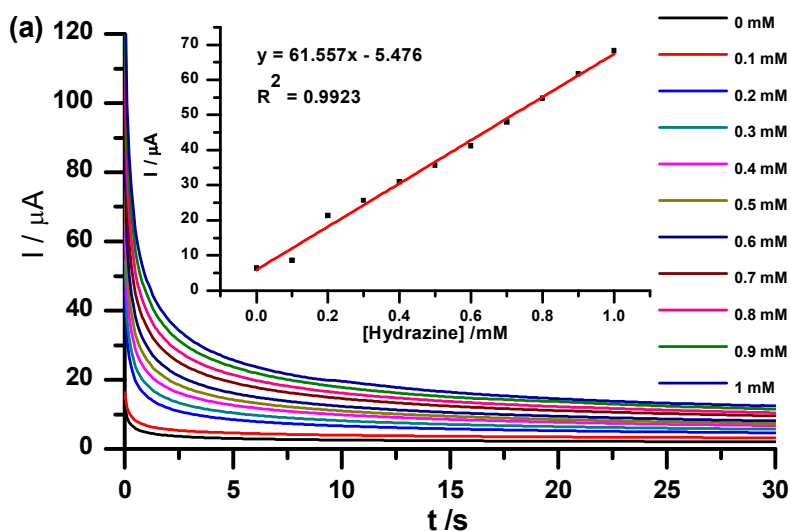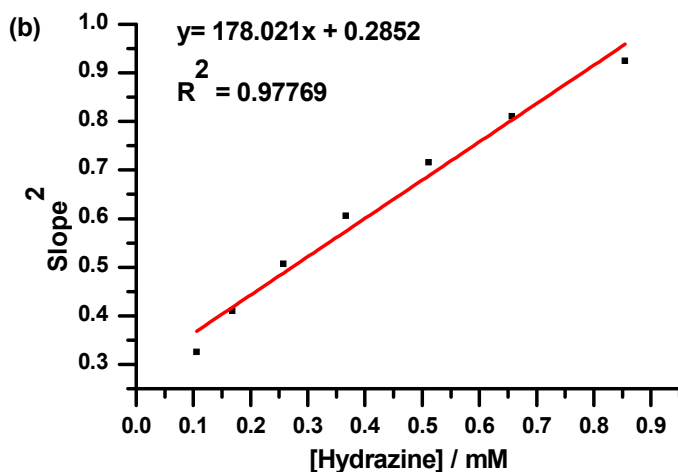
[Hydrazine] / mM

Figure 5.14: (a) Chronoamperogramms for **5b** at different concentrations of hydrazine. (Insert) corresponding calibration curves and (b) plot of hydrazine concentrations versus square of slopes

The limit of detection (LoD) was calculated as explained above using Fig. 5.14(a) (insert) and were found to be 2.43 µM for **5b-**AgNPs, 4.66 µM for AgNPs and 5.68 µM for **5b**. **5b-**AgNPs shows the better LoD value than those for **5b** and AgNPs. The improvement in the LoD value for **5b**-AgNPs could be due to the synergistic effect of AgNPs as discussed above. Thus, **5b**-AgNPs has lower LoD and higher than some reported literature values [33], but worse than for asymmetrical complexes **3** and **4**, Table 5.1.

5.1.4.4. Electrochemical impedance spectroscopy (EIS)

The EIS was employed (done for **5b** as an example) to determine the charge transfer resistance (R_{ct}) which gives information on the charge transfer kinetics in the presence of hydrazine. The Nyquist plot in Fig. 5.15(a) is a plot of –Z'' vs. Z', where Z' = real component and Z'' = imaginary component. The comparative R_{ct} values obtained from Nyquist plot are given in Table 5.2. The lower the R_{ct} value the better the charge transfer kinetics. **5b**-AgNPs showed the least R_{ct} which implies

incorporating **5b** with AgNPs results in an improved electron transfer. The apparent charge transfer rate constants (k_{app}) is inversely proportional to R_{ct}, Eqn. 4.3 [146].

5b-AgNPs gave the largest k_{app} value again showing that incorporating **5b** with AgNPs results in an improved charge transfer rate, Table 5.2.

A plot of phase-shift vs. log frequency (Fig. 5.15(b)) provides a complementary information on frequency which cannot be obtained from the Nyquist plot. The phase angle values for all modified electrode surface studied in this work are less than the ideal 90° for an ideal capacitor [151]. The surfaces with the phase angle shifted to lower frequencies in the Bode plot indicate better catalytic efficiency therefore, **5b**-AgNPs is further confirmed to give better catalytic activity for hydrazine oxidation compared to **5b** and AgNPs which further confirms a synergistic effect. As expected, the solution resistance was approximately equal because the same solution was used thorough out the experiment furthermore, the percentage errors were less than 5% rendering the data reliable.
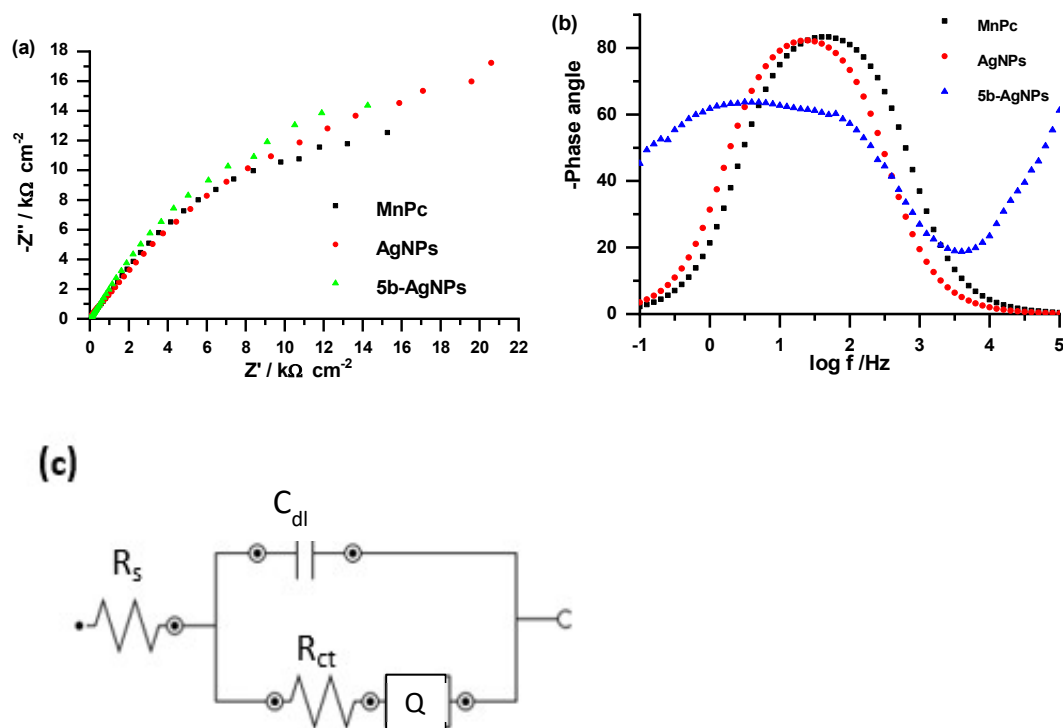
Figure 5.15: The Nyquist (a) and bode (b) plots obtained using the modified electrodes in 0.20 M NaOH containing 2 mM hydrazine (c) is Randles model used for fitting where C = capacitance and Q= Constant phase element.

Table 5.2: A summary of EIS data for AgNPs, **5b** and **5b**-AgNPs and in 0.2 M NaOH containing 2 mM hydrazine.

Electrode	R_s (kΩ cm^{-2})	R_{ct} (kΩ cm^{-2})	k_{app} (cms^{-1})	Error (%)
AgNPs	5.49	40.60	0.78	3.23
5b	5.04	56.35	0.53	4.62
5b-AgNPs	6.39	32.27	1.06	3.75

5.2. Hydrogen peroxide detection

Complexes **1a**-adsorbed, **1b**, **1c** and conjugates with QDs were employed

5.2.1. Cyclic voltammetry

The electrocatalysis of hydrogen peroxide is an interesting study as it shows both the oxidation and reduction peaks. However, the reduction peak suffers from oxygen reduction interferences therefore oxidation peaks were used in the following studies. The electrodes modified with MPcs and conjugates showed oxidation peaks in the range of 0.55 - 0.69 V, Fig. 5.16 (Fig. A6 (a)) Table 5.3. The obtained values are comparable to the reported ones 0.62 V for tetra-carboxylic acid phthalocyanine [168]. The incorporation of QDs improved the catalytic activity of **1b**, since a peak was observed only in the presence of the former. For both **1a** and **1c**, there was a slight increase in potential but a huge increase in catalytic currents following conjugation, Table 5.3. Therefore, the conjugates showed better electrocatalytic activity as judged by the higher currents obtained. The highest currents were observed for **1a**-QDs.
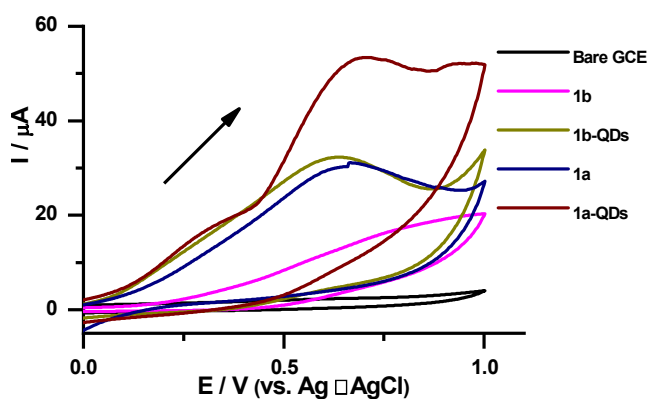
Figure 5.16: Cyclic voltammograms of a selection of modified electrodes in 1mM hydrogen peroxide. Scan rate 100 mVs^{-1}

5.2.2. Kinetic studies

Cyclic voltammetry (Fig. 5.17(a)) was used to investigate the effect of varying scan rate during the oxidation of 1 mM hydrogen peroxide in pH 7 buffer solution using the **1a**-QDs electrode (as an example and also because it showed the highest catalytic currents as described above).
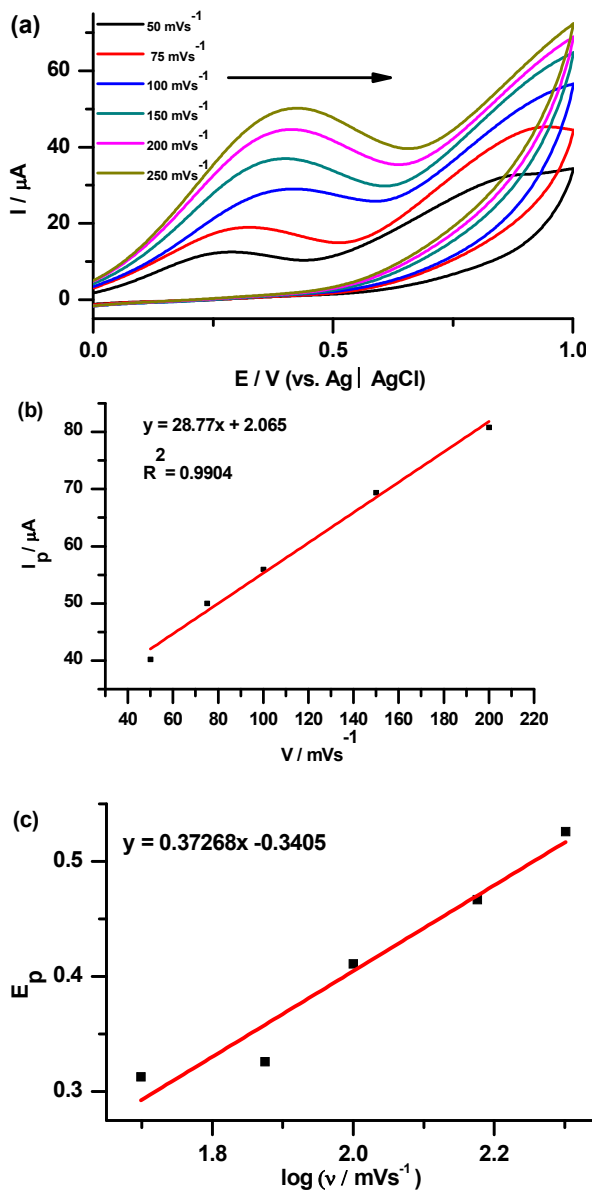
Figure 5.17: (a) cyclic voltammograms of **1a**-QDs electrode in 1 mM H_2O_2 in pH 7 buffer, at different scan rates (50, 75, 100,150 and 200 mVs^{-1}, inner to outer). (b) Plot of peak oxidation current against the scan rate and (c) Plot of peak potential (E_p) against the logarithm of scan rate (log v).

The oxidation potentials shifted to more positive values with the increase of the scan rate, which is a characteristic of an irreversible diffusion controlled process and it is governed by the equation 5.5.

A linear plot of Ip vs scan rate was observed for oxidation of hydrogen peroxide on **1a**-QDs, Fig. 5.17(b), confirming adsorption. For molecules that adsorb on the electrode surface, current depends on the scan rate as observed in Fig. 5.17(b).

The plot of E_p vs log v (Fig. 5.17 (c)) gave a linear relationship and its Tafel slope was found to be 242 mV dec^{-1} for **1a**-QDs, Table 5.3. As stated above, Tafel slopes higher than the normal 60-120 mV decade^{-1} have no kinetic meaning and are usually indicative of an electrode surface passivation [164]. For **1a** and **1b**-QDs, Tafel slopes are within the 60-120 mV decade^{-1}. Tafel slopes increased in the presence of QDs, Table 5.3.

Since the Tafel slope values in some cases were more than 60 – 120 mV/decade in the presence of QDs also Fig. 5.17(b) shows adsorption, hence the adsorptive properties of hydrogen peroxide were probed using linear sweep voltammetry to monitor the interaction of the solutes and the GCE, Fig. 5.18.
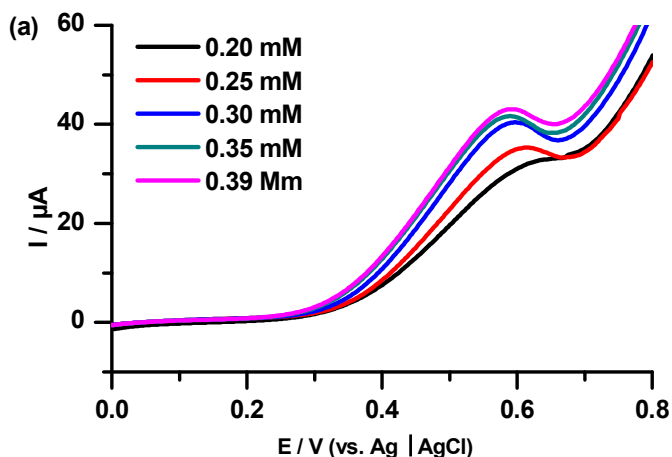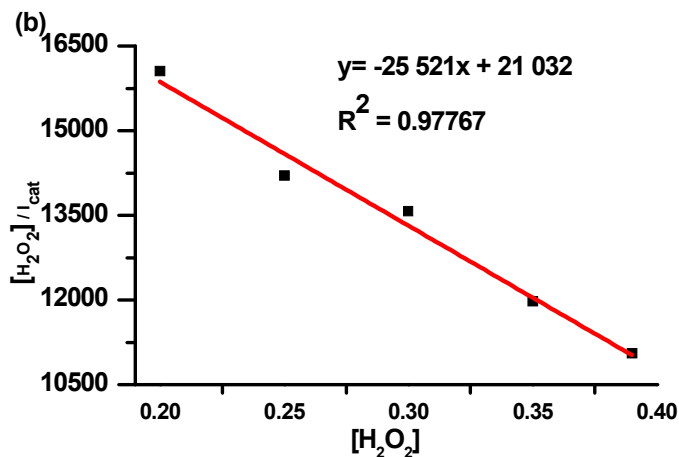
Figure 5.18: (a) linear sweep voltammograms (b) Langmuir adsorption isotherm plot for **1a**-QDs in 1mM hydrogen peroxide in pH 7 buffer.

The voltammograms were analysed using the Langmuir adsorption isotherm theory [169] Eqn. 5.11. The plot $[H_2O_2]/I_{cat}$ Vs. $[H_2O_2]$ showed a linear relationship which is evidence that there is adsorption at the electrode.

$$\frac{[H_2O_2]}{I_{cat}} = \frac{1}{\beta I_{max}} + \frac{[H_2O_2]}{I_{max}} \qquad 5.11$$

where β is adsorption equilibrium constant, I_{cat} is catalytic peak current (obtained from Fig 5.18(a) for different concentrations at the peak potential of 0.69 V vs Ag/AgCl) and I_{max} is maximum current (which is obtained from the slope of $[H_2O_2]/I_{cat}$ Vs. $[H_2O_2]$). The adsorption equilibrium constant β is related to electrochemical Gibbs free energy change (ΔG^0) by equation 5.12:

$$\Delta G^0 = -RTln\beta \qquad 5.12$$

where R and T are gas constant and temperature respectively. From the slope and the intercept in Fig. 5.18 (b), the adsorption equilibrium constant β was determined to be 1.21×10^3 M^{-1}. The Gibbs free energy change (ΔG^0) was calculated from Eqn.

5.12 using adsorption equilibrium constant β, and ΔG^0 was found to be -17.60 kJ mol^{-1}. The negative ΔG^0 shows that the adsorption of hydrogen peroxide on **1a**-QDs is a spontaneous process and the high value means there is strong adsorption at the electrode surface, which further consolidates high Tafel slope obtained. The ΔG^0 value is comparable to those reported elsewhere in the literature (-25.40 kJ mol^{-1}) [169].

Table 5.3 A summary of CV data for the different surfaces in hydrogen peroxide (pH 7). Oxygen reduction reaction (ORR) studies in 0.1 M NaOH saturated with oxygen.

Electrode	E/ V (H_2O_2) oxidation pH 7	Tafel slopes (mV/dec) (H_2O_2)	Background corrected oxidation current (µA) (H_2O_2)	Catalytic rate constant/ $M^{-1}s^{-1}$ (H_2O_2) k	Onset potential (V) (ORR)	Tafel Slopes (mV/dec) (ORR)	Background corrected Currents (µA) (ORR)
Bare GCE	-	-	-				
QDs	-	-	-		-		-
1a-adsorbed	0.56	74	18.49	3.7×10^4	-0.24	97	18.35
1b	-	-	-	4.3×10^4	-0.19	88	21.13
1c	0.55	123	15.32	1.5×10^4	-0.23	105	11.10
1a-QDs	0.69	242	33.61	8.9×10^4	-0.12	79	19.27
1b-QDs	0.60	117	20.55	9.3×10^4	-0.15	63	18.33
1c-QDs	0.61	138	25.92	6.7×10^5	-0.10	118	17.84

5.2.3. Chronoamperometry studies

1a-QDs was employed in chronoamperometry (Fig. 5.19) because it showed superior catalytic activity in terms of current as discussed above. The chronoamperometry data was used to obtain calibration graph from which limits of detection for the oxidation of hydrogen peroxide were determined.
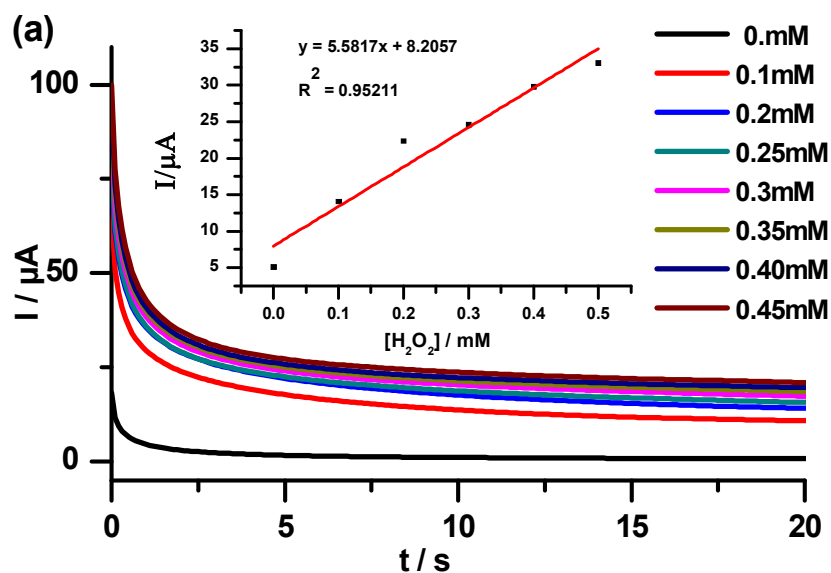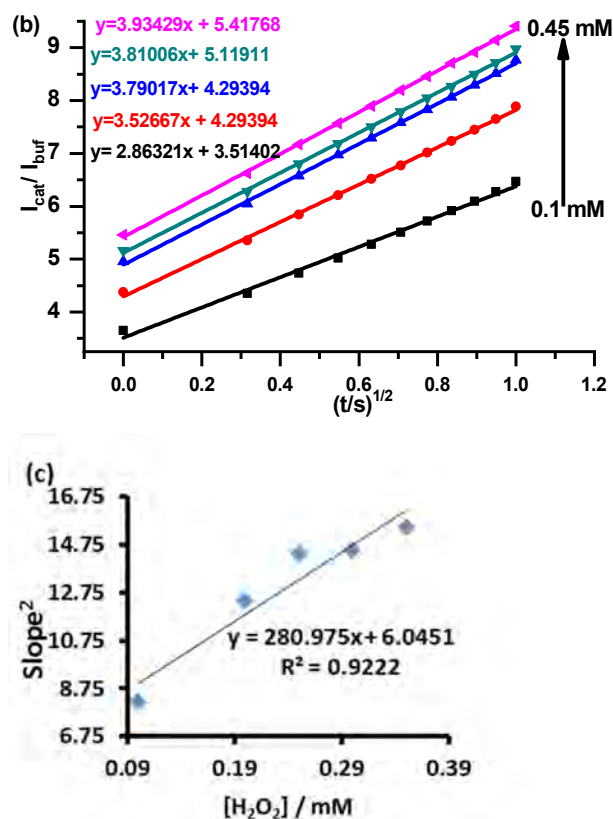
Figure 5.19: (a) Chronoamperograms (insert calibration graph at t = 5s) for **1a**-QDs electrode for 1mM hydrogen peroxide in pH 7 buffer. Potential of 0.69 V (vs Ag/AgCl) applied, (b) plot of t$^{1/2}$ Vs (I$_{cat}$ / I$_{buf}$) and (c) plot of concentration Vs slope^2.

The catalytic rate constants for the detection of hydrogen peroxide were determined using Eqn. 5.6.

Fig. 5.19(b) shows linear plots for the I$_{cat}$/ I$_{buf}$ vs. t$^{1/2}$ for different hydrogen peroxide concentrations, obtained from chronoamperomograms in Fig. 5.19(a). The slopes of these plots were plotted against the concentration of hydrogen peroxide to give another linear relationship shown in Fig. 5.19(c) and represented by Eqns. 5.13.

Oxidation: **1a**-QDs

$$y = 2.8 \times 10^5 [H_2O_2] \left(\frac{s^{-1}}{mM} \right) + 6.0451 \; s^{-1}, R^2 = 0.9222 \qquad 5.13A$$

Oxidation: **1b**-QDs

$$y = 2.9 \times 10^{5} \left[H_2O_2 \right] \left(\frac{s^{-1}}{mM} \right) + 5.8902 \ s^{-1}, R^2 = 0.9324 \qquad 5.13B$$

Oxidation: **1c**-QDs

$$y = 2.1 \times 10^{6} \left[H_2O_2 \right] \left(\frac{s^{-1}}{mM} \right) + 8.3351 \ s^{-1}, R^2 = 0.9013 \qquad 5.13C$$

The obtained values of k range from 1.5×10^4 to 6.7×10^5 $M^{-1}s^{-1}$. These values increase for Pcs in the presence of QDs and they are larger than those reported for hydrogen peroxide electrocatalysis [170]. This indicates a faster rate of hydrogen peroxide electrocatalysis at the surface of the modified electrodes in the presence of QDs.

The limits of detection (LoD) were calculated using 3δ/s as stated above (Fig. 5.19(a, insert), and were found to be 0.023 µM for **1a**-QDs, 1.40 µM for **1b**-QDs and 0.18 µM for **1c**-QDs, Table 5.4, showing the **1a**-QDs to have the best value. The values for **1b**-QDs, **1c**-QDs, and **1a**-QDs are in the range (or smaller) of the best performing electrodes based on Pcs in literature, Table 5.4 [171-173]. From Table 5.4 it can be generally be seen that linking MPcs to the QDs results in the improvement of LoDs of the Pcs.

Comparing the three phthalocyanines when linked to QDs for catalytic oxidation of hydrogen peroxide, shows that **1a**-QDs showed better catalytic activity in terms of current and LoD. The phthalocyanines used in this work were the same what differed was Co, Fe and Mn central metals resulting in deferent behaviour due to the fact that each metal has its specific redox potential [174].

Table 5.4. Comparative electrocatalytic properties of hydrogen peroxide using different catalysts.

Electrode	Reaction	pH	LoD/ µM	Ref
1a	Oxidation	7	4.99	This work
1b	Oxidation	7	9.32	This work
1c	Oxidation	7	6.67	This work
1a-QDs	Oxidation	7	0.023	This work
1b-QDs	Oxidation	7	1.40	This work
1c-QDs	Oxidation	7	0.18	This work
FeTSPc	Oxidation	7	0.13	[171]
CoPc-CSPE	Oxidation	7.5	0.71	[172]
CoPcNP-rPNDGNS	Oxidation	7	0.0048	[173]

FeTSPc = iron tetrasulfonatophthalocyanine, CSPE = Carbon Screen Printed Electrode, rPNDGNS = reduced Phosphorus and Nitrogen Doped Graphene Nanosheets

5.3. Oxygen reduction reaction (ORR)

Complexes **1a**, **1b**, **1c** and conjugates with QDs were employed for oxygen reduction reaction.

5.3.1. Cyclic voltammetry (CV)

Fig. 5.20(b) (and Fig. A6(b)) show comparative CVs of different electrodes in 0.1 M NaOH saturated with oxygen. The ORR activity was clearly observed for all electrodes. There is a shift in the onset potential of the Pcs to less negative values in the presence of QDs with **1c**-QDs showing better performance in terms of onset potential hence **1c**-QDs is employed for further studies on ORR. The onset potential

values for all conjugates are comparable to reported values [175-177]. There was

generally an improvement in currents (except for **1b**, where there is improvement

in potential and not currents) after conjugation of metallophthalocyanines to QDs,

this may be attributed to an increase in electron transfer kinetics consequently

better ORR electrocatalytic performance. It is important to note that for MPcs alone,

there is a clear difference in currents for ORR. But the difference is only small in

the presence of QDs. Generally, the O_2 transport of ORR involves diffusion directly

from electrolyte solution to the reactive sites, it is possible that in the presence of

QDs, the diffusion is limited hence affecting the current. However as stated above,

the currents are higher in the presence of QDs for **1c**-QDs and **1a**-QDs.
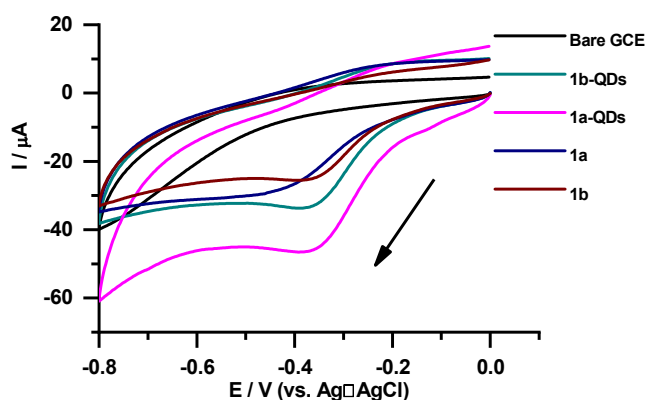
Figure 5.20: Cyclic voltammograms of a selection of modified electrodes in (0.1 M
NaOH saturated with oxygen. Scan rate 100 mVs^{-1}

5.3.2. Kinetics

Cyclic voltammetry (Fig. A7(a)) was used to investigate the effect of varying scan

rate on the response of **1c**-QDs electrode in the reduction of oxygen in 0.1 M NaOH

oxygen saturated solution. The onset reduction potentials shifted to more negative

potentials with the increase of the scan rate, which is a characteristic of an

irreversible process and it is governed by the Eqn. 5.6. The plots of E_p vs $\log v$ (Fig. A7 (b)) gave linear relationships with Tafel slopes within 60-120 mV decade^{-1}, Table 5.3. A linear plot of Ip vs square root of scan rate was observed, Fig. A7(c) confirming diffusion control.

5.3.3. Chronocoulometry

Fig. 5.21 (a) shows the chronocoulometry plots of **1c**-QDs-GCE in both argon saturated and oxygen saturated 0.1 M NaOH solutions. There is higher charge on the oxygen-saturated electrolyte than in the presence of argon, indicating that the electrode is electroactive to towards reduction of oxygen. The charge on the argon saturated electrode may be due to background current, hence it was subtracted from oxygen saturated electrode to plot charge (Q) against the square root of time ($t^{1/2}$) Fig. 5.21 (b).The plot gave a linear response which is a characteristic of a diffusion-controlled process.

(a)

(b)
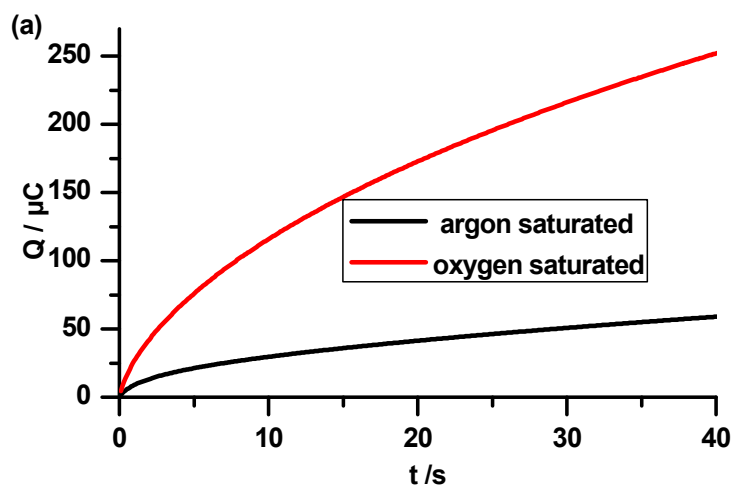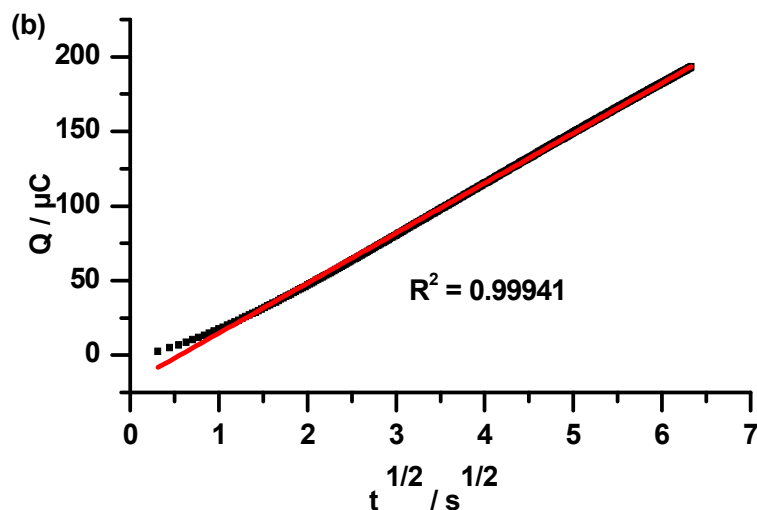
Figure 5.21: (a) Chronocoulometry curves of **1c**-QDs-GCE in 0.1 M NaOH saturated with argon (black line) and with oxygen (red line). (b) Plot of charge (Q) against square root of time ($t^{1/2}$). Applied potential = -0.18 V.

The number electrons (n) involved in the reduction of oxygen can be estimated from the slope of Q vs $t^{1/2}$ plot (Fig. 5.21(b) with a slope of 30.3 $\mu Cs^{1/2}$) according Cottrell Eqn. 5.14 [178]:

$$Q = \frac{2nFACD^{1/2}t^{1/2}}{\Pi^{1/2}} \qquad\qquad 5.14$$

where F is Farraday constant, A is the electroactive surface area (~0.12 cm^2 for **1c**-QDs-GCE, calculated using Randles Sevcik and using [Fe(CN)$_6$]$^{3-/4-}$ in 0.1 M KCl), C is the concentration of oxygen in oxygen saturated 0.1 M NaOH (0.25×10^{-6} mol cm^{-3}) [179], t is time in seconds and D is the diffusion coefficient of oxygen in an aqueous solution (1.9×10^{-5} cm^{2}s^{-1}) [179].

The number of electrons involved in the reduction of oxygen was estimated to be ~ 4. As stated above ORR can either go via a path involving the transfer of two electrons to produce H_2O_2 and the other one involve a direct four electron pathway to produce H_2O. The 4 electron pathway is preferred since the two electron pathway produces H_2O_2 which degrades the membrane and this can lead to cross over of methanol from the anode to cathode, reducing the overall efficiency of the fuel cell [63].

5.3.4. Rotating disk electrode (RDE) studies

The kinetics of ORR on the **1c**-QDs were further probed using RDE hydrodynamics (Fig.5.22). As the rotation rate increases there is an enhancement of the limiting current. Linear correlations using Koutecky- Levich plots, Eqn. 5.15 [180] were obtained indicating diffusion-controlled mass transport.

$$i_L = 0.62nFAD^{2/3} \omega^{1/2} v^{-1/6}C \qquad 5.15$$

where, n, v, D, C and ω are number of electrons transferred in the reaction, kinematic viscosity, diffusion coefficient, concentration and rotation speed and all other parameters retain their usual scientific meaning.
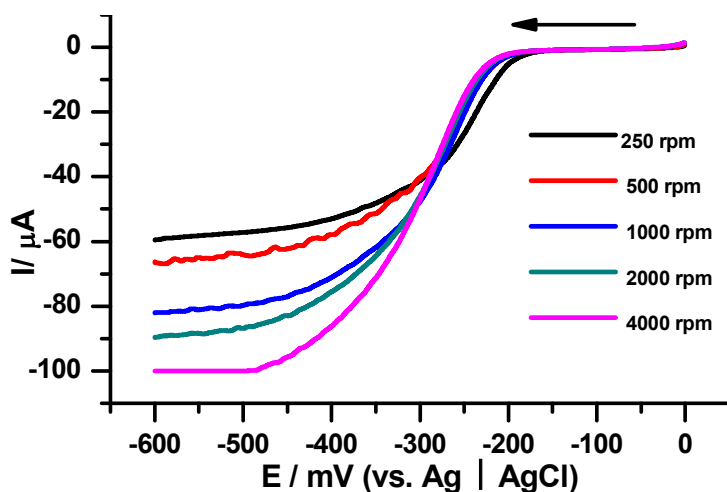
Figure 5.22: Linear sweep voltammograms for ORR in oxygen saturated 0.5 M NaOH on a **1c**-QDs-GCE rotating disk electrode at different rotations. Scan rate: 10 mV/s.

The Koutecky- Levich plots (i^{-1} vs. $\omega^{1/2}$, Fig. A8) were obtained from the experiment data shown in Fig. 5.22. The number of electrons transferred were found to be 3.7, 3.5 and 3.9 (at -0.30, -0.25 and -0.35 V respectively) which is close to 4, typical for direct oxygen reduction pathway.

5.4. 2-Mercaptoethanol (2-ME) detection

Complexes **1a**-adsorbed, **CoPc**, **2** and conjugates with rGONS were employed as examples.

5.4.1. Cyclic voltammetry

Fig. 5.23 shows the behaviour of the different electrodes towards 2-ME oxidation when the electrodes are immersed in 2 mM 2-ME in 0.5 M NaOH solution.

The following conclusions can be reached from the potential data for the oxidation of 2-ME in Table 5.5.

- For the Pcs alone (in the absence of rGONS), there is not much difference in potential showing no effect of the substituent.

- The oxidation potentials improve (become less positive) when rGONS are linked to complexes **2** and **1a** compared to the corresponding Pcs alone. The higher electrocatalytic performance of CoPc conjugates with rGONS compared to Pcs alone could be as a result of electron donation to the phthalocyanine from graphene. It has been reported before that rGONS enhance electrocatalytic behaviour of phthalocyanines [181].

- The oxidation potentials improve (are less positive) when rGONS are linked as opposed to sequentially added for complexes **2** and **1a**, hence showing the importance of linking Pcs to rGONS.

- The potentials reported are an improvement when compared to other reported values (0.91 V and 0.95 for nickel tetra-aminophthalocyanine and nickel tetraamminophthalocyanines-single walled carbon nanotube conjugate respectively) in the literature [182], when a Pc is linked to other nanomaterials.
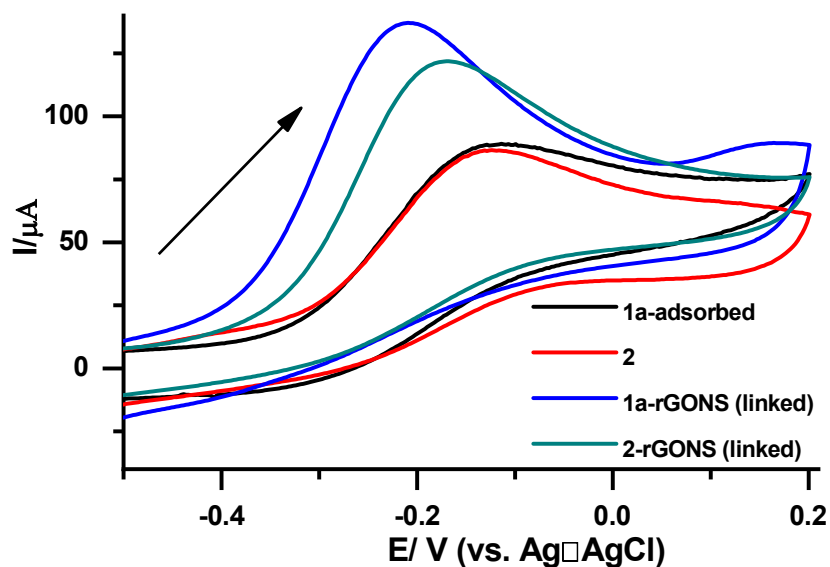
Figure 5.23: Cyclic voltammograms of the modified electrodes in 0.5 M NaOH containing 2 mM 2-ME$^-$ solution. Scan rate = 100 mV/s.

In terms of background corrected current, the following conclusions can be reached from Table 5.5.

- Sequentially modified electrodes gave low currents when compared to linked conjugates. This shows the importance of linking rGONS to Pcs rather than sequentially adding them to modify the electrode.

- Sequentially modified electrodes gave higher currents when compared to Pcs alone showing advantage of incorporating rGONS to Pcs.

5.4.2. Kinetic studies of 2-mercaptoethanol (2-ME) detection

The extent of reversibility of the oxidation reaction taking place at the surface of the modified electrode was studied by varying the scan rate in the presence of 2-ME (2 mM in 0.5 M NaOH). It was found out that increasing scan rate resulted in an increase in peak potential, a characteristic of an irreversible reaction, Fig. 5.24(a). The linear relationship between the square root of scan rate and current, Fig.

5.24(b) indicates diffusion control. This is further confirmed by the slope of the plot of log I_p vs. log v in Fig. 5.24 (c). The slope of that plot can give an information on whether a reaction is diffusion controlled or dominated by adsorption reactions as discussed above. The slope is 1 for adsorption dominated reactions and 0.5 for diffusion controlled reactions [167]. The obtained value of 0.47 is close to 0.5, therefore confirming a diffusion controlled reaction in the potential range of the examined scan rates.
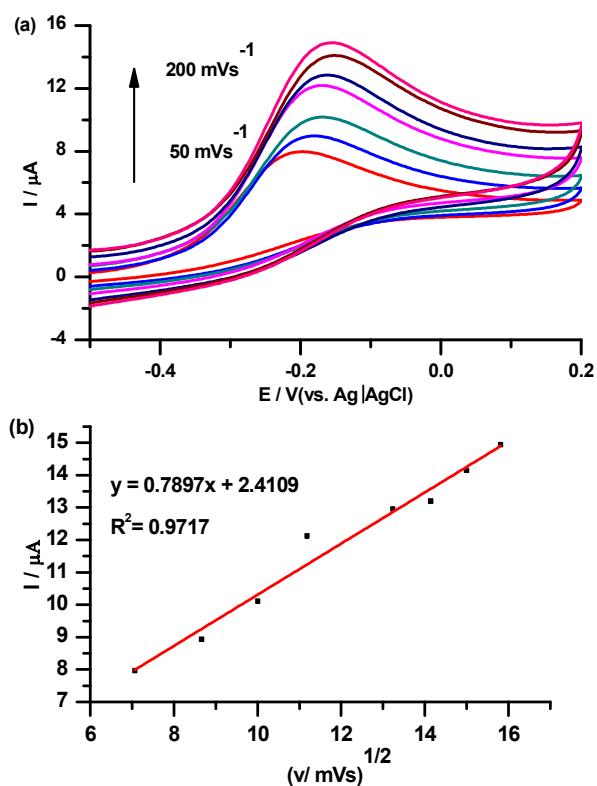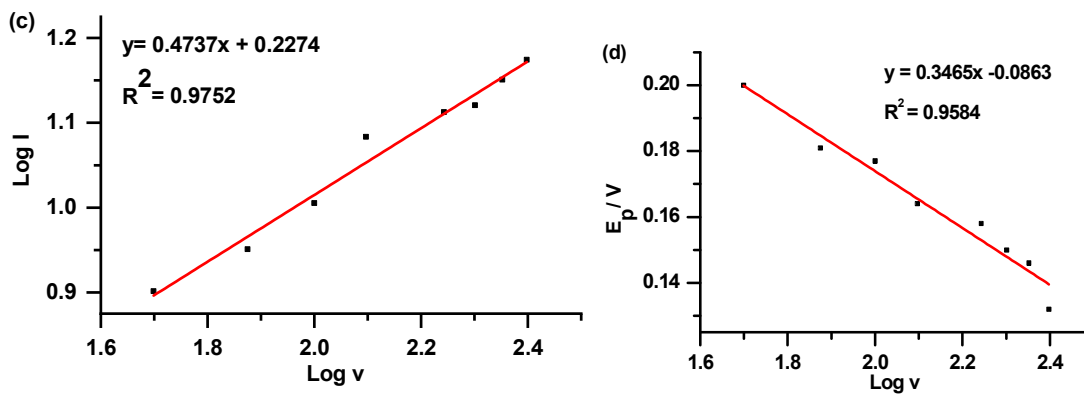
Figure 5.24: Cyclic voltammograms at different scan rates (a) and corresponding plots of (b) peak currents vs. $v^{1/2}$, (c) log current vs. log v and (d) E_P vs log v for **1a-**rGONS in 2 mM 2-ME in 0.5 M NaOH solution. Scan rates: 50-200 mV/s.

The irreversible diffusion controlled reaction electrochemical reactions are governed by Eqn 5.5.

The plot of E_p Vs. log v in Fig. 5.24 (d) gave a linear relationship with Tafel ranging from 76 mV/decade to 254 mV/decade Table 5.6. With the exception of GCE-**2**-rGONS (linked), all Tafel slopes were within the 60-120 mV/dec range.

Table 5.5: Electrochemical parameters, 2-ME oxidation (in 0.5 NaOH) potentials and currents.

Electrode	E/ V (2-ME)	Background corrected current (μA)
Bare GCE	-	-
rGONS	-	-
1a-adsorbed	-0.14	38.69
1a-rGONS (linked)	-0.22	83.60
1a-rGONS (seq)	-0.071	72.66
2	-0.13	40.24
2-rGONS (linked)	-0.19	70.24
2-rGONS (seq)	-0.036	61.38
CoPc	-0.13	26.44
CoPc-rGONS (seq)	-0.003	59.82

seq = sequential.

5.4.3. Stability study

The stability of the electrodes were studied by 20 repetitive cyclic voltammetry scans in 2 mM of 2-ME Fig. 5.25 (using **2-**rGONS as an example). The probes were tested to determine their ability to resist fouling during 2-ME oxidation, **2**-rGONS electrode shows a decrease in current from the first scan which stabilizes after 20 scans which shows that the probes were electrochemically stable. The electrode was left at room temperature for four weeks and was found to show stability.
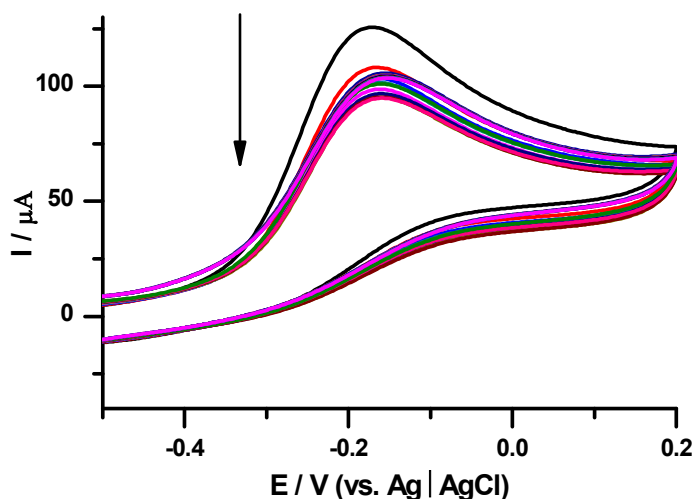
Figure 5.25: Repetitive cyclic voltammograms (20 scans) of bare, **2**-rGONS (linked) in 2-ME (2 mM in 0.5 NaOH).

5.4.4. Chronoamperometry studies

Chronoamperometry was used to determine the limit of detection and catalytic rate constant of the probes (values in Table 5.6). Chronoamperometric experiment was conducted by using the peak potential of the analyte. Chronoamperograms (Fig. 5.26 (a)) were obtained by adding different aliquots of the 2-ME solution.

(a)

$y = 0.262x + 0.169$
$R^2 = 0.96648$

0 mM
0.1 mM
0.2 mM
0.3 mM
0.4 mM
0.5 mM

(b) plot with equations:
y= 0.1966x + 1.058
y= 0.1853x + 1.0145
y= 1734x +0.8759
y= 0.1696x + 0.9626
y= 0.1094x + 1.0092

(c) plot:
y = 31.52901x - 82.43201
R^2 = 0.96241
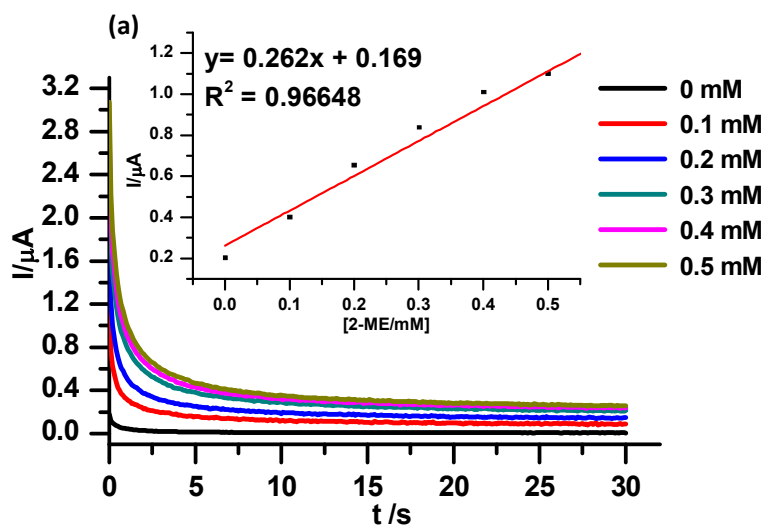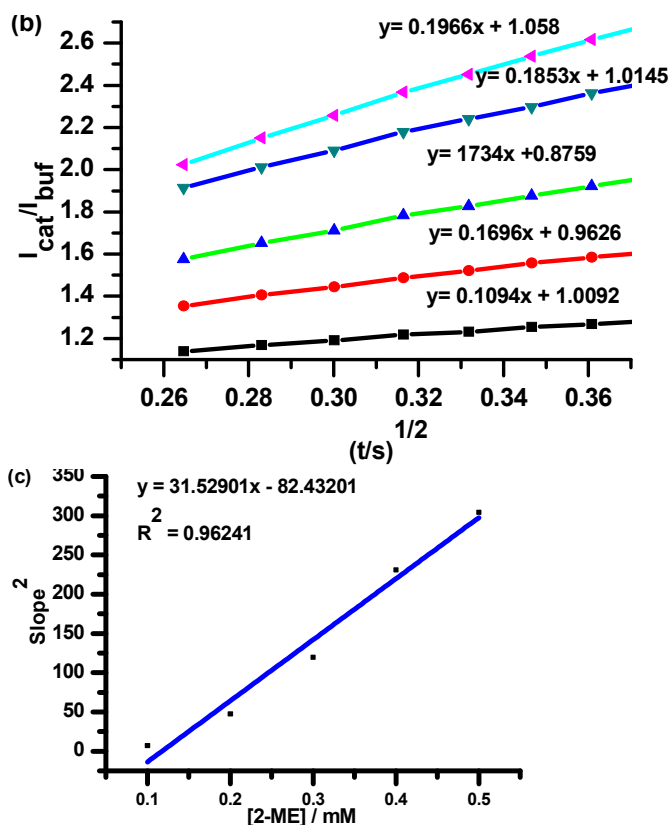
Figure 5.26: (a) Chronoamperograms (insert calibration graph), (b) plots of I_{cat}/I_{buf} vs. $t^{1/2}$ and (c) slope^2 vs. concentration of 2-ME for **2**-rGONS electrode for 2-ME in 0.5 M NaOH.

The sensitivity (Table 5.6) of the probes was the highest for **1a**-rGONS (linked) and **2**-rGONS (linked), which is in agreement with background corrected currents listed in Table 5.5. The rate constant can be evaluated using Eqn. 5.6.

The slopes of the plots of (I_{cat}/I_{buf}) versus $t^{1/2}$ were plotted against the concentration of 2-Me (Fig. 5.26(b)), and the slopes of Fig. 5.26(c) (shown also in Eqn. 5.16) were used calculate the rate constant according to Eqn. 5.6.

$$y = 31.5 \times 10^3 \, [2-ME]\left(\frac{s^{-1}}{mM}\right) - 82.43201 \; s^{-1}, R^2 = 0.96241 \qquad (5.16A)$$

$$y = 89.8 \times 10^4 \, [2-ME] \left(\frac{s^{-1}}{mM}\right) - 103.64822 \; s^{-1}, R^2 = 0.98343 \qquad (5.16B)$$

$$y = 10.2 \times 10^4 \, [2-ME] \left(\frac{s^{-1}}{mM}\right) - 64.75645 \; s^{-1}, R^2 = 0.99652 \qquad (5.16C)$$

$$y = 13.6 \times 10^4 \, [2-ME] \left(\frac{s^{-1}}{mM}\right) - 57.87653 \; s^{-1}, R^2 = 0.99973 \qquad (5.16D)$$

$$y = 31.5 \times 10^3 \, [2-ME] \left(\frac{s^{-1}}{mM}\right) - 73.50987 \; s^{-1}, R^2 = 0.97032 \qquad (5.16E)$$

$$y = 19.2 \times 10^4 \, [2-ME] \left(\frac{s^{-1}}{mM}\right) - 95.38764 \; s^{-1}, R^2 = 0.98894 \qquad (5.16F)$$

$$y = 47.8 \times 10^4 \, [2-ME] \left(\frac{s^{-1}}{mM}\right) - 84.76543 \; s^{-1}, R^2 = 0.98765 \qquad (5.16G)$$

The rate constants were highest for **2**-rGONS(linked) and **1a**-rGONS(linked). The sequentially modified electrodes gave lower rate constants when compared to linked counterparts, showing the importance of linking. With the exception of unsubstituted **CoPc**, sequentially modified electrodes performed better than Pcs alone.

The rate constant for the electro oxidation of 2-ME reported in the literature [182] was lower than reported in this work with or without GONS, Table 5.6. The obtained values were comparable with reported values for other analytes such as amitrole [183], nitrile [154] and asulam [184]. The LoDs were calculated using 3σ/k (as stated above). The best detection limit was obtained for **1a**-rGONS (linked), with the general observation being that including rGONS improved the LoDs of the MPcs and linked rGONS gave better LoDs than sequential modifications.

Table 5.6: Electrochemical parameters, 2-ME oxidation potentials and currents.

Electrode	Tafel slope (mV/decade)	LoD (µM)	Sensitivity (µA mM^{-1})	Catalytic rate constant k (M^{-1}s^{-1})	Reference
1a-adsorbed	84	3.05	4.78	4.32×10^4	This work
1a-rGONS(linked)	98	0.08	12.05	1.52×10^5	This work
1a-rGONS(seq)	119	1.27	8.93	4.99×10^4	This work
2	125	3.42	4.52	3.26×10^4	This work
2-rGONS(linked)	254	0.14	11.21	6.10×10^4	This work
2-rGONS(seq)	79	1.34	8.72	3.97×10^4	This work
CoPc	76	5.20	1.56	2.8×10^4	This work
CoPc-rGONS(seq)	109	2.63	6.34	2.73×10^4	This work
NiTAPc-SWCNT[a]	86	0.15	2.53	2.95×10^3	[182]

[a]NiTAPC-SWCNT = nickel tetra-amino phthalocyanine liked to single-walled carbon nanotubes.

5.5. Conclusions

The developed probes were capable of effective electro oxidation of 2-ME, hydrazine and hydrogen peroxide and electro reduction of oxygen and hydrogen peroxide. The clicked nanomaterials resulted in improvements in detection currents. Conjugates resulted in the lowering of over potentials when compared to individual materials. Electrode modification via grafting and click chemistry improved stability than adsorption method. Complex **1a** gave lowest limit of detection for 2-ME (3.05 µM) detection relative to hydrogen peroxide (4.99 µM) and hydrazine detection (3.28 µM) hence it performs best for 2-ME sensing.

CHAPTER SIX: Nonlinear optics

6. Nonlinear optics

Complex **2** and ZnONPs used as an example

6.1. Nonlinear optical (NLO) studies

The nonlinear absorption behaviour was measured using the open aperture Z-scan technique at a wavelength of 532 nm with 10 ns laser pulse in THF and the optical parameters were evaluated as reported by M. Sheik-Bahae et al [114].
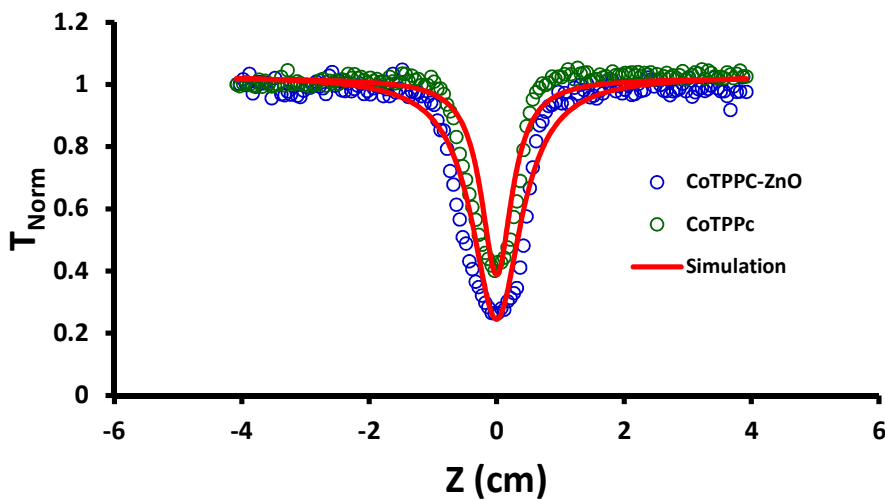
Figure 6.1: Open aperture Z-scan spectra of **2** and **2**-ZnONPs.

Upon analysis along the z-axis of the Z-scan under resonate conditions, it was found out that **2** possessed reverse saturable absorption (RSA) which is characterised by the reduction of T_{Norm} at focus (z=0) (Fig. 6.1). The higher the drop in normalised transmittance (T_{Norm}) at on-focus intensity, the better the material as an optical

limiter. The attenuation of about 61% of the input fluence was recorded for **2** and a higher attenuation of 74% for **2-ZnONPs**, Fig. 6.1**.**

Upon conjugation, both β_{eff}, γ (esu) and Im[$\chi^{(3)}$] increased for **2-ZnONPs** compared to **2** alone, Table 6.1. The data for azide ZnONPs alone could not be provided due to solubility problems. An increase in these values is an indication that incorporating ZnONPs nanoparticles to **2** results in enhancement of nonlinear optical properties. Although the nonlinear optical properties of phthalocyanines can be enhanced by the heavy atom effect [84], the paramagnetic nature of Co in **2** is expected to result in short lived triplet state [185]. As such, the mechanism is proposed to be the excited state absorption (ESA) involving singlet states only as was reported for a GdPc [186] which is paramagnetic, whereby the triplet state is ignored. The reported literature limits range from 10^{-9} to 10^{-15} esu for $Im\left[X^{(3)}\right]$ [187] and the obtained values were within the upper limit of this range. The alkynyl phthalocyanines have been reported to give good nonlinear properties [188] with the $Im\left[X^{(3)}\right]$ values of 3 to 11 $\times$ 10^{-12}, while in this work the obtained values are on the $\times$ 10^{-10} range, so even better.

Table 6.1: Nonlinear optical properties and fluorescence lifetimes of complex **2** and **2-**ZnONPs.

Complex	Im[X(3)] (esu)	I$_{lim}$ (J.cm^{-2})	β_{eff}(cmW^{-1})	γ(esu)
2	2.68 x10^{-10}	0.99	1.51 x10^{-9}	1.47x10^{-28}
2-ZnONPs	5.70 x10^{-10}	0.27	7.10 x10^{-8}	6.92 x10^{-27}

The incident intensity threshold (I_{lim}) limiting is an important parameter for an efficient optical limiter and it is defined as the input fluence at which the transmittance is 50% of the linear transmittance [189]. The value of I_{lim} can be determined by using the plot of transmission vs input fluence (Fig. 6.2). The low value of **2**-ZnONPs (0.27 J.cm^{-2}) relative to **2** (0.99 J.cm^{-2}) (Table 6.1) provides another indication that **2**-ZnONPs is potentially suitable for optical limiting applications. The superior NLO properties of **2**-ZnONPs may be due to ZnONPs nanoparticles because ZnONPs are reported to have optical properties [190, 191]. The I_{lim} values reported in this work are comparable with those obtained when semi-conductor quantum dots are linked to Pcs (0.28 J.cm^{-2}) [192].
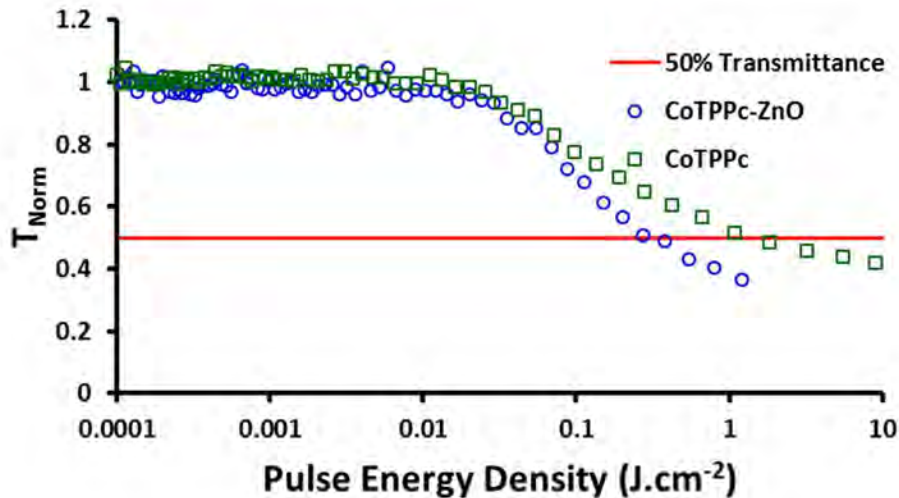
Figure 6.2: Plot of normalized transmission against pulse density of **2** and **2**-ZnONPs.

6.2. Conclusions

Conjugate **2**-ZnONPs showed relatively better optical limiting properties compared to complex **2** alone. The same conjugate showed improved LoD and electrocatalytic behaviour when compared to complex **2.** These makes it a promising nonlinear optical material and platform for low concentration detection of hydrazine.

CHAPTER SEVEN: Conclusions and Future Perspectives

7. 1. Conclusions

Azide functionalised glassy carbon electrodes were successful modified with complexes **1a, 3** and **4** vial click chemistry and used for the detection of hydrazine as a test analyte. Electrodes modified by click chemistry were generally found to give better results compared to electrodeposition and adsorption methods. Complex **3** was found to be better sensor for hydrazine than other probes in terms of detection currents and limits of detection due to its electron-donating ability. Complexes **1a** and **2** were compared when alone and when clicked to rGONS and sequentially added to GCE. The clicked conjugates showed better performance than adsorbed probes and it was observed that clicking results in the resistance to passivation. Generally, the phthalocyanine with benzyl ring resulted in the improvement of the properties of the phthalocyanine with regard to electron transfers and subsequently reduction in over potentials.

This work also demonstrates the advantage of combining MPcs with nanomaterials, rGONS, AgNPs and quantum dots for electrode modification for 2-ME, hydrazine, hydrogen peroxide electrocatalysis and oxygen reduction reaction, this is as a result of synergistic effect. Nanomaterials resulted in enhancement detection of currents of MPcs and resulted in low limits of detection.

Complex **2** and **2-ZnONPs** were explored for both nonlinear optical response and electrocatalytical behaviour. Conjugating complex **2** to ZnONPs resulted in the improvement of both nonlinear optical and electrocatalytic response.

In summary, the presence of nanomaterials resulted in enhanced electrocatalytic properties of the MPcs.

7.2. Future Perspectives

After observing that electrografting and click chemistry electrode modification result in stable phthalocyanine based platform, and incorporation of nanomatarials to phthalocyanines result in improved electrocatalytic properties, it would be interesting to investigate how electrografting and clicking phthalocyanine on the electrode prior modified by nanomaterials would affect the electrocatalysis. While semiconductor based, metallic and carbon based nanomaterials used in this work demonstrates the ability to lower the overpotential of conjugates of Pcs, it will good to try different types of carbon based nanomaterials since they are relatively economically accessible and poses lesser negative environmental effect.

Since **2** employed in this work has aliphatic substituent it will be interesting to try Pcs with aromatic substituents or benzene containing substituent to see how nature of substituents affect nonlinear optical properties. Furthermore, since ZnONPs used in this study should solubility problem, other optically active non-metals should be explored.

References

[1] Ö. Bekaroğlu, Phthalocyanines containing macrocycles, Appl. Organomet. Chem. 10 (1996) 605-622.

[2] A. Braun, J. Tcherniac, The products of the action of acet-anhydride on phthalamide, Ber. Dtsch. Chem. Ges. 40 (1907) 2709-2714.

[3] R.P. Linstead, A.R. Lowe, Phthalocyanine compounds, J. Chem. Soc. (1934) 1031-1033.

[4] D.M. Guldi, A. Gouloumis, P. Vázquez, T. Torres, V. Georgakilas, M. Prato, Nanoscale organization of a phthalocyanine– fullerene system: remarkable stabilization of charges in photoactive 1-d nanotubules, J. Am. Chem. Soc. 127 (2005) 5811-5813.

[5] M. Durmuş, T. Nyokong, Synthesis, photophysical and photochemical properties of tetra-and octa-substituted gallium and indium phthalocyanines, Polyhedron 26 (2007) 3323-3335.

[6] M.O. Liu, C.H. Tai, A.T. Hu, The fluorescent and photoelectric conversion properties of phthalocyanine–perylene tetracarboxylic complexes, J. Photochem. Photobio A: Chem. 165 (2004) 193-200.

[7] Y. Chen, M. Hanack, Y. Araki, O. Ito, Axially modified gallium phthalocyanines and naphthalocyanines for optical limiting, Chem. Soc. Rev. 34 (2005) 517-529.

[8] M. Tian, T. Wada, H. Kimura-Suda, H. Sasabe, Novel non-aggregated unsymmetrical metallophthalocyanines for second-order non-linear optics, J. Mater. Chem. 7 (1997) 861-863.

[9] M. Hanack, T. Schneider, M. Barthel, J.S. Shirk, S.R. Flom, R.G. Pong, Indium phthalocyanines and naphthalocyanines for optical limiting, Coord. Chem. Rev. 219 (2001) 235-258.

[10] L. Guo, G. Ma, Y. Liu, J. Mi, S. Qian, L. Qiu, Optical and non-linear optical properties of vanadium oxide phthalocyanine films, Appl. Phys. B. 74 (2002) 253-257.

[11] L.B. Josefsen, R.W. Boyle, Unique diagnostic and therapeutic roles of porphyrins and phthalocyanines in photodynamic therapy, imaging and theranostics, Theranostics 2 (2012) 916-966.

[12] J.D. Spikes, Phthalocyanines as photosensitizers in biological systems and for the photodynamic therapy of tumors, Photochem. Photobiol. 43 (1986) 691-699.

[13] S. Uchida, J. Xue, B.P. Rand, S.R. Forrest, Organic small molecule solar cells with a homogeneously mixed copper phthalocyanine: C 60 active layer, Appl. Phys. Lett. 84 (2004) 4218-4220.

[14] S. Mori, M. Nagata, Y. Nakahata, K. Yasuta, R. Goto, M. Kimura, M. Taya, Enhancement of incident photon-to-current conversion efficiency for phthalocyanine-sensitized solar cells by 3D molecular structuralization, J. Am. Chem. Soc. 132 (2010) 4054-4055.

[15] V. Crowl, Consumer Demands in the Paint Industry, J. Soc. Dyer. Colour. 81 (1965) 545-552.

[16] M.K. Halbert, R.P. Baldwin, Electrocatalytic and analytical response of cobalt phthalocyanine containing carbon paste electrodes toward sulfhydryl compounds, Anal. Chem. 57 (1985) 591-595.

[17] X. Zhang, Z. Wu, X. Zhang, L. Li, Y. Li, H. Xu, X. Li, X. Yu, Z. Zhang, Y. Liang, Highly selective and active CO_2 reduction electrocatalysts based on cobalt phthalocyanine/carbon nanotube hybrid structures, Nat. Commun. 8 (2017) 14675-14682.

[18] C.C. Leznoff, S.M. Marcuccio, S. Greenberg, A. Lever, K.B. Tomer, Metallophthalocyanine dimers incorporating five-atom covalent bridges, Can. J. Chem. 63 (1985) 623-631.

[19] M. Sommerauer, C. Rager, M. Hanack, Separation of 2 (3), 9 (10), 16 (17), 23 (24)-tetrasubstituted phthalocyanines with newly developed HPLC phases, J. Am. Chem. Soc. 118 (1996) 10085-10093.

[20] M. Bouvet, in Radical Phthalocyanines and Intrinsic Semiconduction, The Porphyrin Handbook, editors (K.M Kadish, R. Guilard, K.M Smith), Academic Press, Amsterdam, Chapter 118, vol. 19 (2003) pages 37-98.

[21] J. Chen, N. Chen, J. Huang, J. Wang, M. Huang, Derivatizable phthalocyanine with single carboxyl group: synthesis and purification, Inorg. Chem. Commun. 9 (2006) 313-315.

[22] N.B. McKeown, in Phthalocyanine materials: synthesis, structure and function, Cambridge University Press, New York, Chapter 2, vol.6 (1998) pages 12-30.

[23] V.N. Nemykin, E.A. Lukyanets, Synthesis of substituted phthalocyanines, Arkivoc i (2010) 136-208.

[24] A.L. Uğur, H.A. Dinçer, A. Erdoğmuş, Synthesis, photophysical and thermal studies of symmetrical and unsymmetrical zinc phthalocyanines, Polyhedron 31 (2012) 431-437.

[25] A. Naumov, E. Kudrik, G. Shaposhnikov, Synthesis and properties of symmetrical and asymmetrical phthalocyanines with D, L-leucine fragments, Chem. Heterocycl. Compd. 40 (2004) 469-474.

[26] V.N. Nemykin, S.V. Dudkin, F. Dumoulin, C. Hirel, A.G. Gurek, V. Ahsen, Synthetic approaches to asymmetric phthalocyanines and their analogues, Arkivoc i (2014) 142-204.

[27] G. de la Torre, C.G. Claessens, T. Torres, Phthalocyanines: The need for selective synthetic approaches, Eur. J. Org. Chem. 2000 (2000) 2821-2830.

[28] J. Vacus, G. Memetzidis, P. Doppelt, J. Simon, The synthesis of unsymmetrically functionalized platinum and zinc phthalocyanine complexes, J. Chem. Soc. Chem. Commun. (1994) 697-698.

[29] D. Akyuz, H. Dincer, A.R. Ozkaya, A. Koca, Electrocatalytic hydrogen evolution reaction with metallophthalocyanines modified with click electrochemistry, Int. J. Hydro. Energy. 40 (2015) 12973-12984.

[30] D. Akyuz, B. Oztas, A. Koca, Immobilization of alkynyl functionalized manganese phthalocyanine via click electrochmistry for electrocatalytic oxygen evolution reaction, Phys. Chem. Chem. Phys. 19 (2017) 26121-26131.

[31] D. Mwanza, S. Mvango, S. Khene, T. Nyokong, P. Mashazi, Exploiting Click Chemistry for the Covalent Immobilization of Tetra (4-Propargyloxyphenoxy) Metallophthalocyanines onto Phenylazide-Grafted Gold Surfaces, Electrochim. Acta. 254 (2017) 89-100.

[32] G. Fomo, N. Nwaji, T. Nyokong, Low symmetric metallophthalocyanine modified electrode via click chemistry for simultaneous detection of heavy metals, J. Electroanal. Chem. 813 (2018) 58-66.

[33] C.S. O'Donoghue, G. Fomo, T. Nyokong, Electrode modification using alkyne manganese phthalocyanine and click chemistry for electrocatalysis, Electroanalysis 28 (2016) 3019-3027.

[34] S.R. Nxele, P. Mashazi, T. Nyokong, Electrode modification using alkynyl substituted Fe (II) phthalocyanine via electrografting and click chemistry for electrocatalysis, Electroanalysis 27 (2015) 2468-2478.

[35] C.S. O'Donoghue, M. Shumba, T. Nyokong, Electrode modification through click chemistry using Ni and Co alkyne phthalocyanines for electrocatalytic detection of hydrazine, Electroanalysis 29 (2017) 1731-1740.

[36] R. Li, P. Zhu, D.K.P. Ng, N. Kobayashi, J. Jiang, Electron-donating or-withdrawing nature of substituents revealed by the electrochemistry of metal-free phthalocyanines, Inorg. Chem. 45 (2006) 2327-2334.

[37] N. Sehlotho,T. Nyokong, Effects of ring substituents on electrocatalytic activity of manganese phthalocyanines towards the reduction of molecular oxygen, J. Electroanal. Chem. 595 (2006) 161-167.

[38] A.A. Saeed, M.N. Abbas, Y.M. Issa, E. Dempsey, Electrocatalytic nitrite determination using iron phthalocyanine modified gold nanoparticles, Electroanalysis 27 (2015) 1086-1096.

[39] C. Medina-Plaza, L. N. Furini, C.J .L. Constantino, J. A. De Saja, M.L. Rodriguez-Mendez, Synergistic electrocatalytic effect of nanostructured mixed films formed by functionalised gold nanoparticles and bisphthalocyanines, Anal. Chim. Acta. (2014) 95-102.

[40] M. Pal, V. Ganesan, Effect of gold nanoparticles on the electrocatalytic reduction of oxygen by silica encapsulated cobalt phthalocyanine, J. Electroanal. Chem. (2012) 7-11.

[41] T. Yoshida, M. Tochimoto, D. Schlettwein, D. Wöhrle, T. Sugiura, H. Minoura, Self-assembly of zinc oxide thin films modified with tetrasulfonated metallophthalocyanines by one-step electrodeposition, Chem. Mater. 11 (1999) 2657-2667.

[42] K.E. Sekhosana, E. Amuhaya, T. Nyokong, Nonlinear optical behavior of neodymium mono-and bi-nuclear phthalocyanines linked to zinc oxide nanoparticles and incorporated into poly acrylic acid, Polyhedron 105 (2016) 159-169.

[43] Y. Xing, Q. Chaudry, C. Shen, K.Y. Kong, H.E. Zhau, L.W. Chung, J.A. Petros, R.M. O'regan, M.V. Yezhelyev, J.W. Simons, Bioconjugated quantum dots for multiplexed and quantitative immunohistochemistry, Nat. Protoc. 2 (2007) 1152-1165.

[44] P.J. Cameron, X. Zhong, W. Knoll, Monitoring the covalent binding of quantum dots to functionalized gold surfaces by surface plasmon resonance spectroscopy, J. Phys. Chem. C. 111 (2007) 10313-10319.

[45] N.C. Murray, D.J. Norris, M.G. Bawendi, Synthesis and characterization of nearly monodisperse CdE (E= sulfur, selenium, tellurium) semiconductor nanocrystallites, J. Am. Chem. Soc. 115 (1993) 8706-8715.

[46] S.R. Nxele, T. Nyokong, Conjugation of azide-functionalised CdSe/ZnS quantum dots with tetrakis (5-hexyn-oxy) Fe (II) phthalocyanine via click chemistry for electrocatalysis, Electrochim. Acta. 194 (2016) 26-39.

[47] S. Khene, T. Nyokong, Redox activity of CdTe quantum dots linked to nickel tetraaminophthalocyanine: Effects of adsorption versus electrodeposition on the catalytic oxidation of chlorophenols, Microchem. J. 99 (2011) 478-485.

[48] S. Khene, T. Nyokong, Characterization of Quantum Dots, Single Walled Carbon Nanotubes and Nickel Octadecylphthalocyanine Conjugates, Int. J. Nanosci. 11 (2012) 1250022 – 1250032.

[49] S. Nyoni, T. Nyokong, Development of Graphene/CdSe Quantum Dots-Co Phthalocyanine Nanocomposite for Oxygen Reduction Reaction, Electroanalysis 26 (2014) 2261-2272.

[50] Y. Zhang, Y.W. Tan, H.L. Stormer, P. Kim, Experimental observation of the quantum Hall effect and Berry's phase in graphene, Nature 438 (2005) 201-204.

[51] X. Zhao, Q. Zhang, D. Chen, P. Lu, Enhanced mechanical properties of graphene-based poly (vinyl alcohol) composites, Macromolecules 43 (2010) 2357-2363.

[52] P. Blake, E. Hill, A. Castro Neto, K. Novoselov, D. Jiang, R. Yang, T. Booth, A. Geim, Making graphene visible, Appl. Phys. Lett. 91 (2007) 063124-063127.

[53] Z. Liu, Q. Liu, Y. Huang, Y. Ma, S. Yin, X. Zhang, W. Sun, Y. Chen, Organic photovoltaic devices based on a novel acceptor material: graphene, Adv. Mater. 20 (2008) 3924-3930.

[54] Y.H. Lu, M. Zhou, C. Zhang, Y.P. Feng, Metal-embedded graphene: a possible catalyst with high activity, J. Phys. Chem. C. 113 (2009) 20156-20160.

[55] J.D. Fowler, M.J. Allen, V.C. Tung, Y. Yang, R.B. Kaner, B.H. Weiller, Practical chemical sensors from chemically derived graphene, ACS nano. 3 (2009) 301-306.

[56] A. Dato, V. Radmilov, Z. Lee, J. Phillips, M. Frenklach, Substrate-free gas-phase synthesis of graphene sheets, Nano Lett. 8 (2008) 2012-2016.

[57] D. Li, M.B. Muller, S. Gilje, R.B. Kaner, G.G. Wallace, Processable aqueous dispersions of graphene nanosheets, Nat. Nanotechnol. 3 (2008) 101-105.

[58] V.C. Tung, M.J. Allen, Y. Yang, R.B. Kaner, High-throughput solution processing of large-scale graphene, Nat. Nanotechnol. 4 (2009) 24-29.

[59] K.S. Novoselov, A.K. Gein, S.V. Morozov, D. Jiang, Y. Zhang, S.V. Dubonos, I.V. Grigorieva, A.A. Firsov, Electric field effect in atomically thin carbon films, Science 306 (2004) 666-669.

[60] R. Li, D. Zhang, Y. Zhou, X. Wang, G. Guo, Synthesis and characterization of a novel binuclear iron phthalocyanine/reduced graphene oxide nanocomposite for non-precious electrocatalyst for oxygen reduction, Sci. Chin. Chem. 59 (2016) 746-751.

[61] I.S. Hosu, Q. Wang, A. Vasilescu, S.F. Peteu, V. Raditoiu, S. Railian, V. Zaitsev, K. Turcheniuk, Q. Wang, M. Li, Cobalt phthalocyanine tetracarboxylic acid modified reduced graphene oxide: a sensitive matrix for the electrocatalytic detection of peroxynitrite and hydrogen peroxide, RSC adv. 5 (2015) 1474-1484.

[62] M. Shumba, T. Nyokong, Electrode modification using nanocomposites of boron or nitrogen doped graphene oxide and cobalt (II) tetra aminophenoxy phthalocyanine nanoparticles, Electrochim. Acta. 196 (2016) 457-469.

[63] M. Shumba, T. Nyokong, Electrocatalytic activity of nanocomposites of sulphur doped graphene oxide and nanosized cobalt phthalocyanines, Electroanalysis 28 (2016) 3009-3018.

[64] S. Nyoni, T. Nyokong, Electrocatalytic behahiour of cobalt tetraamino-phthalocyanine in the presence of a composite of reduced graphene nanosheets and of multi-walled carbon nanotubes, Electrochim. Acta. 136 (2014) 240-249.

[65] V. Mani, A. Vilian, S.M. Chen, Graphene oxide dispersed carbon nanotube and iron phthalocyanine composite modified electrode for the electrocatalytic determination of hydrazine, Int. J. Electrochem. Sci. 7 (2012) 12774-12785.

[66] V. Mani, S.T. Huang, R. Devasenathipathy, T.C. Yang, Electropolymerization of cobalt tetraamino-phthalocyanine at reduced graphene oxide for electrochemical determination of cysteine and hydrazine, RSC advc. 6 (2016) 38463-38469.

[67] M.S. Polyakov, T.V. Basova, M. Göksel, A. Şenocak, E. Demirbaş, M. Durmuş, B. Kadem, A. Hassan, Effect of covalent and non-covalent linking of zinc (II) phthalocyanine functionalised carbon nanomaterials on the sensor response to ammonia, Synth. Met. 227 (2017) 78-86.

[68] H. Hosseini, M. Mahyari, A. Bagheri, A. Shaabani, A novel bioelectrochemical sensing platform based on covalently attachment of cobalt phthalocyanine to graphene oxide, Biosens. Bioelectron. 52 (2014) 136-142.

[69] T. Taniguchi, H. Tateishi, S. Miyamoto, K. Hatakeyama, C. Ogata, A. Funatsu, S. Hayami, Y. Makinose, N. Matsushita, M. Koinuma, A Self-Assembly Route to an Iron Phthalocyanine/Reduced Graphene Oxide Hybrid Electrocatalyst Affording an Ultrafast Oxygen Reduction Reaction, Part. Part. Sys. Char. 30 (2013) 1063-1070.

[70] H. Xu, J. Xiao, B. Liu, S. Griveau, F. Bedioui, Enhanced electrochemical sensing of thiols based on cobalt phthalocyanine immobilized on nitrogen-doped graphene, Biosen. Bioelectron. 66 (2015) 438-444.

[71] L. Cui, T. Pu, Y. Liu, X. He, Layer-by-layer construction of graphene/cobalt phthalocyanine composite film on activated GCE for application as a nitrite sensor, Electrochim. Acta. 88 (2013) 559-564.

[72] A. Baron, C. Herrero, A. Quaranta, M.F. Charlot, W. Leibl, B. Vauzeilles, A. Aukauloo, Efficient electron transfer through a triazole link in ruthenium (ii) polypyridine type complexes, Chem. Comm. 47 (2011) 11011-11013.

[73] S. Pearton, D. Norton, K. Ip, Y. Heo, T. Steiner, Recent advances in processing of ZnO, J. Vac. Sci. Technol. 22 (2004) 932-948.

[74] Y.H. Ni, X.W. Wei, J.M. Hong, Y. Ye, Hydrothermal preparation and optical properties of ZnO nanorods, Mat. Sci. Eng. B. 121 (2005) 42-47.

[75] M. Ristić, S. Music, M. Ivanda, S. Popović, Sol–gel synthesis and characterization of nanocrystalline ZnO powders, J. Alloys Compd. 397 (2005) L1-L4.

[76] N. Scarisoreanu, D. Matei, G. Dinescu, G. Epurescu, C. Ghica, L. Nistor, M. Dinescu, Properties of ZnO thin films prepared by radio-frequency plasma beam assisted laser ablation, Appl. Surf. Science. 247 (2005) 518-525.

[77] J.J. Wu, S.C. Liu, Low-temperature growth of well-aligned ZnO nanorods by chemical vapor deposition, Adv. Mater. 14 (2002) 215-218.

[78] S.S. Chang, S.O. Yoon, H.J. Park, A. Sakai, Luminescence properties of Zn nanowires prepared by electrochemical etching, Mater. Lett. 53 (2002) 432-436.

[79] R.C. Wang, C.C. Tsai, Efficient synthesis of ZnO nanoparticles, nanowalls, and nanowires by thermal decomposition of zinc acetate at a low temperature, Appl. Phys. A. 94 (2009) 241-245.

[80] S. Aziz, R. Mohamad, M. Mahdavi-Shahri, Green microwave-assisted combustion synthesis of zinc oxide nanoparticles with Citrullus colocynthis (L) Schrad: characterization and biomedical applications, Molecules 22 (2017) 301-314.

[81] S. Ahmed, M. Ahmed, B.L. Swami, S. Ikram, A review on plants extract mediated sythesis of silver nanoparticles for antimicrobial applications: green expertise, J. Adv. Res. 7 (2016) 17-28.

[82] K.M.A. El-Nour, A.A. Eftaiha, A. Al-Warthan, R.A. Ammar, Synthesis and applications of silver nanoparticles, Arab. J. Chem. 3 (2010) 135-140.

[83] A.J. Jeevagan, S.A. John, Synthesis of non-peripheral amine substituted nickel (II) phthalocyanine capped gold nanoparticles and their immobilization on electrode for the electrocatalytic oxidation of hydrazine, RSC Adv. 3 (2013) 2256-2264.

[84] O.M. Bankole, T. Nyokong, Azide-derivatized gold nanosphere "clicked" to indium and zinc phthalocyanines for improved nonlinear optical limiting, J. Mol. Struct. 1136 (2017) 309-320.

[85] A. Maringa, T. Mugadza, E. Antunes, T. Nyokong, Characterization and electrocatalytic behaviour of glassy carbon electrode modified with nickel nanoparticles towards amitrole detection, J. Electroanal. Chem. 700 (2013) 86-92.

[86] A. Maringa, T. Nyokong, Behavior of palladium nanoparticles in the absence or presence of cobalt tetraaminophthalocyanine for the electrooxidation of hydrazine, Electroanalysis 26 (2014) 1068-1077.

[87] A. Maringa, T. Nyokong, The influence of gold nanoparticles on the electroactivity of nickel tetrasulfonated phthalocyanine, J. Porphyrins Phthalocyanines, 18 (2014) 642-651.

[88] M. Delamar, R. Hitmi, J. Pinson, J.M. Saveant, Covalent modification of carbon surfaces by grafting of functionalized aryl radicals produced from electrochemical reduction of diazonium salts, J. Am. Chem. Soc. 114 (1992) 5883-5884.

[89] T. Menanteau, M. Dias, E. Levillain, A.J. Downard, T. Breton, Electrografting via diazonium chemistry: the key role of the aryl substituent in the layer growth mechanism, J. Am. Chem. Soc. 120 (2016) 4423-44297.

[90] G. Liu, T. Bocking, J.J. Gooding, Diazonium salts: Stable monolayers on gold electrodes for sensing applications, J. Electroanal. Chem. 600 (2007) 335-344.

[91] P. Wu, M. Malkoch, J.N. Hunt, R. Vestberg, E. Kaltgrad, M. Finn, V.V. Fokin, K.B. Sharpless, C.J. Hawker, Multivalent, bifunctional dendrimers prepared by click chemistry, Chem. Commun. (2005) 5775-5777.

[92] Z.P. Demko, A Click Chemistry Approach to Tetrazoles by Huisgen 1, 3-Dipolar Cycloaddition: Synthesis of 5-Acyltetrazoles from Azides and Acyl Cyanides, Angew. Chem. Int. Ed. 41 (2002) 2113-2116.

[93] F.G. Banica, A. Ion, in Electrocatalysis-based kinetic determinations, Encyclopedia of Analytical Chemistry, editor (R.A. Mayers) J. Wiley & Sons Ltd. New York, (2000) pages 11115-11125.

[94]. W. Lu, N. Li, W. Chen, Y. Yao, The role of multiwalled carbon nanotubes in enhancing the catalytic activity of cobalt tetraaminophthalocyanine for oxidation of conjugated dyes, Carbon 47 (2009) 3337-3345.

[95] H.S. Yin, Y.L. Zhou, S.Y. Ai, Preparation and characteristic of cobalt phthalocyanine modified carbon paste electrode for bisphenol A detection, J. Electroanal. Chem. 626 (2009) 80-88.

[96] J. Oni, P. Westbroek, T. Nyokong, Voltammetric detection of vitamin B1 at carbon paste electrodes and its determination in tablets, Electroanalysis 14 (2002) 1165-1168.

[97] J.H. Zagal, Metallophthalocyanines as catalysts in electrochemical reactions, Coord. Chem. Rev. 119 (1992) 89-136.

[98] J.H. Zagal, S. griveau, J.F. Silva, T. Nyokong, F. Bedioui, Metallophthalocyanine-based molecular materials as catalysts for electrochemical reactions, Coord. Chem. Rev. 254 (2010) 2755-2791.

[99] L. Carlsen, B.N. Kenessov, S.Y. Batyrbekova, A QSAR/QSTR study on the environmental health impact by the rocket fuel 1, 1-dimethyl hydrazine and its transformation products, Environ. Health Insights. 1 (2008) 11-20.

[100] D. Elder, D. Snodin, A. Teasdale, Control and analysis of hydrazine, hydrazides and hydrazones—genotoxic impurities in active pharmaceutical ingredients (APIs) and drug products, J. Pharm. Biomed. Anal. 54 (2011) 900-910.

[101] J.E. Troyan, Properties, production, and uses of hydrazine, Ind. Eng. Chem, 45 (1953) 2608-2612.

[102] E. Orgilés-Calpena, F. Aran-Ais, A.M. Torró-Palau, C. Orgilés-Barceló, Influence of the chain extender nature on adhesives properties of polyurethane dispersions, J. Disper. Sci. Technol. 33 (2012) 147-154.

[103] M. Ali, M. Jesmin, S. Salam, J. Khanam, M. Islam, M. Islam, Pesticidal Activities of Some Schiff Bases Derived from Benzoin, Salicylaldehyde, Aminophenol and 2, 4 Dinitrophenyl Hydrazine, J. Sci. Res. 1 (2009) 641-646.

[104] M. Lefèvre, E. Proietti, F. Jaouen, J.P. Dodelet, Iron-based catalysts with improved oxygen reduction activity in polymer electrolyte fuel cells, Science. 324 (2009) 71-74.

[105] R.L. Myers, in The 100 most important chemical compounds: a reference guide, Greeenwood puclishing group, Westport, Chapter 47, (2007) pages 144-146.

[106] B. Halliwell, J.M. Gutteridge, in Free radicals in biology and medicine, Oxford University Press, New York, Chapter 2, vol. 2 (2015) pages 30-75.

[107] M.V. Marshall, L.P. Cancro, S.L. Fischman, Hydrogen peroxide: a review of its use in dentistry, J. Periodontol. 66 (1995) 786-796.

[108] W.H. Glaze, J.W. Kang, D.H. Chapin, The chemistry of water treatment processes involving ozone, hydrogen peroxide and ultraviolet radiation, Ozone Sci. Eng. 9 (1987) 335-352.

[109] W. Eul, A. Moeller, N. Steiner, in Hydrogen peroxide, Kirk-Othmer Encyclopedia of chemica technology, editor (J. Kroschwitz), John Wiley & Sons, Hobeken, vol. 13 (2001) pages 1-58.

[110] P.G. Datskos, I. Sauers, Detection of 2-mercaptoethanol using gold-coated micromachined cantilevers, Sens. Actua. B Chem. 61 (1999) 75-82.

[111] S. Griveau, M. Gullpi, J. Pavez, J.H. Zagal, F. Bedioui, Cobalt Phthalocyanine-Based Molecular Materials for the Electrocatalysis and Electroanalysis of 2-Mercaptoethanol, 2-Mercaptoethanesulfonic Acid, Reduced Glutathione and l-Cysteine, Electroanalysis 15 (2003) 779-785.

[112] Y. Chen, L. Gao, M. Feng, L. Gu, N. He, J. Wang, Y. Araki, W.J. Blau, O. Ito, Photophysical and optical limiting properties of axially modified phthalocyanines, Mini Rev. Orga. Chem. 6 (2009) 55-65.

[113] K. E. Sekhosana, E. Amuhaya, T. Nyokong, Nanosecond nonlinear optical limiting properties of new trinuclear lanthanide phthalocyanines in solution and as thin films, Polyhedron 85 (2015) 347-354.

[114] M. Sheik-Bahae, A.A. Said, E.W. Van Stryland, High-sensitivity, single-beam n_2 measurements, Opt. lett. 14 (1989) 955-957.

[115] P. Allongue, M. Delamar, B. Desbat, O. Fagebaume, R. Hitmi, J. Pinson, J.M. Saveant, Covalent modification of carbon surfaces by aryl radicals generated from the electrochemical reduction of diazonium salts, J. Am. Chem. Soc. 119 (1997) 201-207.

[116] Y.A. Sütcüler, A.M. Sevim, T.Ç. Çanak, İ.E. Serhatlı, A. Gül, A novel polystyrene with non-symmetrical zinc phthalocyanines as terminal group, Dyes Pigm. 144 (2017) 58-68.

[117] X.F. Zhang, X. Shao, H. Tian, X. Sun, K. Han, Synthesis, fluorescence, excited triplet state properties and singlet oxygen generation of para-(tert-butylphenoxy) substituted phthalocyanines containing group IV A central elements, Dyes Pigm. 99 (2013) 480-488.

[118] O.M. Bankole, J. Britton, T. Nyokong, Photophysical and non-linear optical behavior of novel tetra alkynyl terminated indium phthalocyanines: Effects of the carbon chain length, Polyhedron 88 (2015) 73-80.

[119] P. Sen, M. Managa, T. Nyokong, New type of metal-free and Zinc (II), In (III), Ga (III) phthalocyanines carrying biologically active substituents: Synthesis and photophysicochemical properties and photodynamic therapy activity, Inorg. Chim. Acta. 491 (2019) 1-8.

[120] H. Dinçer, H. Mert, B.N. Şen, A. Dağ, S. Bayraktar, Synthesis and characterization of novel tetra terminal alkynyl-substituted phthalocyanines and their star polymers via click reaction, Dyes Pigm. 98 (2013) 246-254.

[121] M. Shumba, T. Nyokong, Electrocatalytic application for gold nanoparticles decorated sulfur-nitrogen co-doped graphene oxide nanosheets and nanosized cobalt tetra aminophenoxy phthalocyanine conjugates, Electrochim. Acta. 236 (2017) 212-220.

[122] A. Kumar, M. Zafaryab, A. Umar, M. Rizvi, H. Ansari, S. Ansari, Relief of oxidative stress using curcumin and glutathione functionalized ZnO nanoparticles in HEK-293 cell line, J. Biomed. Nanotechnol. 11 (2015) 1913-1926.

[123] W. Bian, F. Wang, H. Zhang, L. Zhang, L. Wang, S. Shuang, Fluorescent probe for detection of Cu^{2+} using core-shell CdTe/ZnS quantum dots, Luminescence 30 (2015) 1064-1070.

[124] K.E. Sekhosana, T. Nyokong, The nonlinear absorption in new lanthanide double decker pyridine-based phthalocyanines in solution and thin films, Opt. Mater. 47 (2015) 211-218.

[125] S.N. Alam, N. Sharma, L. Kumar, Synthesis of graphene oxide (GO) by modified hummers method and its thermal reduction to obtain reduced graphene oxide (rGO), Graphene 6 (2017) 1-18.

[126] P. Solís-Fernández, R. Rozada, J. Paredes, S. Villar-Rodil, M.J. Fernández-Merino, L. Guardia, A. Martínez-Alonso, J. Tascón, Chemical and microscopic analysis of graphene prepared by different reduction degrees of graphene oxide, J. Alloys Compd. 536 (2012) S532-S537.

[127] S. Eigler, C. Dotzer, F. Hof, W. Bauer, A. Hirsch, Sulfur species in graphene oxide, Chem. Eur. J. 19 (2013) 9490-9496.

[128] Y. Pan, W. Chen, S. Lu, Y. Zhang, Novel aqueous soluble cobalt phthalocyanine: synthesis and catalytic activity on oxidation of 2-mercaptoethanol, Dyes Pigm. 66 (2005) 115-121.

[129] K.I. Ozoemena, T. Nyokong, Comparative electrochemistry and electrocatalytic activities of cobalt, iron and manganese phthalocyanine complexes axially co-ordinated to mercaptopyridine self-assembled monolayer at gold electrodes, Electrochim. Acta. 51 (2006) 2669-2677.

[130] J. Mack, N. Kobayashi, M.J. Stillman, Re-examination of the emission properties of alkoxy-and thioalkyl-substituted phthalocyanines, J. Inorg. Biochem. 104 (2010) 310-317.

[131] F. Aytan Kiliçarslan, B. Keskin, İ. Erden, A. Erdoğmuş, Synthesis, characterization and electrochemical properties of new phthalocyanines, J. Coord. Chem. 70 (2017) 2671-2683.

[132] K. Sakamoto, E. Ohno-Okumura. Syntheses and functional properties of phthalocyanines, Materials 2 (2009) 1127-1179.

[133] T. Nyokong, Electronic spectral and electrochemical behavior of near infrared absorbing metallophthalocyanines, Functional Phthalocyanine Molecular Materials, J. Jiang Springer, Berlin (2010) pages 45-87.

[134] C.C. Leznoff, L.S. Black, A. Hiebert, P.W. Causey, D. Christendat, A. Lever, Red manganese phthalocyanines from highly hindered hexadecaalkoxyphthalocyanines, Inorg. Chim. Acta. 359 (2006) 2690-2999.

[135] L. Li, J.F. Zhao, N. Won, H. Jin, S. Kim, J.Y. Chen, Quantum dot-aluminum phthalocyanine conjugates perform photodynamic reactions to kill cancer cells via fluorescence resonance energy transfer, Nanoscale Res. Lett. 7 (2012) 1-8.

[136] T.M. Klapotke, Recent developments in the chemistry of covalent azides, Chem. Ber. 130 (1997) 443-452.

[137] M.J. Stillman, T. Nyokong, in Phthalocyanines: properties and applications, editors (C.C. Leznoff, A.B.P. Lever) VCH Publishers, New York, Chapter 3, vol. 1 (1989) pages 133-289.

[138] S. Eigler, Y. Hu, Y. Ishii, A. Hirsch, Controlled functionalization of graphene oxide with sodium azide, Nanoscale 5 (2013) 12136-12139.

[139] Z. Xu, H. Li, W. Li, G. Cao, Q. Zhang, K. Li, Q. Fu, J. Wang, Large-scale production of graphene by microwave synthesis and rapid cooling, Chem. Commun. 47 (2011) 1166-1168.

[140] M. Qi, Z. Ren, Y. Jiao, Y. Zhou, X. Xu, W. Li, J. Li, X. Zheng, J. Bai, Hydrogen kinetics on scalable graphene growth by atmospheric pressure chemical vapor deposition with acetylene, J. Phys. Chem. C. 117 (2013) 14348-15353.

[141] N.M. Mahmoodi, S.M. Maroofi, M. Mazarji, G. Nabi-Bidhendi, Preparation of modified reduced graphene oxide nanosheet with cationic surfactant and its dye adsorption ability from colored wastewater, J. Surfactants Deterg. 20 (2017) 1085-1093.

[142] J. Mack, M.J. Stillman, N. Kobayashi, Application of MCD spectroscopy to porphyrinoids, Coord. Chem. Rev. 251 (2007) 429-453.

[143] J. Zhou, F. Zhao. Y. Wang, Y. Zhang, L. Yang, Size-controlled synthesis of ZnO nanoparticles and their photoluminescence properties, J. lumin. 122 (2007) 195-197.

[144] Z.M. Khoshhesab, M. Sarfaraz, M.A. Asadabad, Preparation of ZnO nanostructures by chemical precipitation method, Synth. React. Inorg. Met. Org. Nano-Metal Chem. 41 (2011) 814-819.

[145] P.K. Prajapati, A.Kumar, S.L. Jain, First photocatalytic synthesis of cyclic carbonates from CO_2 and epoxides using $CoPc/TiO_2$ hybrid under mild conditions, ACS Sustain. Chem. Eng. 6 (2018) 7799-7809.

[146] J. Pillay, K.I. Ozoemena, R.T. Tshikhudo, R.M. Moutloali, Monolayer-protected clusters of gold nanoparticles: impacts of stabilizing ligands on the heterogeneous electron transfer dynamics and voltammetric detection, Langmuir 26 (2010) 9061-9068.

[147] J.J. Gooding, V.G. Praig, E. A.H. Hall, Platinum-Catalyzed Enzyme Electrodes Immobilized on Gold Using Self-Assembled Layers, Anal. Chem. 70 (1998) 2396-2402.

[148] C.A. Caro, F. Bedioui, J.H. Zagal, Electrocatalytic oxidation of nitrite on a vitreous carbon electrode modified with cobalt phthalocyanine, Electrochim. Acta. 47 (2002) 1489–1494.

[149] Z. Li, M. Lieberman, W. Hill, XPS and SERS study of silicon phthalocyanine monolayers: umbrella vs octopus design strategies for formation of oriented SAMs, Langmuir 17 (2001) 4887–4894.

[150] E.M. Orazem, B. Tribollet, An intergrated approach to electrochemical impediance spectroscopy, Electrem. Acta 53 (2008) 7360-7366.

[151] J. Pillay, K.I. Ozoemena, Single-walled carbon nanotube-induced crystallinity on the electropolymeric film of tetraaminophthalocyaninatonickel (II) complex: impact on the rate of heterogeneous electron transfer, Chem. Phys. Lett. 441 (2007) 72-77.

[152] D. Nkosi, J. Pillay. K.I. Ozoemena, K. Nouneh, M. Oyama, Heterogeneous electron transfer kinetics and electrocatalytic behaviour of mixed self-assembled ferrocenes and SWCNT layers, Phys. Chem. Chem. Phys. 12 (2010) 604-613.

[153] M. Coates, T. Nyokong, Characterization of glassy carbon electrodes modified with carbon nanotubes and iron phthalocyanine through grafting and click chemistry, Electrochim. Acta. 91 (2013) 158-165.

[154] A. Maringa, E. Antunes, T. Nyokong, Electrochemical behaviour of gold nanoparticles and Co tetraaminophthalocyanine on glassy carbon electrode, Electrochim. Acta. 121 (2014) 93-101.

[155] J. Pavez, M. Paez. A. Ringuedé, F. Bedioui, J. H. Zagal, Effect of film thickness on the electro-reduction of molecular oxygen on electropolymerized cobalt tetra-aminophthalocyanine films, J. Solid State Electrochem. 9 (2005) 21–29.

[156] K.I. Ozoemena, Anodic oxidation and amperometric sensing of hydrazine at a glassy carbon electrode modified with cobalt (II) phthalocyanine–cobalt (II) tetraphenylporphyrin (CoPc-(CoTPP) 4) supramolecular complex, Sensors 6 (2006) 874-891.

[157] D.A. Geraldo, C.A. Togo. J. Limson, T. Nyokong, Electrooxidation of hydrazine catalyzed by noncovalently functionalized single-walled carbon nanotubes with CoPc, Electrochim. Acta. 53 (2008) 8051-8057.

[158] Q.Y. Peng, T.F. Guarr, Electro-oxidation of hydrazine at electrodes modified with polymeric cobalt phthalocyanine, Electrochim. Acta. 39 (1994) 2629-2632.

[159] S. Dutta, C. Ray. S. Mallick, S. Sarkar, A. Roy, T. Pal, Au@ Pd core–shell nanoparticles-decorated reduced graphene oxide: a highly sensitive and selective platform for electrochemical detection of hydrazine, RSC Adv. 5 (2015) 51690-51700.

[160] T. Nyokong, in N4-macrocyclic metal complexes, editors (J.H. Zagal, F. Bedioui, J.P. Dodelet) Springer, New York, Chapter 7 (2006) pages 315-347.

[161] F. Tasca, F.J. Recio, R. Venegas, D.A. Geraldo, M. Sancy, J.H. Zagal, Linear versus volcano correlations for the electrocatalytic oxidation of hydrazine on graphite electrodes modified with MN4 macrocyclic complexes, Electrochim. Acta. 140 (2014) 314-319.

[162] D.A. Venegas-Yazigi, G.I. Cárdenas-Jirón, J.H. Zagal, Theoretical study of the electron transfer reaction of hydrazine with cobalt (II) phthalocyanine and substituted cobalt (II) phthalocyanines, J. Coord. Chem. 56 (2003) 1269-1275.

[163] A. Salimi, K. Abdi, Enhancement of the analytical properties and catalytic activity of a nickel hexacyanoferrate modified carbon ceramic electrode prepared by two-step sol–gel technique: application to amperometric detection of hydrazine and hydroxyl amine, Talanta 63 (2004) 475-483.

[164] J. Sun, Y.H. Fang. Z.P. Liu, Electrocatalytic oxygen reduction kinetics on Fe-center of nitrogen-doped graphene, Phys. Chem. Chem. Phys. 16 (2014) 13733-13740.

[165] A.S. Adekunle, K.I. Ozoemena. Insights into the electro-oxidation of hydrazine at single-walled carbon-nanotube-modified edge-plane pyrolytic graphite electrodes electro-decorated with metal and metal oxide films, J. Solid State Electr. 12 (2008) 1325-1336.

[166] Z. Galus, in Fundamentals of electrochemical analysis, Halsted Press, New York (1976) pages 249-280.

[167] S. Corona-Avendaño, M. Ramirez-Silva, M. Romero-Romo, A. Rojas-Hernández, M. Palomar-Pardavé, Influence of the $HClO_4$ concentration on the ß-CD electropolimerization over a carbon paste electrode and on dopamine's electrochemical response, Electrochim. Acta. 89 (2013) 854-860.

[168] P. Mashazi, K.I. Ozoemena, T. Nyokong, Tetracarboxylic acid cobalt phthalocyanine SAM on gold: Potential applications as amperometric sensor for H_2O_2 and fabrication of glucose biosensor, Electrochem. Acta. 52 (2006) 177-186.

 [169] A.S. Adekunle, K.I. Ozoemena. Electrocatalytic oxidation of diethylaminoethanethiol and hydrazine at single-walled carbon nanotubes modified with Prussian blue nanoparticles, Electroanalysis 22 (2010) 2519-2528.

[170] R. Ojania, J.B. Raoof, R. Babazadeh, Electrocatalytic oxidation of hydrogen peroxide using iodide as mediator; application for its simple and selective determination, J. Chin. Chem. Soc. 57 (2010) 1042-1049.

[171] Q. Chen, D. Li, Q. Zhu, H. Zheng, J.G. Xu, Application of iron-tetrasulfonatophthalocyanine as a new mimetic peroxidase in the determination of hydrogen peroxide with p-hydroxyphenylpropionic acid as a substrate, Anal. Chem. Acta. 381 (1999) 175-182.

[172] Z.H. Li, H. Guedri, B. Viguier, S.G. Sun, J.L. Marty, Optimization of hydrogen peroxide detection for a methyl mercaptan biosensor, Sensors 13 (2013) 5028-5039.

[173] M. Shumba, T. Nyokong, Development of nanocomposites of phosphorus-nitrogen co-doped graphene oxide nanosheets and nanosized cobalt phthalocyanines for electrocatalysis, Electrochim. Acta. 213 (2016) 529-539.

[174] G.I. Cárdenas-Jiron, M.A. Gulppi, C.A. Caro, R. del Río, M. Páez, J.H. Zagal, Reactivity of electrodes modified with substituted metallophthalocyanines. Correlations with redox potentials, Hammett parameters and donor–acceptor intermolecular hardness, Electrochim. Acta. 46 (2001) 3227-3235.

[175] K. Gong, F. Du, Z. Xia, M. Durstock, L. Dai, Nitrogen-doped carbon nanotube arrays with high electrocatalytic activity for oxygen reduction, Science 323 (2009) 760-764.

[176] Z.S. Wu, S. Yang, Y. Sun, K. Parvez, X. Feng, K. Müllen, 3D nitrogen-doped graphene aerogel-supported Fe_3O_4 nanoparticles as efficient electrocatalysts for the oxygen reduction reaction, J. Am. Chem. Soc. 134 (2012) 9082-9085.

[177] C. Zhang, F.R.F. Fan, A.J. Bard, Electrochemistry of oxygen in concentrated NaOH solutions: solubility, diffusion coefficients, and superoxide formation, J. Am. Chem. Soc. 131 (2009) 177-181.

[178] S. Wang, D. Yu, L. Dai, Polyelectrolyte functionalized carbon nanotubes as efficient metal-free electrocatalysts for oxygen reduction, J. Am. Chem. Soc. 133 (2011) 5182-5185.

[179] T. Kinumoto, M. Inaba, Y. Nakayama, K. Ogata, R. Umebayashi, A. Tasaka, Y. Iriyama, T. Abe, Z. Ogumi, Durability of perfluorinated ionomer membrane against hydrogen peroxide, J. Power Sources. 158 (2006) 1222-1228.

[180] S. Treimer, A. Tang, D.C. Johnson, A Consideration of the application of Koutecký-Levich plots in the diagnoses of charge-transfer mechanisms at rotated disk electrodes, Electroanalysis 14 (2002) 165-171.

[181] P. Lei, Y. Zhou, R. Zhu, Y. Liu, C. Dong, S. Shuang, Facile synthesis of iron phthalocyanine functionalized N, B–doped reduced graphene oxide nanocomposites and sensitive electrochemical detection for glutathione, Sens. Actuators B Chem. 297 (2019) 126756-126763.

[182] T. Mugadza, T. Nyokong, Synthesis, characterization and the electrocatalytic behaviour of nickel (II) tetraamino-phthalocyanine chemically linked to single walled carbon nanotubes, Electrochim. Acta. 55 (2010) 6049-6057.

[183] T. Mugadza, T. Nyokong, Electrocatalytic oxidation of amitrole and diuron on iron (II) tetraaminophthalocyanine-single walled carbon nanotube dendrimer, Electrochim. Acta, 55 (2010) 2606-2613.

[184] M.P. Siswana, K.I. Ozoemena, T. Nyokong, Electrocatalysis of asulam on cobalt phthalocyanine modified multi-walled carbon nanotubes immobilized on a basal plane pyrolytic graphite electrode, Electrochim. Acta, 52 (2006) 114-122.

[185] J.R. Darwent, P. Douglas, A. Harriman, G. Porter, M.C. Richoux, Metal phthalocyanines and porphyrins as photosensitizers for reduction of water to hydrogen, Coord. Chem. Rev. 44 (1982) 83-126.

[186] M.G. Vivas, L. de Boni, L. Gaffo, C.R. Mendonca, Investigation of ground and excited state photophysical properties of gadolinium phthalocyanine, Dyes Pigm. 101 (2014) 338-343.

[187] D. Dini, M. Hanack, In Phthalocyanines: Properties and Materials, editors (K. Kadish, K. Smith, R. Guilard), Chapter 107, Academic Press, New York, vol. 17 (2003) pages 1-31.

[188] M.P. Cifuentes, M.G. Humphrey, Alkynyl compounds and nonlinear optics, J. Organomet. Chem. 689 (2004) 3968-3981.

[189] Q.W. Song, C. Zhang, R. Gross, R. Birge, Optical limiting by chemically enhanced bacteriorhodopsin films, Opt. Lett. 18 (1993) 775-777.

[190] M. Kahouli, A. Barhoumi, A. Bouzid, A. Al-Hajry, S. Guermazi, Structural and optical properties of ZnO nanoparticles prepared by direct precipitation method, Superlattices Microstruct. 85 (2015) 7-23.

[191] R. Javed, M. Usman, S. Tabassum, M. Zia, Effect of capping agents: structural, optical and biological properties of ZnO nanoparticles, Appl. Surf. Sci. 386 (2016) 319-326.

[192] S. Mgidlana, D.O. Oluwole, T. Nyokong, Fabrication of efficient nonlinear optical absorber using Zn phthalocyanine-semiconductor quantum dots conjugates, Polyhedron 159 (2019) 102-115.

Appendix
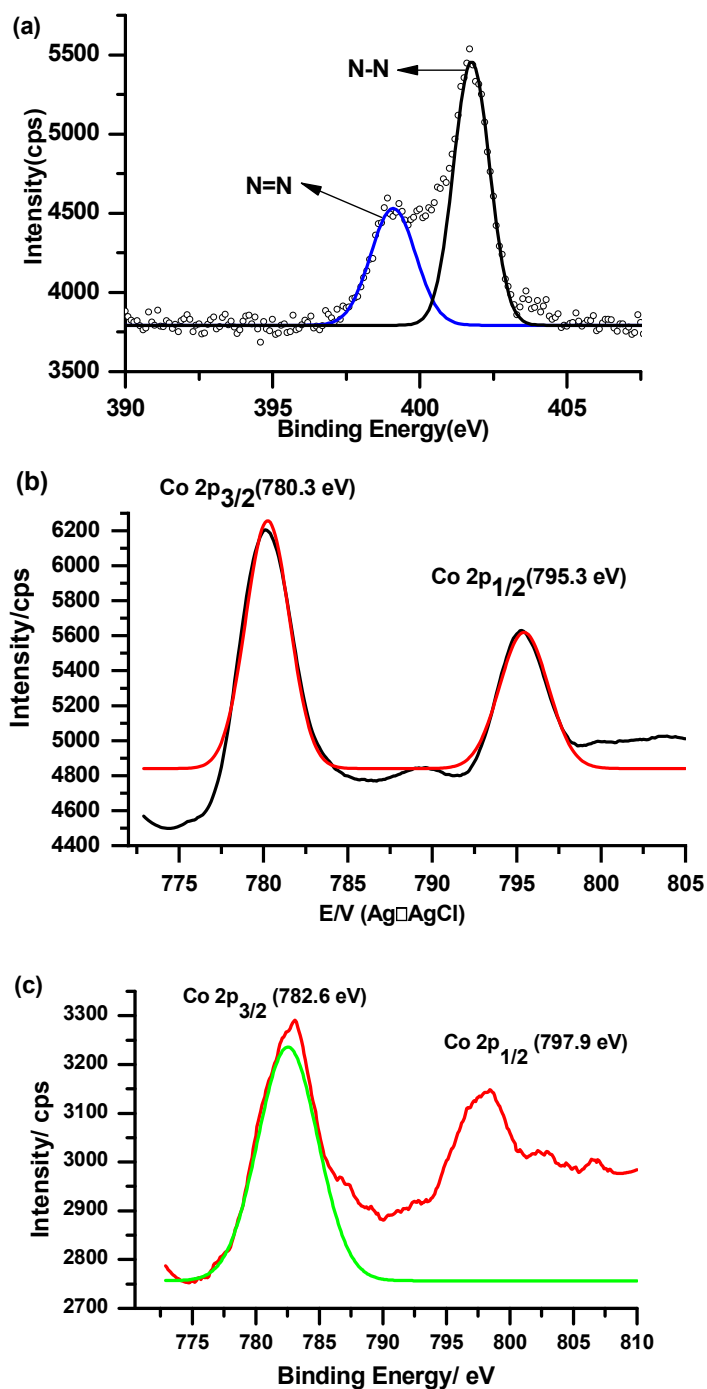
Figure A1: XPS deconvoluted N 1s spectrum for complex **4** alone (a), Co 2p spectra of (b) complex **4** and (c) **4**-clicked
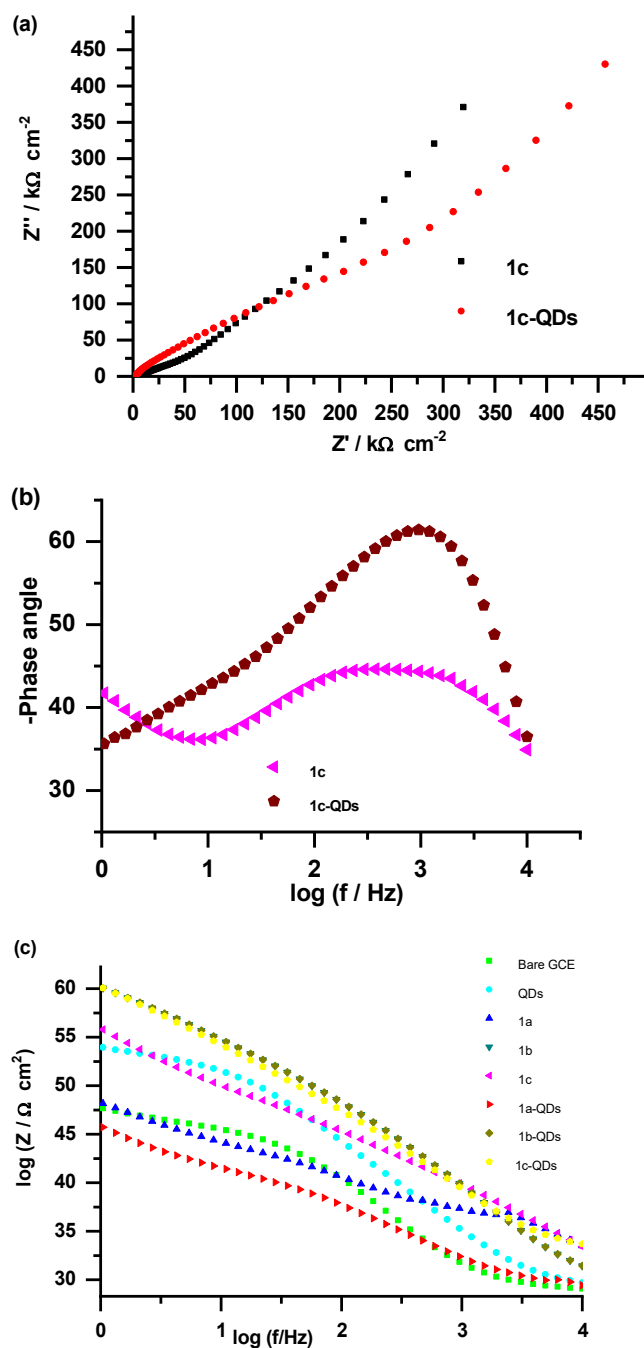
Figure A2: (a) Nyquist plot, (b) bode plots (-phase angle vs log (f/Hz)) and (c) Log (Z/ Ω cm^2) vs log (f/Hz) in 0.1 M KCl containing 1 mM [Fe(CN)$_6$]$^{3-/4-}$ solution.

SEM HV: 20.00 kV   SEM MAG: 753 x   VEGA\\ TESCAN
WD: 20.09 mm   Det: SE   20 µm
SEM MAG: 753 x   Date(m/d/y): 01/17/20   Rhodes University SEM
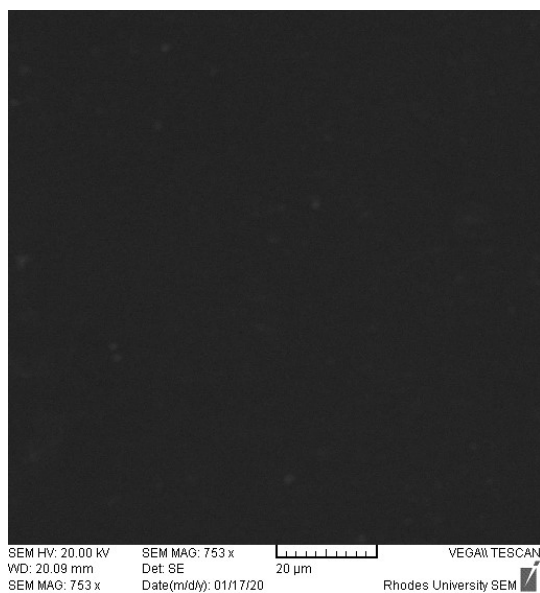
Figure A3: SEM image of bare GCE

(a)

SEM HV: 20.00 kV   SEM MAG: 4.57 kx   VEGA\\ TESCAN
WD: 19.53 mm   Det: SE   5 µm
SEM MAG: 4.57 kx   Date(m/d/y): 01/17/20   Rhodes University SEM

Spectrum 4

Full Scale 5207 cts Cursor: 0.000   keV

(b)
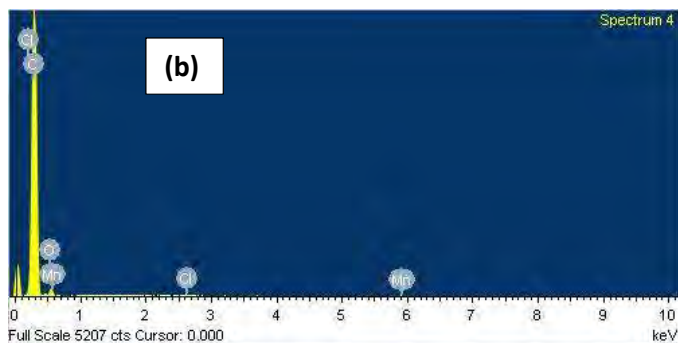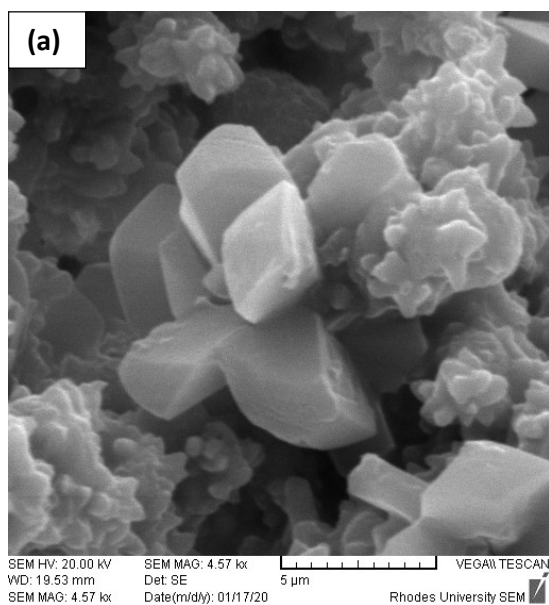
Figure A4. (a) SEM image of **5b** and the corresponding (b) EDX spectrum.
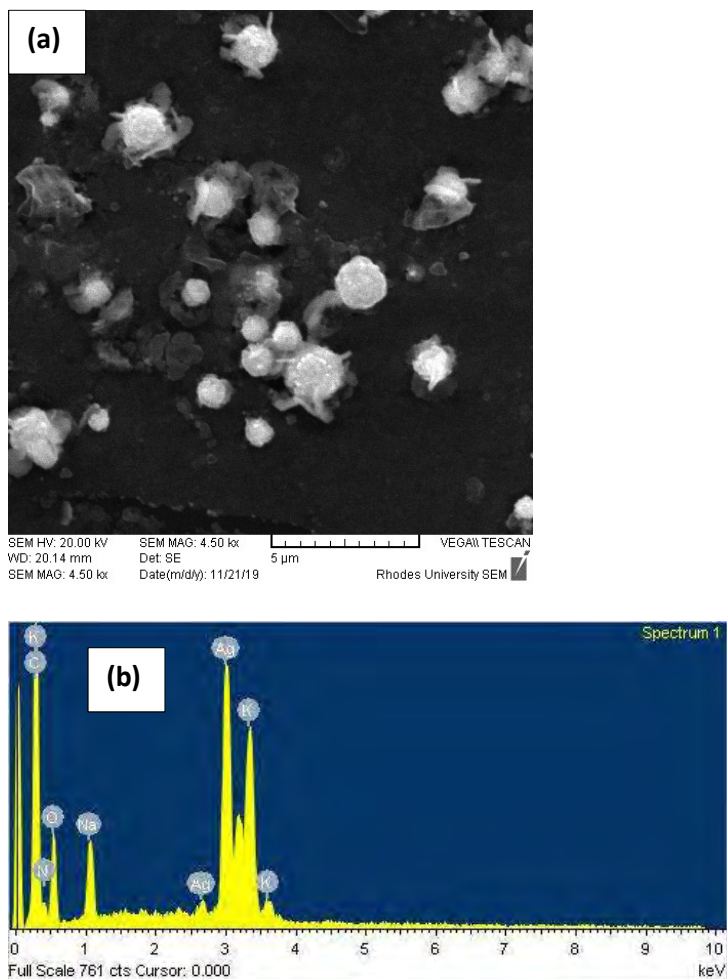
Figure A5: (a) SEM image of AgNPs and the corresponding (b) EDX spectrum.

(b)
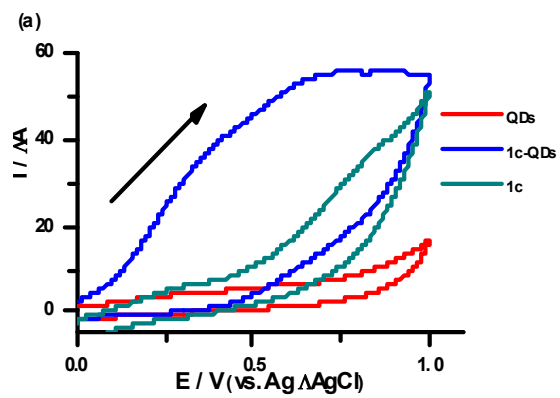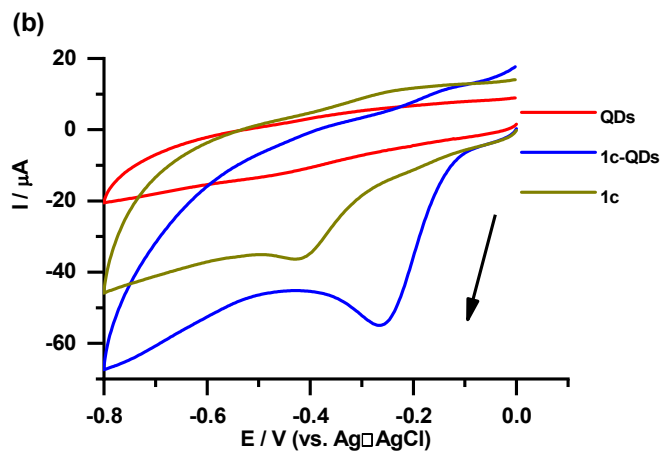
Figure A6: Cyclic voltammograms of a selection of modified electrodes in (a) 1mM hydrogen peroxide (purged with argon) and (b) in 0.1 M NaOH saturated with oxygen, for **1c**, **1c**-QDs and QDs. Scan rate 100 mVs^{-1}

(a)

(b)

$y = -0.13258x - 0.05969$

$R^2 = 0.98999$
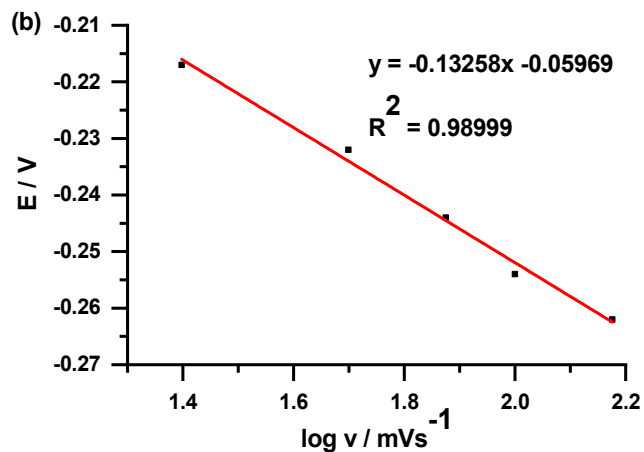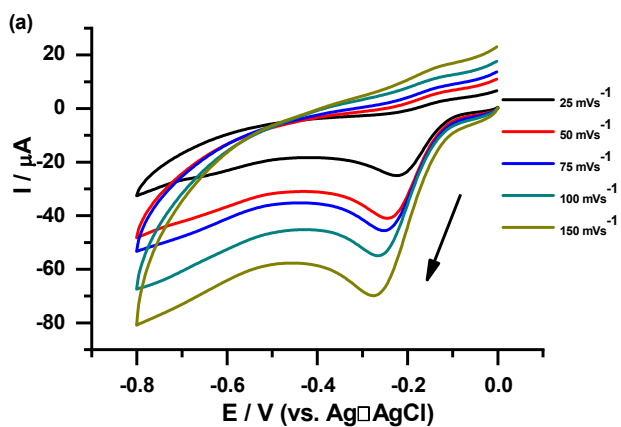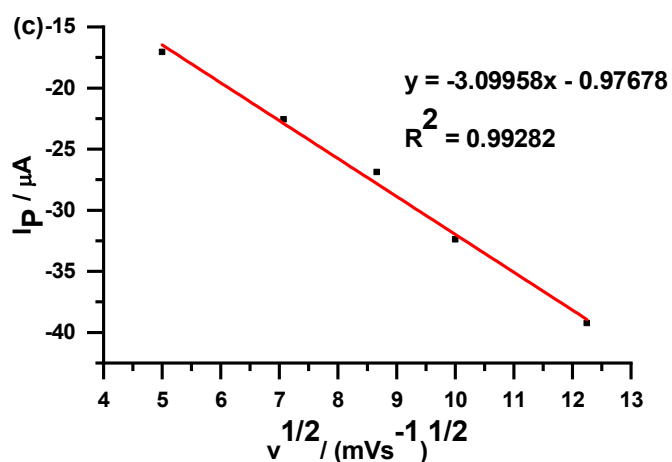
Figure A7: (a) cyclic voltammograms of **1c**-QDs electrode at different scan rates (25, 50, 100,150, 200 and 250 mVs^{-1}, inner to outer), (b) plot of peak potential (E$_p$) against the logarithm of scan rate (log v), and (c) plot of current versus the square root of scan rate. All in the presence of 0.1 M NaOH saturated with oxygen.
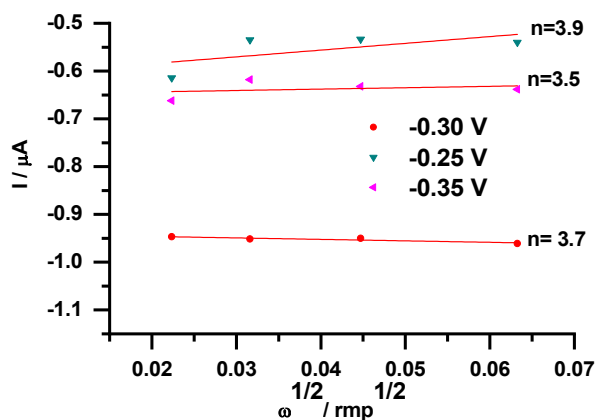

Figure A8. The Koutecky- Levich plots (I vs. $\omega^{1/2}$)